Application of Dynamic Nuclear Polarisation and other advanced Magnetic Resonance methods for studies of $A\beta_{(1-40)}$ interactions with lipids

By Caitlin Connolly, MSc

Thesis submitted to the University of Nottingham for the degree of Doctor of Philosophy

December 2023

Contents

Abbreviations

Lipids, proteins, and biological relevance

Aβ - Amyloid Beta

AD - Alzheimer’s Disease

AICD - APP Intracellular Domain

APP - Amyloid Precursor Protein

BACE1 - β secretase-1 enzyme

CHC - Central Hydrophobic Cluster

CTF - Carboxyterminal Fragment

Chol - Cholesterol

CHC - Central Hydrophobic Cluster

DMPC - 1,2-dimyristoyl-sn-glycero-3-phosphocholine

DMPG - 1,2-Dimyristoyl-sn-glycero-3-phosphoglycerol

DMPS - 1,2-dimyristoyl-sn-glycero-3-phospho-L-serine

IDE - Insulin-degrading enzyme

LM - Lipid Mimic

GM1 - Ganglioside GM1

PA - Phosphatidic acid

PC – Phosphatidylcholine

PE - Phosphatidylethanolamine

PG - Phosphatidylglycerol

P:L - Protein-to-Lipid ratio

POPC - 1-palmitoyl-2-oleoyl-glycero-3-phosphocholine

POPS - 1-palmitoyl-2-oleoyl-sn-glycero-3-phosphoethanolamine

POPG - 1-palmitoyl-2-oleoyl-sn-glycero-3-phospho-(1'-rac-glycerol)

POPS - 1-palmitoyl-2-oleoyl-sn-glycero-3-phospho-L-serine

PSEN1 or 2 - Presenilin 1 or 2

PS – Phosphatidylserine

sAPPβ - secreted APPβ

Sphin - Sphingomyelin

SPM - Synaptic Plasma Membranes

Other chemicals

DMSO - Dimethyl Sulfoxide

HFIP - Hexafluroisopropanol

NaOH - Sodium Hydroxide

Magnetic resonance

CE - Cross Effect

CSA - Chemical Shift Anisotropy

DARR - Dipolar Assisted Rotational Resonance

DNP - Dynamic Nuclear Polarisation

EPR - Electron Paramagnetic Resonance

FID - Free Induction Decay

FT - Fourier Transform

FWHM - Full Width Half Maxima

HDPE - High-Density Polyethylene

MAS - Magic Angle Spinning

μw - Microwave

NMR - Nuclear Magnetic Resonance

PRE - Paramagnetic Relaxation Enhancement

POST-C7 - Permutationally Offset Stabilised-C7

RF - Radiofrequency

ssNMR - solid-state Nuclear Magnetic Resonance

Other techniques

AFM - Atomic Force Microscopy

CD - Circular Dichroism

DEER - Double Electron-Electron Resonance

EM - Electron Microscopy

HPLC - High-Performance Liquid Chromatography

PCA - Principal Component Analysis

SH - Spherical Harmonic

TEM - Transmission Electron Microscopy

Abstract

The structural characterisation of Amyloid Beta (Aβ) interacting with cellular membranes models has previously used Circular Dichroism (CD) and Electron Microscopy (EM), however, these methods lack atomic resolution. This is overcome by the use of solid-state Nuclear Magnetic Resonance (ssNMR) which provides information at an atomic level. ssNMR is a commonly used method in several disciplinaries but has proved useful in the structural determination of many biological systems. Although ssNMR has been employed in the structural determination of proteins, including Aβ, its application has been limited due to low sensitivity. Dynamic Nuclear Polarisation (DNP) utilises microwave (μw) irradiation to increase NMR signals, allowing for the secondary structure elucidation of proteins. This method has been shown to increase protein signals by orders of magnitude and is an efficient method when investigating protein systems.

The Aβ peptide has been proposed to be the main cause of various downstream events leading to Alzheimer's disease (AD), due to the dysregulation of its production and clearance within the brain. The exact mechanism causing neuronal cell death is unclear, however, the direct interaction of Aβ with cellular membranes is thought to be of key importance. Earlier studies suggested that Aβ fibrils, the thermodynamic end point of the peptide's self-assembly pathway, were the main causative agent in AD. However, the lack of correlation between fibrillar concentration and AD severity led to the proposal that other neurotoxic intermediate species may be present and responsible for neurodegeneration. This includes oligomers of various sizes and protofibrils, a meta-stable shorter fibrillar structure, as well as other fibrillar polymorphs. Characterisation of Aβ interactions with lipid membranes, including biologically relevant systems, at a range of stages of the self-assembly pathway is therefore an important goal.

The main aim of this thesis is to apply DNP enhanced ssNMR to investigate the structure of $A\beta_{(1-40)}$ during interactions with a range of membranes, including biologically relevant systems. This also includes studies of the interaction between DNP additives and membrane structure. The second part of this thesis focuses on the application of Spherical Harmonic (SH) techniques to Double Electron-Electron Resonance (DEER) datasets along with Principal Component Analysis (PCA) to characterise orientation selection and deduce distance measurements in a variety of biomolecules with the end goal of applying this method to $A\beta_{(1-40)}$ datasets.

Firstly, understanding the interaction between DNP additives, such as the polarising agent and the cryoprotectant glycerol, and lipid membranes is crucial for investigating membrane dynamics and protein-membrane interactions as well as ensuring physiological conditions are maintained throughout the later stages of experimentation. A protocol was adapted for the production of a Lipid Mimic (LM) membrane system which mimics the outer leaflet of Synaptic Plasma Membranes (SPMs), introducing biologically relevant systems. This chapter employs ^{13}C Paramagnetic Relaxation Enhancement (PRE) measurements to probe the insertion depth of the AMUPol biradical into lipid membranes, focusing on 1,2-dimyristoyl-sn-glycero-3-phosphocholine (DMPC) either alone or part of the Lipid Mimic (LM) system. The ability of glycerol to partition into the membrane is highlighted, influencing the biradical-membrane proximity. Changes to the lipid membrane structure were also assessed by analysing static and Magic Angle Spinning (MAS) ^{31}P Chemical Shift Anisotropy (CSA) spectra in a range of membrane systems. This is possible due to the phosphate groups contained within the lipid headgroups which can reveal changes in the structure and dynamics of the membrane induced by the dopant and cryoprotectant.

Secondly, ssNMR with signals enhanced by DNP was conducted to probe the structure and conformational changes of $A\beta_{(1-40)}$ in a range of membrane systems including the biologically relevant LM system. DNP enhancements of a factor of ~11-50 were seen for lipid and protein ^{13}C spins under a range of conditions. Sample conditions were optimised to give maximum protein to lipid binding and ensure lipid homogeneity. 2D Double-Quantum Single-Quantum (DQSQ) correlation and Dipolar Assisted Rotational Resonance (DARR) spectroscopy was shown to be effective when studying labelled residues within the $A\beta_{(1-40)}$ proteins. Useful contacts were determined via 2D DARR spectroscopy, allowing for a predicted $A\beta_{(1-40)}$ structural model to be produced. DQSQ spectra was shown to be beneficial in reducing natural abundance lipid and glycerol ^{13}C signals which otherwise crowd spectra. Secondary chemical shifts of the labelled residues within $A\beta_{(1-40)}$ have suggested a β-sheet conformation either at initial or later stage binding with a simple membrane. ^{1}H-detection is employed to determine the secondary structure of fibrils with comparisons made to DNP regarding sensitivity and resolution. This work demonstrates the exciting possibility of determining the structure of the protein at different stages of the self-assembly process.

This work has also demonstrated the effective use of complementary studies between DNP enhanced NMR, room temperature NMR, High-Performance Liquid

Chromatography (HPLC), Transmission EM (TEM) and Atomic Force Microscopy (AFM) to evaluate the structure of $A\beta_{(1-40)}$ and the conformational changes it undergoes when interacting with lipid membranes.

Finally, SH-techniques were applied to examine a range of published DEER datasets along with PCA to characterise the degree to which orientation selection affects them. Distance distribution analysis is conducted following PCA, offering a detailed comparison of the obtained distances with those reported in the original publications. Effects of biradical flexibility and field strength on the number of Principal Components (PCs) was evaluated. This work provides the basis for distance measurements across a variety of samples, wider than initially thought, including a varying level of flexibility of biradicals, with the aim of utilising this method in the study of distances in $A\beta_{(1-40)}$.

Acknowledgements

Firstly, I would like to thank my supervisor, Dr Alexey Potapov for your help, support, and guidance throughout my postgraduate study. I feel very lucky to be involved in such a multidisciplinary study and having the opportunities I have had. Thank you for your support through COVID, adapting to research how we had to and for always helping to continue our work.

A huge thank you to Thomas Deo who provided initial training and mentoring, as well as the tea chats over a nitrogen fill. My work would not have been possible without some of the amazing work you did previously. Thanks to Marco Mais for his NMR support whilst battling an ongoing stream of system and software problems with me.

None of this would be possible without the DNP managers Subhradip Paul and Paolo Cerreia Vioglio as well as Dr Walter Kockenberger for DNP training, problem solving and distanced help throughout the years. Without you all my patience for the DNP would have been a lot smaller.

Thank you to Andrew Peters for making my 5am lab trips possible, and to Sarah Wolf who provided lab support, laughs and the odd SPMIC ghost story. Wouldn't have enjoyed cleaning fridges with anyone else.

From the BDI I would like to thank Dr Huw Williams and Dr Kevin Butler who allowed me time on the room temperature systems, again providing training and technical support. Thank you for finding ways to allow me to continue my work from home.

I would also like to thank Denise McLean and Michael Fay from the nmRC for their TEM operating, training, and guidance and for adapting to COVID with me. Also, Rhys Griffiths and Andrea Bombana from the Chemistry department for their HPLC training and help with sample running during COVID. Thank you to Vladimir Korolkov from park systems for allowing us access to his amazing equipment.

I would like to thank Abi Spicer, Dr Alex Daniel, Daniel Cocking, Natalie Rhodes and Sebastian Coleman for your constant support in and out of work, for the many tea breaks, for the python help, and constant guidance for each other. It's been a privilege to go through the PhDs together. I wish for those who have not yet completed the best of luck. Thank you for Dr Griffin for being a woman in STEM inspiration and for all your years of university support and friendship, as well as the rest of the science alliance.

Thank you to my family for keeping me going through my many years of university. Thank you for my stubborn attitude and providing an atmosphere where I believed I would be able to do this backed with ongoing love and support. Thank you to Becky for being the reason I got into science in the first place. I really would not be where I am without any of you.

One last final thanks to Adam who was there with a cup of tea or home cooked meal when I wouldn't have moved off my laptop for hours. Thanks for putting up with me and my many jobs whilst going through this. You really have provided a different level of support.

1. Introduction

Over the past 100 years our understanding of Alzheimer's disease (AD) has expanded dramatically and there are now a number of hypotheses attempting to explain the pathology of the disease. However, research still lacks a singular theory which would integrate existing research and explain variability in the disease development between patients. This is now at the forefront of AD research[1].

AD is a complex neurodegenerative disease and the most common form of dementia, with an ever-increasing global cost partially attributed to an aging population[2]. It involves the aggregation of proteins, chronic inflammation, and neuronal cell loss and currently has no cure. Due to the complexity of AD, the neurotoxicity associated with the disease is also thought to include a combination of genetic and environmental factors which affect the brain over time[3]. The Amyloid Beta (Aβ) protein is at the centre of AD research and is one of the major hallmarks of the disease, along with neurofibrillary tau tangles. The amyloid cascade hypothesis suggests that the dysregulation in the production and clearance of the Aβ protein is mainly responsible for the pathogenesis of AD[4]. This theory alone has influenced the nature of research carried out over the past few decades, however several therapeutics aimed at reducing the production or aggregation of Aβ have failed in later trials and this has brought more focus to this area[5].

Aβ is produced by proteolytic cleavage of the Amyloid Precursor Protein (APP) by β secretase-1 enzyme (BACE1) forming secreted APPβ (sAPPβ) and a carboxyterminal fragment (CTF). The CTF is then sequentially cleaved by γ-secretase forming Aβ of varying length, normally between 38-43 amino acids, as well as the amino terminal APP intracellular domain (AICD) segment. APP is an integral membrane protein expressed in several tissues particularly in the synapses of neurones. Supporting evidence for the amyloid cascade hypothesis is the prevalence of AD in individuals who carry mutations in APP or presenilin 1 or 2 (PSEN1 or 2) which are present within γ-secretase. These mutations increase the production of longer, more self-aggregating forms of Aβ such as $A\beta_{(1-42)}$. The other major common form within the brain is $A\beta_{(1-40)}$, a shorter, less aggressive self-aggregating form of the protein. However there is an important inconsistency between the level of Aβ accumulation and deposition and neuronal loss and cognitive decline implying there are other important factors contributing the disease progression[6]. One of the proposed

neurotoxic mechanisms is now suggested to be due to the presence of Aβ assemblies differing in structure from amyloid fibrils[7].

Aβ has the ability to self-assemble into several structures, where Aβ fibrils are the stable endpoint to the self-assembly pathway, and intermediary structures include oligomers and meta-stable protofibrils. Amyloid fibrils are insoluble with structural models showing U-shaped conformations, where the β-strand segments form an in-register, parallel β-sheet[8]. These fibrils usually have diameters from 2 to 20 nm and several micrometres in length[9]. However, it has been shown that there is a large level of variation in the protein structures from published work. Electron and Atomic Force Microscopy (AFM) showed long unbranching fibrils made up from protofilaments which often twist around one another to form the mature fibril. To further this, cryo-Electron Microscopy (EM) indicated a single fibril was comprised of four protofilaments wound around a central core. The structure of Aβ has been shown to differ dramatically depending on the stage of the self-assembly pathway[10]. Protofibrils for example have been shown to be shorter in length than mature fibrils with a greater curvature. D23N- $A\beta_{(1-40)}$ protofibrils contain residues that form β strands that interact through hydrophobic side chain contacts. However the supramolecular structure differs in that the alternating antiparallel alignment of the $A\beta_{(1-40)}$ molecules creates a double-layered antiparallel cross-β unit[11]. Oligomers are shown to be more compact enclosed structures some of which are thought to be composed of antiparallel β-sheets comprising β-hairpins. The twisted shape of the oligomers with hydrophobic surfaces and exposed hydrogen-bonding edges allows the structure to be compact[12]. One of the main findings of published works is that the conformation in nonfibrillar intermediates is similar to the stable conformation in fibrils. However most data indicates that the in-register parallel beta sheets are not present in non-fibrillar intermediates[13]. There is also evidence to suggest that conformations similar to the U-shape conformation in mature fibrils are populated at several earlier stages of the pathway before the formation of ordered β-sheets and before the formation of large oligomers[14]. The interaction of such intermediary structures with cellular membranes is thought to be of key importance to the neurotoxicity caused by Aβ. However, these interactions are still not fully understood.

Simulations have now allowed investigation of the time evolution of monomer folding events of $A\beta_{(1-40)}$ along the self-assembly pathway. Initially $A\beta_{(1-40)}$ monomers are in random coil conformation. Contacts are then formed between L34-V36 and the C-terminal region. Contacts are then made between the Central Hydrophobic Cluster (CHC) from residues L17-A21 and E22-G29, the CHC and residues A30-M35 and

CHC and C-terminal region which are associated with a turn structure in residues E22-G29, creating the first structural element[15,16]. Contacts can then develop between the N-terminal region and CHC. Long range contacts can then develop between the N- and C-terminal region. Overall, the folding starts at the C-terminal and progresses towards the N-terminal[15]. Important electrostatic interactions between pairs of charged amino acids are crucial in the formation of oligomeric structures including interactions between negatively charged D1 and E3 and positively charged K16 for example. The process of fibril formation from monomeric structures is considered to originate from a high entropic barrier and unfavourable thermodynamic event. The aggregation is initiated by a conformational change from random coil or α-helix into a β-strand. β-sheet conformations maximise hydrophobic interactions, with the formation of fibrils dependant on nucleation and fibril elongation rate. The addition of monomeric molecules to existing nuclei is thermodynamically favourable and occurs by hydrogen bonding to the axis of the amyloid nucleus[17]. These simulations have provided an important insight into the structural changes that occur within the protein which is relevant in its relation so AD.

Several mechanisms explaining the neurotoxicity of Aβ have been proposed. It is theorised that Aβ can interact with cell membranes directly, either by inserting itself into the membrane and forming pore like structures, or, by binding to the surface of the membrane. Insertion is thought to trigger cell death by membrane leakage[18,19], which increases with higher Aβ-to-lipid ratio[20]. Depending on the membrane structure, insertion can also cause membrane permeabilization and often leads to Aβ structures similar to cation selective ion channels. These voltage independent channels can be blocked by zinc molecules leading to a destabilisation of ionic homeostasis due to increased calcium influx. This eventually leads to apoptosis of neuronal cells[18]. Aβ binding also often leads to the acceleration of amyloidogenesis, which is easily affected by peptide concentration of membrane structure[18,21].

The study of the interactions between Aβ and biologically relevant membrane models *in vitro* provides useful information regarding the possible neurotoxic effects of the peptide, as well as the structural changes that occur and how the membrane structure can effect this. This is vital in AD research. One important model previously used in research is the Lipid Mimic (LM) model which mimics the outer leaflet of Synaptic Plasma Membranes (SPMs) which when disrupted by Aβ is a suspected neurotoxic mechanism. This model includes components such as charged phospholipids, Cholesterol (Chol), Sphingomyelin (Sphin) and Ganglioside GM1 (GM1).

The fundamental structure of the SPM and other cellular membranes is the phospholipid bilayer consisting of two layers of the phospholipids with a hydrophobic interior and hydrophilic exterior. Depending on the structure of the phospholipid head and therefore the structure of the membrane, the structural changes that occur in the Aβ protein when it interacts with membranes can be very different. Depending on the membrane structure, Aβ can either be firmly anchored to the membrane preventing release and aggregation, or the membrane can accelerate aggregation ultimately leading to neuronal cell death. This is due to a combination of electrostatic and hydrophobic interactions which contribute differently depending on the membrane structure. In a study focusing on multilamellar 1,2-dimyristoyl-*sn*-glycero-3-phosphocholine (DMPC) and 1,2-Dimyristoyl-sn-glycero-3-phosphoglycerol (DMPG) vesicles, where the surface potential was varied, the presence of acidic lipid caused a significant increase in concentration of surface-associated peptide, preventing its release. This was stabilised by the hydrophobic terminal and promoted an α-helical conformation. The membrane resulted in deeper insertion of the peptide. When Aβ was present in its monomeric form, charged membranes caused an accumulation of surface associated Aβ leading to accelerated aggregation due to the 2D nature of the membrane which acted as an aggregation-template. Surface associated Aβ also shows a large population of β-sheet structures which contribute to the aggregation process. This is increased when the negative surface potential increases, shown in membranes with greater concentrations of negatively charged lipids. Interactions in this case were mainly driven by electrostatic compared to hydrophobic interactions[22].

Another study investigating the impact of the phospholipid headgroup on the kinetics of Aβ fibril assembly found that the headgroup largely affects the lag-times of fibrillar formation whilst the growth time are all similar in six different lipids. The three anionic headgroups used, Phosphatidic acid (PA), Phosphatidylserine (PS) and Phosphatidylglycerol (PG) all accelerated fibril formation whilst Phosphatidylcholine (PC) and sphin inhibited fibril formation[23]. Zwitterionic Phosphatidylethanolamine (PE) has also been shown to behave as an anionic phospholipid within bilayers and accelerate Aβ fibril formation[24]. The size of the headgroup can slightly affect the lag-time, where smaller heads can accelerate fibril formation, such as PA and PE. Overall, the size, shape, and charge of the headgroup influences the alignment of Aβ monomers and concentration on the membrane surface. This increases the opportunity for monomers to form primary nucleating oligomers and reduce lag-times for fibril formation. All of the lipids used within this work contained 16:0 and 18:1 acyl-chains due to their high abundance within neurones[23]. The length of the acyl chain is

another factor which can affect the structure of Aβ as well as Aβ generation. Comparing fatty acids of three different chain lengths, longer chain lengths were shown to increase the levels of APP, BACE1 and PS1, increasing Aβ production[25]. The length of the carbon chain is also known to affect the degradation of Aβ via Insulin-degrading enzyme (IDE), important in Aβ homeostasis. Shorter-chained PC lipids (PC10:0-14:0) significantly stimulated the degradation of Aβ as well as causing changes in the IDE sorting[26].

As stated earlier, Sphin and Chol are important components of LM membranes modelling SPMs. Sphin is a dominant sphingolipid in membranes of mammalian cells, playing roles in signal transduction, whereas Chol has important membrane functions maintaining structural integrity and regulates the membrane fluidity. Both are known to co-enrich the same membrane compartments where the presence of Sphin can affect Chol homeostasis. In the plasma membrane they can form microdomains known as lipid rafts and act as platforms for signalling and trafficking events. These domains are also often more ordered than the surrounding phase in biological membranes. Lipid rafts play a crucial role in AD as they can promote the generation of Aβ, facilitate the aggregation processes of the protein and host neuronal receptors where neurotoxicity and memory impairments of the Aβ oligomers are transduced. Sphin can bind the peptide on the cell membrane surface and initiate fibrillation, while Chol present in the lipids deeper regions interacts with the hydrophobic regions of Aβ which also promoted aggregation[27].

One final component of LM models found in mammalian cellular membranes is GM1. This is the most common ganglioside found within mammalian SPMs and is enriched within lipid rafts. It has many modulatory functions and is associated with the development and differentiation of neuronal tissue. Published work has suggested that the aggregation of Aβ is delayed with increasing GM1 concentration[28] however GM1 clusters have been shown to induce the pathological aggregation of Aβ[29]. The basic functions covered here demonstrate the importance of using biologically relevant membrane systems while investigating the effect of the membrane on Aβ. Understanding the role of individual components of the membrane may also influence the nature of AD therapeutics.

Qiang et al.[20] used a series of experiments to characterise the structure of Aβ when interacting with LM membranes modelling SPMs include Circular Dichroism (CD) and Electron Microscopy (EM).The findings included that the addition of sphin and GM1 increased the populations of α-helices at the initial stage of binding suggesting that

the membrane surface properties effect the binding conformations. These interactions have also been shown to respond to different Protein-to-Lipid ratios (P:L) with the populations of α-helices vs β-strand increasing with the P:L, however this may be attributed to the increasing GM1:peptide. HPLC results showed that the protein to the SPM mimicking membrane binding increased upon incubation, a trend seen across several P:L ratios. Whilst these methods provide insight into the structure of Aβ when interacting with lipid membrane systems, they lack atomic resolution. This may be overcome by the use of Solid-state Nuclear Magnetic Resonance (ssNMR).

SsNMR is a commonly used method in a variety of fields and has been used as an analytical tool in a plethora of research. Since the first measurement in 1938 which won Rabi the Nobel Prize (1944), the technology and equipment used has advanced rapidly now making it widely available. Simply, NMR manipulates the interactions between specific nuclei and an external magnetic field which is possible due to an intrinsic property, spin. In the absence of a magnetic field, the atoms face all possible directions in a random order. Placing the nuclei into a magnetic field aligns with the direction of the magnetic field and splits the degenerate energy levels. In the presence of an oscillating magnetic field, such as in the case of radio waves, which is applied perpendicular to the static magnetic field, the spins transition between the energy levels. The difference in population between these states is the measured NMR signal. SsNMR of proteins employs multidimensional experiments to gain a structural image of the protein. Each nucleus within the protein exists in a distinct chemical environment resulting in discrete chemical shifts which can be assigned. For example, this methodology allows for ^{13}C backbone assignment[30] and with the addition of isotopic protein labelling ^{13}C and ^{15}N correlations can be made[31] as well as other heteronuclear quantum correlations.

Whilst ssNMR has been beneficial to investigate the structure of Aβ as well as the interactions of Aβ fibrils and membrane systems, ssNMR is limited by sensitivity. The use of higher magnetic fields and larger quantities of the sample overcome this issue; however, it is not always practical in an experimental setting. Although magnetic fields are now available up to 28.2 T at the time of writing[32], it is extremely resource consuming to develop this. When investigating biomolecules in biologically relevant conditions, low molecular concentrations in comparison to other molecules not under investigation pose an issue. This limitation may be overcome by the application of Dynamic Nuclear Polarisation (DNP) which utilises lower temperatures and electron spin polarization transfer to nuclear spins, which is achieved by microwave (μw) irradiation of the EPR spectrum, followed by NMR acquisition of nuclear signals. This

has been shown to increase protein signals by several orders of magnitude and has been utilised in the characterisation of several biological systems[33]. There are several mechanisms of DNP, with the Cross Effect (CE) an efficient polarisation transfer scheme for biological systems. This is a three-spin system technique whereby two unpaired electrons are introduced into the sample in the form of a biradical. In short, two spin eigenstates connected by an electron-electron-nuclear flip-flop-flip transition are degenerate allowing for polarisation transfer when one of the electrons is selectively irradiated, increasing the overall population difference and therefore signal[34]. The development of more efficient radicals, advanced gyrotrons and DNP methodology development, DNP enhanced ssNMR has become an effective tool in the investigation of protein structure and dynamics. Due to the cryogenic temperatures required for DNP it is possible to take structural snapshots of Aβ which may undergo conformational changes in typical room temperature NMR. It has previously been employed to investigate the successive stages of Aβ with several intermediary samples being taken along the self-assembly pathway[14]. However, there is limited work investigating the interaction of Aβ with biologically relevant lipid membranes via DNP enhanced ssNMR.

Whilst DNP is a valuable method when investigating the structure of proteins, it is generally implemented at cryogenic temperatures and requires the use DNP additives such as glycerol and dopant. Applying methods to assess the structure of proteins such as Aβ is more biologically relevant with methods that are undertaken at temperatures closer to physiological conditions and do not require the need for external additives. The development of MAS ssNMR means that proton detection is now a suitable alternative method to assess the structure of proteins. Although some literature differs in the definition of fast and ultra-fast MAS it is generally defined as 40-65 kHz as fast and above this as ultra-fast MAS (Agilent Technologies). This method has already allowed the site-specific backbone assignment of amyloid fibril domains at slower spinning speeds of 12 kHz[35], however much faster speeds are now available. This method provides an option for obtaining structural information of the Aβ protein at different stages of the self-assembly pathway as well as the possibility of gaining information on its interactions with cellular membranes under physiological conditions.

Another method beneficial in the study of distance measurements in biomolecules is Electron Paramagnetic Resonance (EPR). The application of pulse EPR involves measuring the dipolar interaction between a pair of paramagnetic spin labels enabling distance measurements to be made. Orientation information can also be determined

from pulse EPR techniques such as Double Electron-Electron Resonance (DEER) applications. Instead of exciting nuclear spins as done in NMR, pulses excite the spins of unpaired electrons. DEER spectroscopy stands as a powerful tool in structural biology, enabling the measurement of distances between paramagnetic centres in biomolecules. Recent work has used DEER spectroscopy and molecular modelling to probe the structure of Aβ oligomers. It has been shown that spherical harmonic expansions can be used on DEER datasets to make distance measurements in a model biradical as well as characterising orientation selection, important in biomolecules[36]. With this comes the possibility of applying this method to other DEER datasets as well as the future use of applying this to more datasets focusing on the Aβ protein.

The background and techniques briefly described above form the basis for this thesis.

Thesis aims and chapter overview

The main aim of this thesis is to apply DNP enhanced ssNMR and other advanced magnetic resonance techniques to study the biomolecular structure of the Aβ protein when interacting with membrane systems.

- This will provide information relevant in AD research and contribute to our current understanding of the involvement of Aβ, specifically its structure when interacting with biologically relevant membranes.
- Due to the nature of DNP and the additives required, the interplay between polarising agent and glycerol, and lipid membrane is also of key focus. This thesis utilises methods such as Paramagnetic Relaxation Enhancement (PRE) and ^{31}P Chemical Shift Anisotropy to assess the insertion depth of the AMUPol biradical into the membrane in the presence and absence of glycerol, used as the cryoprotectant in DNP experimentation.
- DNP has been applied to a wide range of protein/lipid systems investigating the structure of $A\beta_{(1\text{-}40)}$ and its changes as a function of time when added to biologically relevant membranes. Initial stage experimentation includes the use of 1-palmitoyl-2-oleoyl-sn-glycero-3-phosphoglycerol (POPG) lipid, an abundant anionic lipid within nature. This was mainly to test the preparation protocol and deduce whether the structure of $A\beta_{(1\text{-}40)}$ could be determined at several points of incubation time when interacting with lipid membranes via DNP enhanced ssNMR.
- In order to investigate the structure of Aβ when interacting with more complex, biologically relevant systems, the LM system was then produced. This model

is crucial for understanding the nature of $A\beta_{(1-40)}$ in physiological conditions with a relevance to AD and includes DMPC, anionic 1,2-dimyristoyl-*sn*-glycero-3-phospho-L-serine (DMPS), Sphin, Chol and GM1.

- Proton detection is applied to $A\beta_{(1-40)}$ fibrils as an alternative method of DNP to assess resolution and sensitivity and allow measurements to be taken at room temperature without the need for additives required for DNP. High spinning speeds achievable in this work were up to 65 kHz.

The second aim of the thesis is to apply Spherical Harmonic (SH) techniques to several DEER datasets to characterize orientation selection and distance distributions in biomolecules with the later aim of investigating distance measurements within $A\beta_{(1-40)}$.

- Several raw and scraped datasets were obtained from published work with a range of systems with a range of biradicals of varying flexibility.
- Distance distribution analysis was conducted on all datasets which allowed comparisons to the published work.

A brief overview of each chapter is given below:

Chapter 2 introduces relevant NMR and DNP theory as well as the techniques which have been applied experimentally throughout.

Chapter 3 explores the insertion depth of the DNP dopant AMUPol into lipid membranes and the effect of glycerol on this. Membrane samples include the Lipid Mimic (LM) system as well as simpler membrane systems. The disruption to the vesicle membrane homogeneity upon addition of DNP additives is also explored. These experiments utilise ssNMR experiments on systems with ^{1}H frequencies of 600 and 800 MHz.

Chapter 4 presents a number of 1D and 2D ssNMR experiments that were applied to $A\beta_{(1-40)}$ samples introduced into a number of lipid membrane systems, including simple one-component systems, lipid mimic, and brain extract samples. Methodology stages are optimised to increase membrane homogeneity and optimal protein to lipid binding. The protein to lipid ratio (P:L) and membrane components are investigated in relation to the protein to lipid binding. Methods are applied to reduce natural abundance ^{13}C signals and determine the secondary structure of $A\beta_{(1-40)}$ over a range of incubation periods. Proton detection is also applied to mature fibrils to assess their secondary chemical structure.

Chapter 5 applies spherical harmonic (SH) techniques to examine experimental DEER datasets. Principle Component Analysis (PCA) is used to characterize the degree to which orientation selection affects the data. Distance distribution analysis is conducted, and the results compared to the published work, forming a basis for methodology which can be applied to other pulse EPR distance enhancements in a range of biomolecules including $A\beta_{(1\text{-}40)}$.

References

1. Decourt, B., D'Souza, G. X., Shi, J., Ritter, A., Suazo, J. & Sabbagh, M. N. The Cause of Alzheimer's Disease: The Theory of Multipathology Convergence to Chronic Neuronal Stress. *Aging Dis.* **13**, 37 (2022).

2. Nandi, A., Counts, N., Bröker, J., Malik, S., Chen, S., Han, R., Klusty, J., Seligman, B., Tortorice, D., Vigo, D. & Bloom, D. E. Cost of care for Alzheimer's disease and related dementias in the United States: 2016 to 2060. *npj Aging* **10**, 13 (2024).

3. Eid, A., Mhatre, I. & Richardson, J. R. Gene-environment interactions in Alzheimer's disease: A potential path to precision medicine. *Pharmacol. Ther.* **199**, 173–187 (2019).

4. Hardy, J. & Higgins, G. Alzheimer's disease: the amyloid cascade hypothesis. *Science (80-.).* **256**, 184–185 (1992).

5. Zhang, Y., Chen, H., Li, R., Sterling, K. & Song, W. Amyloid β-based therapy for Alzheimer's disease: challenges, successes and future. *Signal Transduct. Target. Ther.* **8**, 248 (2023).

6. Ricciarelli, R. & Fedele, E. The Amyloid Cascade Hypothesis in Alzheimer's Disease: It's Time to Change Our Mind. *Curr. Neuropharmacol.* **15**, 926–935 (2017).

7. Gong, Y., Chang, L., Viola, K. L., Lacor, P. N., Lambert, M. P., Finch, C. E., Krafft, G. A. & Klein, W. L. Alzheimer's disease-affected brain: Presence of oligomeric Aβ ligands (ADDLs) suggests a molecular basis for reversible memory loss. *Proc. Natl. Acad. Sci.* **100**, 10417–10422 (2003).

8. Tycko, R. Solid-State NMR Studies of Amyloid Fibril Structure. *Annu. Rev. Phys. Chem.* **62**, 279–299 (2011).

9. Almeida, Z. L. & Brito, R. M. M. Structure and Aggregation Mechanisms in Amyloids. *Molecules* **25**, 1195 (2020).

10. Rambaran, R. N. & Serpell, L. C. Amyloid fibrils. *Prion* **2**, 112–117 (2008).

11. Lu, J.-X., Qiang, W., Yau, W.-M., Schwieters, C. D., Meredith, S. C. & Tycko, R. Molecular Structure of β-Amyloid Fibrils in Alzheimer's Disease Brain Tissue. *Cell* **154**, 1257–1268 (2013).

12. Kreutzer, A. G. & Nowick, J. S. Elucidating the Structures of Amyloid Oligomers

with Macrocyclic β-Hairpin Peptides: Insights into Alzheimer's Disease and Other Amyloid Diseases. *Acc. Chem. Res.* **51**, 706–718 (2018).

13. Tycko, R. Molecular Structure of Aggregated Amyloid-β: Insights from Solid-State Nuclear Magnetic Resonance. *Cold Spring Harb. Perspect. Med.* **6**, a024083 (2016).

14. Potapov, A., Yau, W.-M., Ghirlando, R., Thurber, K. R. & Tycko, R. Successive Stages of Amyloid-β Self-Assembly Characterized by Solid-State Nuclear Magnetic Resonance with Dynamic Nuclear Polarization. *J. Am. Chem. Soc.* **137**, 8294–8307 (2015).

15. Yun, S., Urbanc, B., Cruz, L., Bitan, G., Teplow, D. B. & Stanley, H. E. Role of Electrostatic Interactions in Amyloid β-Protein (Aβ) Oligomer Formation: A Discrete Molecular Dynamics Study. *Biophys. J.* **92**, 4064–4077 (2007).

16. Lazo, N. D., Grant, M. A., Condron, M. C., Rigby, A. C. & Teplow, D. B. On the nucleation of amyloid β-protein monomer folding. *Protein Sci.* **14**, 1581–1596 (2005).

17. Bharadwaj, P. R., Dubey, A. K., Masters, C. L., Martins, R. N. & Macreadie, I. G. Aβ aggregation and possible implications in Alzheimer's disease pathogenesis. *J. Cell. Mol. Med.* **13**, 412–421 (2009).

18. Niu, Z., Zhang, Z., Zhao, W. & Yang, J. Interactions between amyloid β peptide and lipid membranes. *Biochim. Biophys. Acta - Biomembr.* **1860**, 1663–1669 (2018).

19. Bharadwaj, P., Solomon, T., Malajczuk, C. J., Mancera, R. L., Howard, M., Arrigan, D. W. M., Newsholme, P. & Martins, R. N. Role of the cell membrane interface in modulating production and uptake of Alzheimer's beta amyloid protein. *Biochim. Biophys. Acta - Biomembr.* **1860**, 1639–1651 (2018).

20. Cheng, Q., Hu, Z.-W., Doherty, K. E., Tobin-Miyaji, Y. J. & Qiang, W. The on-fibrillation-pathway membrane content leakage and off-fibrillation-pathway lipid mixing induced by 40-residue β-amyloid peptides in biologically relevant model liposomes. *Biochim. Biophys. Acta - Biomembr.* **1860**, 1670–1680 (2018).

21. Relini, A., Marano, N. & Gliozzi, A. Probing the interplay between amyloidogenic proteins and membranes using lipid monolayers and bilayers. *Adv. Colloid Interface Sci.* **207**, 81–92 (2014).

22. Bokvist, M., Lindström, F., Watts, A. & Gröbner, G. Two Types of Alzheimer's β-Amyloid (1–40) Peptide Membrane Interactions: Aggregation Preventing Transmembrane Anchoring Versus Accelerated Surface Fibril Formation. *J. Mol. Biol.* **335**, 1039–1049 (2004).

23. Khursheed, A. & Viles, J. H. Impact of Membrane Phospholipids and Exosomes on the Kinetics of Amyloid-β Fibril Assembly. *J. Mol. Biol.* **436**, 168464 (2024).

24. Her, C., Filoti, D. I., McLean, M. A., Sligar, S. G., Alexander Ross, J. B., Steele, H. & Laue, T. M. The Charge Properties of Phospholipid Nanodiscs. *Biophys. J.* **111**, 989–998 (2016).

25. Liu, J.-J., Zhang, W., Wang, S.-S., Jia, Z.-Q., Shi, Y.-H., Yang, L. & Shi, R.-L. Effects of chain length of saturated fatty acids on Aβ generation in SH-SY5Y cells. *Neurosci. Lett.* **698**, 169–172 (2019).

26. Mett, J., Lauer, A. A., Janitschke, D., Griebsch, L. V., Theiss, E. L., Grimm, H. S., Koivisto, H., Tanila, H., Hartmann, T. & Grimm, M. O. W. Medium-Chain Length Fatty Acids Enhance Aβ Degradation by Affecting Insulin-Degrading Enzyme. *Cells* **10**, 2941 (2021).

27. Devanathan, S., Salamon, Z., Lindblom, G., Gröbner, G. & Tollin, G. Effects of sphingomyelin, cholesterol and zinc ions on the binding, insertion and aggregation of the amyloid Aβ 1−40 peptide in solid-supported lipid bilayers. *FEBS J.* **273**, 1389–1402 (2006).

28. Hu, J., Linse, S. & Sparr, E. Ganglioside Micelles Affect Amyloid β Aggregation by Coassembly. *ACS Chem. Neurosci.* **14**, 4335–4343 (2023).

29. Matsuzaki, K. Formation of Toxic Amyloid Fibrils by Amyloid β -Protein on Ganglioside Clusters. *Int. J. Alzheimers. Dis.* **2011**, 1–7 (2011).

30. Wei, Q., Chen, J., Mi, J., Zhang, J., Ruan, K. & Wu, J. NMR Backbone Assignment of Large Proteins by Using 13 C α -Only Triple-Resonance Experiments. *Chem. – A Eur. J.* **22**, 9556–9564 (2016).

31. Gibbs, E. B. & Kriwacki, R. W. Direct detection of carbon and nitrogen nuclei for high-resolution analysis of intrinsically disordered proteins using NMR spectroscopy. *Methods* **138**–**139**, 39–46 (2018).

32. Berkson, Z. J., Björgvinsdóttir, S., Yakimov, A., Gioffrè, D., Korzyński, M. D., Barnes, A. B. & Copéret, C. Solid-State NMR Spectra of Protons and

Quadrupolar Nuclei at 28.2 T: Resolving Signatures of Surface Sites with Fast Magic Angle Spinning. *JACS Au* **2**, 2460–2465 (2022).

33. Gauto, D., Dakhlaoui, O., Marin-Montesinos, I., Hediger, S. & De Paëpe, G. Targeted DNP for biomolecular solid-state NMR. *Chem. Sci.* **12**, 6223–6237 (2021).

34. Corzilius, B. Theory of solid effect and cross effect dynamic nuclear polarization with half-integer high-spin metal polarizing agents in rotating solids. *Phys. Chem. Chem. Phys.* **18**, 27190–27204 (2016).

35. Falk, A. S. & Siemer, A. B. Dynamic domains of amyloid fibrils can be site-specifically assigned with proton detected 3D NMR spectroscopy. *J. Biomol. NMR* **66**, 159–162 (2016).

36. Potapov, A. Application of spherical harmonics for DEER data analysis in systems with a conformational distribution. *J. Magn. Reson.* **316**, 106769 (2020).

2. Nuclear Magnetic Resonance and Dynamic Nuclear Polarisation theory and methodology

2.1 Introduction

All atoms possess an intrinsic property, known as spin, which is a form of angular momentum, however, it is not produced by the rotation of the particle. Nuclear Magnetic Resonance (NMR) in simple terms manipulates these nuclear spins. In the absence of an external magnetic field, particles with spin have spin polarisation axes pointing in all possible directions. When nuclei are placed into a static magnetic field, the atoms tend to align with the field. Applying an oscillating magnetic field along the perpendicular axis of the static magnetic field, causes the spins to transition between their degenerate energy levels, which are split. The population difference between the states is effectively the NMR signal. The larger the population difference the larger the NMR signal.

The understanding of the mechanisms behind NMR and the ability to manipulate the magnetic field and electromagnetic pulses has led to overcoming some of the limitations first encountered in earlier NMR studies, and is now a common method used by scientists in a plethora of fields[1].

This chapter introduces the theory behind NMR as well as some of the basic techniques which can be used in structural elucidation, which are relevant to the work presented in later chapters of this thesis. Brief descriptions of the equipment used in order to achieve NMR and Dynamic Nuclear Polarisation (DNP) enhanced NMR spectra as well as some of the pulse sequences used in order to achieve structural elucidation are also discussed.

2.2 Principles of NMR

A nucleus with a spin I placed into a static magnetic field yields $2I + 1$ energy levels, a phenomenon known as the nuclear Zeeman effect[2]. Figure 2.1A) shows this schematically for a spin $I = \frac{1}{2}$. The Boltzmann distribution causes the lower energy

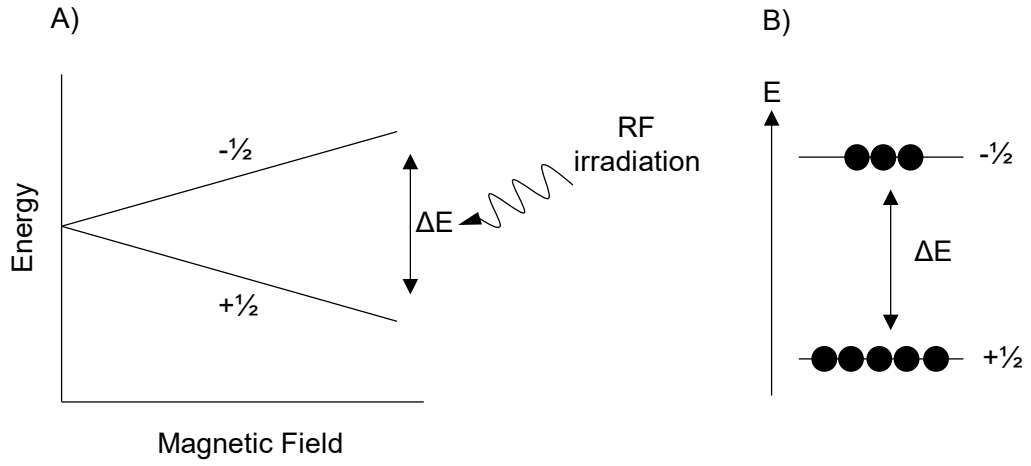

Figure 2.1 *A) Diagram of the Zeeman splitting of a spin = ½ nucleus in an external magnetic field. B) Representation of the two energy levels showing the spin populations of each of those two levels.*

eigenstates to be more populated than the higher energy eigenstates also represented in Figure 2.1B).

The Hamiltonian of the Zeeman interaction is represented by:

$$\hat{H}_Z = -\gamma\hbar B_0 \hat{I}_Z, \tag{2.1}$$

where $\hat{I}_Z$ is the vector of spin angular momentum parallel to the external magnetic field, B_0 and γ is the gyromagnetic ratio. The strength of the external magnetic field and the gyromagnetic ratio determine the difference in the energy levels, *ΔE*, due to Zeeman splitting:

$$\Delta E = \gamma\hbar B_0. \tag{2.2}$$

An oscillating magnetic field at the Larmor frequency, $\omega_0 = \gamma B_0$ may induce transitions between the sublevels of the spin system. At the magnetic fields typically used in NMR, the nuclear Larmor frequencies of most nuclei belong to the radiofrequency range. The magnetic properties of nuclei used in this thesis work are shown in Table 2.1.

Table 2.1 *Natural abundance, gyromagnetic ratio, and Larmor frequency at 14.1 T*[3]*.*

Isotope	Spin	Natural abundance	Gyromagnetic ratio γ/10^7 rad s^{-1} T^{-1}	^{1}H NMR frequency @ 14.1 T / MHz
^{1}H	½	99.98	26.75	600.1
^{13}C	½	1.07	6.73	150.9
^{15}N	½	0.36	-2.71	60.8
^{31}P	½	100	10.84	242.9

NMR spectroscopy is a study of the transitions between Zeeman nuclear spin states, which is achieved by irradiation of the spin active nuclei close to the Larmor frequency in an external magnetic field.

2.3 Bulk magnetisation

As shown in Figure 2.1B), a spin of ½ has two possible energy levels represented as $m_z = \frac{1}{2}$ and $m_z = -\frac{1}{2}$ states, denoted for brevity as ↑ and ↓ respectively. The total magnetic moment of the sample, or sample magnetization, is given by:

$$M = \mu_{\uparrow} N_{\uparrow} + \mu_{\downarrow} N_{\downarrow}, \tag{2.3}$$

where μ are the magnetic moments and $N_{\uparrow}$, $N_{\downarrow}$ are the number of spins in states ↑ and ↓ respectively. Since:

$$\begin{aligned} \mu_{\uparrow} &= \frac{\gamma\hbar}{2} \\ \mu_{\downarrow} &= -\frac{\gamma\hbar}{2}, \end{aligned} \tag{2.4}$$

the total sample magnetization can be calculated as:

$$M = \frac{\gamma\hbar}{2}(N_{\uparrow} - N_{\downarrow}). \tag{2.5}$$

Larger sample magnetization leads to larger signal strength in NMR experiments. However, instead of magnetization it is more convenient to characterize the sample using a dimensionless quantity called polarization, defined as:

$$P = \frac{N_{\uparrow} - N_{\downarrow}}{N_{\uparrow} + N_{\downarrow}}, \tag{2.6}$$

Since an ensemble of spins follows the Boltzmann distribution (schematically shown in Figure 2.1B), the polarization can be calculated as:

$$P = tanh\left(\frac{\Delta E}{2K_b T}\right), \tag{2.7}$$

where K_b is the Boltzmann constant and T is temperature. Therefore, greater NMR signals, i.e., greater experimental sensitivity, can achieved by performing experiments at higher fields and lower temperatures.

2.4 Effect of a radio frequency pulse

Solving a Hamiltonian containing both the term for static magnetic field as presented in Eq. 2.1, and an oscillating magnetic field is possible. It is more intuitive, however, to describe the effect of an RF pulse using a semiclassical model, which assumes an isolated spin $\frac{1}{2}$ interacting with the external magnetic fields.

In a semiclassical model, each spin $\frac{1}{2}$ can be represented with a magnetic dipole. In the absence of an external magnetic field, the magnetic dipoles are oriented at random, thus giving a net zero magnetic moment as shown in Figure 2.2A). If an external magnetic field is applied, the nuclei partially align with respect to the magnetic field thus giving a non-zero net magnetization of the sample as shown schematically in Figure 2.2B). Lower temperatures and a higher B_0 magnetic field also results in a greater net magnetisation as shown in Figure 2.2C).

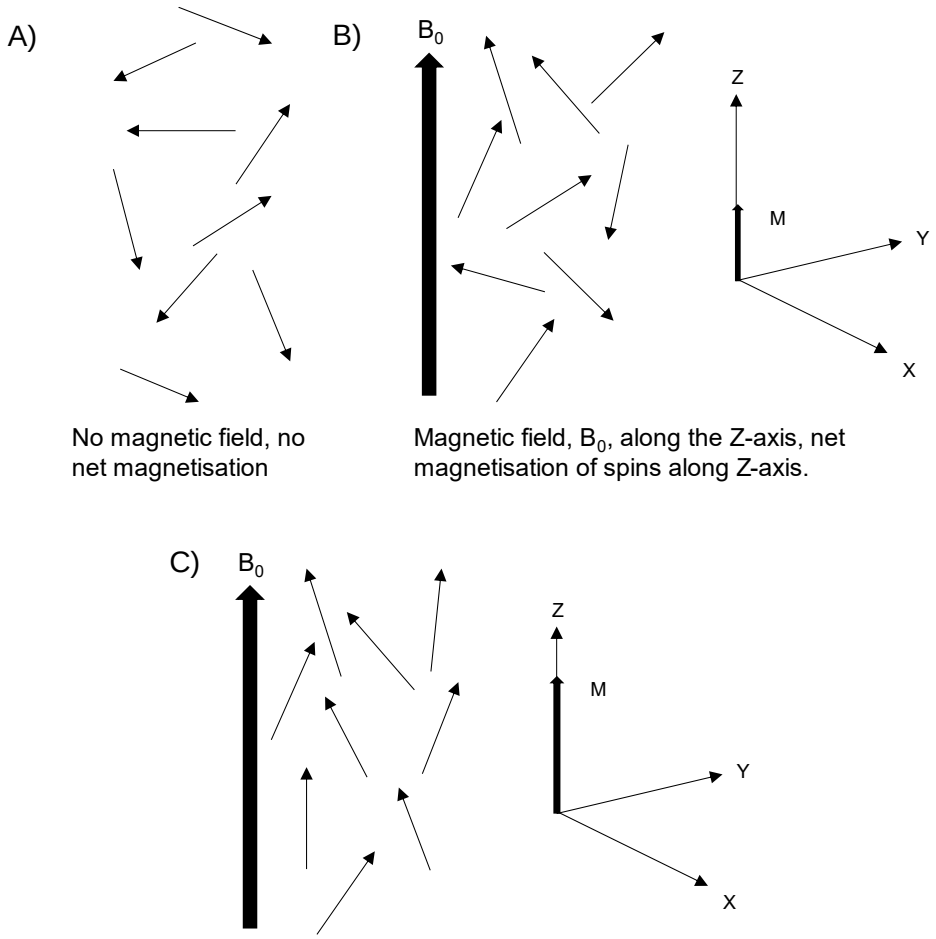

Figure 2.2 *Semiclassical model of bulk spin magnetisation. A) In the absence of an external magnetic field, spin vectors are arranged randomly resulting in no net magnetisation. B) In the presence of a magnetic field, spins partially align in the direction of the magnetic field which results in bulk magnetisation. C) Higher fields and lower temperatures result in greater net bulk magnetisation in the direction of the applied magnetic field due to Boltzmann distributions.*

The time dependency of the macroscopic magnetisation, M, is described by the Bloch equation:

$$\frac{d\vec{M}}{dt} = \gamma\vec{M} \times \vec{B}_{eff}. \tag{2.8}$$

The vector M results from the interaction of the magnetization with the effective external magnetic field $\vec{B}_{eff}$. In the frame rotating around z-axis with the frequency ω_0:

$$\vec{B}_{eff} = \vec{B} - \frac{\omega_o}{\gamma}\vec{e}_z. \quad (2.9)$$

If the rotating frame frequency equals the nuclear Larmor frequency, then $\vec{B}_{eff} = 0$.

A magnetic field oscillating at a frequency ω_{RF} with an amplitude B_1 produces an effective magnetic field:

$$\vec{B}_{eff} = B_1\vec{e}_x + \frac{\omega_{RF} - \omega_o}{\gamma}\vec{e}_z. \quad (2.10)$$

For the on-resonance magnetic field, this reduces to $\vec{B}_{eff} = B_1\vec{e}_x$. According to Eq. 2.8 such field causes a rotation of the equilibrium magnetization M_z around the x-axis. Applying an RF pulse for a duration, t_p, rotates the magnetisation around the x-axis by an angle:

$$\theta = \omega_1 t_p. \quad (2.11)$$

Therefore, following a RF pulse with θ =90°, also called a $\frac{\pi}{2}$ pulse, shown in Figure 2.3 the initial z-magnetization turns into y-magnetization and stays aligned along y-axis in the rotating frame. However, in the laboratory frame that would correspond to a y-magnetization precessing around the field B_0 with the nuclear Larmor frequency.

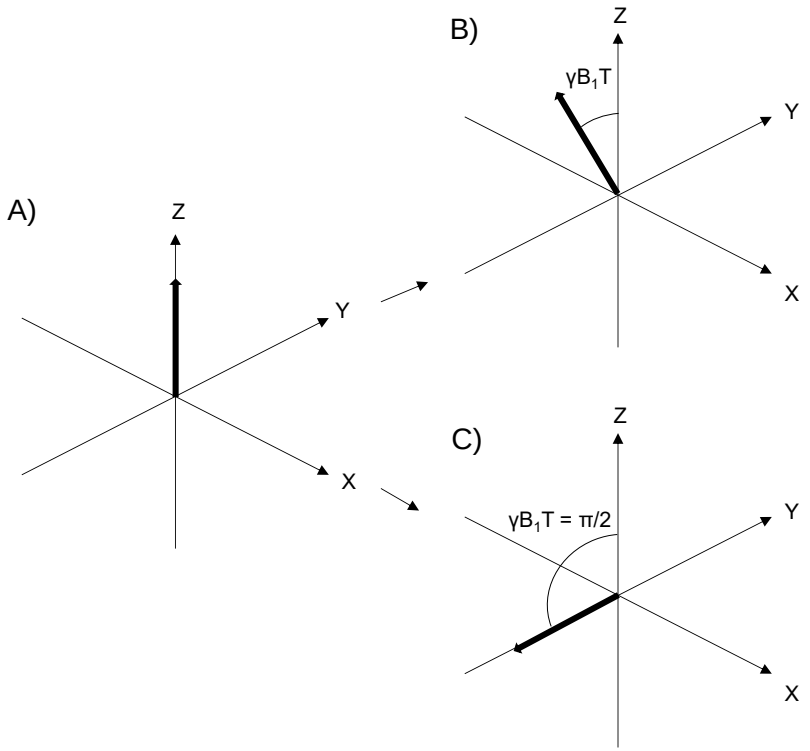

Figure 2.3 *Diagram showing the effect of RF pulses on a nuclear spin. A) Thermal equilibrium with an external magnetic field applied along the z-axis with the arrow representing the bulk magnetisation of the sample. B) After a RF pulse of length T, power γB_1 and phase y (rotation about y-axis), the bulk magnetisation is rotated by an angle $\gamma B_1 T$ away from the z-axis, leaving the magnetisation vector in the xz plane. C) When $\gamma B_1 T = \pi/2$, the magnetisation is rotated to point along the -y-axis.*

This oscillating magnetic field produced by this magnetization induces a voltage across a pickup coil. This induced voltage is detected by the sensitive electronics of the NMR spectrometer and represents the basis of the NMR signal from which the NMR spectra are obtained by Fourier Transform (FT). This process is shown in Figure 2.4.

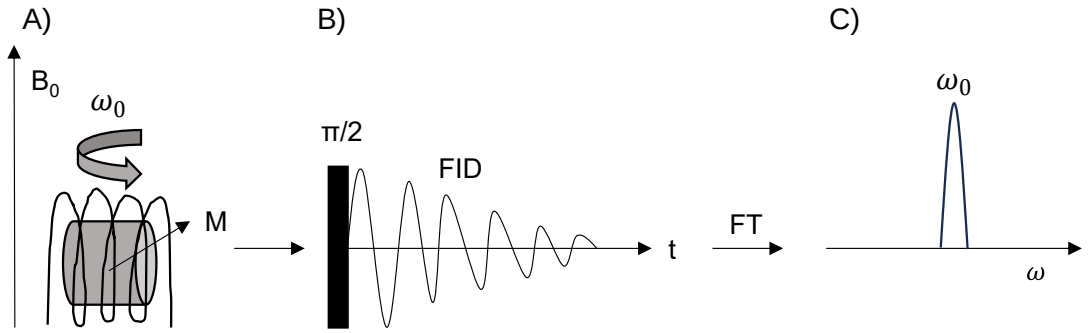

Figure 2.4 *A) Oscillating magnetic field produced by magnetization induces a voltage across a coil. B) An FID is produced after radiofrequency pulse. C) This is then Fourier transformed to produce the signal.*

It is important to note that an interactions of a spin with the RF field can also be described in the language of quantum mechanics. Specifically, one should consider the spin system evolution under the following Hamiltonian:

$$\hat{H}_{RF} = -\gamma\hbar B_1 \cos(\omega_{RF} t)\, \hat{I}_x, \tag{2.12}$$

however, for brevity it will not be discussed here.

2.5 Nuclear spin relaxation

In the laboratory frame with the external magnetic field B_0 along z-axis Eq. 2.8 can be written as its components:

$$\begin{aligned} \frac{dM_x}{dx} &= \gamma M_y B_0 \\ \frac{dM_y}{dx} &= -\gamma M_x B_0 \\ \frac{dM_z}{dx} &= 0. \end{aligned} \tag{2.13}$$

Ideally, this represents a magnetization precessing around the direction of field B_0. However, for an ensemble of spins there are numerous dissipative processes that drive this magnetization towards an equilibrium defined by the Boltzmann distribution. The Bloch equations, Eq. 2.13, then become:

$$\frac{dM_x}{dx} = \gamma M_y B_0 - \frac{M_x}{T_2}$$
$$\frac{dM_y}{dx} = -\gamma M_x B_0 - \frac{M_y}{T_2} \qquad (2.14)$$
$$\frac{dM_z}{dx} = -\frac{M_z - M_0}{T_1}.$$

The constants T_1 and T_2 are known as longitudinal and transverse relaxation times respectively, they depend on various spin-lattice and spin-spin relaxation processes. On the microscopic level, relaxation arises due to tiny random fluctuations of the local magnetic field experienced by the nuclei. Such fluctuations cause either energy transitions or loss of spin coherence.

T_1 relaxation, also known as longitudinal relaxation, is the process where the z component of the bulk magnetisation is restored. This is the component parallel to the static magnetic field. T_1 also quantifies the rate of energy transfer from the nuclear spin system to neighbouring molecules, also known as the lattice. This relaxation is therefore also known as spin-lattice relaxation and restores the Boltzmann equilibrium. The lattice causes a fluctuating magnetic field experienced locally. The RF pulse affects all of the spins in the same way, the pulse is coherent. The local field is randomly different at the site of each spin in any instant, the field is incoherent. One of the most common sources of the local fluctuating fields for spin ½ nuclei is the dipolar interaction. T_1 relaxation can be measured using an inversion-recovery pulse sequence where the magnetisation is inverted to the -z axis. A varying time period allows the relaxation to occur followed by a final 90° pulse and recording of the FID.

T_2 relaxation is defined as the transverse relaxation whereby the xy component of the bulk magnetisation decays, following a simple exponential decay. After an RF pulse the spins are coherent, and all aligned. This synchronicity is gradually lost due to field inhomogeneities experienced by the individual spins. It is also related to the linewidth at Full Width Half Maxima (FWHM). This relaxation does not produce an energy transfer from the spins to the lattice and is termed spin-spin relaxation. T_2 relaxation is measured by a spin echo pulse which eliminates the field inhomogeneity contribution and allows measurements of T_2. T_1 and T_2 relaxation are related since an increase in z magnetisation is not possible without a reduction in either the x or y magnetisation.

Relaxation can be an important tool in NMR for example with Paramagnetic Relaxation Enhancement (PRE) measurements. This is a technique whereby

paramagnetic ions are introduced into a sample, often in the form of a biradical, and can act as a source of relaxation. The PRE arises from magnetic dipolar interactions between unpaired electrons in a paramagnetic centre and a nucleus resulting in an increase in nuclear relaxation rates. Because the magnetic moment of the unpaired electron is large, the PRE can be measurable up to 35 Å. While both T_1 and T_2 PRE rates can be measured, it is generally considered that T_2 measurements provide the most reliable and accurate data. Many PRE studies have made use of a simplistic approach in which the ratio of peak intensities of samples are evaluated. This can provide information on where the biradical sits within the membrane and can also be used for structural determination due to the r^{-6} depedance[4]. This method has previously been used in the study of biomolecules including actin-binding proteins[5], maltose-binding protein[6] and can also be used in drug discovery[7]. PRE analysis has also shown that $A\beta_{(1-40)}$ monomers and seeds of $A\beta_{(1-42)}$ interact via their C-terminal region in a parallel fashion with the N-terminal region not contributing to the interaction[8]. The distribution of biradicals in lipid membranes can be measured via the ^{1}H and ^{13}C spectral intensities. It has previously been shown that AMUPol caused the largest intensity reduction to the lipid headgroup signals in the ^{1}H spectra and the top of the acyl chains showing where the biradical sits in the membrane[9]. As shown in Chapter 3, this method is used to investigate the binding of the biradical in LM samples containing AMUPol with and without glycerol, an important step in DNP sample optimisation.

2.6 Spin interactions

Under external magnetic fields, there are a number of interactions which are experienced by the nuclear spins, including those with the field, known as external interactions, also known as the Zeeman interaction, and those with other nuclear and electronic spins, known as internal interactions, represented by the Hamiltonian:

$$\hat{H} = \hat{H}_{\text{ext}} + \hat{H}_{\text{int}}. \quad (2.15)$$

The Zeeman interaction , $\hat{H}_z$ with radiofrequency radiation, $\hat{H}_{RF}$ is shown as:

$$\hat{H}_{ext} = \hat{H}_z + \hat{H}_{RF}. \quad (2.16)$$

The internal interactions include chemical shift, $\hat{H}_{CS}$, J-coupling, $\hat{H}_J$, dipolar coupling, $\hat{H}_{DD}$, quadrupolar coupling, $\hat{H}_Q$ and hyperfine coupling, $\hat{H}_{HF}$ as shown:

$$\hat{H}_{int} = \hat{H}_{CS} + \hat{H}_J + \hat{H}_{DD} + \hat{H}_Q + \hat{H}_{HF.} \quad (2.17)$$

2.6.1 Chemical shift

All nuclei resonate at their respective Larmor frequencies, however the shielding effect of the electrons produces an additional magnetic field $\vec{B}_s = \sigma\vec{B}_0$, where σ is chemical shift tensor with components:

$$\sigma = \begin{pmatrix} \sigma_{xx} & \sigma_{xy} & \sigma_{xz} \\ \sigma_{yx} & \sigma_{yy} & \sigma_{yz} \\ \sigma_{zx} & \sigma_{zy} & \sigma_{zz} \end{pmatrix}. \quad (2.18)$$

The Hamiltonian of the chemical shift is then given by:

$$\hat{H}_{cs} = \gamma\hat{\vec{I}}\sigma\vec{B}_0 = \gamma\left(\hat{I}_x\sigma_{xz} + \hat{I}_y\sigma_{yz} + \hat{I}_z\sigma_{zz}\right). \quad (2.19)$$

In the high field approximation, i.e., the nuclear Zeeman interaction is much greater than all other interactions, and the latter reduces to:

$$\hat{H} = \gamma\hbar B_0\hat{I}_Z\sigma_{zz.} \quad (2.20)$$

The value of the component σ_{zz} depends on the magnitude of the principal components of tensor σ ($\sigma_{11}, \sigma_{22}, \sigma_{33}$) and its orientation with respect to the external magnetic field. In a sample where all orientations are equally probable, e.g., molecules in frozen solutions, the NMR spectrum would follow a powder pattern shown in Figure 2.5.

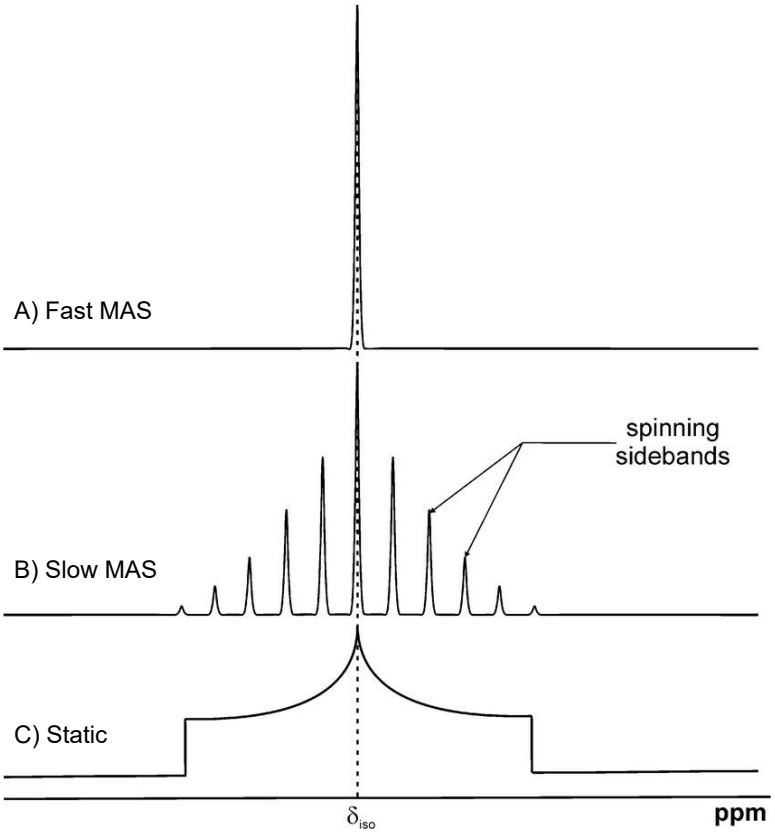

Figure 2.5 *Solid-state NMR spectrum obtained under A) fast MAS, B) slow MAS and C) static conditions. Spinning sidebands are highlighted*[10].

The Chemical Shift Anisotropy (CSA) is described in more detail in Chapter 3. The main elements consist of the isotropic chemical shift, σ_{iso}, anisotropy σ_{aniso} and asymmetry, η. Examples of the powder pattens created when the elements are of certain values is also shown in Figure 2.5. These terms are also defined:

$$\sigma_{iso} = \frac{1}{3}(\sigma_{11} + \sigma_{22} + \sigma_{33})$$
$$\sigma_{aniso} = \sigma_{33} + \sigma_{iso} \qquad (2.21)$$
$$\eta = \frac{\sigma_{22} - \sigma_{11}}{\sigma_{aniso}}.$$

CSA patterns show detail on the local environments and can show interactions such as those between peptides and cellular membrane systems. This is typical for solid state NMR spectroscopy, whereas sufficiently fast random reorientation of molecules under conditions of solution NMR eliminates the anisotropy. However, for solid-state samples, Magic Angle Spinning (MAS) can be applied to remove anisotropic interactions as will be explained further in the Section 2.7. MAS is a useful technique that allows us to simplify the spectra and improve resolution and sensitivity.

In NMR experiments the resonant frequencies are reported with respect to the reference frequency which in the case of ^{1}H and ^{13}C is the Larmor frequency of

Tetramethyl Silane (TMS) due to its strong signal. The chemical shift, σ, or the fractional difference between the resonance frequency ν and the resonance frequency of TMS, is then given by:

$$\sigma = 10^6 \frac{\nu - \nu_{TMS}}{\nu_{TMS}}. \quad (2.22)$$

Analysis of chemical shift values allows the information about the local environment to be gained and can be used to identify certain groups and atoms within a molecule. In particular in proteins amino acids have ^{13}C chemical shifts depending on the local ψ and Ψ angles in the polypeptide chain. In other words, the chemical shift of amino acids depends on the secondary structure, i.e., α-helices, β-sheets, of the protein segment where it is located. It turns out that certain secondary structure elements produce their own typical effect on the chemical shifts, known as the secondary chemical shifts:

$$\Delta\sigma = \sigma_{observed} - \sigma_{random\ coil}, \quad (2.23)$$

where $\sigma_{observed}$ is the observed chemical shift and $\sigma_{random\ coil}$ is the chemical shift of the same residue in a protein with random coil conformation[11]. There is a correlation between the chemical shifts of specific carbon atoms where they either have a more positive or negative shift when in an α-helix or β-sheet conformation when compared to random coil confirmation which is summarised in Table 2.2[11].

Table 2.2 *Correlations between the chemical shifts of specific carbon atoms when in an α-helix or β-sheet conformation when compared to random coil confirmation.*

	α-helix	**β-sheet**
C_α	Positive	Negative
C_β	Negative	Positive
CO	Positive	Negative

This allows the elucidation of the secondary structure.

2.6.2 Dipolar coupling

Dipolar coupling results from the additional magnetic field experienced by one spin due to the magnetic dipolar moments of the other spins in its vicinity. In static powder (or frozen solution) samples where the dipole interaction is between two spin-½ nuclei, the NMR spectra forms the Pake Doublet, which has a characteristic line shape. These interactions are shown in Figure 2.6. This coupling is very useful for molecular structural studies since its magnitude depends on the internuclear distance.

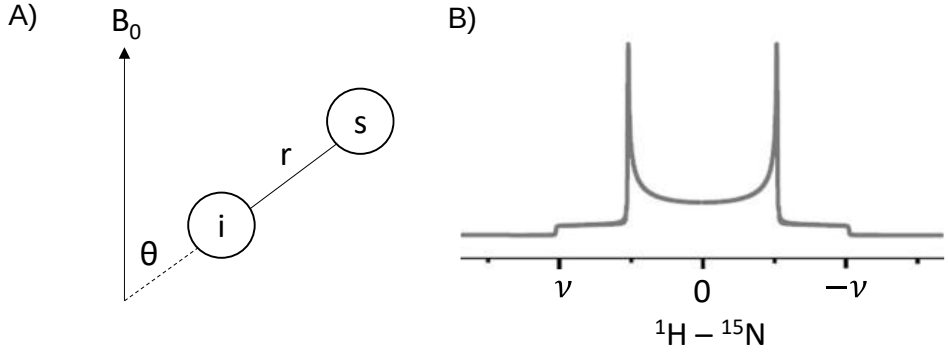

Figure 2.6 *A) Diagram of the through-space dipolar coupling between to spins i and s. B) Simulation of ^{1}H-^{15}N with dipolar interaction Pake doublet extracted from a SLF-2D experiment acquired using PITANSEMA under 11 kHz MAS*[12]*.*

The peaks of the doublet correspond to the signals arising from molecules in which the principal axis of the coupling interaction are perpendicular to the magnetic field. The bottom of the line shape is where it is parallel to the magnetic field.

The dipole-dipole Hamiltonian between two homonuclear spins can be shown:

$$\widehat{H}_{DD} = \frac{1}{2} b_{is}(1 - 3cos^2\theta_{is})\left(3\hat{I}_{iz}\hat{I}_{sz} - \hat{I}_i.\hat{I}_s\right)$$
$$b_{is} = \frac{\mu_0 \gamma_i \gamma_s \hbar}{4\pi {r_{is}}^3}, \tag{2.24}$$

where γ_i and γ_s are the gyromagnetic ratios of both spins, r is the distance between the spins and θ_{is} is the angle between the external magnetic field and the vector between the two spins.

In the case of heteronuclear dipolar couplings, Eq. 2.24 can be simplified to:

$$\widehat{H}_{DD} = \frac{1}{2} b_{is}(1 - 3cos^2\theta_{is})\left(\hat{I}_{iz}\hat{I}_{sz}\right). \tag{2.25}$$

2.7 MAS

NMR of static powder samples or solids poses the issue of powder pattens or CSA patterns which are difficult to analyse and cause a significant overlap when many species are present. This can be overcome by the fast spinning of the sample at the 'Magic Angle' of 54.73° with respect to the applied magnetic field.

This method was first introduced Raymond Andrew in 1958[13]. The sample is rotated around the axis tilted in relation to the external magnetic field as shown in Figure 2.7.

Dipolar coupling and CSA have an angular dependence shown in Eq. 2.26:

$$\sim 3cos^2\,\theta - 1. \qquad (2.26)$$

The interactions are therefore averaged to zero when the magic angle is applied as shown:

$$3cos^2\,\theta - 1 \;=\; ½(3cos^2\theta_R - 1)(\,3cos^2\beta - 1). \qquad (2.27)$$

β represents the angle between the z-axis of the shielding tensor principal axis frame and the spinning axis and takes on all possible values in a powder. If the magic angle is not set properly, there can be significant line broadening.

In order for the MAS to reduce the powder pattern to a single line the spinning rate must be fast, around 3 or 4 factors greater than the anisotropy being 'spun out'. Any slower will create spinning sidebands which are set at the spinning rate apart and radiate out from the line at the isotropic chemical shift. However, the spinning sidebands can be useful as they determine the details of anisotropic interaction which

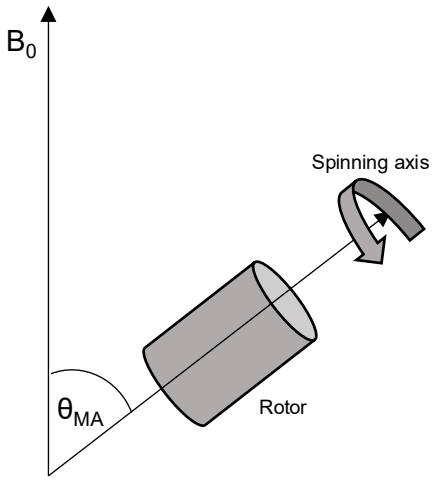

Figure 2.7 *Diagram of the rotor containing the sample orientated at $\theta_{MA} = 54.7^o$ with respect to the B_0 field.*

are averaged out by MAS. The combination of both MAS and decoupling allows for resolved spectra to be obtained, allowing for the structures of proteins and peptides to be determined. 2.8 Heteronuclear decoupling

When studying nuclei such as ^{13}C, coupling between this and the network of ^{1}H nuclei results in broadening of the spectrum that cannot be completely removed by MAS, which becomes problematic in studies of biomolecules, e.g., proteins in lipid membranes addressed in this thesis work. Applying a continuous RF pulse at the Larmor frequency of the ^{1}H, while at the same time acquiring the ^{13}C signal, removes this broadening by averaging the coupling between the nuclei, known as decoupling, as shown in Figure 2.8.

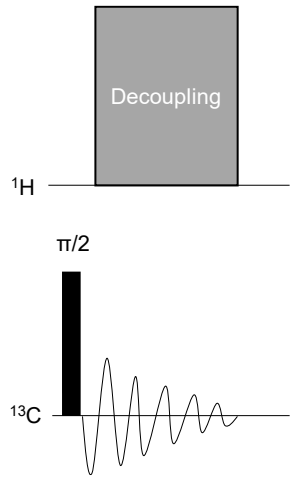

Figure 2.8 *Pulse sequence involved in the heteronuclear decoupling of nuclei. The decoupling pulse is applied during the acquisition time of the X nuclei.*

If the applied RF field is near the Larmor frequency it becomes capable of decoupling the nuclei, for example the heteronuclear coupling between ^{1}H and ^{13}C. The irradiation affects the z-component of a proton spin, which has a similar resonance as the RF pulse. The exact mechanism involves the proton spin to transition between the α and the β state. The rate of this oscillation is determined by the amplitude of the RF field, ω_1. As long as the transitions between the spin states is fast compared to the strength of the coupling, the two coupled nuclei will not experience an indirect dipole interaction. In samples, the protons are also coupled together via homonuclear coupling therefore the irradiation only needs to be at one nuclear frequency as homonuclear dipolar coupling between the protons means that any frequency along the proton spectrum is transmitted to all coupled protons. This then effects all the other z-components of the protons through the coupled network.

The two common methods used in solid-sate NMR (ssNMR) and in this thesis are Two-Pulse Phase Modulated decoupling (TPPM)[14] and Small Phase Incremental Alteration with 64-steps (SPINAL-64)[15] decoupling. Both of which have been shown to be effective in the removal of heteronuclear coupling and reducing line broadening effects.

2.9 Essential techniques in ssNMR

Apart from the application of MAS and dipolar decoupling, there are a number of techniques which are used for acquiring NMR signals. 1D and 2D experiments can be used to gain information about the environment of a nucleus as well as structural information. Utilising RF pulses in specific sequences can manipulate the polarisation transfer between nuclei due to dipolar interactions. This allows for more detailed spectra to be formed as well as enhancing the signal of certain nuclei with low natural abundancy such as ^{13}C.

However, complex molecules can also produce overcrowded 1D spectra. Utilising 2D spectra can allow for individual amino acid chemical shift determination and structural elucidation. Several 1D and 2D methods have been applied in this thesis which has allowed the conformational changes of the Amyloid Beta (Aβ) protein in some biological membranes to be tracked, with the main methods described below.

2.9.1 Cross polarisation

Cross polarisation (CP) allows the polarisation to be transferred from protons to other nuclei that are usually less abundant. This is achieved via irradiation of both nuclei at their correct Larmor frequencies, satisfying the Hartmann-Hahn condition. Applying this method under MAS conditions is as shown:

$$\gamma^I B_1^I = \gamma^S B_1^S + n\omega_r. \tag{2.28}$$

Where ω_r is the MAS frequency, where n can be 1, 2, and B_1^I and B_1^S are the applied magnetic fields to both channels, whereby meeting this condition sets an equal energy gap between the proton and X spins. This condition is met during a contact pulse between the two channels as shown in Figure 2.9. Since this method is based on dipolar interactions, it is sensitive to internuclear distances and the mobility of molecules, allowing CP to be nucleus selective. For example, proton – $\alpha^{13}C$ CP, increasing the signal mainly of the $\alpha^{13}C$.

Figure 2.9 shows the pulse sequence used for CP experiments for the increase in signal of low γ-nuclei, such as ^{13}C.

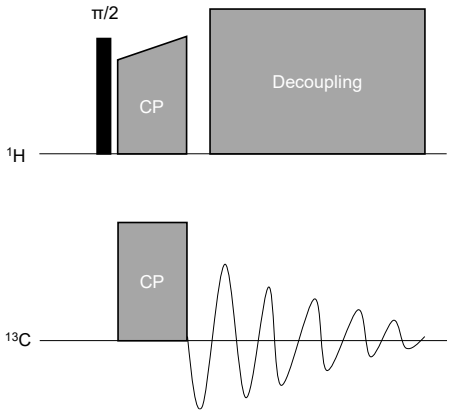

Figure 2.9 *Pulse sequence used for cross polarisation, enhancing the signal of lower abundance nuclei such as ^{13}C.*

The basic sequence first involves a proton 90° pulse which brings the magnetisation into the transverse plane. A contact CP pulse is then applied to both channels in which magnetisation is transferred from the proton to the low γ-nuclei.

2.9.2 POST-C7

The use of dipolar recoupling sequences are valuable in the application of MAS ssNMR and are used for excitation of DQ coherence which can probe internuclear distances and torsion angles. POST-C7 is an example of such a sequence. The C7 element is based upon Levitt's symmetry based pulse sequences which was improved by the Permutationally Offset stabilised (POST) pulse element to give POST-C7[16], also known as a Double-Quantum single-Quantum (DQSQ) method. DQSQ POST-C7 is a common way to remove lipid and glycerol background signals from spectra. The single quantum shift is shown in the direct dimension and the double quantum shift shown in the indirect dimension. The sum of the SQ chemical shifts due to the spins exchanging magnetisation via dipolar interaction show as cross peaks in the indirect dimension. Whilst some SQ signal can persist after the DQ filtering, the spectra produced tend to be dominated by the magnetisation build up between ^{13}C nuclei which are separated by one bond. This is due to the phase cycling behaviour of the pulse sequence[17]. The C7 element converts the longitudinal magnetisation into DQ coherence, which after an evolution time, is reconverted into observable magnetisation by a second C7 sequence[18]. Using proteins which are ^{13}C labelled at specific residues means two ^{13}C nuclear spins separated by one bond is ~10000x more likely than in lipids where the natural abundance is 1%. This allows for

one bond correlations and the assignment of cross peaks as well as the reduction of lipid and background signals. Figure 2.10 shows the POST-C7 pulse sequence.

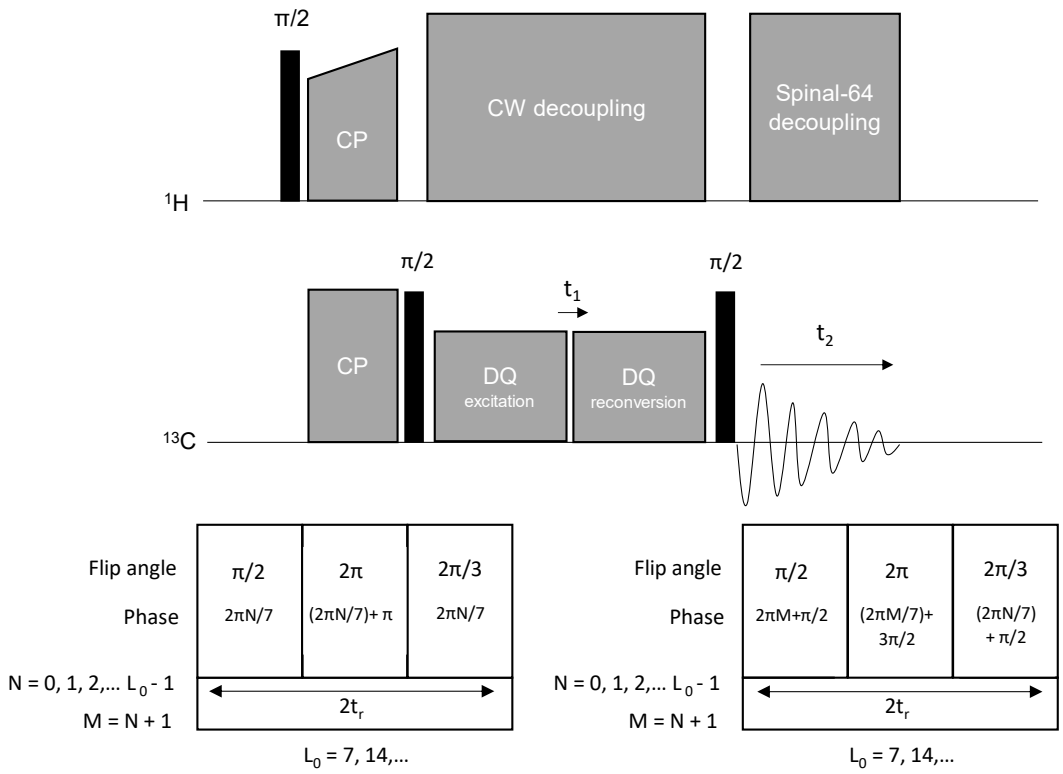

Figure 2.10 *Pulse sequence for POST-C7 DQSQ experiment. The DQ excitation and reconversion are looped L_0 times, which is set to a multiple of 7. The phase is incremented by 2π/7 after each loop. The nutation frequency is set to 7x the MAS frequency so that one DQ loop takes exactly two rotor periods.*

The sequence consists of a DQ excitation and reconversion period which contain the POST-C7 pulse elements. For nuclei such as ^{13}C, ω_1, is set to 7x the ω_r, which is the MAS frequency. 7 POST-C7 pulse elements fit into exactly two rotor cycles. The excitation and reconversion blocks are repeated L_0 times, where L_0 is a multiple of 7. With each repeat of the basic sequence element, the phase is incremented by 2π / 7 so that after L_0 loops the phase cycle is reset. Excitation periods are set dependant on the dipolar coupling strength and therefore the separation. For one bond interactions short excitation periods are chose. In a review of the efficiency of four recoupling pulse sequences, POST-C7 was shown to have the highest experimental DQ efficiency of 61% compared to 55% for the next highest sequence[19].

2.9.3 DARR

Dipolar Assisted Rotational Resonance (DARR) is a useful method in contact assignment and structural calculations. The experiment is a second order dipolar

recoupling scheme which can be used to observe long range ^{13}C-^{13}C correlations. The simpler version of DARR is known as Proton Driven Spin Diffusion (PDSD). The mechanism behind DARR is a spin diffusion between two nearby carbons, assisted by neighbouring proton spins. Random flip-flops between the protons causes fluctuations of the ^{13}C nuclear frequencies, so that a dipolar interaction between the two ^{13}C is experienced for a short time. Unlike PDSD, a weak RF is applied on the protons in a DARR sequence, so dipolar recoupling between the two ^{13}C occurs.

DARR also has the advantage of probing distances which are intra and inter-residue. Assignment of cross peaks at short mixing times means the polarisation transfer by dipolar interactions would occur mostly for directly bonded nuclei, probing intra-residue contacts, dominating the spectra. Longer mixing times allows for long range distance correlations to be observed, therefore probing inter-residue contacts. The pulse sequence for the DARR experiment is shown in Figure 2.11.

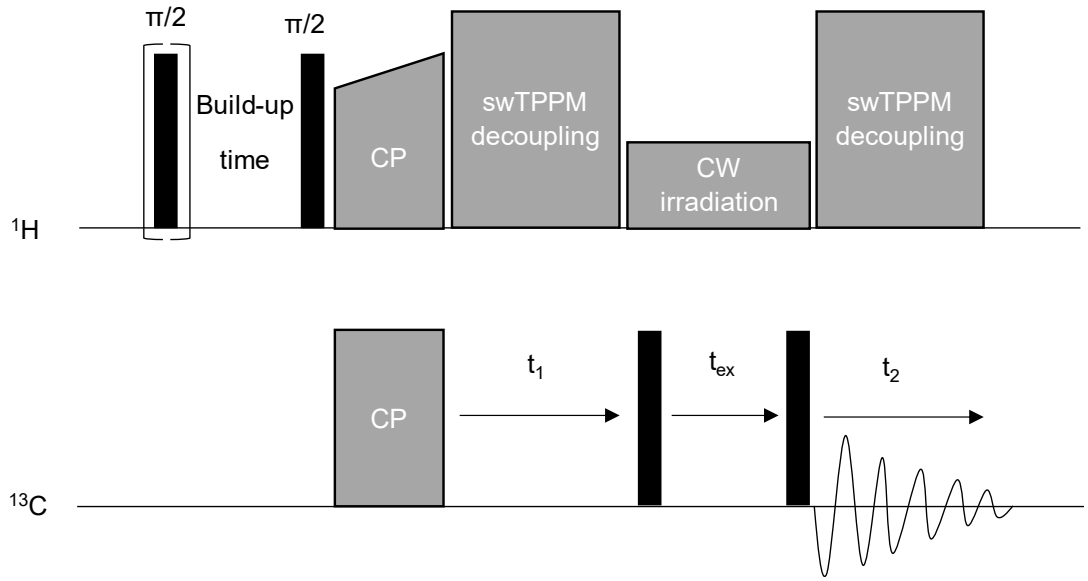

Figure 2.11 *Pulse sequence for the DARR experiment. A CP step is followed by t_1 which is incremented. During t_{ex} magnetisation build up occurs between ^{13}C spins while continuous wave irradiation is applied to the protons at a power level equivalent to the rotation rate of MAS.*

A CP step allows the magnetisation transfer from proton to ^{13}C which is then exchanged between other ^{13}C nuclei which are close in space during an exchange time, t_{ex}. During this exchange time, continuous wave (CW) irradiation is applied to the proton at a power level equal to the rotation rate. The DARR pulse on the ^{1}H channel, which is in this thesis work is equal to one MAS frequency, causes recoupling of the proton and ^{13}C dipolar interactions, allowing magnetisation to be transferred via

the protons. Setting the exchange time allows the difference between intra and inter-residue contacts to be probed. Cross-peaks are again produced which can allow contact assignment.

Both 2D POST-C7 and DARR have been implemented in this thesis work and allows for structural information to be gained, in this case conformational data of the $A\beta_{(1-40)}$ protein.

2.10 Ultrafast MAS and proton detection

Although the use of standard 3.2 mm rotors in MAS ssNMR provides important detail for the structural determination of proteins and biomolecules, the use of smaller rotors and higher spin rates can have advantages. Currently, speeds over 170 kHz have been record using a 0.5 mm rotor[20]. Most applications of biological NMR are based on ^{13}C detection due to the ability to resolve carbon atoms compared to protons, where there is insufficient averaging of large ^{1}H-^{1}H dipole interactions by MAS. Increasing the MAS frequency, the proton linewidths can be reduced making proton detection a desirable alternative. With the need for smaller rotors such as 1.3 and 0.7 mm, sample quantity required is reduced. Under fast MAS conditions the proton dipolar couplings are significantly averaged out and the use of low power irradiation for heteronuclear decoupling becomes possible. As a result, the sample heating due to RF fields becomes significantly smaller. Therefore, overall fast MAS rises to the opportunity of studying biological compounds that may only be available in small quantity. A representation of a homonuclear ^{1}H detected pulse sequence for 2D hCH correlations with CP and water suppression is shown in Figure 2.12.

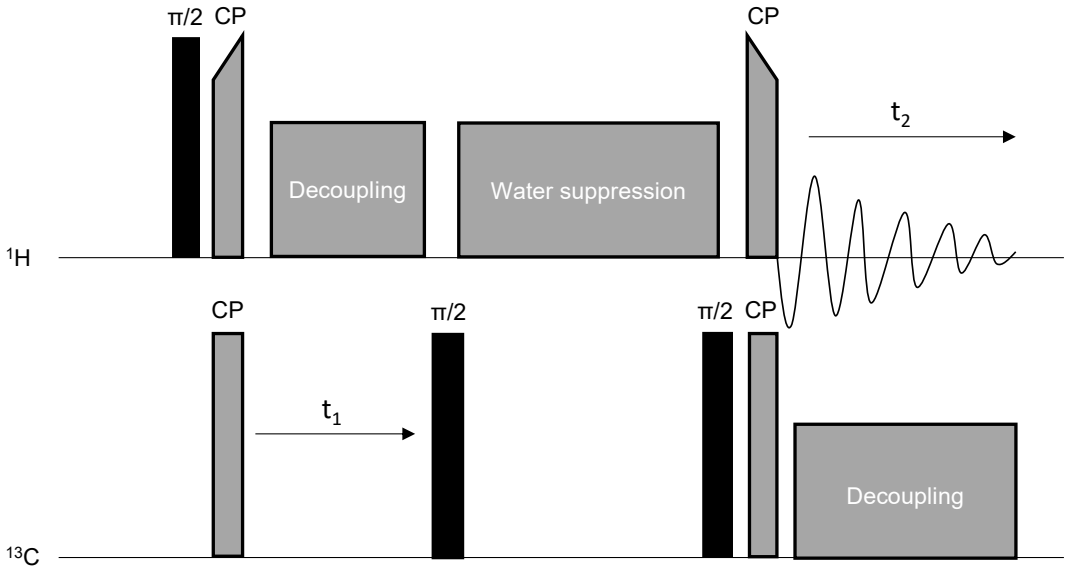

Figure 2.12 *Pulse program for ^{1}H detected experiment for hCH homonuclear correlation. A CP step is followed by a 90° pulse on the carbon channel. This is then followed by water suppression and CP back to the proton channel.*

After an initial 90° pulse on the proton channel a CP step is applied. This is then followed by decoupling and suppression of water ^{1}H signals, with another 90° pulse on the X channel. CP is then applied with acquisition on the proton channel and decoupling on the X channel occurring simultaneously.

In previous work, high spinning speeds of 60 kHz have been shown to be insufficient in measuring ^{1}H CSA due to the incomplete suppression of ^{1}H dipolar couplings. This justifies the need for higher magnetic fields beyond 1 GHz and ultrafast MAS beyond 100 kHz[21]. A more recent study allowed for the protein proton side chain assignments of a hepatitis B viral capsid assembled from 120 core-protein dimers using 160 kHz spinning speeds and a field of 1.2 GHz. This combination allowed the assignment of 61% of the aliphatic protons of the core-protein, opening up possibilities for further structural studies of biomolecules[22]. Relaxation data was acquired from the model protein ubiquitin with MAS frequencies at 126 kHz again showing the need for ultra-high spinning speeds above 111 kHz[23]. However, this methodology has allowed the 110 resonance assignments of a Zinc loaded superoxide dismutase in short times with good resolution at lower spinning speeds of 60 kHz[24]. This however involved triple resonance $^{1}H/^{13}C/^{15}N$ pulse sequences with addition CP and 90° pulse steps. It has also been demonstrated that the use of MAS frequencies of 30 kHz the ^{1}H NMR peaks are narrow enough to provide sensitivity gains by proton detection in two different peptides[25]. In this thesis work, hCH methodology was applied to investigate

the conformational structure of $A\beta_{(1-40)}$ fibrils which is discussed further in Chapter 4 and allowed some residue assignments at 65 kHz.

2.11 NMR hardware

There are a number of hardware components that are used together for ssNMR. This includes a stable magnet capable of producing a homogeneous field, a RF transmitter and receiver able to produce and detect RF signals, A MAS unit, control of matching conditions as well as probes and rotors capable of achieving suitable MAS frequencies. A cabinet is used to store the different spectrometer units and power connections as well as providing shielding from external radiation. This includes the Acquisition Control system (AQS), Magnet system, in the case of Bruker the Bruker Smart Magnet System (BSMS) and the Variable Temperature Unit (VTU), which can all be accessed by a connected computer, as well as other amplifiers. The principal units are described briefly below.

2.11.1 The magnet

The main magnetic field B_0 is produced by a superconducting magnet. The superconducting material provides zero resistance below a certain temperature which is usually achieved by liquid helium temperatures. A chamber of liquid nitrogen surrounds the helium absorbing external heat and reducing the helium boil off rate, optimising cost effectiveness. The homogeneity of the magnetic field is adjusted via shimming the current carrying coils. Figure 2.13 shows a diagram of the inside of a typical NMR magnet.

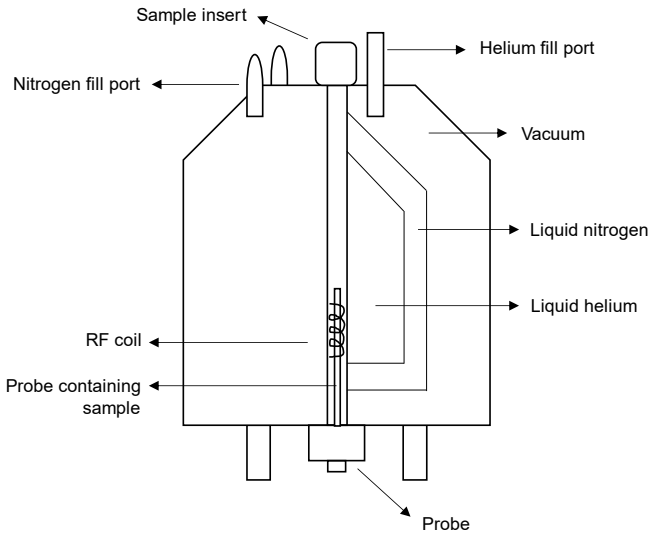

Figure 2.13 *Diagram showing the main features of a NMR magnet, allowing the B_0 magnetic field to be maintained and NMR signal produced.*

2.11.2 The probehead and MAS

Recent advances in ssNMR now means there are a range of probeheads capable of holding a range of different NMR rotors of various diameters, such as 3.2 mm, 2.5 mm, 1.3 mm, and 0.7 mm sample rotors. Probes can be tuned to a particular resonance frequency making signals selective for specific nuclei, such as ^{1}H, ^{13}C, ^{19}F and ^{31}P. The probe is placed in the centre of the magnetic field in which the sample can be placed. RF coils are contained within the probe, tuned to the specific nuclear frequency, allowing RF signals to be produced, exciting the nuclei contained within the sample and the resultant signals generated by nuclear relaxation to be received.

Table 2.3 highlights rotor size compared to its associated sample volume as well as maximum MAS frequency.

Table 2.3 *Rotor size as well as sample volume and maximum MAS frequency achievable (Bruker).*

Rotor Diameter (mm)	Sample volume (μL)	Maximum MAS frequency (kHz)
7	360	7
4	106	15
3.2	47	24
1.9	12	42
1.3	3	67
0.7	0.4	111

In order to achieve the high MAS frequencies needed for narrow line widths on NMR spectra, a Pneumatic Unit (PU) is required. The rotor is spun inside a stator located at the top of the probe. Drive and bearing pressure are directed onto the rotor via the stator allowing MAS. Bearing pressure raises the rotor within the stator allowing frictionless rotation while the drive pressure allows rotation facilitated by drive cap fins present on the rotor.

2.11.3 NMR at the University of Nottingham

The University of Nottingham houses a four channel 800 MHz NMR spectrometer including $^{1}H/^{13}C/^{15}N,^{31}P$ probe allowing high field NMR. The set up is shown in Figure 2.14.

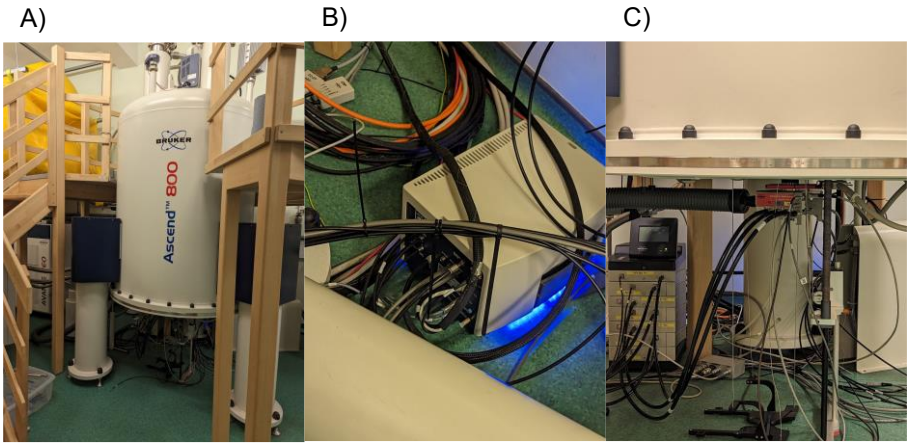

Figure 2.14 *800 MHz set up at the University of Nottingham. A) 800 MHz (^{1}H Larmor frequency) magnet with cabinet. B) MAS unit and C) selected probe inserted into the base of the magnet.*

The selection of probes available for the 800 MHz system has allowed experiments to be done on lipid membrane samples where the effect of DNP dopant and glycerol is assessed as discussed in Chapter 3. This includes 1.3 mm and 2.5 mm rotors with HCN and HXY probes, as well as high MAS proton detection as discussed in Chapter 4.

2.12 DNP theory

DNP builds on the fundamentals of ssNMR with the added benefit of utilising microwave (μw) irradiation to increase sensitivity. DNP involves transferring electron thermal polarization to the coupled nuclei by irradiating Electron Paramagnetic Resonance (EPR) transitions with μw of appropriate frequency. Dynamic Nuclear Polarisation was proposed by Overhauser in the early 1950's which shortly led to the demonstration of experimental DNP on both solid metals and solutions by Carver and Slichter[26]. Later there were developments of other mechanisms of DNP, such as solid effect, cross-effect and thermal mixing that work in dielectric solids[27–30]. Throughout the 80's, experimentation was undertaken on static samples due to the absence of MAS technology for use with DNP. The mid 80's saw several groups use radical enriched polymers and MAS DNP such as Wind et al. in 1985[31]. Griffin and Temkin in 1993, 1995, and 2003 noted higher μw strengths which led to signal enhancement due to the development of high-power μw sources, such as gyrotrons, which were first reported at 5 T[32]. At the end of the 90's there was a plethora of research being undertaken due to the gyrotrons advancement. 2003 also reported enhancements of a factor of >10,000 in liquid state NMR. For the same intensity peak it took one scan with DNP and >20,000 scans taking 65 hours without DNP[33]. 2009 saw the

commercial instrument of 400 MHz DNP NMR system which led to a rapid development of research in the field[34]. Since this time there are now a number of laboratories which have access to 400-800 MHz systems worldwide across a range of research studies, from drug targeting, complex structural investigations, and chemical analysis. These successful applications have in turn stimulated research in developing new and more efficient methods to perform DNP using both continuous wave (CW) and pulsed μw sources[35]. There are several DNP strategies commonly used including, the Overhauser effect, the solid effect, thermal mixing and the Cross-Effect (CE).

The Overhauser effect was the first system proposed for systems with mobile electrons, mainly conducting solids and liquids. It is a two spin system comprising one nucleus and one electron. For this method to be successful it relies on Zero Quantum (ZQ) and Double Quantum (DQ) relaxation pathways with differing relaxation rates leading to enhanced nuclear polarisation. In insulating solids, a significant Overhauser DNP enhancement is observed. This method also requires less μw power[36]. This method has also been shown to be effective in observing enhancements in small molecules in solution[37]. Whilst much of the low-field Overhauser DNP research focuses on 1D NMR experiments to study molecular dynamics and hydration dynamics, recent work has also shown its application in 2D J-resolved spectroscopy to improve spectral resolution[38]. Unlike other mechanisms the Overhauser effect allows for the hyperpolarisation of liquids and whilst it can be used at high-fields there has been growing interest in the use of this method in low and ultra-low field MRI[39].

The solid effect was the first method that was used to observe DNP enhancements in insulating solids. Like the Overhauser effect, the solid effect is a two-spin method requiring one electron and one nucleus. The microwave field induces flip-flop transitions between the electron spins and the near nuclear spins which is the transferred via spin diffusion to other nuclear spins[40]. As well as solids it has also been shown to be effective in samples containing DMPC in the fluid phase. The solid effect is also shown to be effective in solid, non-conducting materials at low temperatures of 100K or below[41].

Thermal mixing is an effective method for the orientation of nuclear spins in polarised targets and hyperpolarisation for MRI[42]. The fundamental process is a triple spin flip with two electron spins and one nuclear spins. The μw pulse reduces the polarisation of some electron spins which is then spread over all the electron spins via spin diffusion. The interaction between the electron spins and the nuclear spin via the

hyperfine interaction transfers the electron spin polarisation[29]. Thermal mixing has been shown to be effective in a number of samples including sodium pyruvate and is dependent on the temperature and radical concentration. Current research focuses on the trade-off between radical concentration and electron relaxation times, improving the efficacy of this DNP mechanism[43].

Whilst all mechanisms have their own merits, it is important to consider the DNP efficiencies in a biological setting. The Overhauser effect is mainly used in liquid samples not relevant for the work presented in the rest of this thesis work. The solid effect is not very efficient at high magnetic fields due to its ~B_0^{-2} dependence. Although applying larger μw strengths can result in sufficient polarisation transfer efficiency, the CE, and the development of specially designed biradicals is often the preferred method in biological samples[44]. Thermal mixing is also not suitable due to the requirement of of several electrons that are dipolar coupled at high concentrations and as a result show broadened EPR linewidths. Although thermal mixing is more efficient than the solid effect, the requirement of high electron concentrations is now suitable for biological samples due to severe broadening of the NMR signals by PRE effects.

At high magnetic fields the CE is widely used for MAS-DNP. The CE has also already been shown to be successful in enhancing ssNMR signals via DNP to study the interactions of Aβ with lipid systems such as POPC/POPG membranes[45], synaptic rat membranes[19] as well as deduce the structure of the protein alone at several stages of the self-assembly pathway[46]. The CE is also effective at low concentrations of proteins and with Aβ interacting with complex lipid membranes[19]. This is important in biological samples where proteins of interest often have low concentrations in physiological conditions. In this thesis we primarily work under conditions where the most efficient mechanism is the CE which is described in detail below.

2.13 CE under MAS

CE DNP is a DNP mechanism that occurs in a system consisting of the two electron spins and one nuclear spin. As shown in Figure 2.15, the $|\alpha_1\beta_2\alpha_n\rangle$ and $|\beta_1\alpha_2\beta_n\rangle$ energy levels have very close energies, which are nearly degenerate. This is why the eigenstates of this pair of levels are the mixture of the $|\alpha_1\beta_2\alpha_n\rangle$ and $|\beta_1\alpha_2\beta_n\rangle$ states due to the effect of the electron-nuclear hyperfine coupling and electron-electron dipole-dipole interaction.

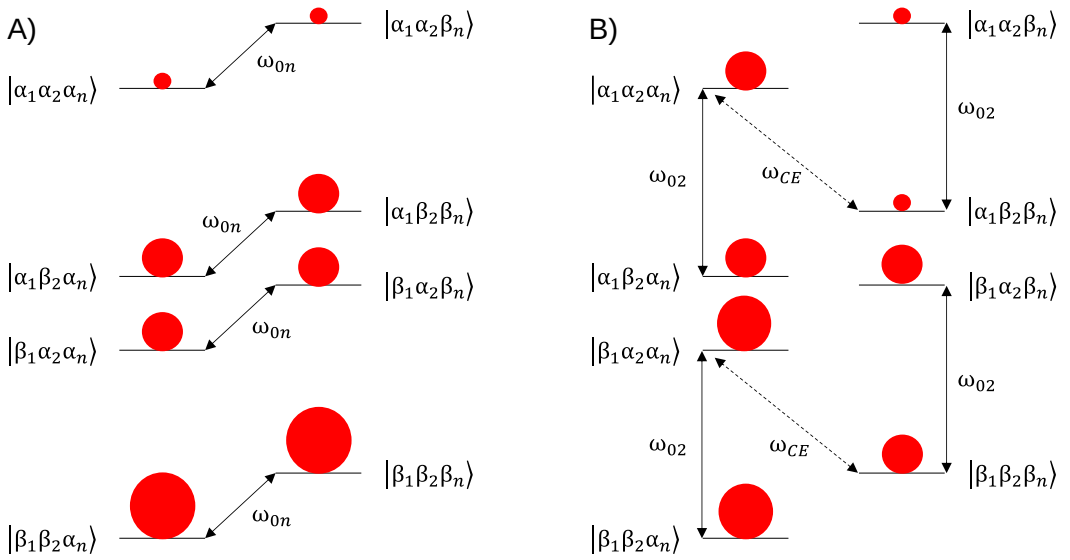

Figure 2.15 *Energy level diagram showing the cross-effect DNP mechanism. The eight energy levels are present due to hyperfine and dipolar coupling. A) Population distribution at thermal equilibrium of a three-spin system. B) μw irradiation at the Larmor frequency of electron two causes an increase in nuclear α spin state population resulting in increased signal and DNP enhancement.*

For static samples, μw irradiation at ω_{0S1} causes an allowed single quantum transition of that electron and a simultaneous forbidden DQ transition of the other. This results in a greater population difference in nuclear α state, giving a larger NMR signal. The maximum signal enhancement that could be achieved under these conditions is:

$$\epsilon = \frac{\gamma_e}{\gamma_N}, \tag{2.29}$$

where γ_e and γ_N are the gyromagnetic ratios of electron and nucleus respectively. For ^{1}H this would amount to a NMR signal enhancement factor of $\epsilon \sim 660$[47].

Under MAS conditions the mechanism shown in Figure 2.15 is only valid at certain points of the rotor cycle, where the energy levels of the three-spin system cross with one another. μw irradiation excites one of the electrons, while the level crossings happen over several rotor cycles causing three-spin flips leading to non-equilibrium nuclear polarization. However, one major drawback is nuclear depolarisation. This is observed through a decrease in the NMR signal under MAS in the presence of unpaired electrons without μw irradiation. The reduction compensates for a smaller difference of electron polarisation until a new equilibrium is reached, below the nuclear Boltzmann thermal equilibrium. Under MAS conditions, the lack of μw irradiation reflects a depolarised nuclear state compared with static conditions[48]. Biradical choice

is a key factor in nuclear depolarisation. The smaller g-tensors distance leads to a reduction in crystal orientation contributing to the CE and a reduction of the electron polarisation difference. Biradicals influence the DNP enhancement leading to lower hyperpolarisation but less depolarisation[49,5049].

2.14 Biradical choice

For the CE to function one requires a pair of radicals located at a rather close distance from one another. Polarizing agents based on a nitroxide biradical have proven to be much more effective compared to monoradicals where one has to rely on the two radicals approaching one another by chance[51,52].

Apart from the length of the linker in a biradical the relative orientation of the TEMPO nitroxide radical rings within the biradical is also an important factor for the MAS DNP efficiency[49]. In CE DNP effective coupling of the two electron spins is crucial to its polarisation transfer. It has been suggested that increasing the sum of the electron-electron dipolar coupling and exchange coupling will increase the CE DNP enhancement. It has also been proposed that altering the exchange coupling without changing the dipolar coupling can maximise DNP enhancement and reduce nuclear depolarisation[53,54]. To allow the 'flip-flop-flip' mechanism of two coupled electrons and a dipolar coupled nuclear spin in CE DNP, the electrons, which are present within the biradical should have an EPR linewidth larger than the nuclear Larmor frequency. Increased DNP enhancement can be achieved by higher μw power, however the interference between the dipolar and exchange coupling occurs regardless of the μw power. An optimum electron spin relaxation time (t_{1e}) is needed to obtain an optimum EPR saturation, however again the interference between couplings exists. This has led to a large effort in optimising the chemical linker joining the two electron (nitroxide) centres, solubility, electron spin relaxation rates and molecular geometry of the polarising agent.

Common biradicals used in CE MAS DNP include AMUPol, TOTAPOL and TEKPol, with their structures shown in Figure 2.16[55].

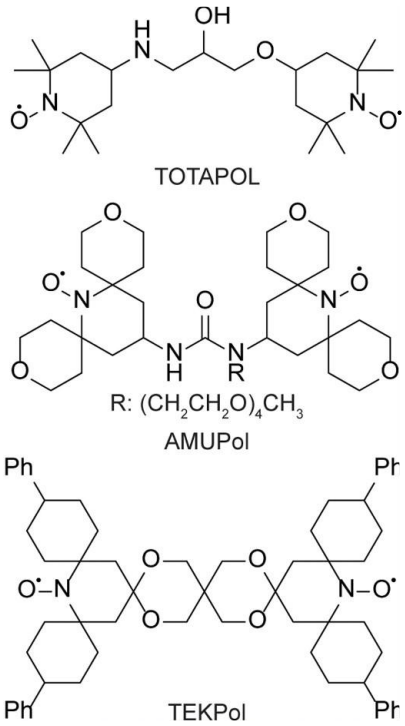

Figure 2.16 *Chemical structures of commonly used biradicals used in CE MAS DNP enhanced NMR experiments, including TOTAPOL, AMUPol and TEKPol*[55]*.*

A typical concentration of biradical is between 5-50 mM and the choice of biradical is also dependant on the sample such as the choice of solvent. With the development of higher magnetic fields, the optimisation of radical choice continues. For example, TOTAPOL contains a hydroxyl and amine moiety increasing the solubility of the biradical in an aqueous environment. Utilising a 2.5 mm rotor large DNP enhancements of a factor of up to 290 were achieved, potentially due to more efficient μw penetration into the sample. It is also an important biradical in the study of cells and proteins as it is also highly soluble in media containing salt and glycerol making it appropriate for DNP of biological systems[52]. AMUPol is also commonly used in the study of biological systems due to its stability and water solubility compared to TOTAPOL. In a study comparing the DNP enhancements of AMUPol to TOTAPOL, as well as other newly developed radicals such as POPAPOL in cellular lysates, AMUPol was found to have the highest enhancement of a factor of ~54, with TOTAPOL exhibiting a lower enhancement of a factor of ~10. The relative DNP enhancement, which takes into build-up times was also found to be 24 for AMUPol compared to 7 with TOTAPOL[56]. TEKPol, a derivative of bTbK, has been found to have a high saturation factor making it an efficient polarising agent with enhancements of over a factor of ~200 in samples at 9.4T and 100K and enhancements of a factor of ~33 and ~12 at 180K and 200K respectively. DNP enhancements of over a factor of 160 are obtained MAS frequencies of 15kHz when

utilising TEKPol[57]. It was suggested that due to the fact TEKPol is not water soluble and can produce better enhancements in organic solvents than AMUPol, it would sit in the membrane vesicles providing good enhancement to membrane systems. It was found that AMUPol and TEKPol follow the same trends with varying concentration, both of which showing optimum enhancement at 10 mM. However, it was shown that AMUPol still produces higher DNP enhancements than TEKPol when the radical was pre-incorporated into lipid vesicle samples (53 compared to 14 respectively). Interestingly, when the radical was added to the membrane after vesicle formation, AMUPol produced a significantly higher enhancement[19].

2.15 DNP hardware

Similar to standard NMR hardware, there are a number of components required to carry out MAS DNP. Although the theory has been known previously, the development of high magnetic fields, μw sources of sufficient strengths and probes capable of maintaining fast MAS frequencies now makes MAS DNP available with several systems across the country. The main components include the spectrometer itself, or the magnet, the gyrotron capable of producing μw irradiation and specifically designed probes designed to house samples and maintain stable MAS. The additional components specific to MAS DNP not previously covered in Section 2.11 are discussed briefly below. Currently Bruker offer a range of MAS DNP systems with μw gyrotrons operating up to 527 GHz which are summarised in Table 2.4.

Table 2.4 *Properties of current commercially available Bruker MAS DNP systems (Bruker)*.

Magnetic field (T)	MW frequency (GHz)	EPR wavelength (mm)	^{1}H NMR frequency (MHz)
9.4	263	1.14	400
14.1	395	0.76	600
18.8	527	0.57	800
21.1	593	0.51	900

2.15.1 The spectrometer

As with standard NMR hardware, a superconducting magnet with field-sweep capability is located in a helium vessel surrounded by a radiation shield which is cooled by a cryogenic refrigerator. Low temperatures are required in MAS DNP to increase nuclear and electron t_1 times and to ensure the various DNP mechanisms are efficient. For temperatures of 100 K – 180 K liquid nitrogen is sufficient, where the

boiled off nitrogen gas is also used in drive and bearing lines allowing rotor spinning. Copper coils surrounding the liquid nitrogen are heated resulting in nitrogen gas[47]. Samples below 90 K require helium cooling and can reach low temperatures of 20 K. Increased MAS are essential in improving the resolution of NMR, however DNP has achieved slower MAS rates than that of room temperature NMR due to the higher viscosity of nitrogen gas. Probes have now been developed to accommodate 0.7 mm rotors meaning spinning speeds of 65 kHz at high fields of 21.15 T[58].

2.15.2 The gyrotron

The development of the gyrotron was a key moment in the development of MAS DNP pioneered by the Griffin group. This was first reported at 5 T in which a 20 W cyclotron resonance maser, or gyrotron, was used as a 140 GHz μw source[32]. In a common 527 GHz gyrotron, a magnetic field of a 10 T superconducting magnet is utilised. An electron gun produces high power μw (>10 W), more suitable for high-field DNP.

2.15.3 Probes

Up to date various low-temperature MAS DNP probes are available commercially (including 0.7, 1.3, 1.9 and 3.2 mm probes with an automated inset/eject capability allowing the probe to stay at low temperature even with a change of sample) compatible with a range of systems (Bruker). They are also specially designed to maintain high MAS rates of 40 kHz. Higher field DNP such as the 800 or 900 MHz ^{1}H frequency spectrometers achieve higher signal enhancements with smaller-diameter rotors due to coupling the μw irradiation to the smaller sample.

2.15.4 DNP at the University of Nottingham

The University of Nottingham is home to a MAS DNP facility comprising a Bruker AVANCE III 600 MHz (^{1}H Larmor frequency) three-channel NMR spectrometer. The Ascend 14.09 T cryomagnetic and 7.2 T (395 GHz) gyrotron are the main components of the system. The facility and its components are shown in Figure 2.17. A 3.2 mm HXY low temperature MAS probe is configured for DNP ssNMR for mainly biological applications.

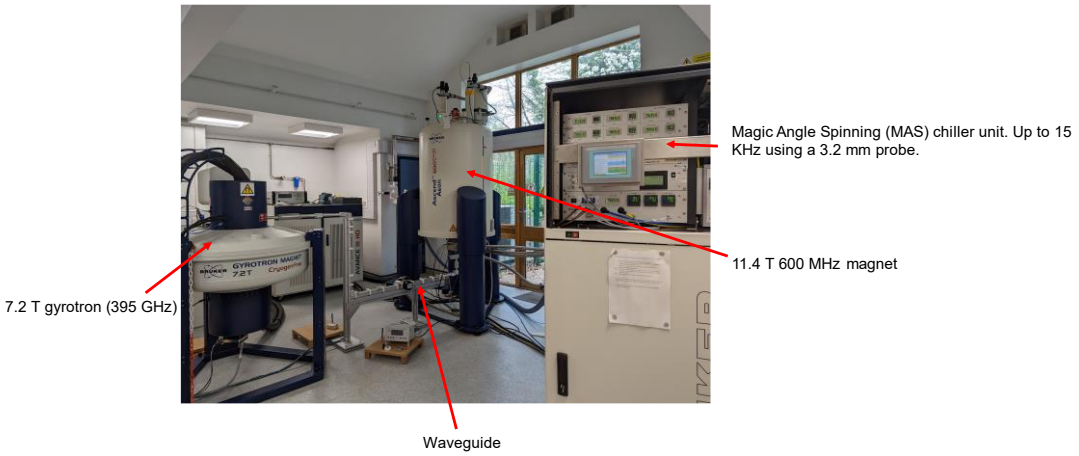

Figure 2.17 *University of Nottingham DNP facility with individual components labelled.*

The combination of these components with recent developments in the technology associated with MAS DNP now makes DNP a more accessible and commonly used method in a field of research. Chapter 4 focuses on the experiments undertaken utilising MAS DNP to study the structure of $A\beta_{(1\text{-}40)}$ interacting with a range of lipid mimic membrane systems.

2.16 References

1. Reuhs, B. L. & Simsek, S. Nuclear Magnetic Resonance. in *Food analysis* 151–163 (2017).

2. Ozerov, R. P. & Vorobyev, A. A. Elements of Quantum Mechanics. in *Physics for Chemists* 423–496 (Elsevier, 2007).

3. Stovell, M. G., Yan, J.-L., Sleigh, A., Mada, M. O., Carpenter, T. A., Hutchinson, P. J. A. & Carpenter, K. L. H. Assessing Metabolism and Injury in Acute Human Traumatic Brain Injury with Magnetic Resonance Spectroscopy: Current and Future Applications. *Front. Neurol.* **8**, 426 (2017).

4. Clore, G. M. Practical Aspects of Paramagnetic Relaxation Enhancement in Biological Macromolecules. in 485–497 (2015).

5. Huang, S., Umemoto, R., Tamura, Y., Kofuku, Y., Uyeda, T. Q. P., Nishida, N. & Shimada, I. Utilization of paramagnetic relaxation enhancements for structural analysis of actin-binding proteins in complex with actin. *Sci. Rep.* **6**, 33690 (2016).

6. Hocking, H. G., Zangger, K. & Madl, T. Studying the Structure and Dynamics of Biomolecules by Using Soluble Paramagnetic Probes. *ChemPhysChem* **14**, 3082–3094 (2013).

7. Softley, C. A., Bostock, M. J., Popowicz, G. M. & Sattler, M. Paramagnetic NMR in drug discovery. *J. Biomol. NMR* **74**, 287–309 (2020).

8. Yamaguchi, T., Matsuzaki, K. & Hoshino, M. Interaction between soluble Aβ-(1–40) monomer and Aβ-(1–42) fibrils probed by paramagnetic relaxation enhancement. *FEBS Lett.* **587**, 620–624 (2013).

9. Liao, S. Y., Lee, M., Wang, T., Sergeyev, I. V. & Hong, M. Efficient DNP NMR of membrane proteins: sample preparation protocols, sensitivity, and radical location. *J. Biomol. NMR* **64**, 223–237 (2016).

10. Rudraksha Dutta Majumdar. A Nuclear Magnetic Resonance spectroscopic investigation of the molecular structure and aggregation behavior of Asphaltenes. *PhD thesis, Univ. Lethbridge* (2010).

11. Wishart, D. S. & Sykes, B. D. The 13C Chemical-Shift Index: A simple method

for the identification of protein secondary structure using 13C chemical-shift data. *J. Biomol. NMR* **4**, 171–180 (1994).

12. Das, B. B., Lin, E. C. & Opella, S. J. Experiments Optimized for Magic Angle Spinning and Oriented Sample Solid-State NMR of Proteins. *J. Phys. Chem. B* **117**, 12422–12431 (2013).

13. Magic angle spinning in solid state n.m.r. spectroscopy. *Philos. Trans. R. Soc. London. Ser. A, Math. Phys. Sci.* **299**, 505–520 (1981).

14. Bennett, A. E., Rienstra, C. M., Auger, M., Lakshmi, K. V. & Griffin, R. G. Heteronuclear decoupling in rotating solids. *J. Chem. Phys.* **103**, 6951–6958 (1995).

15. Fung, B. M., Khitrin, A. K. & Ermolaev, K. An Improved Broadband Decoupling Sequence for Liquid Crystals and Solids. *J. Magn. Reson.* **142**, 97–101 (2000).

16. Levitt, M. H. Symmetry-Based Pulse Sequences in Magic-Angle Spinning Solid-State NMR. in *Encyclopedia of Magnetic Resonance* (John Wiley & Sons, Ltd, 2007).

17. Jung, K. J., Katz, J., Boxt, L. M., Hilal, S. K. & Cho, Z. H. Breakthrough of Single-Quantum Coherence and Its Elimination in Double-Quantum Filtering. *J. Magn. Reson. Ser. B* **107**, 235–241 (1995).

18. Karlsson, T., Brinkmann, A., Verdegem, P. J. E., Lugtenburg, J. & Levitt, M. H. Multiple-quantum relaxation in the magic-angle-spinning NMR of spin pairs. *Solid State Nucl. Magn. Reson.* **14**, 43–58 (1999).

19. Thomas Deo. Applications of Dynamic Nuclear Polarisation in biological systems. *PhD thesis, Univ. Nottingham* (2020).

20. Samoson, A. H-MAS. *J. Magn. Reson.* **306**, 167–172 (2019).

21. Zhang, R., Hong, Y., Ravula, T., Nishiyama, Y. & Ramamoorthy, A. High-resolution proton-detected MAS experiments on self-assembled diphenylalanine nanotubes enabled by fast MAS and high magnetic field. *J. Magn. Reson.* **313**, 106717 (2020).

22. Callon, M., Luder, D., Malär, A. A., Wiegand, T., Římal, V., Lecoq, L., Böckmann, A., Samoson, A. & Meier, B. H. High and fast: NMR protein–proton

side-chain assignments at 160 kHz and 1.2 GHz. *Chem. Sci.* **14**, 10824–10834 (2023).

23. Penzel, S., Oss, A., Org, M.-L., Samoson, A., Böckmann, A., Ernst, M. & Meier, B. H. Spinning faster: protein NMR at MAS frequencies up to 126 kHz. *J. Biomol. NMR* **73**, 19–29 (2019).

24. Knight, M. J., Webber, A. L., Pell, A. J., Guerry, P., Barbet-Massin, E., Bertini, I., Felli, I. C., Gonnelli, L., Pierattelli, R., Emsley, L., Lesage, A., Herrmann, T. & Pintacuda, G. Fast Resonance Assignment and Fold Determination of Human Superoxide Dismutase by High-Resolution Proton-Detected Solid-State MAS NMR Spectroscopy. *Angew. Chemie Int. Ed.* **50**, 11697–11701 (2011).

25. Wickramasinghe, A., Xiao, Y., Kobayashi, N., Wang, S., Scherpelz, K. P., Yamazaki, T., Meredith, S. C. & Ishii, Y. Sensitivity-Enhanced Solid-State NMR Detection of Structural Differences and Unique Polymorphs in Pico- To Nanomolar Amounts of Brain-Derived and Synthetic 42-Residue Amyloid-β Fibrils. *J. Am. Chem. Soc.* **143**, 11462–11472 (2021).

26. Maly, T., Debelouchina, G. T., Bajaj, V. S., Hu, K.-N., Joo, C.-G., Mak–Jurkauskas, M. L., Sirigiri, J. R., van der Wel, P. C. A., Herzfeld, J., Temkin, R. J. & Griffin, R. G. Dynamic nuclear polarization at high magnetic fields. *J. Chem. Phys.* **128**, 052211 (2008).

27. Hovav, Y., Feintuch, A. & Vega, S. Theoretical aspects of dynamic nuclear polarization in the solid state – The solid effect. *J. Magn. Reson.* **207**, 176–189 (2010).

28. Hovav, Y., Feintuch, A. & Vega, S. Theoretical aspects of dynamic nuclear polarization in the solid state – The cross effect. *J. Magn. Reson.* **214**, 29–41 (2012).

29. Wenckebach, W. T. Dynamic nuclear polarization via the cross effect and thermal mixing: A. The role of triple spin flips. *J. Magn. Reson.* **299**, 124–134 (2019).

30. Hu, K.-N. Polarizing agents and mechanisms for high-field dynamic nuclear polarization of frozen dielectric solids. *Solid State Nucl. Magn. Reson.* **40**, 31–41 (2011).

31. Wind, R. A., Duijvestijn, M. J., van der Lugt, C., Manenschijn, A. & Vriend, J. Applications of dynamic nuclear polarization in 13C NMR in solids. *Prog. Nucl. Magn. Reson. Spectrosc.* **17**, 33–67 (1985).

32. Becerra, L. R., Gerfen, G. J., Temkin, R. J., Singel, D. J. & Griffin, R. G. Dynamic nuclear polarization with a cyclotron resonance maser at 5 T. *Phys. Rev. Lett.* **71**, 3561–3564 (1993).

33. Ardenkjær-Larsen, J. H., Fridlund, B., Gram, A., Hansson, G., Hansson, L., Lerche, M. H., Servin, R., Thaning, M. & Golman, K. Increase in signal-to-noise ratio of > 10,000 times in liquid-state NMR. *Proc. Natl. Acad. Sci.* **100**, 10158–10163 (2003).

34. Rosay, M., Tometich, L., Pawsey, S., Bader, R., Schauwecker, R., Blank, M., Borchard, P. M., Cauffman, S. R., Felch, K. L., Weber, R. T., Temkin, R. J., Griffin, R. G. & Maas, W. E. Solid-state dynamic nuclear polarization at 263 GHz: spectrometer design and experimental results. *Phys. Chem. Chem. Phys.* **12**, 5850 (2010).

35. Tan, K. O., Yang, C., Weber, R. T., Mathies, G. & Griffin, R. G. Time-optimized pulsed dynamic nuclear polarization. *Sci. Adv.* **5**, (2019).

36. Can, T. V., Ni, Q. Z. & Griffin, R. G. Mechanisms of dynamic nuclear polarization in insulating solids. *J. Magn. Reson.* **253**, 23–35 (2015).

37. Keller, T. J., Laut, A. J., Sirigiri, J. & Maly, T. High-resolution Overhauser dynamic nuclear polarization enhanced proton NMR spectroscopy at low magnetic fields. *J. Magn. Reson.* **313**, 106719 (2020).

38. Keller, T. J. & Maly, T. Overhauser dynamic nuclear polarization (ODNP)-enhanced two-dimensional proton NMR spectroscopy at low magnetic fields. *Magn. Reson.* **2**, 117–128 (2021).

39. Fehling, P., Buckenmaier, K., Dobrynin, S. A., Morozov, D. A., Polienko, Y. F., Khoroshunova, Y. V., Borozdina, Y., Mayer, P., Engelmann, J., Scheffler, K., Angelovski, G. & Kirilyuk, I. A. The effects of nitroxide structure upon 1H Overhauser dynamic nuclear polarization efficacy at ultralow-field. *J. Chem. Phys.* **155**, (2021).

40. Wenckebach, W. T. The Solid Effect. *Appl. Magn. Reson.* **34**, 227 (2008).

41. Kuzhelev, A. A., Dai, D., Denysenkov, V. & Prisner, T. F. Solid-like Dynamic Nuclear Polarization Observed in the Fluid Phase of Lipid Bilayers at 9.4 T. *J. Am. Chem. Soc.* **144**, 1164–1168 (2022).

42. Wenckebach, W. T. Dynamic nuclear polarization via thermal mixing: Beyond the high temperature approximation. *J. Magn. Reson.* **277**, 68–78 (2017).

43. Epasto, L. M., Maimbourg, T., Rosso, A. & Kurzbach, D. Unified understanding of the breakdown of thermal mixing dynamic nuclear polarization: The role of temperature and radical concentration. *J. Magn. Reson.* **362**, 107670 (2024).

44. Akbey, Ü. & Oschkinat, H. Structural biology applications of solid state MAS DNP NMR. *J. Magn. Reson.* **269**, 213–224 (2016).

45. Deo, T., Cheng, Q., Paul, S., Qiang, W. & Potapov, A. Application of DNP-enhanced solid-state NMR to studies of amyloid-β peptide interaction with lipid membranes. *Chem. Phys. Lipids* **236**, 105071 (2021).

46. Potapov, A., Yau, W.-M., Ghirlando, R., Thurber, K. R. & Tycko, R. Successive Stages of Amyloid-β Self-Assembly Characterized by Solid-State Nuclear Magnetic Resonance with Dynamic Nuclear Polarization. *J. Am. Chem. Soc.* **137**, 8294–8307 (2015).

47. Hu, K.-N., Debelouchina, G. T., Smith, A. A. & Griffin, R. G. Quantum mechanical theory of dynamic nuclear polarization in solid dielectrics. *J. Chem. Phys.* **134**, 125105 (2011).

48. Stern, Q., Cousin, S. F., Mentink-Vigier, F., Pinon, A. C., Elliott, S. J., Cala, O. & Jannin, S. Direct observation of hyperpolarization breaking through the spin diffusion barrier. *Sci. Adv.* **7**, (2021).

49. Mentink-Vigier, F. Optimizing nitroxide biradicals for cross-effect MAS-DNP: the role of g -tensors' distance. *Phys. Chem. Chem. Phys.* **22**, 3643–3652 (2020).

50. Thurber, K. R. & Tycko, R. Theory for cross effect dynamic nuclear polarization under magic-angle spinning in solid state nuclear magnetic resonance: The importance of level crossings. *J. Chem. Phys.* **137**, (2012).

51. Hu, K.-N., Yu, H., Swager, T. M. & Griffin, R. G. Dynamic Nuclear Polarization

with Biradicals. *J. Am. Chem. Soc.* **126**, 10844–10845 (2004).

52. Song, C., Hu, K.-N., Joo, C.-G., Swager, T. M. & Griffin, R. G. TOTAPOL: A Biradical Polarizing Agent for Dynamic Nuclear Polarization Experiments in Aqueous Media. *J. Am. Chem. Soc.* **128**, 11385–11390 (2006).

53. Equbal, A., Tagami, K. & Han, S. Balancing dipolar and exchange coupling in biradicals to maximize cross effect dynamic nuclear polarization. *Phys. Chem. Chem. Phys.* **22**, 13569–13579 (2020).

54. Tagami, K., Equbal, A., Kaminker, I., Kirtman, B. & Han, S. Biradical rotamer states tune electron J coupling and MAS dynamic nuclear polarization enhancement. *Solid State Nucl. Magn. Reson.* **101**, 12–20 (2019).

55. Plainchont, B., Berruyer, P., Dumez, J.-N., Jannin, S. & Giraudeau, P. Dynamic Nuclear Polarization Opens New Perspectives for NMR Spectroscopy in Analytical Chemistry. *Anal. Chem.* **90**, 3639–3650 (2018).

56. Ackermann, B. E., Lim, B. J., Elathram, N., Narayanan, S. & Debelouchina, G. T. A Comparative Study of Nitroxide-Based Biradicals for Dynamic Nuclear Polarization in Cellular Environments. *ChemBioChem* **23**, (2022).

57. Zagdoun, A., Casano, G., Ouari, O., Schwarzwälder, M., Rossini, A. J., Aussenac, F., Yulikov, M., Jeschke, G., Copéret, C., Lesage, A., Tordo, P. & Emsley, L. Large Molecular Weight Nitroxide Biradicals Providing Efficient Dynamic Nuclear Polarization at Temperatures up to 200 K. *J. Am. Chem. Soc.* **135**, 12790–12797 (2013).

58. Berruyer, P., Björgvinsdóttir, S., Bertarello, A., Stevanato, G., Rao, Y., Karthikeyan, G., Casano, G., Ouari, O., Lelli, M., Reiter, C., Engelke, F. & Emsley, L. Dynamic Nuclear Polarization Enhancement of 200 at 21.15 T Enabled by 65 kHz Magic Angle Spinning. *J. Phys. Chem. Lett.* **11**, 8386–8391 (2020).

3. The effect of Dynamic Nuclear Polarisation sample content on the lipid membrane

3.1 Introduction

Samples required for Dynamic Nuclear Polarisation (DNP) enhanced solid-sate Nuclear Magnetic Resonance (ssNMR) experiments for the study of peptide/lipid interactions consist of several components that may not necessarily be inert with respect to one another. As a result, the interaction of a peptide/protein with the lipid bilayer may be affected. Firstly, producing significant DNP enhancements via the cross-effect requires the use of a stable biradical as a polarizing agent[1]. Several nitroxide-based polarizing agents, including TOTAPOL[2], AMUPol[3], TEMPOL[4] and DOTOPA[5] were shown to have good solubility in aqueous solutions that enable their applications for studies of biomolecules. Still, depending on their chemical structure, polarizing agents have a preference for a hydrophobic or hydrophilic phase[6], which could have an effect on the biradical partitioning in the presence of amphipathic lipid bilayers. In addition, a biradical may have a specific affinity to certain lipid headgroups[7].

Secondly, a biradical should typically be dissolved in a solution which contains a cryoprotecting component. This component e.g., glycerol in the commonly used mixture of d_6-glycerol/D_2O/H_2O 60/30/10 w/w%[8], yields a glassy matrix when the solution is frozen. Without a cryoprotectant, the biradical electron spins relax too fast for good DNP enhancements, which is thought to happen due to exclusion of the polarizing agent from the ice crystals[9]. The presence of a cryoprotectant may in turn affect the lipid bilayer due to a change in dielectric constant and viscosity. In the context of this work, it is therefore important to investigate the effects of DNP sample content on the lipid bilayer in more detail. Some of the most commonly used lipids and membrane components used in the investigation of membrane/protein interactions utilising DNP, including those presented in this chapter and their abbreviations are shown in Table 3.1.

Table 3.1 *Abbreviations of some commonly used lipids and membrane components used in the investigation of membrane/protein interactions as well as those used in this work.*

Abbreviation	Lipid
DMPC	1,2-dimyristoyl-sn-glycero-3-phosphocholine
DMPS	1,2-dimyristoyl-sn-glycero-3-phospho-L-serine
Chol	Cholesterol
Sphin	Sphingomyelin
GM1	Ganglioside GM1
POPC	1-palmitoyl-2-oleoyl-glycero-3-phosphocholine
POPG	1-palmitoyl-2-oleoyl-sn-glycero-3-phospho-(1'-rac-glycerol)
POPS	1-palmitoyl-2-oleoyl-sn-glycero-3-phospho-L-serine
POPE	1-palmitoyl-2-oleoyl-sn-glycero-3-phosphoethanolamine

Many DNP enhanced ssNMR studies of membrane-bound proteins have found DNP enhancements to be significantly lower than those achieved in non-membrane systems. Studies on an *E. coli* membrane using DNP found enhancements between a factor of ~10-30[10], and enhancements of a factor of ~32 were found for a signal protein bound to a reconstituted Sec translocon[11]. Salnikov et al. investigated the DNP enhancements of several lipid-anchored biradicals in a range of lipid membrane systems. They found a range of enhancements, from a factor of ~2 in a POPS membrane, with either bTbK or AMUPol/Chol which possesses a lipid-anchoring unit, to a factor of ~49 for a PyPol-C16 lipid anchoring biradical in a POPC membrane, indicating the importance of lipid and biradical choice[12]. DNP of pharmaceutical solids however, have found enhancements of up to a factor of ~92 for compounds such as ambroxol HCl, and a factor of ~260 for histidine HCl[13]. This difference between membrane bound and non-membrane bound compounds was suggested to be due to the inability for the radical to be uniformly distributed through complex membrane systems[6]. It has also been previously reported that the presence of methyl groups and their motion near unpaired electrons causes increased relaxation of the electron-spin polarisation, significantly reducing the DNP enhancement[14].

Deuteration has been suggested to overcome the decreased enhancement caused by increased relaxation, whether this be the radical, solvent or either membrane or protein. Solvent deuteration has been a common method for several years with many

DNP experiments utilising deuterated glasses as well as using partially deuterated solvents[1,15]. The level of protein deuteration has also been shown to overcome short relaxation times. Perdeuteration of the protein produces DNP enhancements of a factor of ~120 compared to ~31 in fully protonated samples[16]. However, deuteration has not always been shown to increase the DNP enhancement. A study quantifying the relative sensitivity enhancement between AMUPol and TOTAPOL, no net enhancement sensitivity increase was found between a deuterated membrane compared with its protonated form[17]. Another study investigated the potential increase in enhancement with deuteration to either one of the two palmitoyl fatty acid chains of the phospholipids[6]. Only one fatty acid was chosen due to the fact that even though deuteration of the entire membrane has been shown to give increased membrane protein DNP signals, a decrease in CP magnetisation from ^{1}H to other atoms was exhibited[17]. Regardless of which fatty acid chain was deuterated, no increase in DNP enhancement of the ^{13}C signals was observed[6]. Although, despite the fact that lower enhancements in membrane systems are typical when using DNP, experimental time is reduced, and sensitivity is increased, demonstrating the benefit of using DNP-enhanced ssNMR[10].

Liao et al. examined several preparation protocols for DNP samples of lipid bilayers, and the effects of protocol details on the sensitivity and resolution of DNP-enhanced NMR spectra, which included, the radical membrane mixing method, deuteration level, radical type (AMUPol and TOTAPOL), cryoprotectant type (glycerol and DMSO) and the effects of headgroup (specifically PE and PC). Also, the location of biradical with respect to the membrane has been studied by the Paramagnetic Relaxation Enhancements (PRE) in the room-temperature ssNMR spectra of lipids in the presence of a polarizing agent. It was found that a) direct titration provides significantly higher DNP enhancement compared to the centrifugation sample preparation technique, b) AMUPol provides a fourfold higher DNP enhancement compared to TOTAPOL, c) the DNP enhancements in protonated and deuterated lipid membranes are similar, d) cryoprotecting glycerol gave a higher enhancement of a factor of ~1.5 compared to DMSO, and e) PE lipid membranes gave sharper signals for disordered peptide residues, showing effects of the membrane on protein interaction[17].

Work by Thomas Deo furthered this and systematically explored the content of glycerol, the biradical type and concentration on the disruption to the lipid bilayer[18]. Firstly, by measuring T_1 and T_2 of ^{13}C under DNP conditions (temperatures of ~100 K) it was found that the presence of glycerol was crucial for obtaining a homogeneous distribution of radical. Secondly, it was found that signal enhancements increased with

the concentration of AMUPol, however, at higher AMUPol concentrations the effects of paramagnetic bleaching and depolarisation lead to a signal loss. An optimal concentration of AMUPol, balancing between these effects, and providing reasonable resolution, was found experimentally. Finally, the DNP enhancements of sample with highly hydrophobic TEKPol and water-soluble AMUPol biradicals were compared to one another. When pre-incorporated into the lipid membrane, TEKPol was shown to have a higher DNP enhancement than AMUPol, however, AMUPol produced the highest DNP enhancement when mixed with the membrane after lipid membrane formation. This suggests that AMUPol is a more efficient polarising agent when added and dissolved in the bulk solvent, compared to when it is closely associated with lipid molecules. AMUPol was therefore the preferred biradical for this thesis work, with mixing the biradical into the membrane after lipid membrane formation as the chosen method.

With the sample and DNP matrix optimised, the biradical position in a simple membrane system was assessed utilising the PRE methodology, as well as changes to the lipid membrane by assessing the static and MAS ^{31}P spectra of the sample. PRE occurs due to hyperfine interactions between unpaired radical electron and nuclear spins which has an r^{-6} distance dependence.

The relative PRE in the lipid NMR spectra at each lipid position is given by a ratio S/S_0, where S and S_0 are the signal intensity of the lipid resonance with and without the polarising agent, also referred to as the DNP dopant , and glycerol respectively. For lipids with charged PC headgroup (POPC and DMPC), it was found that with 10 mM AMUPol, a characteristic decline in PRE was observed from the first headgroup resonance to the last one. The C2 position of the POPC lipid showed a local minima whereby the radical anchored to the lipid causing signal attenuation in this region. For lipids with charged PG headgroup (POPG), no evidence was shown for significant differences in the interactions of biradical with the uncharged diol group of POPG compared to the charged POPC tertiary amine. In both samples, the headgroup signals were more attenuated than lipid tail signals[18].

The addition of glycerol was shown to have large effects on the attenuation of lipid signals in the headgroup region of POPG and the Θ position of the lipid tail. This is consistent with the theory of glycerol partitioning into the lipid bilayer which allows the biradical to interact more closely with the lipid resulting in a higher PRE. The biradical may also be less soluble in a glycerol-containing environment, making it more favourable energetically to be solubilised in lipids. DNP enhancement is also therefore

higher as the biradical can sit more closely to the nuclear spins. Interestingly, in a POPG lipids, no signal attenuation is observed at the Θ position in a glycerol containing sample[18].

The use of other biradicals and their effects on PRE in a simple lipid environment were also assessed. TEKPol has been shown to cluster in aqueous DNP environments, leading to unfavourable enhancement and relaxation properties. At several positions in POPC lipids, TEKPol produces a differing PRE, most notably at the headgroup β position, where signal attenuation is stronger than that produced by AMUPol. TEKPol is therefore suggested to penetrate deeper into the hydrophobic part of lipid bilayer. However, a similar trend to AMUPol is shown, where the attenuation is more pronounced in the head region compared to the lipid tail[18].

^{31}P chemical shift anisotropy (CSA) patterns arising from PO^{4-} in lipid headgroups are shown to be highly sensitive to changes in structure and dynamics of phospholipid membranes[19]. Isotropic chemical shifts can also provide information about the lipid structure. Comparing samples of a POPC/POPG mixture, with 10 mM AMUPol, 60% glycerol by volume and both 10 mM AMUPol and 60% glycerol by volume, minimal changes were observed in the CSA patterns under static conditions, suggesting minimal effects on the lipid structure by the DNP dopant and glycerol. This is an important feature when investigating membrane proteins under conditions which mimic cellular membranes. When the ^{31}P spectra was recorded under 15 kHz MAS, there were some differences in the spectra when AMUPol and glycerol were added. Individually adding the DNP dopant or glycerol caused line broadening in both POPG and POPC peaks, with AMUPol interacting more with POPG and glycerol with the neutral headgroup of POPC. The linewidth appears the largest with the addition of both dopant and glycerol[18].

These results give a good insight into the effects of the DNP dopant and glycerol on lipid structure and how polarisation is transferred in a membrane and protein sample. However, a membrane made of lipids of one kind is a very simplistic model for a real biological membrane. The addition of compounds such as Chol and GM1 to create a Lipid Mimic (LM) system that reproduces the membrane of a human cell, investigating the effects of the DNP dopant and glycerol in these conditions will help to further optimise sample conditions to give improved DNP enhancements. Details of the individual components used to make the LM system and their effects on the membrane and protein binding are discussed further in Chapter 4.

Lipids are known to exist in distinct membrane phases. In the solid crystalline phase lipids are highly ordered creating a compact lipid environment. If the lipid hydrocarbon chains are tilted with respect the crystalline phase the membrane enters the gel phase, reliant on the hydration level of the membrane. The fluid or liquid phase of the membrane has highly disordered lipids with increased lateral and rotational diffusion of the lipids. The change from the gel phase to the liquid phase arises at temperatures specific to each lipid known as the transition temperature[20]. It is also important to consider the effects of components such as Chol and GM1 as well as the biradical and glycerol on these phase transition.

This chapter aims to explore the effect of AMUPol, glycerol and the DNP sample content on the LM system, specifically, the partitioning of AMUPol into the bilayer. AMUPol interaction with the bilayer and the changes in the bilayer structure were probed using room-temperature ssNMR experiments.

3.2 Sample preparation

The LM preparation protocol was adapted from work by Qiang et al.[21].

3.2.1 PRE measurements

Either pure DMPC lipid (20 mg) or the LM system containing DMPC (13.2 mg), DMPS (2.74 mg), Sphin (9.86 mg), Chol (2.52 mg) and GM1 (3 mg) were co-dissolved in chloroform, which corresponds to a molar ratio of 1.5:0.3:1:0.5:0.15 respectively and sonicated in a water bath for five minutes to ensure complete dissolving. Solvent was then removed by drying under a stream of N_2 and placed under vacuum to completely remove the chloroform. The resulting lipid film was rehydrated with phosphate buffer (13.4 ml, 10 mM, pH 7.4) and then agitated at room temperature for one hour. This was followed by ten cycles of freeze-thaw between liquid nitrogen and 37^{o}C and five-minute sonication resulting in homogeneous membranes. Each lipid suspension was split into three identical aliquots and centrifuged (26000 rpm, one hour). The remaining supernatant was removed by pipette to give a membrane pellet, with the remaining H_2O in the sample being recorded. The DNP dopant and glycerol were then added meaning the three samples included 1) reference sample – not altered, 2) AMUPol (10 mM) and 3) AMUPol (10 mM) + Glycerol (60%) by volume. The samples were vortexed for ten minutes to ensure the complete mixing of additives with lipid membranes. Hydration levels in all samples was reduced to ~40% using a lyophiliser. The samples were packed into 3.2 mm rotors using a home built packing tool. Packing

very viscous membrane pellets into NMR rotor was done using a high-density polyethylene (HDPE) tool. The tool holds the rotor in one ection with a smaller component being screwed into place below as shown in Figure 3.1A). The sample can then be scraped via a spatula from the centrifuge tube and placed into the conical part of the larger component, which has a small hole leading to the open top of the rotor shown Figure 3.1B). The tool is specifically designed to fit into a Beckman Coulter centrifuge rotor as shown in Figure 3.1C). Centrifugation at ~3000 RPM for around ten seconds forces the sample into the rotor without disrupting the sample itself.

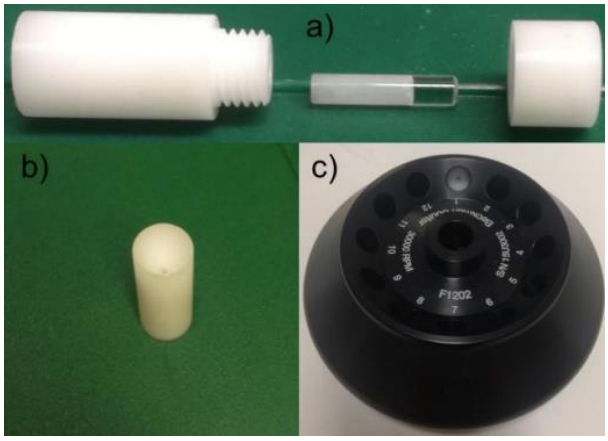

Figure 3.1 *Home-built packing tool for sample preparation. A) The rotor fits into a hole inside the larger component, the smaller screws onto the bottom to hold the rotor in place. B) The membrane is placed into the conical part of the larger section of the tool which has a hole above the open end of the rotor. C) The tool fits inside a centrifuge rotor with centrifugation forcing the sample into the rotor.*

SsNMR experiments were carried out using a Bruker Avance III 800MHz spectrometer with a 3.2 mm ^{1}H and ^{13}C tuned probe. The cross polarisation (CP) experiment was carried out with a MAS rate of 8 kHz and 1024 acquisitions. All spectra were referenced to adamantane with a CH signal at 38.48 ppm. The samples were maintained at 20°C during acquisition. Spectra were processed using TopSpin® version 4.0.7 software, which was used to determine signal strength with ω-1 alkyl taken as the normalisation reference. Previous work has used ω as the reference[17], however, in this work ω-1 was found to provide a better signal intensity thus reducing error.

3.2.2 ^{31}P measurements

Several models were subject to the analysis of ^{31}P NMR spectra.

1. Pure DMPC.
2. DMPC/ DMPS with molar ratios of 1.5:0.3 respectively.
3. DMPC/DMPS/Chol with molar ratios of 1.5:0.3:1:0 respectively.
4. LM system containing DMPC/DMPS/Sphin/Chol/GM1 with molar ratios of 1.5:0.3:1:0.5:0.15 respectively.

Sample components were co-dissolved in chloroform and sonicated in a water bath for five minutes to ensure complete dissolving. Solvent was then removed by drying the sample under a stream of N_2 and placing under vacuum to completely remove the chloroform. The resulting lipid film was rehydrated with Tris-HCl and agitated at room temperature for one hour. The same freeze-thaw, dopant and glycerol addition and rotor packing protocol was followed as stated in the Section 3.2.1 however a 2.5 mm rotor was used.

The ^{31}P-NMR spectra were collected using a Bruker Avance III spectrometer (600 MHz ^{1}H NMR frequency) equipped with H/X/Y probe. MAS-NMR spectra were recorded at 15 kHz spinning speed with SPINAL-64 ^{1}H decoupling using 1024 scans. Static spectra were recorded with SPINAL-64 ^{1}H decoupling using 81920 scans. All spectra were referenced to adamantane with a ^{13}C CH signal at 38.48 ppm as a secondary chemical shift reference. The samples were also maintained at 20°C during acquisition.

3.3 Biradical position within a lipid membrane

The depth of biradical insertion into the membrane is important for understanding whether a polarizing agent has affinity to the membrane and whether it might be causing a change in it. To this end, we apply the technique of ^{13}C PRE measurements that has been shown to detect interactions between an unpaired electron of a paramagnetic site and protons up to distances of ~35 Å[22].

DMPC lipid signal assignments in a pure DMPC sample and in a LM mixture are shown in Figure 3.2. It is not possible to assign all peaks within the LM system as each lipid type produces signals which overlap, making assignment difficult, explaining only why the signals from DMPC lipids were used for PRE calculations. Some line broadening has also occurred due to these other lipid signals, however full assignment of the DMPC signals was still possible.

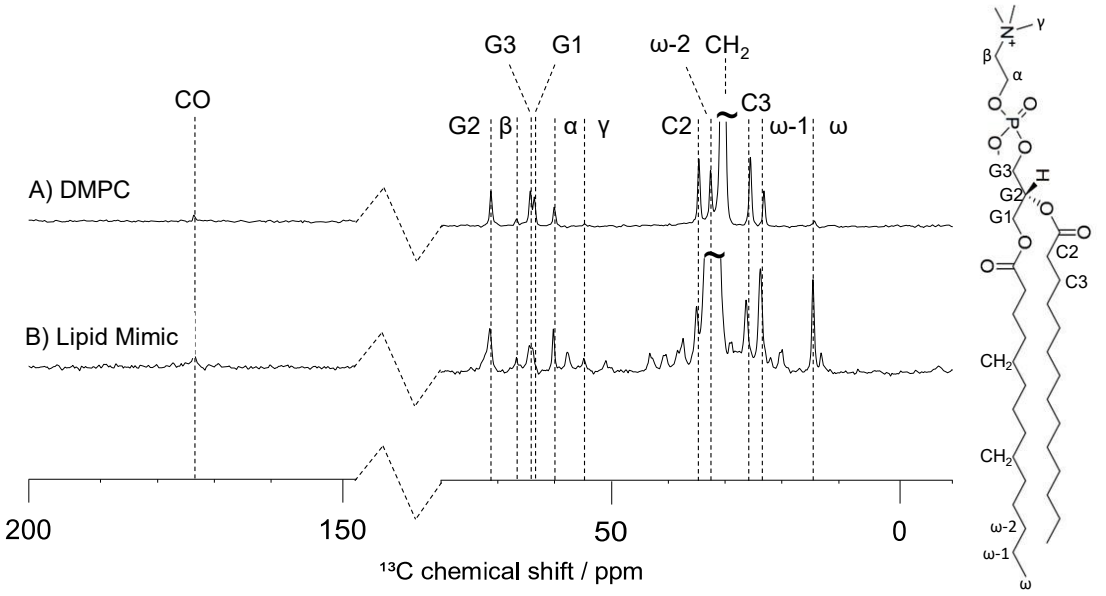

Figure 3.2 *^{13}C CP spectra of A) DMPC bilayer B) LM system containing DMPC/DMPS/Sphin/Chol/GM1 with molar ratios of 1.5:0.3:1:0.5:0.15 respectively. DMPC structure is shown with individual positions named to the right of the spectra, correlating to peaks shown within the spectra, which are highlighted with dotted lines.*

An assignment of the full LM system as used in this work was not found in the literature; however several NMR studies have focused on DMPC lipids[9]. Comparing assignments of pure DMPC lipids to those DMPC signals within a more complex system allows us to have a better understanding of how the structure and dynamics of the lipid membranes change in more complex models. This is relevant when exploring how proteins interact with these membranes and studying proteins under biological conditions. The addition of dopants has also been investigated in simple membranes such as DMPC[17], however has not in the LM system.

The addition of dopants, specifically AMUPol, as well as the addition of glycerol, to lipid membranes has been the subject of several studies[16,17]. It is an important factor in relation to DNP enhancements of protein signals when examining protein interactions with those membranes. It is important that the dopants do not cause significant changes to the membranes before protein addition. In order to be biologically relevant, negligible changes in the membrane due to dopants are necessary. Insertion of AMUPol biradical was investigated with and without the addition of glycerol in a pure DMPC lipid membranes as well as the more complex LM. Figure 3.3 shows signal attenuation in these membrane systems due to paramagnetic AMUPol polarising agent with and without glycerol.

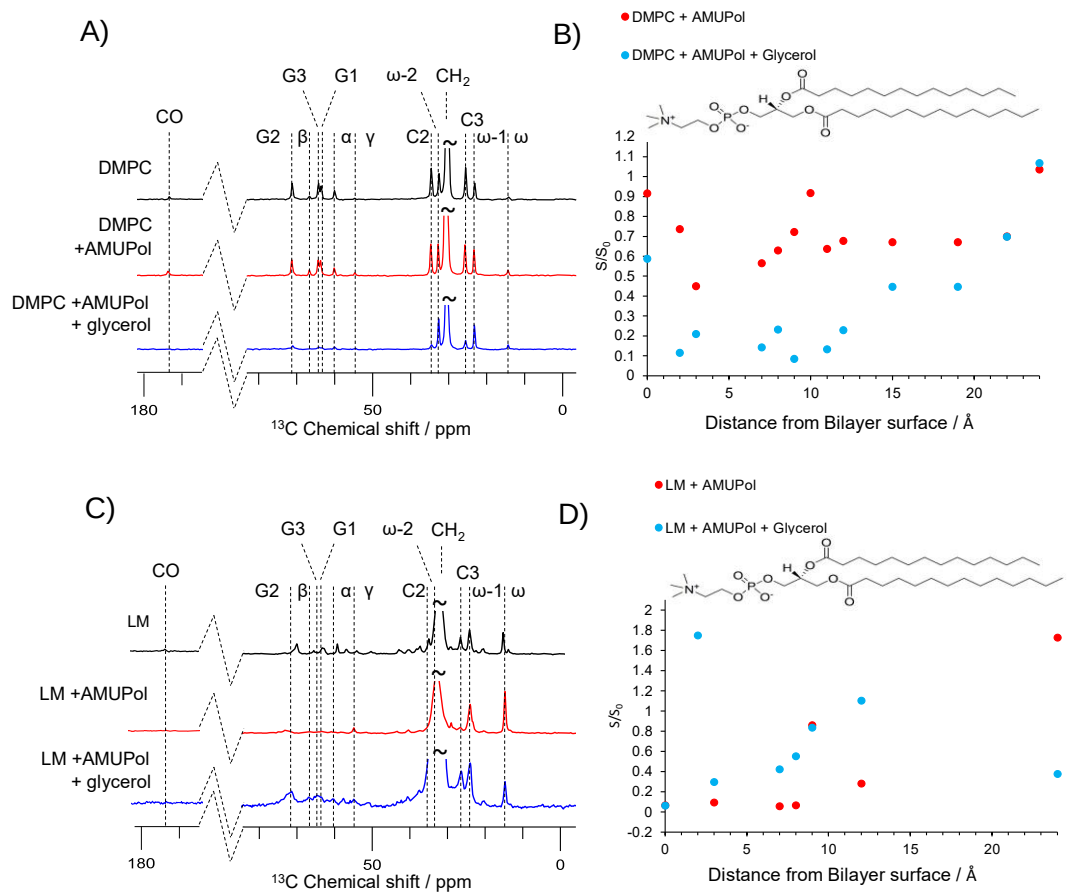

Figure 3.3 *Summary of PRE measurements. A) ^{13}C CP spectra of (black) DMPC lipid bilayers in buffer, (red) in buffer with 10 mM AMUPol, (blue) in buffer with 10 mM AMUPol and 60% glycerol by volume. B) S/S_0 due to PRE extracted from spectra shown in A) with DMPC + 10 mM AMUPol (red) and DMPC + 10 mM AMUPol + 60% glycerol by volume (blue). C) ^{13}C CP spectra of (black) LM system containing DMPC/DMPS/Sphin/Chol/GM1 with molar ratios of 1.5:0.3:1:0.5:0.15 respectively, in buffer, (red) in buffer with 10 mM AMUPol, (blue) in buffer with 10 mM AMUPol and 60% glycerol by volume. D) S/S_0 due to PRE extracted from spectra shown in C) with LM + 10 mM AMUPol (red) and LM + 10 mM AMUPol + 60% glycerol by volume (blue).*

Figure 3.3B) and D) shows a DMPC lipid indicating the distance from the bilayer surface of the assigned signals vs PRE. Starting with the pure DMPC lipid, PRE analysis shown in Figure 3.3B), in glycerol's absence, the residual intensities in the ^{13}C spectra are higher than in the glycerol-protected sample, indicating glycerol has an important role in signal attenuation. This corroborates previous work which concludes that glycerol has the ability to partition to the membrane-water interface[24]. This allows the biradical to interact more closely with the membrane resulting in a greater PRE. In some lipid samples it is suggested that this has consequences regarding DNP enhancements when both AMUPol and glycerol are present. Higher

enhancements in samples may actually be due to this partitioning ability of glycerol and the fact the biradical is closer to the nuclear spins in the LM system[18].

Figures 3.3A) and B) show a characteristic decline in PRE of the headgroup region, from γ to α, present in pure DMPC lipids. This confers with previous work observing DMPC lipid membranes[17]. This is due to AMUPol molecules within the solvent interacting with the lipid head group. Local minima in previous work was seen at the acyl chain residues C2[18] and C3, and the other at the head group γ for the DMPC, AMUPol PRE, however local minima here is seen at the α position[17]. A local maximum is observed at the Carbonyl site, suggesting the AMUPol is unable to anchor as well around this residue, with the nitroxide site away from this position. The signal-to-noise ratio for the CO peak in the AMUPol + 60% glycerol was too low for accurate integration as seen in Figure 3.3A). In other simple membrane systems such as that of POPC, a characteristic decrease is observed from the first to the last headgroup resonance[17,18]. The transition temperature of DMPC is shown to be near 24.1°C[25] and we therefore expect the lipid to be in the gel phase due to experimentation being undertaken at 20°C. However, small fluctuations in temperature which cannot be accurately measured in the sample may occur which needs to be considered.

The PREs of signals from DMPC are different in the pure DMPC lipid sample, shown in Figure 3.3B) and in DMPC-containing LM bilayers as shown in Figure 3.3D). In LM samples, the addition of glycerol affects a smaller number of NMR signals when compared to pure DMPC lipid bilayers. Given that glycerol was previously found to partition into water-membrane interface in pure DMPC lipids[24], this finding suggests that there is a specific component, or components, in the LM mixture which may prevent the glycerol partitioning into the membrane as well when compared to simpler lipid membranes. As a result, AMUPol cannot penetrate deeper into the membrane due to the presence of glycerol compared to pure DMPC bilayers. It is important to note that Chol has the ability to induce conformational ordering of the disordered fluid phase chains promoting a liquid ordered phase, where the membrane plane has a liquid structure and ordered fatty acid chains[26]. As the temperature is 20°C during acquisition we would expect the DMPC lipids within the LM sample to be more ordered than the 100% DMPC sample which would in turn affect the ability of glycerol to partition into the membrane. The 100% DMPC sample may be closer to the fluid phase than expected.

There is no characteristic decline in PRE in the headgroup for the LM sample with AMUPol and 60% glycerol. The Cβ atom has unexpectedly large intensity, suggesting

that neither glycerol nor AMUPol can interact with this site well. Again, compared to the DMPC sample this suggests that another compound may be interacting with the DNP dopant and glycerol. This could be the presence of Chol affecting the phase transition temperature. It has also been demonstrated that gangliosides such as GM1 have a preference to partition into the ordered domains of the membrane and can destabilise the phase coexistence[27]. Due to the complexity of the membrane, it is difficult to assess the contribution of each individual component of the LM sample and how this effects the lipid phase as well as the interactions of glycerol and the biradical. This may also explain some of the line broadening seen within the LM spectra compared to the 100% DMPC spectra due to changes in the mobility of the membrane as there are lipid phase changes attributed to the addition of LM components as well as the biradical and glycerol. It was not possible to record the intensity of several sites of the DMPC in the LM membrane due to the low signal-to-noise as shown by Figure 3.3C). This included CO, C2, CH_2 and ω-2 carbon atoms in the AMUPol and AMUPol + glycerol samples, as well as the β-site in the AMUPol only sample.

In order to properly assess the contribution of the components in the LM system, further PRE measurements on the individual components need to be conducted in the presence of the DNP dopant and glycerol. This may allow for potential assignment of other constituents in the LM spectra. Also, it may give more insight into the phase behaviour of the membrane and how each individual component changes this and in turn how this affects the interaction with the biradical and glycerol.

3.4 Effects of DNP dopant and glycerol on lipid bilayer structure

Biological membranes are composed of various lipid molecules which differ by their chains and headgroups. The lipid molecules are amphipathic meaning that they consist of a hydrophilic headgroup and hydrophobic chain. Those in turn are made, respectively, of a phosphate group and a diglyceride with either a saturated or unsaturated acyl chain. This amphipathic character gives phospholipids the ability to form their distinctive bilayer or liposome structures. Certain headgroups of these phosphates can alter the surface chemistry of a bilayer and can function as anchors for other molecules such a proteins[28]. The lipid headgroups contain PO_4^- where ^{31}P CSA patterns reveal changes in the structure and dynamics of the phospholipid membranes. The CSA (Δσ) arises from the surrounding electromagnetic environment of the nucleus and is partially averaged out by molecular motions. As discussed in Chapter 2.6.1, the CSA is comprised of three parameters: anisotropy, asymmetry,

and the isotropic chemical shift, which is where the signal would appear if fast molecular motion was applied, such as MAS in NMR, which averages out the anisotropy[29]. CSA and dipolar coupling are not present in isotropic liquids due to the time averaging of the interactions with the external magnetic field due to molecular tumbling. The rotation achieved in MAS is enough to replicate this motion in solid samples when set to the 'Magic Angle' of 54.74˚ compared to the magnetic field[30]. Also stated in Chapter 2, the $(3cos^2\theta - 1)$ dependence of dipolar couplings and CSA means at the magic angle the interactions are averaged to zero[31]. Expanding what was discussed in Chapter 2.6.1, the chemical shift is a second ranked tensor, where a matrix of components can be formed. In the Principal axis system, the tensor is diagonal and is given as a sum of its isotropic and anisotropic part as shown in Eq. 1:

$$\begin{pmatrix} \sigma_{11} & 0 & 0 \\ 0 & \sigma_{22} & 0 \\ 0 & 0 & \sigma_{33} \end{pmatrix} = \begin{pmatrix} \sigma_{iso} & 0 & 0 \\ 0 & \sigma_{iso} & 0 \\ 0 & 0 & \sigma_{iso} \end{pmatrix} + \begin{pmatrix} \sigma_{11}^{CSA} & 0 & 0 \\ 0 & \sigma_{22}^{CSA} & 0 \\ 0 & 0 & \sigma_{33}^{CSA} \end{pmatrix}, \quad (3.1)$$

where the principal values are:

$$\sigma^{11} > \sigma^{22} > \sigma^{33}, \quad (3.2)$$

and the isotropic chemical shift is defined as:

$$\sigma_{iso} = \frac{1}{3}(\sigma_{11} + \sigma_{22} + \sigma_{33}), \quad (3.3)$$

Two other parameters are used to describe the chemical shift, the CSA and the chemical shift asymmetry (η) where:

$$\Delta\sigma = \sigma_{33} - \frac{1}{2}(\sigma_{11} + \sigma_{22}), \quad (3.4)$$

and the chemical shift asymmetry is defined as[32]:

$$\eta = \frac{\sigma_{22} - \sigma_{11}}{\sigma_{33} - \sigma_{iso}} = \frac{\sigma_{22}^{CSA} - \sigma_{11}^{CSA}}{\sigma_{33}^{CSA}}. \quad (3.5)$$

The addition of DNP dopants, such as AMUPol, as well as glycerol, to membranes have been shown to interact with lipid membranes, which is supported by the PRE data presented earlier in this chapter in the case of DMPC and a LM system. These dopants may disrupt the lipid structure which is also supported by the fact that lipid structure is widely affected depending on sample conditions[33]. As previously stated,

minimal disruption to the membrane is required in order to assess protein membrane interactions under a biological settings.

Warschawski et al. previously assessed the differences in ^{31}P static CSA and MAS isotropic chemical shifts for several lipids over a range of temperature and the results were compiled in tables for easy comparison[29]. Using different lipids allowed easy comparison between headgroups and concluded that certain lipids such as POPE was sensitive to temperature and could be studied in the gel phase at 0^{o}C. Under MAS the isotropic chemical shift varied between lipids depending on headgroup as well as temperature. They also found the combination of certain lipid headgroups together could result in changes in dynamics or changes in lipid headgroup orientation. This highlights the importance of assessing CSA and isotropic chemical shifts when studying biological membrane systems[29].

In this study the ^{31}P CSA patterns and isotropic chemical shifts were analysed to determine whether the lipid membrane is significantly perturbed by the DNP dopant AMUPol, and glycerol. Differences in this disturbance were compared between a simple single component DMPC membranes and more complex membranes containing components such as other lipids, Chol, and ganglioside, to the point of a LM bilayer.

CSA of static samples

The CSA patterns were recorded for the four membrane models with and without the DNP dopant and glycerol, consisting of either: i) no addition, ii) 10 mM AMUPol or iii) 10 mM AMUPol and 60% glycerol by volume as shown in Figure 3.4.

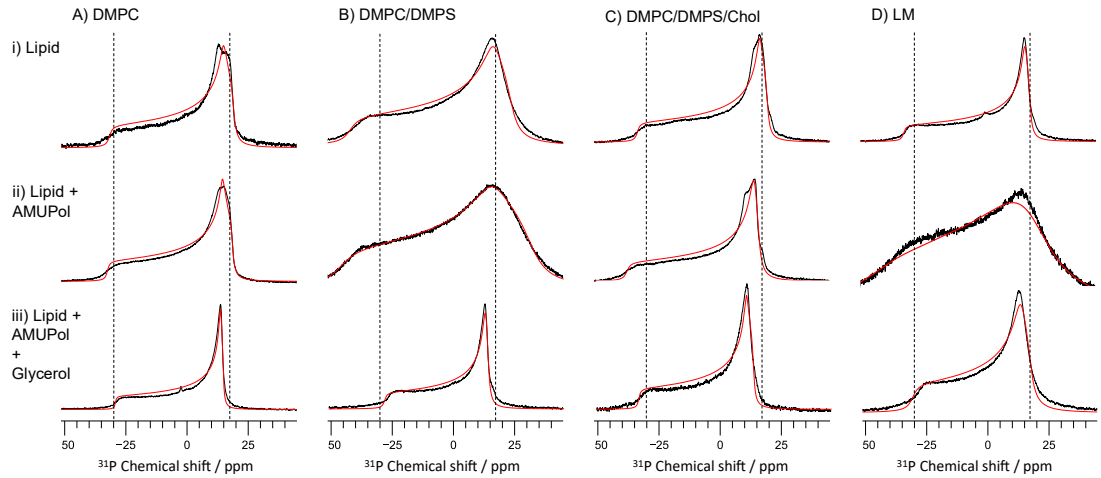

Figure 3.4 *^{31}P spectrum of samples containing lipid with i) no added dopants, ii) 10mM AMUPol, and iii) 10mM AMUPol and 60% Glycerol by volume. A) Pure DMPC lipids, B) DMPC/DMPS with molar ratios of 1.5:0.3 respectively, C) DMPC/DMPS/Chol with molar ratios of 1.5:0.3.0.5 respectively, D) LM samples containing DMPC/DMPS/Sphin/Chol/GM1 with molar ratios of 1.5:0.3:1:0.5:0.15 respectively. (Black) actual recorded spectra, (red) best fit spectra simulated by Dmfit used to calculate values in Table 3.2. All spectra were recorded under static conditions with 81920 acquisitions and SPINAL-64 ^{1}H decoupling during acquisition.*

For the spectra shown in Figure 3.4A) and C), with DMPC and DMPC/DMPS/Chol, there are minor differences in the observed CSA patterns and the parameters produced with Dmfit[34] when AMUPol or AMUPol + glycerol are added. This suggests that for those specific membrane models, the DNP dopant and glycerol do not have strong structural effects on the lipid membrane structure. This is important when trying to study membrane protein interactions under physiological conditions. Interestingly, as seen in Figure 3.4B) and 3.4D), upon the addition of AMUPol to the DMPC/DMPS and LM samples, there are large changes within the individual spectra. The spectra presented in 3.4Bii) and 3.4Dii), are characteristic of gel-ordered phase lipid membranes, while all the other spectra presented are indicative of fluid phase membranes[35]. The change of phase in the lipid membrane seems to be induced by AMUPol and seems to be reverted to the fluid phase by the addition of glycerol. As stated above, DMPC has a phase transition temperature of 24.1°C whereas DMPS has a transition temperature of 35°C, we would therefore expect that all the spectra from the DMPC/DMPS sample to be in the gel phase. However, the sample with no additives does not fully represent this and shows more motion within the membrane. As it is difficult to accurately measure the temperature inside the sample during acquisition this is difficult to assess.

The LM sample contains Chol, Sphin and GM1, all of which are present in lipid raft microdomains which are known to float freely within the liquid disordered bilayer of the cell and can cluster to form more ordered structures. The ability of these rafts to exist as distinct liquid-ordered regions of the membrane could explain the presence of fluid phase spectra within the LM sample[36], with AMUPol promoting more ordered lipid structures within these samples. AMUPol is suspected to bind differently to different components of the sample, affecting the lipid ordering and therefor phase. At first glance, the change shown in Figure 3.4Aii), pure DMPC lipids, to Figure 3.4Bii), DMPC/DMPS, suggests that DMPS is solely the component which causes the AMUPol to bind differently to the lipid membrane, altering the CSA pattern. However, this is then reversed upon the addition of Chol as shown in Figure 3.4Cii). As Chol is shown to affect the fluidity of the membrane. It would be expected that the addition of Chol promotes a more gel phase membrane due to increasing rigidity and lowering the phase transition temperature[26]. However, this is not the case. Where there are noted phase transitions, this also affects the T_2 relaxation time, resulting in changes to the spectra. The spectra shown in 3.4Bii) and 3.4Dii) suggests an increased T_2 relaxation which can be indicative of phase transition. Another possibility is that AMUPol may be binding to the headgroup in these samples and with the addition of glycerol is then able to bind further down the lipid due to partitioning increasing homogeneity within the sample. Other combinations of these five components will need to be analysed in order to get a better understanding of how AMUPol interacts with certain constituents of a sample.

Importantly, comparing all the spectra from Figure 3.4i) to 3.4iii), upon addition of both AMUPol and glycerol, there are little changes between the observed CSA patterns. This suggests little perturbance to the membranes upon the addition of the DNP dopant and glycerol. As we are interested in samples which contain both AMUPol and glycerol for further DNP and NMR analysis, this ensures that it is possible to study membranes and their interactions with proteins under physiological conditions.

Table 3.2 contains the ^{31}P CSA parameters of all the samples taken from simulations of the spectra shown in Figure 3.4. It is clear to note that the full spectral width decreases in all samples upon the addition of AMUPol and glycerol, meaning that there is more molecular motion. This could be due to a more fluid lipid membrane with the membrane entering the fluid phase. Previously, a decrease in spectral width was seen upon the addition of AMUPol and glycerol to a POPC/POPG 3:1 membrane, which is less than with the LM components. It was also shown that glycerol by itself produced the largest difference in linewidth from a sample with no added dopant or

glycerol. Glycerol was thought to affect the fluidity of the membrane and increase the molecular motion, resulting in a more homogenous environment, shown by decreased linewidth. This could explain the spectral changes in 3.4Bii) and 3.4Dii), compared to 3.4Biii) and 3.4Diii) when glycerol is added, increasing the fluidity of the membrane. The addition of AMUPol reduces this increased motion, maybe again due to the limitation of glycerol partitioning into the membrane in the presence of AMUPol[18]. Increases in temperature also affect the CSA patterns, mainly, higher temperatures which increase the fluidity of lipid membranes as they enter phase transition and reduce the CSA width, indicating higher molecular motion as shown in a POPC lipid membrane[37].

Table 3.2 *^{31}P CSA parameters of samples containing pure DMPC lipids, DMPC/DMPS with molar ratios of 1.5:0.3 respectively, DMPC/DMPS/Chol with molar ratios of 1.5:0.3.0.5 respectively, LM samples containing DMPC/DMPS/Sphin/Chol/GM1 with molar ratios of 1.5:0.3:1:0.5:0.15 respectively, and the dopant required for DNP with 10 mM AMUPol and with glycerol with 10 mM AMUPol + 60% glycerol by volume. CSA components including tensors and isotropic chemical shift are shown.*

Lipid composition		CSA component				
		$\delta_{zz} - \delta_{iso}$ /ppm	**$\delta_{xx} - \delta_{iso}$ /ppm**	**$\delta_{yy} - \delta_{iso}$ - ppm**	**δ_{iso} /ppm**	**Full spectral width/ppm**
DMPC		32.42	-18.25	-14.17	-1.92	50.67
	+ AMUPol	32.73	-18.41	-14.32	-1.38	51.14
	+ AMUPol/ glycerol	28.98	15.05	-13.93	-0.90	44.03
DMPC/DMPS		41.3	-24.15	-17.16	-0.25	65.45
	+ AMUPol	46.47	-31.09	-15.37	-1.52	77.56
	+ AMUPol/ glycerol	27.91	-14.49	-13.40	-0.58	42.41
DMPC/DMPS/ Cholesterol		34.33	-18.69	-15.64	-1.83	53.02
	+ AMUPol	30.28	-16.57	-13.71	-1.27	46.85
	+ AMUPol/ glycerol	30.28	-16.57	-13.71	-1.27	46.85
Lipid mimic (DMPC/DMPS/ Chol/Sphin/ GM1		33.70	-17.87	-15.83	-1.10	51.57
	+ AMUPol	43.04	-18.44	-17.33	1.82	65.12
	+ AMUPol/ glycerol	30.66	-17.22	-13.44	-1.12	47.88

The CSA parameters were derived from Dmfit[34] and are defined as Principal values $|\sigma_{zz} - \sigma_{iso}| > |\sigma_{xx} - \sigma_{iso}| > |\sigma_{yy} - \sigma_{iso}|$

- σ_{iso} is the isotropic chemical shift defined as $\frac{1}{3}(\sigma_{zz} + \sigma_{yy} + \sigma_{xx})$

MAS spectra

^{31}P NMR spectra recorded under 15 kHz MAS show very similar patterns to the spectra taken under static conditions. The results are shown in Figure 3.5.

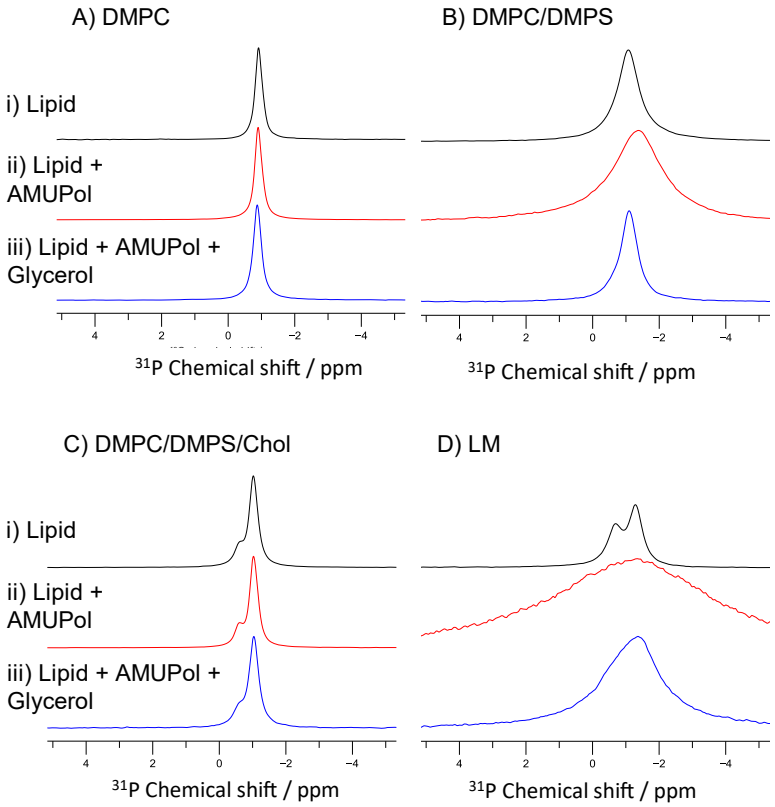

Figure 3.5 *^{31}P spectrum of samples containing lipid with, black) no added dopants, red) 10 mM AMUPol, and blue) 10 mM AMUPol and 60% glycerol by volume. A) Pure DMPC lipids, B) DMPC/DMPS with molar ratios of 1.5:0.3 respectively, C) DMPC/DMPS/Chol with molar ratios of 1.5:0.3.0.5 respectively, D) LM samples containing DMPC/DMPS/Sphin/Chol/GM1 with molar ratios of 1.5:0.3:1:0.5:0.15 respectively. All spectra were recorded at 15 kHz MAS and 1024 acquisitions.*

The spectra shown in Figure 3.5Bii), with DMPC/DMPS + AMUPol, and 3.5Dii) LM + AMUPol sample under MAS conditions also show some phase differences between the lipid membranes as shown in Figure 3.4 where the data is recorded under static conditions. Again, these changes seem to be relieved by the addition of glycerol. Even though MAS averages out spectral broadening due to static anisotropic interactions, the line broadening still remains. Table 3.4 shows the linewidth and isotropic chemical shifts of different samples with and without the DNP dopant and glycerol, taken from the spectra shown in Figure 3.5.

Table 3.3 *Linewidth and isotropic chemical shift parameters of samples containing pure DMPC, DMPC/DMPS with molar ratios of 1.5:0.3 respectively, DMPC/DMPS/Chol with molar ratios of 1.5:0.3.0.5 respectively, LM samples containing DMPC/DMPS/Sphin/Chol/GM1 with molar ratios of 1.5:0.3:1:0.5:0.15 respectively, and the dopant required for DNP with 10 mM AMUPol and with glycerol with 10 mM AMUPol + 60% Glycerol by volume.*

Lipid composition		Component	
		Linewidth/Hz	**δ_{iso} /ppm**
DMPC		63.74	-0.91
	+ AMUPol	62.74	-0.89
	+ AMUPol/ glycerol	71.07	-0.87
DMPC/DMPS		186.39	-1.07
	+ AMUPol	429.95	-1.34
	+ AMUPol/ glycerol	143.50	-1.09
DMPC/DMPS/ Cholesterol		77.39	-1.02
	+ AMUPol	73.23	-1.03
	+ AMUPol/ glycerol	83.12	-1.03
Lipid mimic (DMPC/DMPS/ Chol/Sphin/ GM1		248.88	-1.28
	+ AMUPol	1240.91	-1.27
	+ AMUPol/ glycerol	469.22	-1.35

In Table 3.3, the linewidth is taken as Full Width Half Maxima (FWHM), and also shows the isotropic chemical shift. The extend of the spectral changes, possibly due to a phase transition, shown in Figure 3.5 is highlighted by the line broadening of DMPC/DMPS + AMUPol and LM + AMUPol. AMUPol caused line broadening in these two samples by 243 Hz and 992 Hz respectively. This again suggests a more significant interaction between the biradical and these samples than others. This may reflect a transition into the gel phase represented by the spectral changes. The structure of DMPC/DMPS without Chol and with all the other components must allow a different interaction with AMUPol than seen in other samples. This may be due to the way hydrogen bonding occurs within those samples and the way in which the membrane is organised also impacting the phase behaviour of the membrane. Line broadening in these samples was rapidly reduced when glycerol was added, causing a 42 Hz decrease in DMPC/DMPS linewidth from no added dopants, and 220 Hz increase in the LM sample from no added dopants, both of which are significantly reduced than when AMUPol was added alone. Line broadening may also be attributed to the differing shifts of the DMPC/DMPS lipids within the samples. There seems to

be a significant increase in line broadening of 123 Hz between 100% DMPC and DMPC/DMPS without additives. Although this may be due to differences in the phase of the lipid membrane with the 100% DMPC membrane being more in the liquid phase, this may also be due to the difference is chemical shifts between the two lipids. As this changes with the addition of more components, the environment experienced by the lipids also changes, affecting the chemical shifts of each of the lipids. As only one peak is seen within these samples, it is difficult to fully deduce.

There seems to be no pattern on the field shift direction of the isotropic chemical shift on the addition of dopants. This differs to previous work with POPG and POPC which both saw a 0.02 ppm downfield shift on the addition of AMUPol and a 0.04 ppm up field shift on the addition of glycerol, meaning a cumulative effect was seen on the addition of both the dopant and glycerol, resulting in an overall 0.02 up field shift[18]. This dependency is not seen in the case of DMPC and the other lipids and components presented in this work.

In Figure 3.5C) and 3.5D), the appearance of a second species is visible. It would be expected a second species to also be present in 3.4B) where only two lipids are present, however this may be due to the large molar ratio difference between DMPC and DMPS, with DMPC being the only visible peak. This suggests that upon addition of other components, the amount of DMPC is reduced enough that other species with different chemical environments are able to be recorded via NMR. Line broadening caused by glycerol in the LM sample shown in Figure 3.5 and Table 3.3, is large enough that the two peaks are no longer distinguishable. In the case of POPG and POPC, in all samples with and without dopant and glycerol, two peaks for each lipid were evident[18].

As shown in all previous ^{31}P data, the difference in the spectra between samples without the DNP dopant and glycerol, and spectra with the added dopant and glycerol, shows minimal changes. This suggests that minimal perturbance to the membrane has occurred on the addition of both AMUPol and glycerol. This then allows the investigation of the interactions of proteins with biological membranes under physiological conditions.

3.5 Conclusion and outlook

A protocol was adapted for the production of a LM membrane system, where the main component (i.e., DMPC molecule) could be assigned. This allowed PRE analysis to be done on the simple DMPC membrane and the LM system.

PRE results showed that in the DMPC membrane, AMUPol + glycerol showed greater signal attenuation than with AMUPol alone. For some positions in the LM system this was the opposite case, with AMUPol having greater signal attenuation than when paired with glycerol. Positions where AMUPol + glycerol resulted in more signal attenuation is consistent with the theory that glycerol can partition into the membrane, allowing the biradical to interact more closely with the membrane. It may be possible that one component within the LM system is stopping glycerol from partitioning into the membrane as well. Further studies on membranes produced from different combinations of the LM constituents will need to be done in order to investigate this theory.

^{31}P CSA patterns of the membrane showed that in some cases, including that of DMPC/DMPS and the LM system that AMUPol alone produces spectra indicative of the gel-phase lipid membrane, and a fluid phase when added with glycerol. The important point is that under static and MAS conditions, the membrane spectra without DNP dopant or glycerol showed minimal changes when compared to the spectra of membranes with both AMUPol and glycerol. This means it is possible to investigate these biological membranes with DNP additives and in the presence of proteins under physiological conditions. However, the effect of cryogenic temperatures used in DNP experiments has to be considered when comparisons are to be made with NMR and room temperature experiments which may impact the phase of the membrane which can affect the interactions with AMUPol and glycerol as well as proteins.

Further work on the effect of the components of the biologically relevant LM system and the components required for DNP experiments may give an improved understanding of how polarisation is transferred and lead to improved sample preparation and condition to give improved enhancement as well as understand the phase behaviour of the membranes with these additives.

3.6 References

1. Hu, K.-N., Yu, H., Swager, T. M. & Griffin, R. G. Dynamic Nuclear Polarization with Biradicals. *J. Am. Chem. Soc.* **126**, 10844–10845 (2004).

2. Song, C., Hu, K.-N., Joo, C.-G., Swager, T. M. & Griffin, R. G. TOTAPOL: A Biradical Polarizing Agent for Dynamic Nuclear Polarization Experiments in Aqueous Media. *J. Am. Chem. Soc.* **128**, 11385–11390 (2006).

3. Sauvée, C., Rosay, M., Casano, G., Aussenac, F., Weber, R. T., Ouari, O. & Tordo, P. Highly Efficient, Water-Soluble Polarizing Agents for Dynamic Nuclear Polarization at High Frequency. *Angew. Chemie Int. Ed.* **52**, 10858–10861 (2013).

4. Hocking, H. G., Zangger, K. & Madl, T. Studying the Structure and Dynamics of Biomolecules by Using Soluble Paramagnetic Probes. *ChemPhysChem* **14**, 3082–3094 (2013).

5. Yau, W.-M., Jeon, J. & Tycko, R. Succinyl-DOTOPA: An effective triradical dopant for low-temperature dynamic nuclear polarization with high solubility in aqueous solvent mixtures at neutral pH. *J. Magn. Reson.* **311**, 106672 (2020).

6. Salnikov, E. S., Ouari, O., Koers, E., Sarrouj, H., Franks, T., Rosay, M., Pawsey, S., Reiter, C., Bandara, P., Oschkinat, H., Tordo, P., Engelke, F. & Bechinger, B. Developing DNP/Solid-State NMR Spectroscopy of Oriented Membranes. *Appl. Magn. Reson.* **43**, 91–106 (2012).

7. Tran, N. T., Mentink-Vigier, F. & Long, J. R. Dynamic Nuclear Polarization of Biomembrane Assemblies. *Biomolecules* **10**, 1246 (2020).

8. Mathies, G., Jain, S., Reese, M. & Griffin, R. G. Pulsed Dynamic Nuclear Polarization with Trityl Radicals. *J. Phys. Chem. Lett.* **7**, 111–116 (2016).

9. Allen, B. T. Zero-Field Splitting Parameter of the Mn ++ Ion in Glassy and in Polycrystalline Media. *J. Chem. Phys.* **43**, 3820–3826 (1965).

10. Cheng, C.-Y. & Han, S. Dynamic Nuclear Polarization Methods in Solids and Solutions to Explore Membrane Proteins and Membrane Systems. *Annu. Rev. Phys. Chem.* **64**, 507–532 (2013).

11. Reggie, L., Lopez, J. J., Collinson, I., Glaubitz, C. & Lorch, M. Dynamic Nuclear Polarization-Enhanced Solid-State NMR of a 13 C-Labeled Signal Peptide Bound to Lipid-Reconstituted Sec Translocon. *J. Am. Chem. Soc.* **133**, 19084–

19086 (2011).

12. Salnikov, E. S., Abel, S., Karthikeyan, G., Karoui, H., Aussenac, F., Tordo, P., Bechinger, B. & Ouari, O. Dynamic Nuclear Polarization/Solid-State NMR Spectroscopy of Membrane Polypeptides: Free-Radical Optimization for Matrix-Free Lipid Bilayer Samples. *ChemPhysChem* **18**, 2103–2113 (2017).

13. Hirsh, D. A., Rossini, A. J., Emsley, L. & Schurko, R. W. 35 Cl dynamic nuclear polarization solid-state NMR of active pharmaceutical ingredients. *Phys. Chem. Chem. Phys.* **18**, 25893–25904 (2016).

14. Sato, H., Kathirvelu, V., Fielding, A., Blinco, J. P., Micallef, A. S., Bottle, S. E., Eaton, S. S. & Eaton, G. R. Impact of molecular size on electron spin relaxation rates of nitroxyl radicals in glassy solvents between 100 and 300 K. *Mol. Phys.* **105**, 2137–2151 (2007).

15. Kobayashi, T., Perras, F. A., Chaudhary, U., Slowing, I. I., Huang, W., Sadow, A. D. & Pruski, M. Improved strategies for DNP-enhanced 2D 1H-X heteronuclear correlation spectroscopy of surfaces. *Solid State Nucl. Magn. Reson.* **87**, 38–44 (2017).

16. Akbey, Ü., Franks, W. T., Linden, A., Lange, S., Griffin, R. G., van Rossum, B.-J. & Oschkinat, H. Dynamic Nuclear Polarization of Deuterated Proteins. *Angew. Chemie Int. Ed.* **49**, 7803–7806 (2010).

17. Liao, S. Y., Lee, M., Wang, T., Sergeyev, I. V. & Hong, M. Efficient DNP NMR of membrane proteins: sample preparation protocols, sensitivity, and radical location. *J. Biomol. NMR* **64**, 223–237 (2016).

18. Thomas Deo. Applications of Dynamic Nuclear Polarisation in biological systems. *PhD thesis, Univ. Nottingham* (2020).

19. Weber, D. K., Sani, M.-A., Downton, M. T., Separovic, F., Keene, F. R. & Collins, J. G. Membrane Insertion of a Dinuclear Polypyridylruthenium(II) Complex Revealed by Solid-State NMR and Molecular Dynamics Simulation: Implications for Selective Antibacterial Activity. *J. Am. Chem. Soc.* **138**, 15267–15277 (2016).

20. Startek, J., Boonen, B., Talavera, K. & Meseguer, V. TRP Channels as Sensors of Chemically-Induced Changes in Cell Membrane Mechanical Properties. *Int. J. Mol. Sci.* **20**, 371 (2019).

21. Cheng, Q., Hu, Z.-W., Doherty, K. E., Tobin-Miyaji, Y. J. & Qiang, W. The on-

fibrillation-pathway membrane content leakage and off-fibrillation-pathway lipid mixing induced by 40-residue β-amyloid peptides in biologically relevant model liposomes. *Biochim. Biophys. Acta - Biomembr.* **1860**, 1670–1680 (2018).

22. Clore, G. M. & Iwahara, J. Theory, Practice, and Applications of Paramagnetic Relaxation Enhancement for the Characterization of Transient Low-Population States of Biological Macromolecules and Their Complexes. *Chem. Rev.* **109**, 4108–4139 (2009).

23. Nomura, K., Lintuluoto, M. & Morigaki, K. Hydration and Temperature Dependence of 13 C and 1 H NMR Spectra of the DMPC Phospholipid Membrane and Complete Resonance Assignment of Its Crystalline State. *J. Phys. Chem. B* **115**, 14991–15001 (2011).

24. Lee, M. & Hong, M. Cryoprotection of lipid membranes for high-resolution solid-state NMR studies of membrane peptides and proteins at low temperature. *J. Biomol. NMR* **59**, 263–277 (2014).

25. Lewis, R. N. A. H., Zhang, Y.-P. & McElhaney, R. N. Calorimetric and spectroscopic studies of the phase behavior and organization of lipid bilayer model membranes composed of binary mixtures of dimyristoylphosphatidylcholine and dimyristoylphosphatidylglycerol. *Biochim. Biophys. Acta - Biomembr.* **1668**, 203–214 (2005).

26. Waheed, Q., Tjörnhammar, R. & Edholm, O. Phase Transitions in Coarse-Grained Lipid Bilayers Containing Cholesterol by Molecular Dynamics Simulations. *Biophys. J.* **103**, 2125–2133 (2012).

27. Liu, Y., Barnoud, J. & Marrink, S. J. Gangliosides Destabilize Lipid Phase Separation in Multicomponent Membranes. *Biophys. J.* **117**, 1215–1223 (2019).

28. Divecha, N. & Irvine, R. F. Phospholipid signaling. *Cell* **80**, 269–278 (1995).

29. Warschawski, D. E., Arnold, A. A. & Marcotte, I. A New Method of Assessing Lipid Mixtures by 31P Magic-Angle Spinning NMR. *Biophys. J.* **114**, 1368–1376 (2018).

30. Polenova, T., Gupta, R. & Goldbourt, A. Magic Angle Spinning NMR Spectroscopy: A Versatile Technique for Structural and Dynamic Analysis of Solid-Phase Systems. *Anal. Chem.* **87**, 5458–5469 (2015).

31. Chen, J.-H. & Singer, S. High-Resolution Magic Angle Spinning NMR

Spectroscopy. in *The Handbook of Metabonomics and Metabolomics* 113–147 (Elsevier, 2007).

32. Přecechtělová, J., Padrta, P., Munzarová, M. L. & Sklenář, V. 31 P Chemical Shift Tensors for Canonical and Non-canonical Conformations of Nucleic Acids: A DFT Study and NMR Implications. *J. Phys. Chem. B* **112**, 3470–3478 (2008).

33. Scomparin, C., Lecuyer, S., Ferreira, M., Charitat, T. & Tinland, B. Diffusion in supported lipid bilayers: Influence of substrate and preparation technique on the internal dynamics. *Eur. Phys. J. E* **28**, 211–220 (2009).

34. Massiot, D., Fayon, F., Capron, M., King, I., Le Calvé, S., Alonso, B., Durand, J., Bujoli, B., Gan, Z. & Hoatson, G. Modelling one- and two-dimensional solid-state NMR spectra. *Magn. Reson. Chem.* **40**, 70–76 (2002).

35. Tyler, A. I. I., Clarke, J. A., Seddon, J. M. & Law, R. V. Solid State NMR of Lipid Model Membranes. in 227–253 (2015).

36. Pike, L. J. Lipid rafts: bringing order to chaos. *J. Lipid Res.* **44**, 655–667 (2003).

37. Dave, P. C., Tiburu, E. K., Damodaran, K. & Lorigan, G. A. Investigating Structural Changes in the Lipid Bilayer upon Insertion of the Transmembrane Domain of the Membrane-Bound Protein Phospholamban Utilizing 31P and 2H Solid-State NMR Spectroscopy. *Biophys. J.* **86**, 1564–1573 (2004).

4. Tracking Aβ$_{(1-40)}$ interactions with membrane systems

4.1 Introduction

NMR is now a popular and powerful tool used within several areas of Biology, Chemistry and Physics, in particular in structural and molecular Biology[1]. It is a non-invasive tool which can measure samples directly in solution as well in solid systems leading to protein structure determination. 1982 saw the first published assignment of a basic small protein from the ^{1}H NMR spectrum by Wagner and Wüthrich[2]. However, the natural characteristics of protein aggregates, fibrils and larger macromolecules make them difficult to study under liquid-state NMR and static ssNMR conditions, where sensitivity is already a constraint. For ssNMR, MAS is required to study these proteins and obtain resolved spectra allowing for amino acid correlation and consequent assignment. The past few decades have seen several advances in MAS technology and NMR software and hardware, allowing for the assignment of larger proteins. The development of multi-dimensional analysis and the availability of magnets with stronger magnetic fields means not only can complex biological systems be studied, but their dynamics can also be investigated[3].

NMR is the preferred method in the identification of protein structures, such as investigating the structure of Aβ, compared to more historical methods such as X-ray crystallography due to the lack of crystallisation conditions required[4,5]. As previously described in Section 2.6.1, the chemical shift provides information about the local chemical environment, which can then be used to determine protein structure[6]. This makes NMR an effective method when determining the structure of isolated Aβ proteins, including fibrillary structures, which are the thermodynamic end-point of the self-assembly process[9].

In NMR a single sample can be subject to a number of 1D and 2D experiments, which allows for individual residue assignment and conformation determination by utilising secondary chemical shifts. Simple 1D CP spectra show chemical shifts of all resonances in the sample, however with more complex samples the spectra can become overcrowded. To avoid this, 2D experiments are used to achieve appropriate spectra. This utilises two spin interaction correlations when two nuclear spins are close in space, leading to less crowded spectra than seen in 1D spectra. A simple 2D experiment and spectra are schematically shown in Figure 4.1.

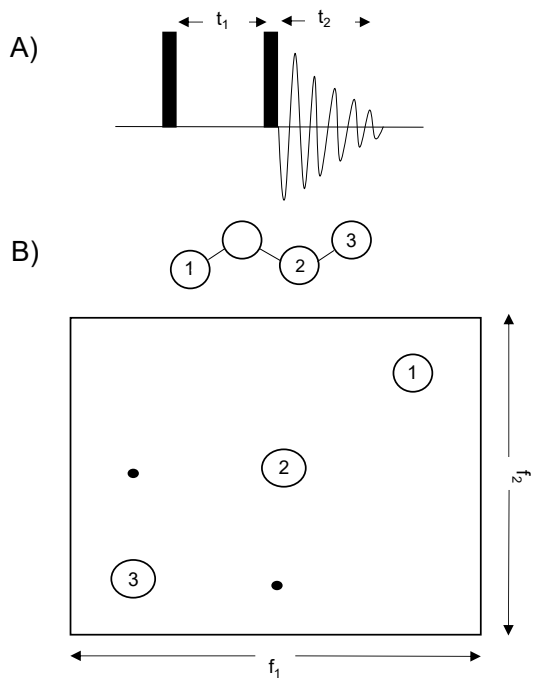

Figure 4.1 *A) Schematic showing a basic pulse sequence for a 2D experiment. A RF pulse is applied causing the nuclear spins to evolve under a specific interaction over an incremented time interval t_1, also known as a "mixing" time. A second pulse brings the magnetisation into the transverse plane and produces an FID that is recorded in the time interval t_2. B) Schematic spectrum produced by a 2D FT of the dataset obtained by a sequence in A). Correlations between spins in non-equivalent environments are shown by off-diagonal peaks caused by spin interactions. The molecule shown above the spectrum has an interaction between spin 2 and 3 causing the cross-peak in the 2D spectrum. Such interaction is usually due to the spin proximity in space, or due to a chemical bond.*

Tycko et al. investigated the structural basis of $A\beta_{(1\text{-}40)}$ fibrils using ssNMR and EM. A model constructed based on experimental results shows a three-fold symmetry about the fibril growth axis which contains in-register parallel β-sheets with a twisted morphology. It was shown that hydrophobic stabilisation of the fibril was maintained by the majority of the charged and polar sidechains residing on the exterior of the structure[9]. The hydrophobic core created by this parallel nature allows interactions among some of the sidechains, such as Q15 which can fit into a space created by the G37 and G38 residues, which is similar to the 'steric zipper', which has also been observed in other amyloid models[10]. Predicted models from these constraints imply a roughly triangular cross section with a fibril width of 6-7 nm[9]. This predicted threefold computational model is shown in Figure 4.2. The hydrophobic core is also important in the labelling schemes of $A\beta_{(1\text{-}40)}$ used within this thesis work which are discussed later in the methods section of this chapter.

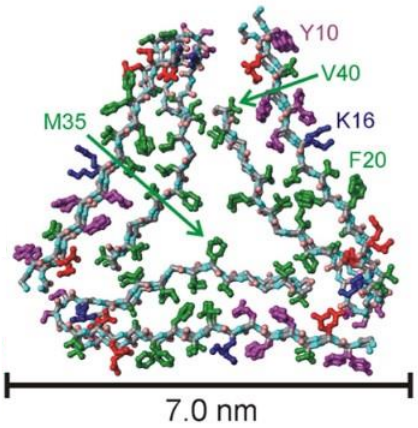

Figure 4.2 *Model taken from Tycko et al[9]. Computational atomic model with applied experimental constraints viewed down the fibril axis. Hydrophobic, polar, negatively charged and positively charged amino acid sidechains are green, magenta, red, and blue, respectively. Backbone nitrogen and carbonyl oxygen atoms are cyan and pink respectively.*

As well as the work presented by Tycko et al. there has been many other predicted amyloid models, including fibril[7], peptide fragment[11] and polymorph structure[12], which have mainly been obtained via ssNMR[13] and cryo-EM[14].

While there was some progress in obtaining atomic level structural models of $A\beta_{(1-40)}$ fibrils, it has been long known in the field that the total amount of Aβ fibrils present in the brain tissue does not correlate with the severity of AD and neurodegeneration[15]. Attention, therefore, has now turned to intermediatory stages of the self-assembly process, such as oligomers, which have now being linked to the proteins toxic effects[16,17]. However, low concentrations of these important intermediates make for difficult structural analysis using ssNMR.

One approach to enhancing protein signals and overcoming the issue of low NMR sensitivity is the use of DNP. Due to the low temperatures of DNP, frozen samples are required, allowing for frozen 'snapshots' of the self-assembly process to be taken, tracking the structural conformation and changes, as a function of time. Samples from four successive stages of the self-assembly process were monitored by DNP enhanced ssNMR exploring intermediatory stages: monomeric, oligomeric, metastable proto-fibrillar and mature fibrillar. In all four stages the predominant conformation was shown to be the extended β-sheet conformation, however, this was reduced in the monomeric and oligomeric stages resulting from a lack of ordered structures prior to the formation of protofibrils. 2D data indicated conformations similar to U-shaped structures, which are shown in mature fibrils, to be present in all stages, even before formation of large oligomers. It is predicted that there is a small population of mature fibrils which develop spontaneously from the initial stages of monomers and

oligomers. This suggests that the structure of fibrils and protofibrils must be significantly different as conversion cannot occur by internal structural rearrangements alone and requires sonication or agitation which breaks protofibrils into fragments allowing for self-assembly into mature fibrils. Proto-fibrils are therefore known as 'off-pathway' intermediates. ^{13}C data shows that hydrogen bonding rearrangement is required for this conversion within the β-sheets. The in-register parallel β-sheet structure of mature $A\beta_{(1-40)}$ fibrils does not exist within the protofibrils[13].

Data from isolated Aβ studies has provided key insights into the structure of the protein at several points along the self-assembly process but has provided little biological relevance. Studies exploring the interaction between the Aβ protein and lipid membrane systems, including membrane proteins, have also been conducted, however, little research has been performed with protein signals enhanced by DNP. The majority of this current research also focuses on the interactions of Aβ fibrils and lipid membranes, instead of possibly more important intermediate stages.

Using ^{1}H-detection under conditions of ultrafast MAS presents a relatively new approach for solving the issue of ssNMR sensitivity. So far, such approach has produced relatively narrow lines allowing protein assignment and was applied to a 153-residue microcrystalline Zn II-loaded superoxide dismutase in very low concentration allowing a structural model to be constructed. Overall the experimental time was reduced compared to ^{13}C correlation spectra[18]. It is also yet unknown whether ^{1}H-detection under condition of ultrafast MAS could compete with DNP-MAS for studies of protein-lipid samples.

Various lipid components, such as those shown in Figure 4.3 which include charged phospholipids[19,20], cholesterol[21], sphingomyelin, ganglioside GM1[22,23], have their own individual effect on the affinity of the Aβ peptide to bind to the lipid bilayer, as well as affecting Aβ induced permeabilization of the membrane, and other membrane properties[16].

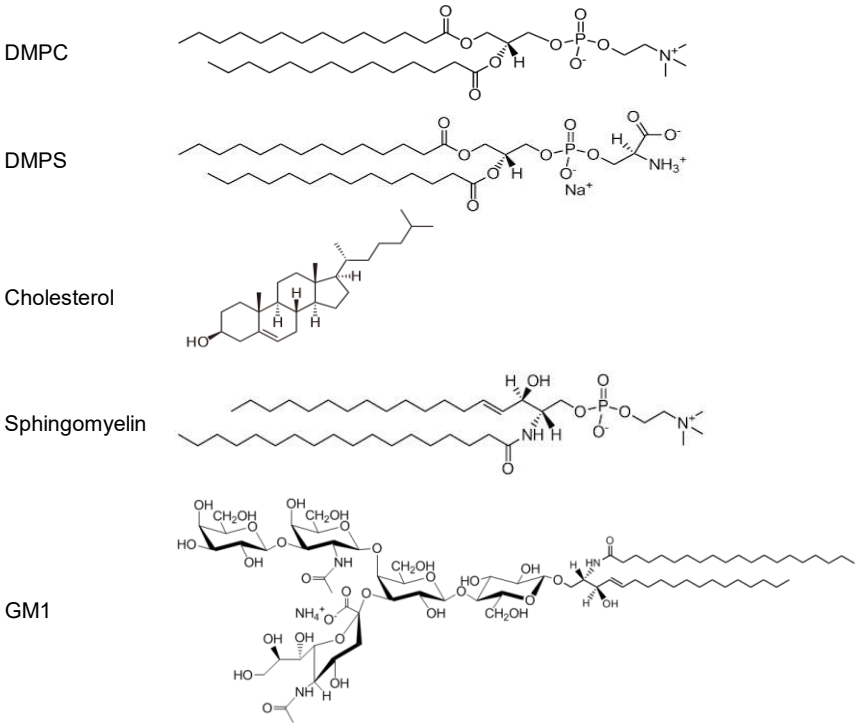

Figure 4.3 *Component molecules for lipid mixtures used in this chapter.*

The formation of micro-domains is promoted by the presence of cholesterol and sphingomyelin, and specific binding sites from the peptide to the membrane may be generated by the presence of GM1. Cholesterol is also involved in cell membrane fluidity by controlling water permeability[21], while sphingomyelin contributes to membrane micro-domains such as lipid rafts[24]. GM1 is not only involved in hydrophobic and hydrophilic interactions but also reduces the fluidity of the plasma membrane allowing for the retention of lipid rafts. GM1 has also being considered as a key factor in maintaining mammalian neuronal functions avoiding neurodegeneration[25]. These interactions have also been shown to respond to different P:L with the populations of α-helices vs β-strand increasing with the P:L, however this may be attributed to the increasing GM1:peptide. Fibrillation pathways have also been shown to be affected by initial states in the membrane, i.e., External Addition (EA) or Pre-Incorporation of Aβ into lipid membranes[19,20].

In this chapter, DNP-enhanced ssNMR and ^{1}H-detection NMR under ultrafast MAS experiments were applied to characterise the structure of a $A\beta_{(1-40)}$ peptide externally added to a simple synthetic lipid vesicle system. The aim was to test the methodology of sample preparation, confirm whether DNP-ssNMR and ultrafast-MAS NMR provide signals of sufficient intensity, and to see whether the peptide conformation could be tracked as a function of time. After which more complex lipid systems were utilised

including the LM system and BE. A complementary set of experimentation was used including TEM, AFM, HPLC, NMR, DNP enhanced NMR and ^{1}H-detection.

4.2 Materials and Methods

Uniformly ^{13}C, ^{15}N- labelled Aβ$_{(1-40)}$ was synthesized manually using routine Fmoc solid-phase peptide synthesis protocols by Qinghui Cheng at Binghampton University, State University of New York. For DNP MAS applications, uniform labelling of the entire protein is not useful due to broad linewidths of ~1.5 – 5 ppm, which would result in poor spectral resolution. Therefore, labels in the protein are placed at a few specific important locations along the protein length. The labelling schemes used in this chapter are shown in table 4.1.

Table 4.1 *Amino acid sequence shown in single letter abbreviation of the Aβ$_{(1-40)}$ protein with the uniformly labelled residues highlighted, corresponding to A) FAIL - F19, A21, I32 and L34, B) FAGV – F20, A21, G29 and V36, C) FVIL – F19, V24, I32 and L34, D) EVFDSKGA - E11,V18, F20,D23,S26,K28,G29,A30.*

Shorthand	Labelling scheme
FAIL	DAEFRHDSGYEVHHQKLV FFAEDVGSNKGAIIGLMVGGVV
FAGV	DAEFRHDSGYEVHHQKLVF FAEDVGSNKGAIIGLMVGGVV
FVIL	DAEFRHDSGYEVHHQKLV FFAEDVGSNKGAIIGLMVGGVV
EVFDSKGA	DAEFRHDSGYEVHHQKLVFFAEDVGSNKGAIIGLMVGGVV

These specific labelling schemes were chosen due to the labelling of amino acids in the hydrophobic regions of the peptide, which are defined as the CHC (residues 16-22) and the C-terminal region (residues 30-40)[26]. These hydrophobic regions are of great interest in the study of Aβ due to their involvement in protein interactions and folding. They are essential in determining the secondary structure of the protein and play a key role in influencing the state of protein aggregation in AD[27]. The use of EVFDSKGA was chosen due to its availability at the time of writing.

External addition of Aβ$_{(1-40)}$ to lipid vesicles

A protocol for the EA of Aβ$_{(1-40)}$ into lipid vesicles was adapted from a protocol by the Qiang group[19]. Lipid constituents were dissolved in chloroform following the lipid film preparation as described in Chapter 3.2. Once the lipid film was formed the sample was rehydrated with phosphate buffer (10 mM, pH 7.4) so the concentration of Aβ$_{(1-}$

$_{40)}$ would be ~25 μM. The lipid sample was then agitated at Room Temperature (RT) for one hour. This was followed by ten cycles of freeze-thaw between liquid nitrogen and 37^{o}C, and then ten cycles of extrusion with 300 nm pore size to give homogeneous vesicles. The number of extrusion cycles was selected based on the trade-off between the total sample preparation time and the sample homogeneity as observed via negatively stained TEM (see Appendix 2 and Appendix 4 for details).

The lipid vesicles before and after addition of $A\beta_{(1-40)}$ were characterised using AFM (see Appendix 3, Appendix 6 and Appendix 7 for details). Appendix 6 shows that the vesicles with and without peptide are very homogenous. They display small variations in size between a small range as shown by the histograms, between 5-35 nm. No structures that can be associated with peptide aggregates can be seen in Appendix 6. This may be due to a low level of protein binding, or the protein being washed away by the washing stage.

The individual vesicles shown in Appendix 7 show no differences between the two prepared samples. The sample containing $A\beta_{(1-40)}$ shows a slightly smaller size, however this is likely due to the small variations between the vesicles of the sample. However, AFM suggests that no major changes have been experienced by the liposomes due to the addition of the protein. Again, no peptide aggregates can be distinguished in Appendix 7 either due to good incorporation of $A\beta_{(1-40)}$ into the membrane showing no external features, or insufficient binding to the membrane.

$A\beta_{(1-40)}$ pretreatment

The initial dissolution of $A\beta_{(1-40),}$ with the aim of breaking the aggregates and making $A\beta_{(1-40)}$ monomeric, was done by either of the two methods:

1) HFIP/NaOH method: dissolution in Hexafluroisopropanol (HFIP) to a concentration of 2 mg/mL, incubation for 45 mins, HFIP removal by lyophilization, and finally, resuspension in 20 mM Sodium Hydroxide (NaOH) (pH~12) solution[13,28,29].
2) DMSO method: dissolution of $A\beta_{(1-40)}$ in DMSO to a final volume of ~1% of the final volume[19].

Using a HPLC-based approach for measuring concentration in the supernatant (*vide infra*), it was shown that binding to DMPC/DMPS (1.5:0.3) membrane with P:L of 1:60 of $A\beta_{(1-40)}$ pretreated with HFIP/NaOH is slightly increased compared to the sample pretreated with DMSO (81% vs 70% of bound peptide respectively). Negatively stained TEM of the two samples pretreated in two different manners shows little difference (see appendix 3).

$A\beta_{(1-40)}$ / POPG sample preparation for DNP

$A\beta_{(1-40)}$ was externally added to POPG vesicles as described above. 1.25 mg of purified and lyophilised $A\beta_{(1-40)}$ peptide was dissolved in 155 µL DMSO and diluted into one of two vesicle solutions giving ~1% (v/v) of DMSO in the final solution and a final P:L of 1:40. One aliquot was incubated for 0-hour and the other for 8-hours. The samples were then centrifuged (26,000 rpm, max g-value 57,440, one-hour) and the remaining supernatant removed by pipette to give a membrane pellet. Supernatant was saved for HPLC analysis to determine the concentration of the remaining $A\beta_{(1-40)}$.

The weight of buffer solution in the membrane was recorded and 5 µL aliquots of solution containing ^{13}C-depleted and deuterated glycerol (D_8-99.5% ^{12}C glycerol)/D_2O/H2O at 6/3/1 w/w (known as the DNP matrix) was directly titrated to the membrane pellets followed by two minutes of vortexing. This was repeated five times to give total volume of added matrix stock of 25 µL, followed by five minutes vortexing to ensure uniform distribution of the radicals. The sample was lyophilised until the total hydration level of the membrane pellet was ~40% by weight. The sample was then added to a 3.2 mm sapphire rotor using home built packing tool.

$A\beta_{(1-40)}$ / lipid mimic

The lipid membrane preparation protocol is identical to that described in Chapter 3.2 with components including DMPC, DMPS, Sphingomyelin, Cholesterol and GM1 (Avanti Polar Lipids) with molar ratios of 1.5:0.3:1:0.5:0.15 respectively. The experiments used either HFIP/NaOH or DMSO pretreatment of $A\beta_{(1-40)}$ as described above. The membrane pellet was collected via centrifugation at 26,000 rpm (max g-value 57,440) overnight. Supernatant was saved for HPLC analysis. The weight of the buffer in the membrane was recorded and the DNP matrix was added following the procedure as above including achieving a hydration level of ~40% by weight. The sample was packed into a 3.2 mm sapphire rotor.

$A\beta_{(1-40)}$ / brain extract

Porcine BE (Avanti Polar Lipids) was used as the lipid membrane for some samples which contained Phosphatidylcholine (PC), Phosphatidylethanolamine (PE), Phosphoinositide (PI), Phosphatidylserine (PS), Phosphatidic acid (PA) and unknown components, by the % weights of 12.6, 33.1, 4.1, 18.5, 0.8 and 30.9% respectively. The desired amount of BE was dissolved in chloroform. N_2 flow was then used to remove liquid and sample was dried in a vacuum for 4+ hours. The lipid film was then suspended in 10 mM phosphate buffer, where the buffer temperature was above the

phase transition of the lipid, and then allowed to hydrate for an hour, vortexing occasionally. The membrane was then subject to eight freeze-thaw cycles between liquid nitrogen and a 55°C water bath. The sample was extruded with 1 μM membrane filter for ten cycles. $A\beta_{(1-40)}$ was pretreated with HFIP/NaOH and added to the lipid vesicles to the concentration of 50 μM. The membrane pellet was collected via centrifugation at 26,000 rpm (max g-value 57,440) overnight. Supernatant was saved for HPLC analysis. The weight of the buffer in the membrane was recorded and the DNP matrix was added following the procedure as above including achieving a hydration level of ~40% by weight. The sample was packed into a 3.2 mm sapphire rotor.

$A\beta_{(1-40)}$ pre-incorporation in lipids

A protocol for the pre-incorporation of $A\beta_{(1-40)}$ into lipid vesicles was adapted from a protocol by the Qiang group[19]. Desired amounts of lyophilised $A\beta_{(1-40)}$ and phospholipid mixtures were co-dissolved in HFIP. The solution was sonicated for five minutes to ensure complete dissolving and then solvent removed with N_2 flow. The remaining lipid/peptide film was dried in a vacuum overnight and rehydrated using 10 mM phosphate buffer (pH 7.4) to the $A\beta_{(1-40)}$ concentration of ~25 μM and the sample was again agitated following the EA protocol. The same packing procedure was followed as above.

HPLC-assisted UV-vis detection of peptide concentration

For the small volume samples prepared for ratio and component analysis, the same lipid preparation protocol was followed as stated with $A\beta_{(1-40)}$ / lipid mimic section, however scaled down so the final volume was 600 μl for each sample. Unlabelled protein (Sigma-Aldrich) was utilised and HFIP/NaOH treated. Sample was again centrifuged (26,000 rpm, max g-value 57,440, overnight), and supernatant collected. Two sets of samples were prepared to investigate the protein to lipid binding:

1) Unlabelled $A\beta_{(1-40)}$ externally added to LM system with varying P:L from 1:20-1:70 with a 0 and an 8-hour incubation.
2) Unlabelled $A\beta_{(1-40)}$ externally added to membranes composed of different components of the LM system following the same molar ratio as stated above with a 1:60 P:L, with 0, 0.5, 4 and 8-hour incubations.

Supernatants from centrifugation were analysed with a reversed-phase C18 analytical-scale column. The $A\beta_{(1-40)}$ elution peaks, such as shown in Figure 4.4A), can be quantified based on 210 nm absorption from a calibration curve from freshly

dissolved $A\beta_{(1-40)}$ in H_2O in the range of 0-50 μM shown in Figure 4.4B). This allows for the quantification of binding of the peptide to membranes. Due to time restrictions presented by COVID-19, only one run for each sample was analysed. Future work would include repetitions of the HPLC tests.

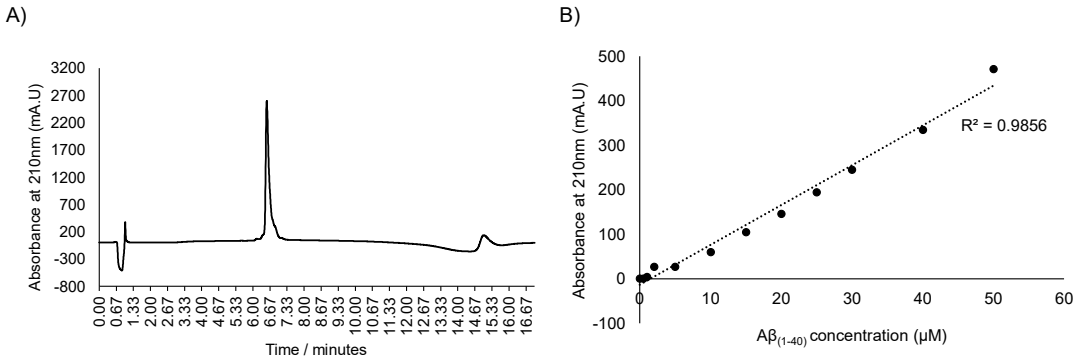

Figure 4.4 *A) HPLC chromatogram from 50 μM freshly dissolved $A\beta_{(1-40)}$ in deionised water, showing a peak at ~6.50 minutes. This peak is used to calculate the integral used to plot the standard curve as shown in B) produced from 0-50 μM freshly dissolved $A\beta_{(1-40)}$ in deionised water. This shows the linear relationship between the concentration of $A\beta_{(1-40)}$ and integrals at 210 nm, with R^2 value shown.*

DNP-enhanced ssNMR

All ssNMR measurements were performed at 100 K on a Bruker ADVANCE III 600 MHz spectrometer with a 395 GHz gyrotron μw source. A 3.2 mm sapphire rotor triple resonance MAS probe was used. MAS and low temperature was maintained using N_2 gas flows from a Bruker chiller unit. All spectra were referenced to adamantane with a CH signal at 38.48 ppm. The acquisition parameters for all experiments are shown in Appendix 8. All spectra were analysed using Topspin®.

^{1}H-detection with ultrafast MAS

The methodology for fibril production for ^{1}H-detection experiments was adapted from the self-assembly protocol by Potapov et al.[13] utilising desired amounts of FAGV-labelled protein. Desired amounts of protein was firstly HFIP/NaOH treated. The pH was then lowered by addition of 250 mM phosphate, pH 7.4, bringing the final buffer concentration to 50 mM. HCl was used to adjust the pH to 7.5 and then incubated for four hours. The sample was then sonicated and incubated at 24^{o}C for 12 h before the sonication incubation procedure was repeated four times until the mature fibrils were complete. Fibril content was confirmed via TEM. The sample was then packed into a 1.3 mm rotor utilising the Bruker rotor packing kit. Another sample was prepared under

the same methodology however containing 10μM Ethylenediaminetetraacetic acid diammonium copper salt solution (Cu-EDTA).

hCH experiments were performed at RT on a Bruker Ascend 800 MHz spectrometer equipped with HXY probe. 2D MAS-NMR spectra was recorded at 65 kHz spinning speed. The acquisition parameters for all experiments are shown in Appendix 8. All spectra were analysed using TopSpin®.

4.3 Results

4.3.1 DNP-enhanced NMR of $A\beta_{(1-40)}$ interacting with POPG vesicles

Upon external addition of $A\beta_{(1-40)}$ to POPG vesicles HPLC-based analysis reveals a rather good binding of $A\beta_{(1-40)}$ to lipids of 77% and 85% for 0-hour incubation and 8-hour incubation respectively. ^{13}C-CP spectra with and without μw irradiation of the FAIL-labelled $A\beta_{(1-40)}$ in a 100% POPG environment at a 1:40 P:L from 0- and 8- hours are shown in Figure 4.5.

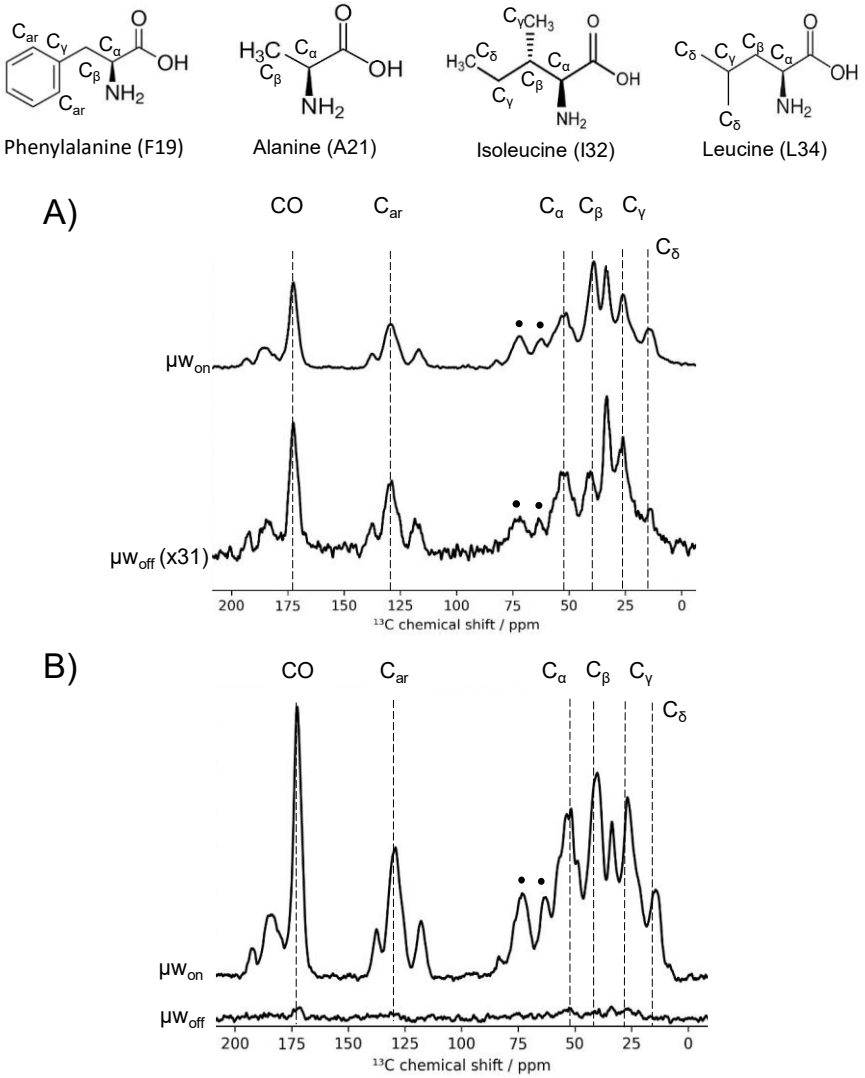

Figure 4.5 *DNP-enhanced ^{13}C CP spectra of $A\beta_{(1-40)}$-lipid bilayer system with (top) and without (bottom) μw irradiation. Sample of FAIL-labelled $A\beta_{(1-40)}$ peptide dissolved in DMSO externally added to 100% POPG with a 1:40 P:L with A) 0-hour and B) 8-hour incubation. For Figure A) the CP measurements were carried out with 16 scans with μw_{on} and 496 scans with μw_{off}. For Figure B) the CP measurements were carried out with 16 scans in both cases. Protein and glycerol peaks are indicated by black dashed lines and dots respectively. Broad linewidths do not allow for specific amino acid assignment at cryogenic temperatures in these 1D spectra.*

Enhancements for each individual protein position from the two samples are also shown in Table 4.2.

Table 4.2 *DNP enhancements at several spectral regions for uniformly FAIL-labelled $A\beta_{(1-40)}$ dissolved in DMSO externally added to 100% POPG with 1:40 P:L.*

Incubation time	P:L	ε_{DNP} enhancement						
		CO	C_α	C_β	C_γ	C_δ	$C_{aromatic}$	Lipid CH_2
0-hour	1:40	18	22	43	18	22	18	18
8-hour	1:40	32	19	32	19	-	26	16

Enhancements for several protein spectral regions are shown to be in the range of a factor of ~18-43 which is more than the observed enhancement of 16 and 19 for the CH_2 lipid peak in the samples for 0- and 8-hour incubation respectively, which is shown at ~33 ppm. Measuring enhancements of some peaks was not possible due to the high levels of noise in the μw off spectra. This suggests more efficient spin polarisation transfer by spin diffusion from the DNP matrix to lipid embedded $A\beta_{(1-40)}$ than to the lipid positions.

DARR experiments utilise a CP step which is followed by magnetisation exchange between nearby ^{13}C nuclei during an exchange time, t_{ex}, whilst CW irradiation is applied to the ^{1}H nuclei at the same power as the rotation rate, as shown in Section 2.9.3 Figure 2.12[30]. The addition of the CW ^{1}H pulse during the exchange time separates this from other methods such as PDSD experiments[31]. Magnetisation transfer can be induced for different distances via the dipolar interaction by setting the exchange time. A short t_{ex} will lead to a dipolar interaction between ^{13}C nuclei that are close in space whereas a longer t_{ex} will lead to transfer between more distant spins.

2D-DARR spectra and 1D slices through them of the samples containing $A\beta_{(1-40)}$ externally added to 100% POPG with a 1:40 P:L ratio with 0 and 8-hour incubation are shown in Figure 4.6. All labelled residues were successfully resolved with both 0.25 and 2 s mixing times which shows predominantly one-bond correlations and inter-residue correlations respectively. Mixing times were set to 0.25 s to excite mainly those one-bond inter-residue correlations although in leucine and phenylalanine two and three bond correlations are also present. The 2D-spectra (and corresponding 1D slices) of both 0-hour and 8-hour samples indicate the presence of noticeable cross-peaks due to the proximity of L34 and I32 methyl groups to the F19 aromatic groups.

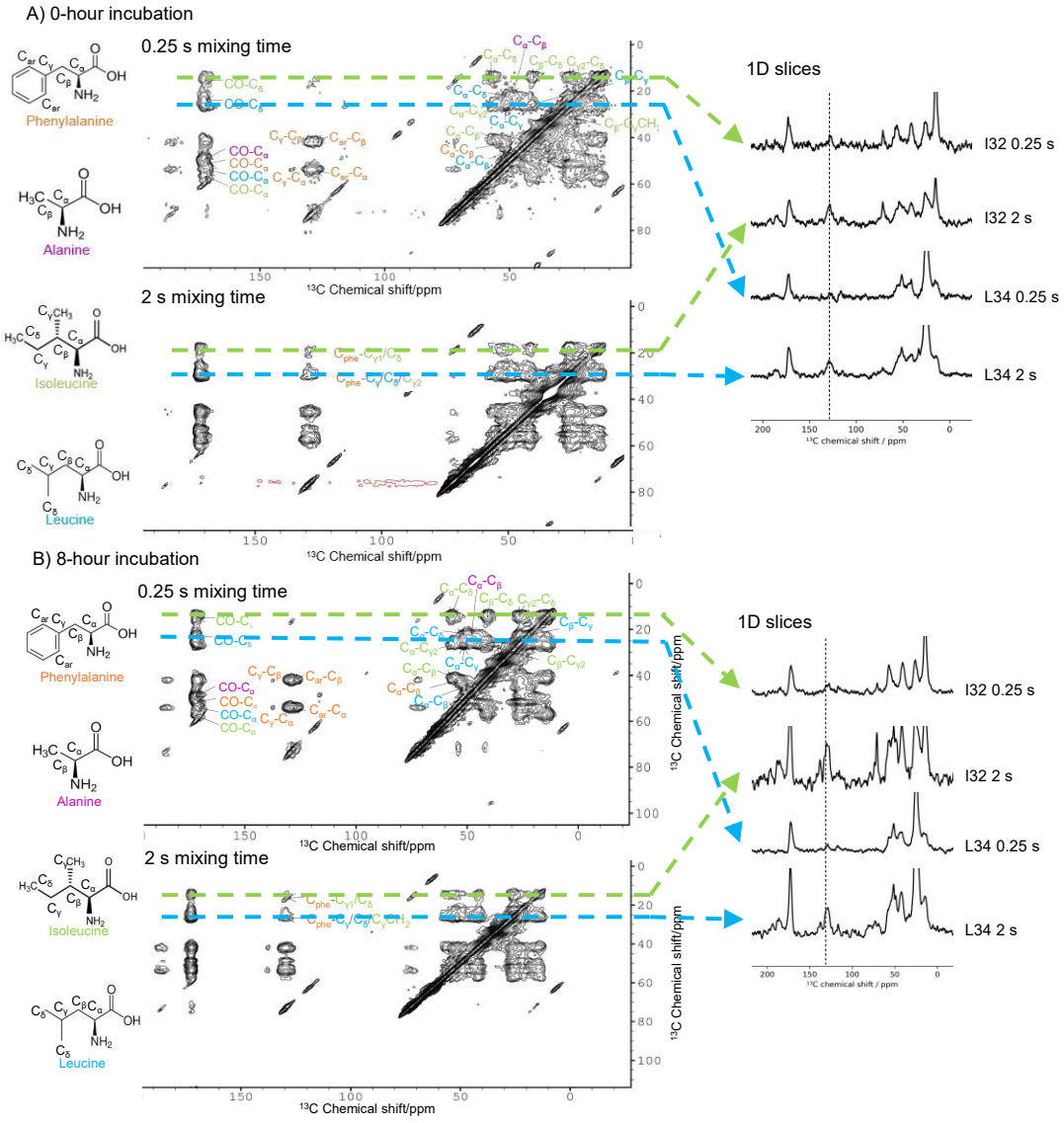

Figure 4.6 *DARR spectra of uniformly FAIL-labelled Aβ(1-40) dissolved in DMSO externally added to 100% POPG lipid membrane with a 1:40 P:L with (top) 0.25 s mixing time and (bottom) 2 s mixing time. A) 0-hour incubation (top) 16 scans in the direct dimension, 300 points in the indirect dimension and a recycle delay of 4.5 s giving predominantly one-bond correlations. (Bottom) 28 scans in the direct dimension, 300 points in the indirect dimension and a 4.5 s recycle delay giving inter-residue correlations. B) 8-hour incubation time (top) 28 scans in the direct dimension, 300 points in the indirect dimension and a recycle delay of 3.5 s giving predominantly one-bond correlations. (Bottom) 28 scans in the direct dimension, 300 points in the indirect dimension and a 3.5 s recycle delay giving inter-residue correlations. All experiments were undertaken in less than 12 hours. 1D slices at the methyl chemical shift of I32 and L34 are shown with A) 0-hour and B) 8-hour incubation. Strong cross peaks are observed with the F19 aromatic group with a 2 s mixing time shown by the black dotted line.*

As shown on Figure 4.6 the use of the DARR experiment also shows background signals and t_1 noise on the spectra. One method of removing this is to use Double-Quantum Filtered (DQF) and Double-Quantum Single-Quantum correlation experiments (see Section 2.9.2). Figure 4.7 shows the ^{13}C-CP spectra of uniformly labelled $A\beta_{(1-40)}$ externally added to 100% POPG membrane with and without incubation, compared with spectra acquired with DQF using POST-C7 sequence. DQF spectra show a significant reduction of the natural abundance ^{13}C due to the lipid and glycerol, compared to that of the protein signal, due to the dominant magnetisation build-up between ^{13}C nuclei one bond apart. The lipid CH_2 peak present in the CP spectra of Figure 4.7 A) and B) (top), at ~33 ppm is clearly visible, however it is not present within the DQF spectra of both 0- and 8-hour incubation samples.

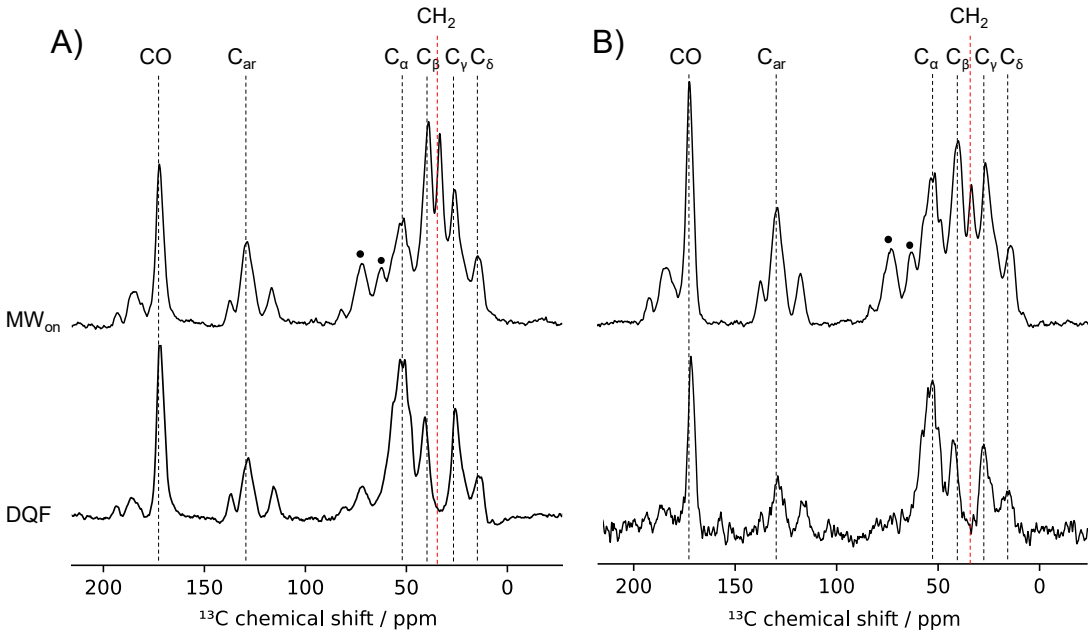

Figure 4.7 *DNP-enhanced ^{13}C-CP (top) and ^{13}C-CP spectra double-quantum filtered (DQF) (bottom) of uniformly FAIL-labelled $A\beta_{(1-40)}$ dissolved in DMSO externally added to 100% POPG with a P:L of 1:40 with A) 0-hour incubation and B) 8-hour incubation. DQF using POST-C7 suppresses the natural abundance ^{13}C lipid and glycerol signals. Protein signals are shown by black lines, glycerol peaks are shown by dots and lipid signals are shown by red lines.*

2D DQSQ experiments were therefore implemented in order to assign peaks and better resolve residues which can then be used to calculate secondary structure chemical shifts and predict the protein conformation. 2D DQSQ were carried out using the POST-C7 pulse sequence. As discussed previously in Section 2.9.2, this gives rise to characteristic cross peaks which appear at the Single Quantum (SQ) shift in

the direct dimension and the DQ shift in the indirect dimension. DQSQ POST-C7 spectra of samples containing $A\beta_{(1-40)}$ externally added to 100% POPG with a 1:40 P:L ratio with 0-hour and 8-hour incubation are shown in Figure 4.8.

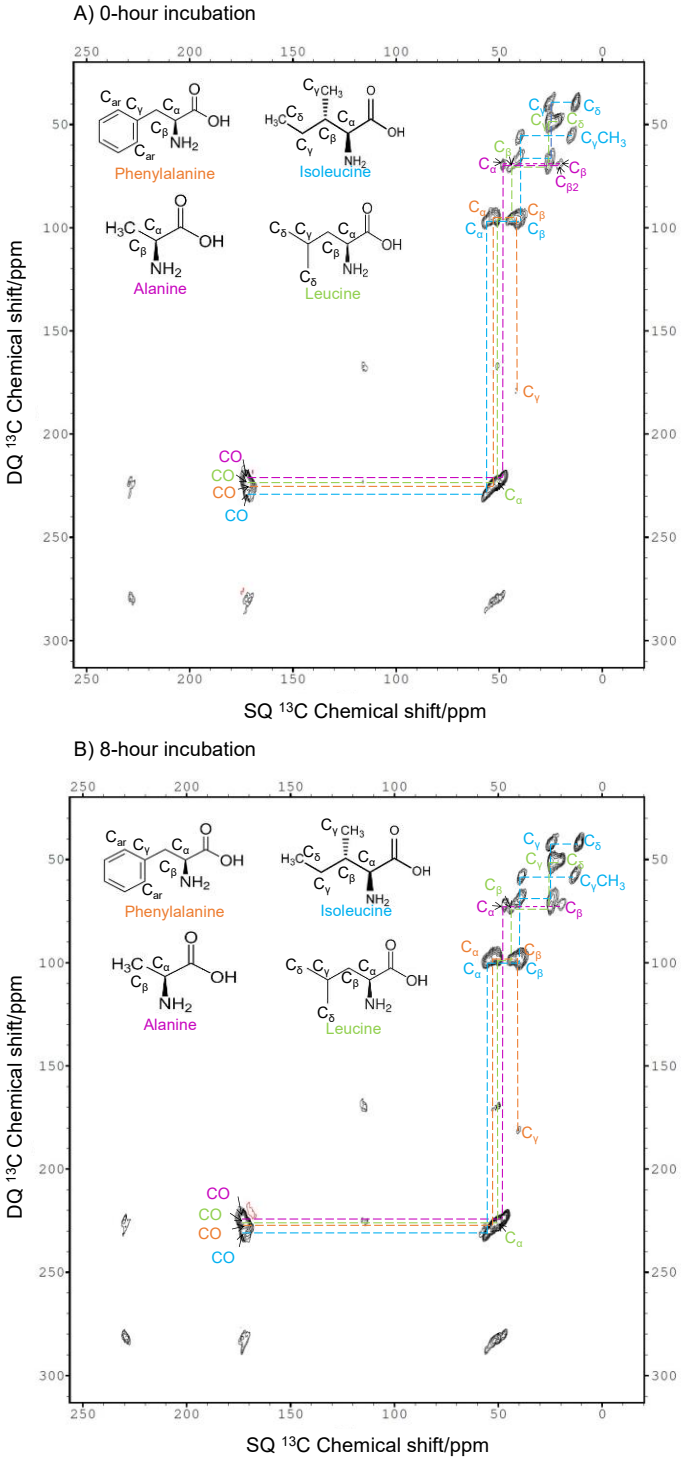

Figure 4.8 *POST-C7 DQSQ correlation spectra of uniformly FAIL-labelled Aβ(1-40) dissolved in DMSO externally added to 100% POPG with a 1:40 P:L followed by a A) 0-hour incubation and B) 8-hour incubation. Spectrum in panel A) was acquired with 128 scans in the direct dimension, 141 points in the indirect dimension and a recycle delay of 4.5 s giving an experimental time of 22 h. Spectrum in panel B) was acquired with 128 scans in the direct dimension, 141 points in the indirect dimension and a recycle delay of 3.5 s giving an experimental time of 20 h.*

Cross peaks in the indirect dimension appear at the sum of the SQ chemical shifts of the spins which are exchanging magnetisation via the dipolar interaction. For example, the C_α-C_β cross peaks appear at the SQ chemical shift of each nucleus (~51 ppm and ~39ppm respectively) in the direct dimension and the sum of those shifts (51 + 38 = 89ppm) in the indirect dimension, varying slightly between each amino acid. One bond correlation experiments with short homonuclear dipolar recoupling times leads to assignments of those cross peaks. 1D slices from Leucine correlation DQ chemical shifts are shown in Figure 4.9 to show the signal-to-noise ratio (S/N) that was achieved.

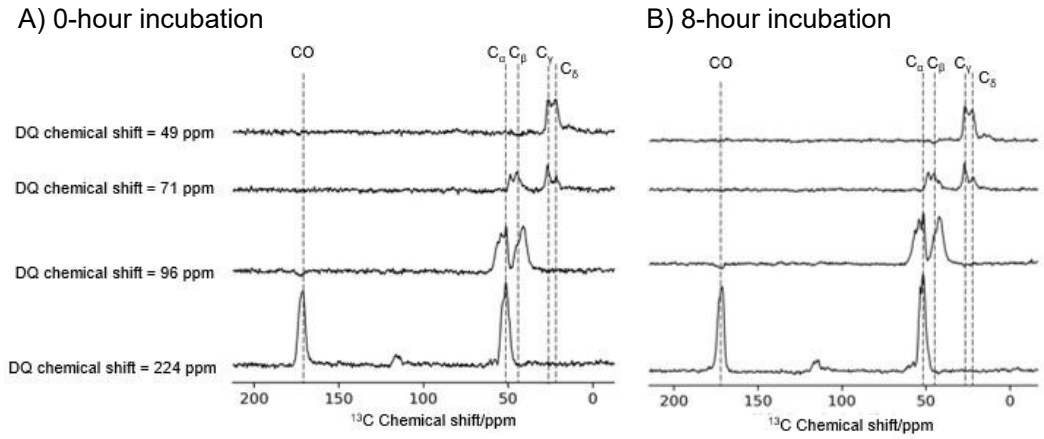

Figure 4.9 *1D slices through the 2D DQ-SQ spectra shown in Figures 4.8 A) and B) and corresponding to 0-hour and 8-hour incubation respectively. Slices are done along the SQ dimension at the DQ frequencies assigned to L34 residue.*

As shown in Figure 4.8, the F19 is distinguishable due to the C_γ - C_β cross peak from the phenyl group, with the C_γ at 138 ppm in the SQ dimension and 179 ppm in the DQ dimension, meaning the C_β is at 41 ppm (179 - 138 = 41). This can then be used to assign the C_α - C_β correlation with C_α at 96 ppm in DQ dimension and 55 ppm in the SQ dimension. Following this pattern all F19 ^{13}C can be resolved, CO can be resolved from the $C_{\alpha,}$ with CO at 171 ppm in the SQ dimension and 226 ppm in the DQ dimension. L34 can also be unambiguously assigned from analysis of correlations with the side chain resonances, the C_γ - C_β gives the chemical shift of the C_β in the SQ dimension which can then be used to resolve the other ^{13}C. Applying this method all four residues can be fully resolved in both the 0 and 8-hour incubation spectra. Two distinct peaks are present for the A21 $C_{\beta,}$ with both 0- and 8-hour incubation, however more identifiable with 0-hour incubation on 2D spectra as shown in Figures 4.8. 1D slices for A21 are shown in Figure 4.10.

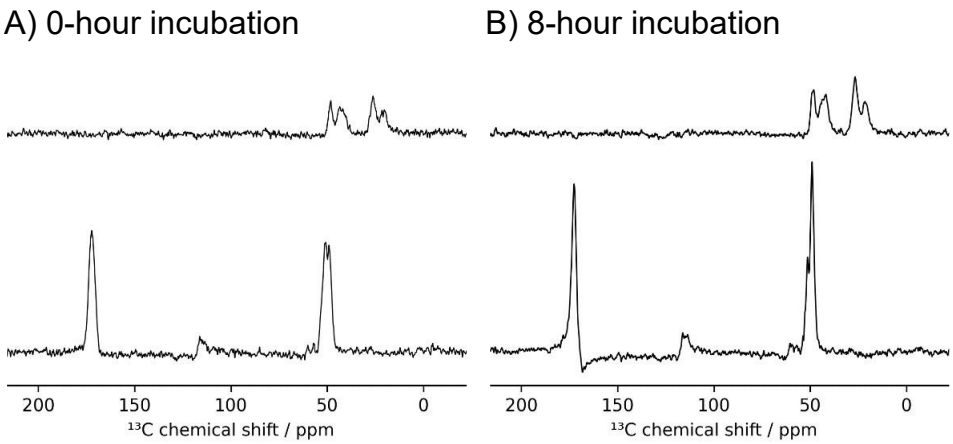

Figure 4.10 *1D slices through the 2D DQ-SQ spectra shown in Figure 4.8 A) and B) and corresponding to 0-hour and 8-hour incubation respectively. Slices are done along the SQ dimension at the DQ frequencies assigned to A21 residue.*

From the DQSQ spectra, secondary chemical shifts could be determined by comparison with the chemical shifts of a random coil conformation. There is a strong correlation between secondary chemical shift and peptide structure. The secondary chemical shift is defined as:

$$\Delta\sigma = \sigma_{observed} - \sigma_{random\ coil} \tag{4.1}$$

As discussed in Section 2.6.1 C_α atoms in β-sheet conformation have a more negative chemical shift than random coil chemical shift, compared to α-helices where the chemical shift is positive. C_β atoms have the opposite behaviour, when present in β-sheets they have a more positive chemical shift when compared to random coil chemical shift. The results of the secondary chemical shift analysis of the chemical shifts resolved in the 2D-spectra in Figure 4.8 are shown in Figure 4.11. In both POPG samples, with and without incubation, the secondary chemical shifts show characteristic β-sheet conformation for all the FAIL residues, as the CO and Cα have more negative chemical shifts and the C_β have more positive secondary chemical shift.

A) 0-hour incubation

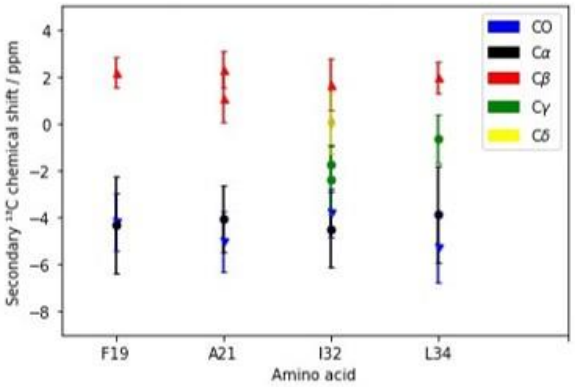

B) 8-hour incubation

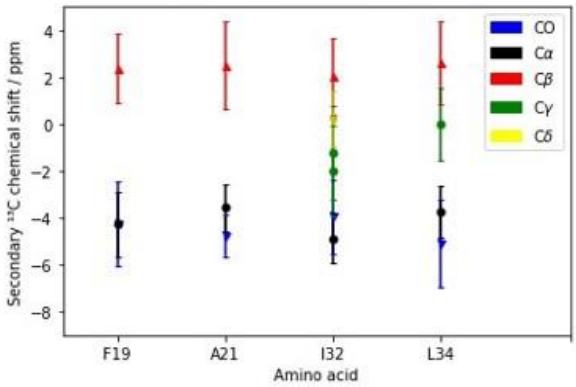

Figure 4.11 *Secondary chemical shifts for the carbon and carbonyl sites in uniformly FAIL-labelled Aβ$_{(1-40)}$ dissolved in DMSO externally added to 100% POPG followed by A) 0-hour and B) 8-hour incubation. Negative CO and C_α values and positive C_β are indicative of β-sheet conformation. Error bars represent the linewidths of the peaks taken from 1D slices of POST-C7 DQSQ spectra.*

Although previous work has suggested that an increase in incubation time increased the protein binding[16], this was not seen in this POPG sample. The protein binding decreased to <1% after 24 hours.

4.3.2 DNP-enhanced NMR of Aβ$_{(1-40)}$ interacting with LM vesicles

DNP-MAS measurements

To assess the conformational changes in Aβ$_{(1-40)}$ in a more biologically relevant environment, a LM system was utilised, containing compounds such as cholesterol, sphingomyelin and GM1 as shown in Figure 4.3. Such compositions mimics the outer leaflet of SPMs, where membrane interactions may occur with the protein once the peptide is released after enzymatic cleavage[16].

Table 4.3 summarizes the results of DNP-enhanced NMR experiments carried on the samples of $A\beta_{(1-40)}$ bound to lipid vesicles under varying conditions (such as P:L ratio and the mode of $A\beta_{(1-40)}$ pretreatment) and of various content, specifically:

- LM: DMPC/DMPS/Sphingomyelin/Cholesterol/GM1 in ratio 1.5:0.3:1:0.5:0.15 respectively.
- LM mixture without GM1, i.e.: DMPC/DMPS/Cholesterol/Sphingomyelin in ratio 1.5:0.3:1:0.5 respectively.
- Lipids from porcine BE.

The observed DNP-enhancements of lipid CH_2 fragment varied from a factor of ~11-50, however, they were typically a factor of ~30. The variation may arise from a difficulty in producing a reproducible homogeneous mixing of the polarising agent with the sample pellet material. Importantly HPLC-based measurements of free $A\beta_{(1-40)}$ in supernatant have shown a rather poor binding (<7% in most cases) of the peptide to the lipid vesicles (summarized in Table 4.3). These results are in striking contrast to the relatively strong binding of $A\beta_{(1-40)}$ to the POPG vesicles described in the previous section. The rather low binding does not seem to be affected by the P:L ratio, method of $A\beta_{(1-40)}$ addition or method of $A\beta_{(1-40)}$ pretreatment, or whether or not the mimic contains GM1. Furthermore, the binding is low for the sample made with porcine BE.

Table 4.3 *Summary of the lipid CH_2 DNP enhancements and the % of protein to lipid binding of $A\beta_{(1-40)}$ externally added (unless stated otherwise) to a range of membranes presented within this chapter.*

Membrane	Labelling scheme	Dissolution method	Incubation time (hours)	P:L	Protein binding to the membrane (%)	Lipid CH_2 Enhancement
DMPC/DMPS	-	HFIP/NaOH	0	1:60	81	-
DMPC/DMPS	-	DMSO	0	1:60	70	-
POPG	FAIL	DMSO	0	1:40	77	18
POPG	FAIL	DMSO	8	1:40	85	16
LM	FAIL	DMSO	0	1:40	-	50
LM	FAIL	DMSO	0	1:100	-	11
LM	FAIL	DMSO	0	1:200	-	18
LM	EVFDSKGA	DMSO	0	1:60	-	17
LM	FAGV	HFIP/NaOH	0	1:40	7	45
LM	FAGV	HFIP/NaOH	8	1:40	<1	38
LM	FAGV	HFIP/NaOH	0	1:20	<1	38
DMPC/DMPS/ Chol/Sphin	FAGV	HFIP/NaOH	0	1:40	<1	32
DMPC/DMPS/ Chol/Sphin	FAGV	HFIP/NaOH	8	1:40	<1	27
Pre-incorporated LM	FAGV	HFIP/NaOH	-	1:40	36	36
POPG	FAGV	HFIP/NaOH	24	1:40	<1	-
BE	FVIL	HFIP/NaOH	15	1:10	6	32
BE	FVIL	HFIP/NaOH	15	1:5	<1	32
BE	FVIL	HFIP/NaOH	5	1:10	-	42

For the sample of $A\beta_{(1-40)}$ with DMSO pretreatment externally added to a LM membrane with a 1:40 P:L and a 0-hour incubation it was possible to determine the enhancements of the protein signals because they were strong enough in the μw_{off} spectra as shown in Figure 4.12. The protein signals measured through the enhancement of aromatic and CO signals were in the order of ~10 whereas the lipids

were enhanced by a factor of ~50. This suggests less efficient spin polarisation transfer by spin diffusion from the DNP matrix to lipid embedded $A\beta_{(1-40)}$ than to the lipid positions.

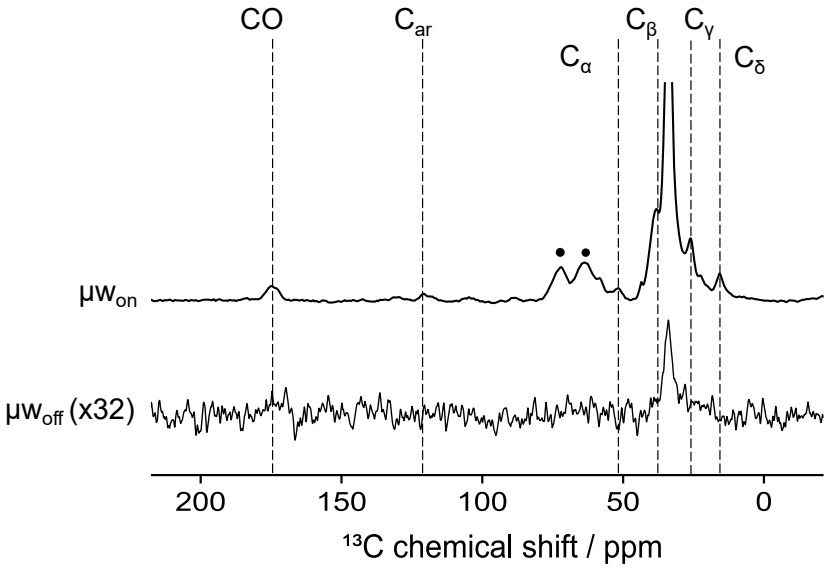

Figure 4.12 *DNP-enhanced ^{13}C-CP spectra of uniformly FAIL-labelled $A\beta_{(1-40)}$ dissolved in DMSO externally added to a LM sample with a 1:40 P:L and a 0-hour incubation with (top) and without (bottom) μw irradiation, with 32 scans in each spectrum. Protein signals are shown by black lines and glycerol peaks are shown by dots.*

DQF experiments were also attempted on most samples, however only a few have demonstrated sufficient $A\beta_{(1-40)}$ peptide NMR signals. For example, $A\beta_{(1-40)}$ peptide signals become visible after a rather long acquisition of 3936 scans for the sample of $A\beta_{(1-40)}$ with HFIP/NaOH pretreatment externally added to a LM with a 1:40 P:L and an 8-hour incubation (shown in Figure 4.13).

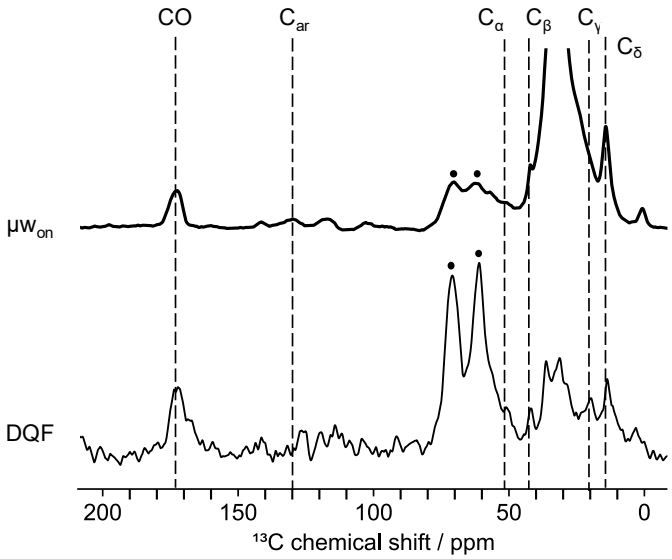

Figure 4.13 *DNP-enhanced (top) ^{13}C-CP spectra acquired with 16 scans, and (bottom) DQF with using POST-C7 pulse sequence acquired with 3936 scans, for the sample of uniformly FAIL-labelled Aβ$_{(1-40)}$ HFIP/NaOH pretreated externally added to a LM sample with a P:L of 1:40 with an 8-hour incubation. Protein signals are shown by black lines and glycerol peaks are shown by dots*

Although all protein peaks can be determined, experimental time for the 1D spectra was 4 hrs. A 2D POST-C7 spectra was ran however is not shown as no cross peaks were visible and individual residues could not be assigned. Experimental time was 16 hrs with 128 scans. In order to achieve a 2D spectra with visible protein peaks, the experimental time required would be impractical.

Factors affecting Aβ$_{(1-40)}$ binding to lipid vesicles.

One factor affecting the protein to lipid binding would be the P:L ratio. Several samples were prepared with varying P:L. For each ratio two samples were prepared, both included protein dissolved in DMSO externally added to the LM system and differed with either a 0- or 8-hour incubation. The results are shown in Figure 4.14.

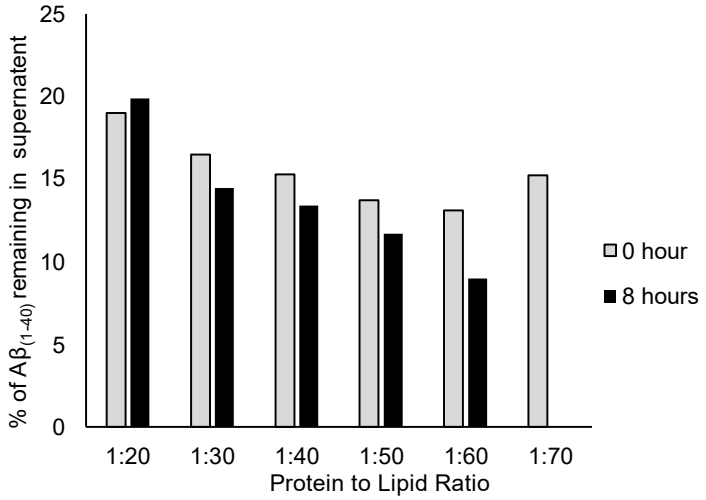

Figure 4.14 *Quantification of $A\beta_{(1-40)}$ in supernatants (reported as the percentage of initial $A\beta_{(1-40)}$) externally added to LM samples with either 0- or 8-hour incubations. P:L was varied from 1:20-1:70.*

Figure 4.14 shows an increase in protein binding with a lower P:L ratio up to 1:60, ranging from 80% binding to 91% binding for the 8-hour incubation samples. This pattern was also seen in the 0-hour samples ranging from 81% binding in 1:20 P:L to 86% binding in 1:60 P:L. An unbinding effect is seen in the 1:70 0-hour sample with a decrease in % binding with 85% protein bound. It is not possible to deduce whether this pattern would be seen in the 8-hour incubation due to inconclusive HPLC results for the 1:70 P:L 8-hour sample. The protein to lipid binding percentages of the samples are also a lot higher than expected based on the 1D spectra from the LM 1:40 sample. The aliquots for this experiment were prepared at much smaller volumes than those needed in DNP samples with unlabelled protein as discussed in the methods section. Samples prepared with a 1:60 P:L showed the best protein binding, suggesting the best signal intensity of DNP spectra. There also seems to be an increase in binding when samples were left to incubate for 8 hours compared to those with no incubation, apart from at higher P:L ratios seen in the 1:20 sample.

Another factor affecting the binding is the lipid composition. A range of samples were prepared with varying components used to produce the LM system, all with the same molar ratios as discussed in the methods section, and varying incubations between 0- and 8- hours. Unlabelled DMSO treated $A\beta_{(1-40)}$ was externally added to a range of lipid membrane systems including components in the LM system such as DMPC, DMPS, Chol, Sphin and GM1. The results of the HPLC analysis of the supernatants are shown in Figure 4.15.

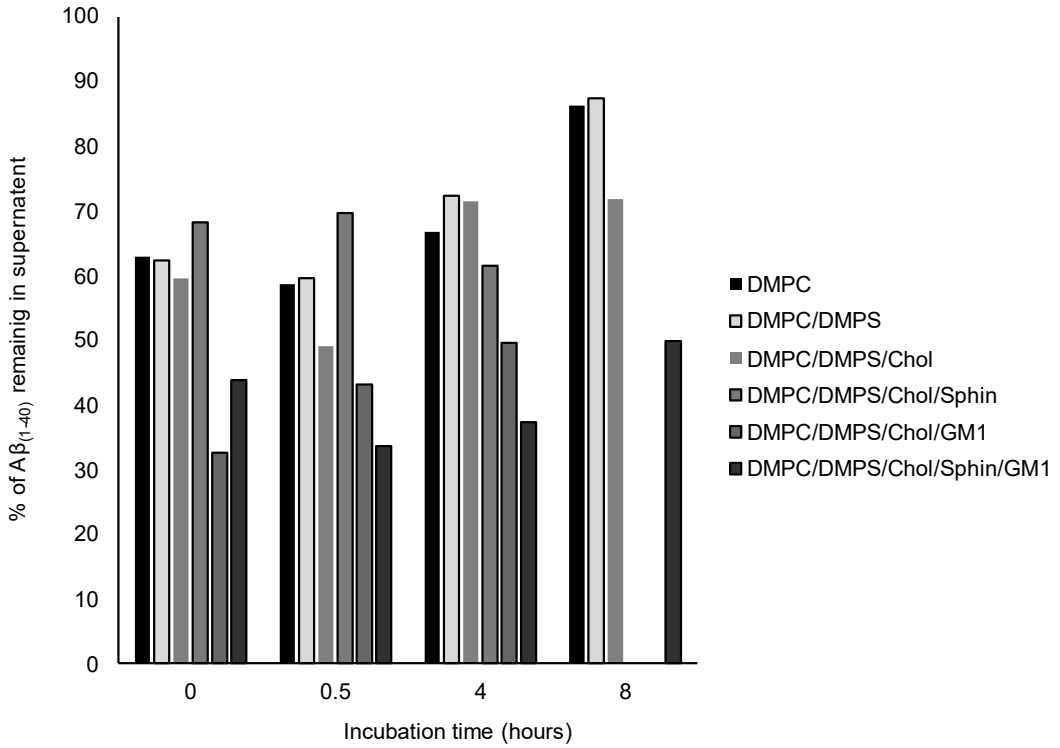

Figure 4.15 *Quantification of $A\beta_{(1-40)}$ in supernatants (reported as the percentage of initial $A\beta_{(1-40)}$) externally added to a variety of samples containing different components used to form LM membrane. Protein was dissolved in DMSO. Samples were subject to either, 0-, 0.5-, 4- or 8-hour incubations, all with a 1:60 P:L. Molar ratios for the DMPC/DMPS/Chol/Sphin/GM1 (LM) are 1.5:0.3:0.5:1:0.15 and are representative for all samples.*

The preparation of lower volume samples increased the % binding of protein to the membrane. It would be expected that the % binding shown in the LM sample for 0-hour incubation with a 1:40 P:L from the P:L comparison dataset would be very similar to the % binding seen in the LM 1:40 P:L 0-hour incubation sample shown in Table 4.3, however the results show a % binding of 87% and 7% respectively, showing large % binding variances between samples of different datasets even when prepared with the same sample methodology.

In general, % binding seems to decrease with incubation time. % binding also tends to decrease with the addition of LM components. Some samples, such as DMPC, DMPC/DMPS, DMPC/DMPS/Chol, DMPC/DMPS/Chol/GM1 and DMPC/DMPS/Chol/Sphin/GM1 (LM) all follow a binding then unbinding mechanism. In four out of five of these cases, 0.5-hour incubation produces the highest protein to membrane binding. For example, with the LM sample, initial % binding of protein to membrane was 56%, increasing to 66% after 0.5-hour incubation and then following

an unbinding effect decreases to 62% then 50% binding. Interestingly, DMPC/DMPS/Chol/Sphin did not follow the patterns presented in other samples. Initial % binding was 31% decreasing to 30% binding after 0.5 hours and increasing 38% binding showing little variation of this sample with incubation time. HPLC of the DMPC/DMPS/Chol/Sphin 8-hour sample was inconclusive.

In all cases of the component comparison dataset, binding ranges from 18%-67% showing large variance between component content and incubation time. The best protein binding was shown by DMPC/DMPS/Chol/GM1 with a 0-hour incubation whilst the lowest binding was shown by DMPC/DMPS with an 8-hour incubation.

4.3.3 Ultrafast-MAS NMR of $A\beta_{(1-40)}$ fibrils

This subsection investigates the level of NMR signals obtained from $A\beta_{(1-40)}$ containing samples with the ultimate aim to test whether the technique could be an alternative to DNP-MAS.

To check whether the pulse sequence could be used to identify individual amino acid residues and find out the spectral resolution, ^{13}C-labelled Alanine was first analysed using an 800 MHz spectrometer at RT and a MAS speed of 65 kHz. The results of 2D-hCH experiment (see Chapter 2.10 for details) are shown in Figure 4.16. There, labelled ^{13}C can be correlated with the protons, giving distinct cross peaks allowing for the secondary structure determination via secondary chemical shifts. The typical observed linewidth in the ^{13}C dimension is ~1.30 ppm (256 Hz) and in ^{1}H dimension ~0.93 ppm (740 Hz). HN protons are also detectable with other cross peaks present between H_α-C_β, H_β-C_α, HN-C_α and HN-C_β. This is most likely due to the relay in magnetisation during the spin-lock period, where the magnetisation is transferred from the ^{1}H to the ^{15}N. This polarisation transfer occurs when the spin-lock rf field amplitudes matches the Hartmann-Hahn condition[32].

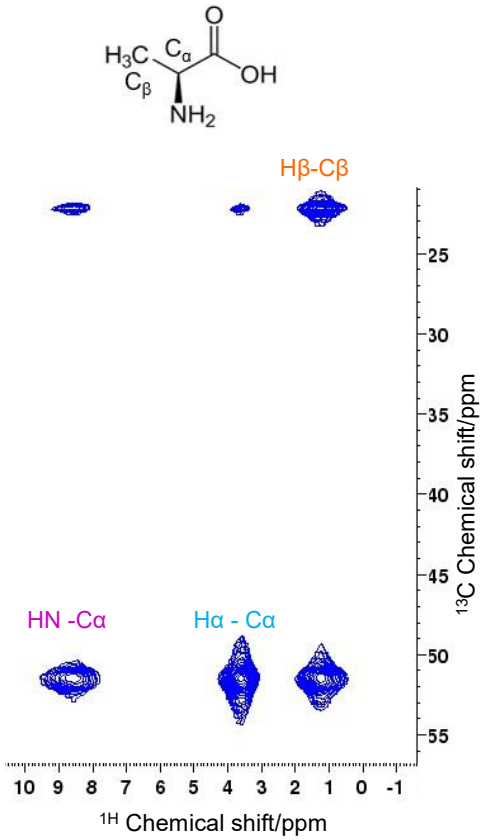

Figure 4.16 *2D hCH correlation spectra of 100% ^{13}C labelled Alanine. Measurement is carried out using 800 MHz RT-NMR with a 1.33 mm rotor and a 65 kHz MAS speed. Acquisition included 8 scans in the direct dimension, 256 points in the indirect dimension and a recycle delay of 1.5 s giving an experimental time of 1 h.*

The next stage was ^{1}H-detection and its application with FAGV labelled residues within $A\beta_{(1\text{-}40)}$ fibrils. TEM was first conducted to confirm the formation of mature $A\beta_{(1\text{-}40)}$ fibrils (see appendix 2 for TEM details). For this, an aliquot was taken from the sample before centrifugation and analysed. The images are shown in Figure 4.17A. Mature fibrils are clearly seen within the sample. No smaller structures can be seen indicating the lack of presence of other $A\beta_{(1\text{-}40)}$ formations of the self-assembly pathway. Fibrils are therefore present within the NMR sample loaded into the rotor meaning 2D analysis is possible.

The results of such are shown in Figure 4.17B (in *blue*). Total experimentation time was just under 45 hrs. Whilst cross peaks can be seen in Figure 4.17B, there is also the presence of noise within the 2D spectra and overcrowding. Some individual cross-peaks can be assigned, however with the addition of line broadening, it is not possible to assign all residues using this spectra alone. Groups of cross-peaks can however be generally assigned as shown on Figure 4.17B.

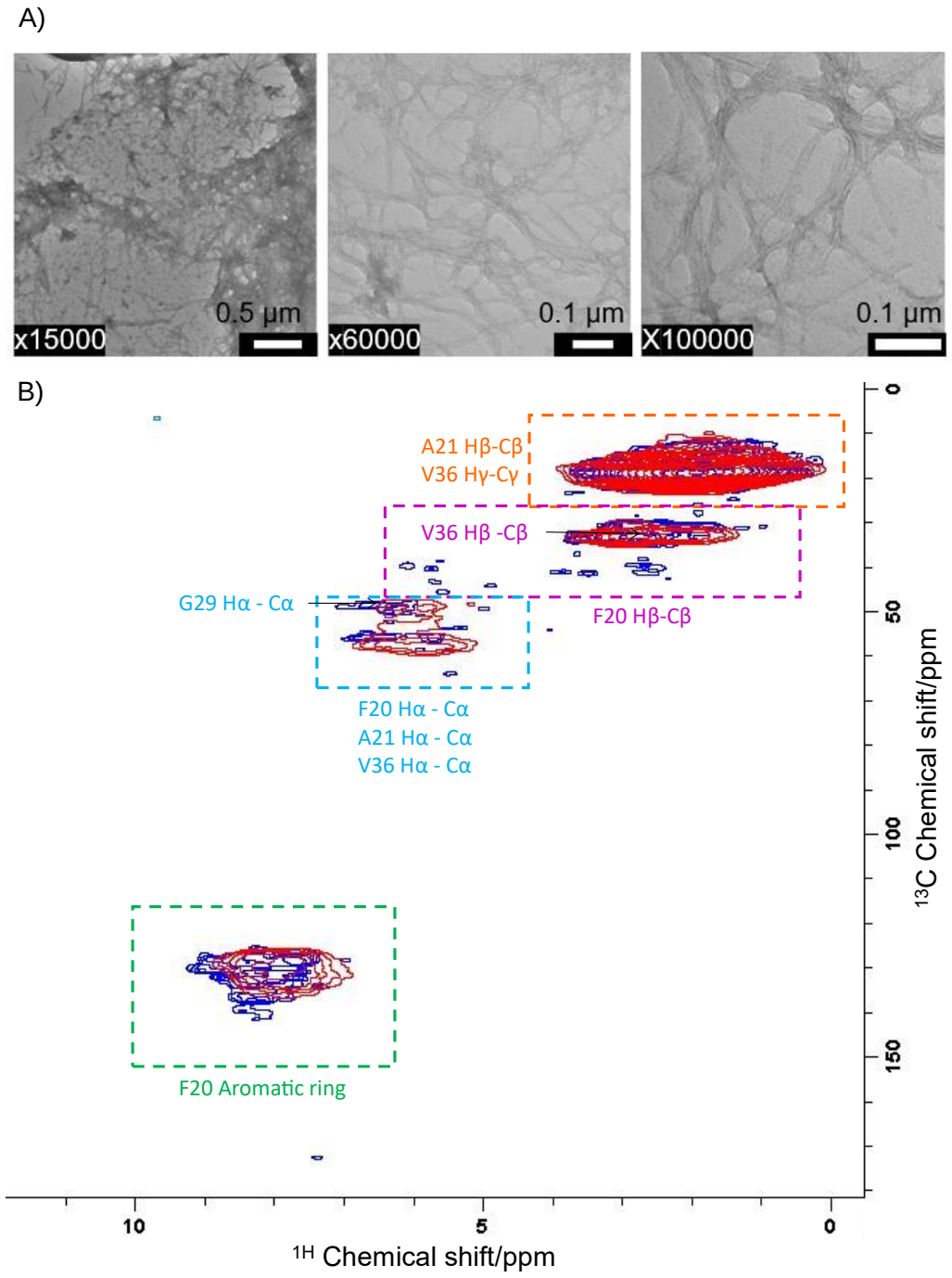

Figure 4.17 *A) Negatively stained TEM images of 100% Aβ(1-40) fibrils. All images are taken from the same sample with (left) 15,000, (middle) 60,000 and (right) 100,000 times magnification. B) 2D hCH correlation spectra of FAGV-labelled Aβ(1-40) fibrils (blue) and after addition of Cu-EDTA (red). (Blue) acquisition included 128 scans in the direct dimension, 602 points in the indirect dimension and a recycle delay of 2 s giving an experimental time of 45 hrs. (Red) acquisition included 128 scans in the direct dimension, 602 points in the indirect dimension and a recycle delay of 0.5 s giving an experimental time of 16 hrs.*

Due to the reduced amount of labelled sample within the sample compared to 100% alanine, it is difficult to deduce if cross peaks between H_{α}-C_{β} and H_{β}-C_{α} are present,

which would assist with protein assignment. More scans may be required to increase protein signal but will significantly increase the experimental time. Whilst not all individual atoms can be assigned, it is possible to assign V36 H_β-C_β and G29 H_α-C_α due to knowledge about their chemical structure and random coil chemical shifts. The V36 C_β has a carbon chemical shift of 33.3 ppm in the fibril sample whilst the G29 C_α has a chemical shift 49.1 ppm chemical shift. As the Cβ has a more positive chemical shift and the Cα has a more negative chemical shift in the fibril sample, compared to the chemical shift in random coil conformation, this suggests a β-sheet conformation at these two positions.

Although the recycle delay of this sample is relatively short at 2 s, the addition of Cu-EDTA is a commonly used method which reduces the recycle delay of samples, allowing for more scans to be obtained during a set experimental time. In this case the recycle delay was reduced to 0.5 s. Figure 4.17 shows the overlaid spectra (in *red*) with Cu-EDTA added to an identical sample. Total experimentation time was reduced to 16 hrs. A large reduction in experimental time compared to the fibril sample without Cu-EDTA.

Comparing the *blue* and *red* spectra, no major shift changes can be seen with the addition of Cu-EDTA concluding that the compound causes no significant structural changes within the fibrils. Also, as there was no observed reduction in signal, the spectra shows no evidence of paramagnetic bleaching which would occur if the Cu-EDTA was to bind to a specific site on the fibril. However, in the Cu-EDTA containing sample, overcrowding and line broadening means that not all individual cross-peaks can be assigned using these spectra alone. However, this does quarter the recycle delay allowing for a shorter experimental time. As there are no major chemical shift changes in the Cu-EDTA fibril sample, this again suggests a β-sheet conformation.

4.4 Discussion

4.4.1 $A\beta_{(1-40)}$ and POPG vesicles

The first stage of experimentation utilised 100% POPG lipids. POPG is an unsaturated negatively charged lipid which can influence the aggregation of $A\beta_{(1-40)}$ with negatively charged phospholipids being shown to accelerate fibrillation[33]. Previous work has shown the assignment of $A\beta_{(1-40)}$ residues using DNP enhanced ssNMR at low concentrations in POPC/POPG membranes which is beneficial for the study of proteins under physiological conditions[34]. Another study demonstrated that the p3 pentamer (residue 17-42) has stronger interactions with POPC/POPG membranes

compared to 100% POPC[20]. Ca2+ ions were also found to form ionic bridges to associate negatively charged residues of the p3 pentamer with negatively charged headgroups of lipid bilayers[20]. DMPG lipid vesicles (similar to POPG however with fully saturated acyl chains) have been shown to induce more α-helical structures in $A\beta_{(1-40)}$ than DMPC[35], present within the LM system which is also of interest when studying the interactions of $A\beta_{(1-40)}$ with membrane systems. Although the structure and physiological properties of this phospholipid differ from the components found within the LM system, such as the DMPC or DMPS phospholipid, it is inexpensive and readily available and so is suitable for testing the methodology of tracking the conformational changes of $A\beta_{(1-40)}$ as a function of time. Overall, the results of this section demonstrate the capacity of DNP-enhanced NMR to characterise the conformation of $A\beta_{(1-40)}$ interacting with POPG vesicles. Specifically, the collected data demonstrate the following:

- DNP-enhancements in a range of 18-43 for various spectral regions and rather good protein to lipid binding of $A\beta_{(1-40)}$ to POPG vesicle of 77 and 85% for 0- and 8-hour incubation respectively, which enables long 2D measurements.
- Short mixing time DARR and DQSQ correlation spectra enable spectral assignment of all FAIL labelled residues within $A\beta_{(1-40)}$ indicating β-sheet conformation.
- Long mixing time DARR reveal the formation of F19-L34 and F19-I32 contacts in $A\beta_{(1-40)}$ bound to POPG vesicles and allow a predicted model to be made.

DNP enhancements in the range of a factor of ~18-43 was seen for $A\beta_{(1-40)}$ when bound to 100% POPG. Studies on $A\beta_{(1-40)}$ protofibrils, fibrils and in high and low-pH environments showed enhancements in the range of 18-80 with the use of triradical dopants[13]. In certain $A\beta_{(1-40)}$ structures such as protofibrils and fibrils, enhancements are lower attributed to clustering of the triradical making DNP less efficient. The choice of AMUPol as a suitable biradical when investigating protein-membrane interactions has been demonstrated in several papers as the biradical does not affect the membrane permeability[36–38]. Previous work with POPG and POPC lipids with the AMUPol biradical saw protein enhancement between 33-40 with a 3:1 POPC/POPG membrane with a 1:20 P:L[34]. Other work showed peptide enhancements of a factor of ~14-40 in a simple DMPC membrane[37]. The enhancements shown within this work may be considered as typical and these good protein DNP enhancements support the methodology used within this work.

Binding of $A\beta_{(1-40)}$ to a POPG membrane showed slight dependence on incubation, with greater binding after an 8-hour incubation. This has also been seen in previous work with LM systems with around an additional 40% more binding after a 4-hour incubation They suggested that initial binding was likely caused by the adsorption of $A\beta_{(1-40)}$ monomers and small oligomers to the membrane which changed with incubation. This could be due to the different types of nucleation and aggregates could be formed quickly after initial binding. $A\beta_{(1-40)}$ would bind to the early nucleation products rather than the membranes[16]. It would be expected that the 0-hour incubation represent monomer species interacting with the POPG membrane, due to the prior use of DMSO. The 8-hour incubation sample is thought to contain more intermediary or protofibril species. Since the conversion from protofibrils to mature fibrils depends on the gradual dissolution of less stable protofibrils and extension of more stable structures. Nucleation of protofibrils is expected to faster compared to the nucleation of mature fibrils prior to sonication, which allows this conversion[13]. Since the conditions of these experiments do not perturb the sample after the addition of protein to the lipid, the presence of a large population of mature fibrils is to be expected. However, the 8-hour incubation sample may contain several intermediary species and further analysis of the samples such as CD spectroscopy needs to be done in order to gain more insight.

In the DQSQ spectra, the 0-hour sample was left to run overnight with 141 scans in the indirect dimension giving an experimental time of ~22 hours, although the Free Induction Decay (FID) had fully decayed after ~100 points, meaning the same spectra could be collected in ~15.5hrs. S/N increases as the square root of the number of scans and therefore as the square root of time. Enhancement for the C_α in the sample containing labelled $A\beta_{(1-40)}$ externally added to 100% POPG with no incubation was 22, meaning an experiment on an equivalent sample without DNP would take 22^2 x 15.5 hrs, equalling 7502-hours, or 312 days. This demonstrates the benefits of using DNP-enhanced ssNMR to provide structural information of proteins such as Aβ in conditions which are beyond the limit of sensitivity for standard NMR.

In both DQSQ spectra, for $AB_{(1-40)}$ bound to 100% POPG with and without incubation, the secondary chemical shifts show characteristic β-sheet conformation. This suggests that the β-sheet $A\beta_{(1-40)}$ structure is stabilised by the outside of the lipid membrane. Comparing data from the samples before incubation and after an 8-hour incubation aimed at investigating structural differences of the protein immediately after Aβ external addition and at the beginning of the fibrillation process. However, the β-sheet structure seems to be stabilised by the membrane and then the fibrillation

process occurs. CD spectroscopy could support this conclusion and show the % of different secondary structures present in each sample.

Previous CD studies have shown structural changes have occurred in the $A\beta_{(1-40)}$ after 4-hours incubation for a range of P:L. This suggests certain on-pathway α-helical intermediates of Aβ formed at the early stages of fibrillation in the presence of membranes[16]. It may be possible that the conformational changes that are taking place are occurring in other sites of the peptide which were not probed by this labelling scheme and other schemes would be necessary to test this hypothesis.

In this case, no such initial α-helical populations were again found analysing secondary chemical shifts despite CD spectra suggestions from previous studies utilising LM systems and components. Also there were larger populations of β-sheet/random coil conformations after incubation reported in previous work with LM systems[16] however the DQSQ does not suggest any significant structural changes between the 0- and 8-hour incubations. Another study also proposed that many of the intermediates present in the fibrillation pathway of Aβ have α- helical structures[39]. As discussed earlier, it is interesting to probe different areas of the protein to assess structural changes. The two distinct peaks present for the A21 $C_{\beta,}$ with both 0- and 8-hour incubation present in the DQSQ spectra are more identifiable with 0-hour incubation. This could be due to the presence of structural heterogeneity, with one sample adopting a β-sheet conformation and another adopting a slightly different conformation, leading to two cross peaks with different chemical shifts present for A21 C_{β}. This conformation may then be stabilised by the membrane promoting the β-sheet conformation. The F19 C_{γ} and aromatic correlations shown in DQSQ spectra have a lower S/N relative to other cross-peaks, when compared to those shown in DARR spectra. This is due to the poor DQ magnetisation build up between spins with high anisotropy in the DQSQ experiments.

Comparing the secondary chemical shifts between samples prepared simultaneously and divided, with one aliquot undergoing incubation, while the other is at the initial point of binding with no incubation, has proven to be a successful method when determining secondary structure changes over time at labelled amino acids. This methodology may be used to assess the protein-membrane interactions between externally added $A\beta_{(1-40)}$ to other membrane systems, including a LM system containing biologically relevant constituents.

Focusing on the DARR spectra, interesting inter-residue correlations between the F19 aromatic group and the I32 and L34 alkyl R-groups are shown with a mixing time of 2

s in both 0 and 8-hour incubations. This demonstrates the proximity of the residues when associated with the POPG lipid. These hydrophobic interactions have been shown in previous work involving $A\beta_{(1-40)}$ and some interactions have also been shown with $A\beta_{(1-42)}$. In both peptides these interactions are demonstrated to be structurally relevant[40,41]. F19 can form sidechains with I32 as well as L34 and, specifically those between F19 and L34, stabilise monomer units when they come into contact with the existing fibrillar structure, making this an interesting area to investigate utilising NMR. A kink in G33 also allows the sidechains of I32 and L34 to point in opposite directions, making contacts with different $A\beta_{(1-40)}$ peptides[42].

Although less common, the F19-I32 contact has been seen in some fibrillary models[9], however is not present in others. Some studies have shown that these residues are too far apart to produce a cross peak, such as those involving $AB_{(1-42)}$[43], and models involving other phospholipid vesicles[17]. In this case there is some cross-peak intensity after 0.25 s due to magnetisation exchange between I32 and L34. The presence of both F19-I32 and F19-L34 contacts in this work are useful distant constraints in determining the structure of $A\beta_{(1-40)}$ when associated with 100% membranes. It demonstrates that the I32 and L34 contacts are facing one-side of an extended peptide strand which is shown schematically in Figure 4.18.

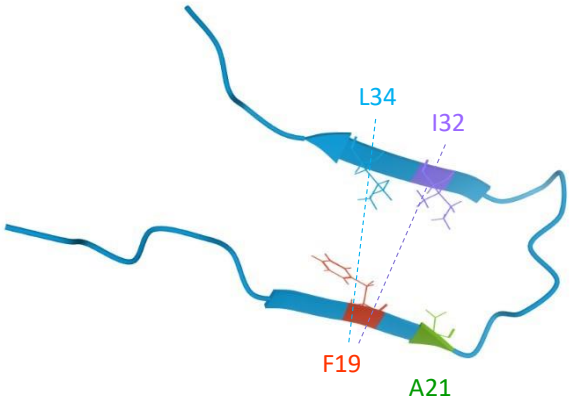

Figure 4.18 *Predicted $A\beta_{(1-40)}$ peptide chain showing an antiparallel β-sheet conformation with F19, A21, I32 and L34 residues (red, green, purple, and blue respectively) highlighted. Based on the constraints acquired from the DARR spectra shown in Figure 4.6 and 4.7 with $A\beta_{(1-40)}$ externally added to 100% POPG with 0- and 8-hour incubations. Adapted from PDB file 2LMQ taken from a fibril model. Dotted lines show the contacts from DARR spectra.*

The labelled amino acids appear to be in close proximity in this model based on the constraints from DARR data and information known about the formation of fibrils and peptide stack. It also suggests that a similar conformation is adopted in monomers prior to fibrillation and small cross-peak intensity seen with 0.25 s mixing time

indicates that the two β-sheet regions may be closer in space than previously thought. To gain insight into the exact distances between these two residues, labelling of the F19 aromatic and I32/L32 methyl group ^{13}C's would be required, utilising an appropriate ^{13}C-^{13}C recoupling scheme. The F19-L34 contact has also been previously detected in several studies of $A\beta_{(1-40)}$ fibrils[9,41,44,45]. Interestingly, the cross peaks observed between F19-I32 and L34 change upon incubation as well as the C_α, C_β or CO chemical shifts of the other labelled residues. The intensity of the cross-peaks increases from the 0-hour to the 8-hour incubation samples, representing the relative number of spins giving rise to the cross peaks increasing. The conformation becomes more apparent within the 8-hour sample so may be stabilised over time by the membrane.

The decrease in protein to lipid binding after 24 hrs coincides with the binding-unbinding theory proposed earlier, as seen with other membrane samples shown in Table 4.3. It may be suggested that the protein begins to bind to itself forming larger aggregates, accumulating more protein with increasing time including initially membrane bound monomers and oligomers. The composition of the membrane and the presence of such modulate molecular packaging of the quaternary structure of $A\beta_{(1-40)}$, however the exact mechanisms remain unknown[46]. Each membrane impacts the binding and aggregation of $A\beta_{(1-40)}$ differently and depending on the incubation period and P:L the protein may favour its own binding rather than to the membrane resulting in low DNP signal. This suggests that the initial stage protein is associated on the outside of the lipid vesicle during the external addition protocol.

4.4.2 $A\beta_{(1-40)}$ and lipid mimic vesicles

Overall, experimental results demonstrate a rather low $A\beta_{(1-40)}$ binding to LM vesicles thereby hindering characterisation of $A\beta_{(1-40)}$ using 2D techniques.

- DNP enhancements of CH_2 lipid fragment were found to be in range of a factor of ~11 to 50 for various lipid compositions and methods of sample preparation.
- However, due to a rather low binding of $A\beta_{(1-40)}$ it is hard to distinguish the enhancements of the protein signals. One successful measurement, however, hint that DNP enhancements for $A\beta_{(1-40)}$ may be lower than those observed for CH_2 lipids.
- Small volume tests were used to the determine the effect on binding of P:L ratio and lipid composition.

The DNP enhancement for LM samples within this work is in the range of a factor of ~11-50 depending on the sample. DNP enhancement is only recorded for the lipid

CH_2 peak as protein S/N is not sufficient to record μw_{off} spectra in a reasonable timeframe. Previously, POPC/POPG samples have been shown to produce lipid CH_2 DNP enhancements in the same order of magnitude with 22 and 53 in 1:100 and 1:200 P:L respectively, showing similar enhancements to this work[34]. Although some samples did not produce protein peaks which allowed the DNP enhancement to be calculated, protein peak enhancements determination was possible in the $A\beta_{(1-40)}$ sample dissolved in DMSO and externally added to the LM system with a 1:40 P:L and a 0-hour incubation. There does seem to be a discrepancy between the enhancements between the lipid CH_2 and the CO protein position which had a DNP enhancement of a factor of 10 and 50 respectively. Work by Tran et al. demonstrated a similar lipid CH_2 and protein CO in two lipid/protein samples where the protein had a 2 mol% relative to lipids[47]. A similar enhancement of the two positions was expected in this case, however, as previously discussed, this may be due to less efficient spin polarisation transfer by spin diffusion from the DNP matrix to lipid embedded $A\beta_{(1-40)}$ than to the lipid positions. Sample mixing may not be thorough enough to ensure homogenous biradical distribution throughout the sample. Either longer mixing times may be needed or additional mixing stages need to be introduced into the methodology.

Previous work has also shown rather good protein signals for $A\beta_{(1-40)}$ pre-incorporated in POPG/POPC/Chol/Spin/GM1 samples, and it was possible to carry out long 2D measurements in them[34]. Our experiments carried out across many of the $A\beta_{(1-40)}$ LM systems, show low levels of protein binding causing issues with DNP experimentation. DNP samples prepared with LM membranes show protein binding in the range <1-7% for external addition protocols, where HPLC was applicable. For external addition methods, maximum binding was achieved when $A\beta_{(1-40)}$ dissolved in HFIP/NaOH was externally added to a LM membrane with a P:L of 1:40 and no incubation. Although the HPLC results suggest a greater level of protein binding to the membrane when $A\beta_{(1-40)}$ is dissolved in HFIP/NaOH compared to DMSO, LM samples with a 1:40 P:L and 0-hour incubation with both pretreatment methods show similar CH_2 enhancements. Both also show low protein signal where secondary structure analysis was not possible. Further investigation on the protein binding via HPLC and secondary structure analysis via CD spectroscopy will need to be done to further assess differences between the samples prepared with two different dissolution methods. Another method of protein integration into the lipid membrane that was tested was the pre-incorporation protocol. For pre-incorporation methods, 36% of protein was bound to the membrane. Although the binding of $A\beta_{(1-40)}$ to the LM

membrane did not achieve sufficient protein binding for 2D NMR secondary structure analysis in both pre-incorporation and external-addition protocols, both methods serve as mimics for biological systems of extracellular aggregation and endosomes respectively.

At higher P:L no such quality spectra could be obtained, although greater protein binding was seen with the pre-incorporation methodology compared to external addition. This could be due to the inclusion of lipids such as DMPC/DMPS affecting the membrane structure and the ability of $A\beta_{(1-40)}$ to bind at the initial stage. Decreasing the P:L from 1:40 to 1:60 in a DNP LM sample reduces the DNP enhancement of the lipid CH_2 from 50 to 17 respectively. Other work utilising the LM system allowed the growth of fibrils for at least two weeks possibly allowing the increased ability of the protein to bind to the membrane[19]. Strong protein signals could be seen on 1D data suggesting that longer 2D experimentation may produce cross peaks leading to residue assignment. Cheng et al. also experienced low protein to lipid binding in several samples with 0-hour incubations with P:L ranging from 1:30-1:120 P:L, with only ~10% protein binding in a 1:30 LM sample with external addition and DMSO. There was a notable increase after a 4-hour incubation[16]. No noticeable increase in binding was reported in this work with DNP LM samples.

As previously stated, the LM system mimics an environment with embedded protein to the membrane system. It has been theorised that fibrillar structures formed after pre-incorporation to the lipid membrane, and their association to the membrane may stabilise the non-fibrillar structures and prevent self-assembly of mature fibrils as well as the formation of specific ionic channels such as the Ca^{2+} channels with Aβ oligomers. Studies have shown that DNP enhanced measurements could be made on pre-incorporated $A\beta_{(1-40)}$ with low P:L such as 1:150 (~0.25 mg $A\beta_{(1-40)}$) with POPC/POPG/cholesterol/ sphingomyelin/GM1 membranes, however spectral quality is affected by t_1 noise[34].

Another model for investigating $A\beta_{(1-40)}$ interactions with biologically relevant membranes is the study of BE. The membrane utilises a variety of compounds such as major biological membrane constituents and unknown constituents. Previous work on total BE with $A\beta_{(1-40)}$ incubated for several weeks showed strong cross peaks on 2D NMR spectra, suggesting good protein binding to the membrane. In this case, the reduction of incubation time resulted in reduced 2D NMR analysis, even when enhancing signals with DNP. One conclusion can be made however, protein to membrane binding was reduced with a greater P:L ratio. Again, this suggests that the

protein may bind to itself forming larger structures outside of the membrane and therefore not be present within the lipid pellet when packed into NMR rotors.

Electrostatic and hydrophobic interactions influence the attachment of $A\beta_{(1-40)}$ to the membrane, the high % of unknown components within the BE membrane makes the prediction of interactions difficult. Work on $A\beta_{(1-42)}$ shows that the protein forms ion channel structures within total BE membranes along with a heterogeneous population of ionic current fluctuations. These fluctuations are shown to differ from current events noted in simpler membranes such as DOPS and POPE lipids. Amyloid beta is therefore suggested to have distinct effects on the BE membranes. These effects were due to oligomeric structures suggested as a predominant toxic species[48]. Another study investigating the binding of $A\beta_{(1-40)}$ to SPMs extracted from the brain tissue of rats also noted an incomplete binding of $A\beta_{(1-40)}$ to the membrane. However secondary chemical shift analysis did suggest a β-sheet conformation from F19, A21 and I32 residues. However, the L34 residue did not follow this pattern along with L34 residues in $A\beta_{(1-40)}$ fibrils from human brain tissues[34].

The P:L has been shown to be an important factor in protein binding to the membrane as well as incubation period. This work shows an increase in protein to lipid binding from 1:20-1:60 P:L, agreeing with previous work[16]. After this point, the protein binding decreases thereafter producing a binding-unbinding affect which was not seen with other low P:L ratios[16]. Further experimentation on incubated lower P:L samples will need to be done to assess this pattern for incubated samples. In most cases incubated samples produces greater protein binding than 0-hour samples, potentially allowing the protein more time to bind to the membrane, also shown with the POPG samples shown in Section 4.3.2. Again this pattern has been seen in other work focusing on protein to lipid binding and P:L[16]. This is contradicted with some DNP samples such as LM 1:40 P:L samples where the binding decreases with incubation. The protein is shown to be highly sensitive to preparation procedure as well as membrane structure as the results of the small volume tests produce greater protein to lipid binding than comparable samples prepared for DNP analysis.

The main difference between the DNP and small volume tests prepared under the same methodology and conditions is firstly the volume. While DNP samples were prepared with a volume of upwards of 10 ml per sample, the small volume tests were prepared with a final volume of 0.6 ml per sample. All samples were subject to the centrifugation methodology, including the same rotor type (Beckman Coulter F1010), speed (26,000 rpm, max g-value 57,440) overnight. This may affect the centrifugation

stage of the methodology. Sample volume is suggested to affect the length of centrifuge spinning as larger volumes spin down more slowly. The use of faster centrifugation speeds or longer centrifugation times may overcome this issue, however due to time constraints and the availability of high-volume sample tubes required for faster spinning, this was not possible. Further HPLC analysis and centrifugal tests will need to be conducted to fully assess this conclusion. The second major difference between the DNP samples and the small volume tests was the origin of the protein used. In the case for DNP samples, synthesised labelled protein was acquired (Binghampton University), however in the case of the small volume tests, unlabelled protein was purchased (Merck). It is unknown whether this sample was synthesised or derived. There may be differences between the two samples including impurity introduced in protein synthesis. A more detailed analysis of the two samples via mass spectroscopy would be required to further investigate this. It is important to note that due to time constraints within this work linked to the COVID-19 pandemic, only one sample set was analysed for the P:L and component HPLC tests were conducted. This decreases the reliability of these datasets and ideally more repeats should be undertaken to support the conclusion. However, as all DNP supernatants were only run once the differences between the protein binding may be accurate as there seems to be no evidence of systematic error as trends can be seen between the incubation time and P:L datasets. Also, HPLC analysis has shown good binding in some samples including the POPG samples which corroborates the good quality spectra obtained. Although repeats will provide useful in obtaining more accurate protein % percentages the overall trends within the data may be considered as reliable.

Each component of the LM has been shown to affect the membrane and its interaction with proteins in various ways, and removal of these components may induce distinct interactions. Protein binding for these samples varies from 13-67% showing large differences depending on the incubation and membrane structure. Cholesterol is involved in cell membrane fluidity by controlling water permeability[21]. Sphingomyelin contributes to membrane micro-domains such as lipid rafts[24]. GM1 is not only involved in hydrophobic and hydrophilic interactions but also reduces the fluidity of the plasma membrane allowing for the retention of lipid rafts. GM1 has also been considered as a key factor in maintaining mammalian neuronal functions avoiding neurodegeneration[25]. Interactions of Aβ and these biologically relevant membranes have been studied extensively. CD spectroscopy has shown that the addition of sphingomyelin and GM1 increased the populations of α-helices at the initial stage of

binding. This suggests that the membrane surface properties effect the binding conformations. The formation of micro-domains is promoted by the presence of cholesterol and sphingomyelin and specific binding sites from the peptide to the membrane may be generated by the presence of GM1. These interactions have also been shown to respond to different P:L with the populations of α-helices vs β-strand increasing with the P:L, however this may be attributed to the increasing GM1:peptide[16]. One component (or components) of the LM system may either reduce the binding of $A\beta_{(1-40)}$ to the membrane or reduce the ability of the DNP matrix to penetrate the membrane as efficiently as with simpler membranes, resulting in reduced biradical mixing and lower DNP enhancement. Again, the issues discussed above regarding protein origin and purity may be relevant in the component analysis explaining protein to lipid binding differences.

4.4.3 hCH ^{1}H-detection

Overall, the results of this section demonstrate the feasibility of ^{1}H-detection via 2D RT NMR, with partial characterisation of $A\beta_{(1-40)}$ fibril conformation. Specifically, this work provides as a benchmark for sensitivity and resolution.

MAS NMR applications in biological systems normally focuses on ^{13}C or ^{15}N detection due to the ability to resolve low γ nuclei atoms at lower spinning speeds. ^{1}H-detection utilised the high γ of protons and allows greater sensitivity which is now possible due to smaller rotor sizes and faster spinning speeds. Previous work has been conducted using HNC_{α} and $HNC_{\alpha}C_{\beta}$ experiments with only 20 kHz MAS spinning speeds, where residues A21 to V39 in $A\beta_{(1-40)}$ fibrils were assigned[49]. This utilised protein derived from recombinant expression in *E.coli* and the use of Cu-EDTA. Based on the two assignments which can be made in the fibril sample in this work, these positions suggest a β-sheet conformation. However more assignments will need to be made in order to support this conclusion. Early work on bundles of aligned fibrils revealed cross-β structures with ribbon like β-sheet segments via x-ray fibre diffraction[50]. More recent work has provided evidence for in-register parallel β-sheets within $A\beta_{(1-40)}$ fibrils using ^{13}C-^{13}C dipole-dipole couplings which aligned hydrophobic residues with themselves[9]. Fibrillar measurements within this thesis are therefor to be expected.

We were able to reduce the sample size utilising a 1.3 mm rotor compared to DNP samples, while also achieving MAS speeds of up to 65 kHz. Due to the minimal sample size, it was difficult to accurately weigh the fibrillar content packed into the rotor. As shown in Chapter 2.11.2. the maximum volume of 1.3 mm rotors is 3 µl which was utilised for RT-NMR experiments, unlike 47 µl required for 3.2 mm rotos used in

DNP analysis. The sample required for ^{1}H detection is therefore lower than that of the DNP samples. For example, 0.5 mg protein was required to grow the fibrils used for RT-NMR experimentation, with not all of the sample being packed into the rotor. DNP however required upwards of 1 mg per sample, for example, 1.25 mg was used in each POPG sample presented above. However, the DNP sample contained a large amount of lipids, it may not be feasible to obtain protein signal from a comparable lipid and protein sample in a 1.3 mm sample as the amount of protein may be too low overall. It has previously been demonstrated that DNP samples with 100% fibrils can be made without lipids, this also included several samples from different stages of the self-assembly pathway without lipids[13].

The overall sensitivity of the hCH spectra seems surprisingly low in both the EDTA absent and containing sample. The Signal to Noise (S/N) between DNP and ^{1}H detection needs to be compared in order to assess the sensitivity of each method. To measure the S/N of DNP spectra and allow comparisons to ^{1}H detection, the DQSQ 0-hour POPG sample was chosen to calculate S/N due to quality 2D spectra as shown in Figure 4.8A). For the DNP POPG sample, a 1D slice was taken through the 2D data from the C_{α}-C_{β} of F19 and I32. The S/N was shown to be 15.78 for the C_{α} peak and was achieved in 22 hrs. For the ^{1}H detection fibril samples a 1D slice was taken from the H_{α}-C_{α} of G29 in both Cu-EDTA absent and containing samples. Without Cu-EDTA, as shown in Figure 4.17B) (*blue*), the S/N of the fibril sample was 3.21 with an experiential time of 45 hrs. With Cu-EDTA, as shown in Figure 4.17B) (*red*) the S/N was shown to be 7.4 with an experimental time of 16 hrs. The S/N of the DNP method shows the greatest S/N overall, with a shorter experimental time compared to ^{1}H detection without Cu-EDTA. Interestingly the S/N of the fibril sample containing Cu-EDTA was shown to be greater than without, however with same experimental parameters and 128 scans in both cases. This may be due to the reduced recycle delay which may be shorter than 0.5 s as the used relaxation time. Samples containing Cu-EDTA show the shortest experimental time whilst also allowing partial spectral assignment. In both experiments ramped 90-100% ^{1}H-^{13}C CP was used and 100-90 ^{13}C-^{1}H CP was used to transfer the magnetisation back to the protons in ^{1}H detection. This ensures a more broadband and efficient magnetisation transfer and is a commonly used method. Due to the uniformly labelled fibrils, it would be expected that this method would provide greater sensitivity than that achieved. In some cases, longer duration transfer back to the protons can result in unwanted longer distance transfer[51]. The addition of water suppression, in this case by the use of continuous wave RF irradiation of 7 kHz, is also a common method to increase sensitivity in ^{1}H

detection spectra. However, there are now several methods of supressing the water signal including the use of Multiple Intense Solvent Suppression Intended for Sensitive Spectroscopic Investigation of Protonated Proteins, Instantly (MISSISSIPPI)[52]. A comparison of spectra using different methods of water suppression may be beneficial in increasing the overall sensitivity of the method.

Assignment of the ^{1}H detection spectra was difficult due to overcrowding and addition of homogeneous line broadening; however, regions of atoms can be assigned. Using the same DQSQ 0-hour POPG spectra the Cα-Cβ slice was taken from F19 and the linewidth measured of the Cα. For the ^{1}H detection fibril sample Hα-Cα G29 slice with the linewidth measured for both Cu-EDTA absent and containing sample. Resolution comparisons can be made by comparing the linewidths. For the DNP sample, a F19 C_{α} linewidth was taken to be ~4.1ppm. For the ^{1}H detection fibril sample without Cu-EDTA, the linewidth was taken to be ~1.84 ppm and for the Cu-EDTA containing sample was taken to be ~1.95 ppm in the ^{1}H dimension. Although, it is difficult to assess the resolution purely based on these measurements due to DNP measurements of ^{13}C and the differing samples and residues. Measurements will need to be taken of the same position in the same sample in both methods. The linewidth may be reduced by faster spinning speeds which are becoming more available. The narrower lines observed under fast MAS typically represent a reduction in line broadening due to homogeneous rather than inhomogeneous effects. Measurements at faster spinning speeds should also be undertaken on the sample to assess the reduction in line broadening and potentially increase resolution.

There are some important factors to consider when assessing the overall resolution difference between the two methods. Within the DNP sample, all labelled residues could be assigned. For some residues within the ^{1}H detection fibrillar sample, overcrowding and signal overlap due to line broadening made this difficult. The DNP samples also contain a large amount of lipid as well as DNP dopant and glycerol which affect the linewidth of the signals. There may be several steps that can be implemented to improve the resolution of ^{1}H detection. The use of other complementary NMR analysis such as ^{13}C-^{13}C correlation analysis provides specific residue carbon correlations for the amino acid backbone and combined with this work will allow individual atoms to be assigned.

Pre-deuteration of lipids has been suggested as a method to improve the efficiency of polarisation transfer by increasing the ^{1}H spin relaxation time[47]. It has however been demonstrated that in certain experiments, such as PDSD experiments, no

effects of pre-deuteration have been observed[53]. As well as the addition of 2D ^{13}C correlation spectra, the application of 3D spectra may prove useful in spectral assignment. This inserts another evolution and mixing period whereby a third time axis is introduced. Previously HSQC-TOCSY and 3D ^{1}H-^{13}C-^{31}P correlation have been useful in assigning macromolecules including proteins[54]. The application of 3D spectroscopy has previously been employed in the structural determination of $A\beta_{(1-40),}$ specifically when in a complex with a glucoside, determining what specific protein residues were involved[55]. 3D spectroscopy coupled with ^{1}H detection may prove useful in protein structure determination. Another way to increase resolution may be to increase the MAS frequency. This method is already employed to reduce the linewidth of solid samples which do not undergo random tumbling as described in chapter 2.7. At the time of writing maximum spinning speeds have been reported of up to 126 kHz. At this speed linewidths are reduced by a factor of ~1.35 compared to MAS speeds of 93 kHz, showing a reduction from 137 to 99 Hz respectively[56]. Since the spectra recorded within this thesis work has a maximum MAS of 65 kHz, increasing the MAS may increase the resolution enough to increase spectral assignment. However, this is limited by the sample content. Increasing spinning speeds reduces the diameter of rotor and reducing maximum volume. Achieving speeds of up to 126 kHz utilised a 0.6 mm rotor with 0.28 mg of protein. Whilst this may be useful in protein determination of pure protein, such as $A\beta_{(1-40)}$ fibrils, the investigation of $A\beta_{(1-40)}$ interacting with lipid mimics may not be possible due to the low protein content resulting in minimal protein signal[56].

DNP and ^{1}H detection RT NMR have been shown to be both beneficial in the structural assignment of $A\beta_{(1-40)}$ within this work. DNP has been shown to provide full spectral assignment within a 22hr timeframe, compared to ^{1}H detection where only a few assignments could be made limited by overcrowding and signal overlap. DNP also produced the greatest S/N when compared to ^{1}H detection. Due to the larger sample volume permitted, lipid/protein interactions may be investigated with signals enhanced by DNP as smaller protein content is required for DNP compared to ^{1}H detection. Due to the cryogenic temperatures required for DNP experimentation it is also possible to take samples from different stages of self-assembly pathways, where there will be no structural changes providing structural snapshots. As ^{1}H-detection is usually done at RT with relatively long experimental times in the case of this thesis work, there is the potential for structural changes to occur during the acquisition time. On the contrary, ^{1}H detection provided some spectral assignment in the shortest 2D experimental time. It also does not require the addition of DNP dopants or glycerol,

however, did require the addition of Cu-EDTA to reduce experimental time. It is noteworthy that this work has demonstrated the lack of structural interference from DNP dopant, glycerol and Cu-EDTA.

Overall, ^{1}H-detection has allowed for a reduction in sample quantity, as well as a reduction of experimental time and provides a good basis for method development. We have also shown that the addition of Cu-EDTA does not alter the structure of the fibrils while reducing the experimental time compared to samples without Cu-EDTA. However, there may be a possibility for combined DNP enhanced ^{1}H detection NMR with higher spinning speeds. Recent work has shown the benefit of utilising DNP with ^{1}H-detection in significantly enhancing sensitivity with low MAS (10 kHz). This can then allow structural determination via indirectly detected ^{14}N NMR spectra without the use for isotopic labelling. DNP is however limited by maximum spinning speeds <14 kHz[57]. However, combinational use of the two methods may provide structural characterisation of $A\beta_{(1\text{-}40)}$ interacting with biologically relevant membranes at different stages of the self-assembly pathway.

4.5 Conclusion

The ability of DNP experiments in this chapter is shown in some cases to probe the structure and conformational changes of $A\beta_{(1\text{-}40)}$. Several optimisation steps were taken to ensure lipid homogeneity and protein monomerisation. For the simple POPG system, DNP enhancements were shown to have a maximum of a factor of ~38 for protein peaks which was to be expected based of previous work. ^{13}C-^{13}C DARR experiments show the cross peaks which can be assigned to specific residues in both inter and intra-residue correlation spectra. However, natural abundance ^{13}C signals from lipids cause significant diagonal and cross peaks. The use of DQ ^{13}C-^{13}C experiments, specifically the use of POST-C7 ^{13}C-^{13}C experiments, can eliminate natural abundance peaks simplifying spectra. For the LM system low binding of the protein has not allowed for successful conformation analysis. Several changes have been implemented in attempt to overcome this.

The results of the secondary chemical shifts of labelled $A\beta_{(1\text{-}40)}$ externally added to POPG membranes suggests a β-sheet structure at both 0- and 8-hour incubations. However due to the low % binding of $A\beta_{(1\text{-}40)}$ to biologically relevant lipid membranes, BE and POPG with longer incubation periods, the secondary structure of the protein in these environments could not be determined. The results of this chapter also shows that there are % binding differences and DNP enhancement differences between the

same samples prepared under the same methodology where the only difference is sample volume and protein origin. Several changes were implemented in this work to attempt to increase protein binding however little improvement was seen. This work does however show the exciting possibility of determining the structure of the protein during processes such as fibrillation. This is due to the cryogenic nature of DNP and the ability of a sample to be flash frozen and then analysed.

^{1}H-detection has also been applied to $A\beta_{(1-40)}$ fibrils with and without Cu-EDTA showing minimal changes to the protein structure whilst reducing experimental time in samples where Cu-EDTA is present. Comparisons have been made in terms of sensitivity and resolution to DNP enhanced NMR experimentation and may provide complimentary future studies.

Complete protein structural determination is not possible at this time due to the line broadening at low temperatures required by DNP. Only a limited number of residues can be labelled. However, this work has shown that using a range of different labelling schemes of $A\beta_{(1-40)}$ can be used to investigate the structures of several regions of the protein.

This work has also demonstrated the effective use of complementary studies between DNP enhanced NMR, HPLC and TEM to evaluate the structure of $A\beta_{(1-40)}$ and the conformational changes it undergoes when interacting with lipid membranes such as POPG, biologically relevant systems and brain extract.

4.6 References

1. Marion, D. An introduction to biological NMR spectroscopy. *Mol. Cell. Proteomics* **12**, 3006–25 (2013).

2. Wagner, G. & Wüthrich, K. Sequential resonance assignments in protein 1H nuclear magnetic resonance spectra. *J. Mol. Biol.* **155**, 347–366 (1982).

3. Quinn, C. M., Wang, M. & Polenova, T. NMR of Macromolecular Assemblies and Machines at 1 GHz and Beyond: New Transformative Opportunities for Molecular Structural Biology. in 1–35 (2018).

4. SUNDE, M. & BLAKE, C. The Structure of Amyloid Fibrils by Electron Microscopy and X-Ray Diffraction. in *Advances in Protein Chemistry Volume 50* 123–159 (1997).

5. Yee, A. A., Savchenko, A., Ignachenko, A., Lukin, J., Xu, X., Skarina, T., Evdokimova, E., Liu, C. S., Semesi, A., Guido, V., Edwards, A. M. & Arrowsmith, C. H. NMR and X-ray crystallography, complementary tools in structural proteomics of small proteins. *J. Am. Chem. Soc.* **127**, 16512–7 (2005).

6. Cavalli, A., Salvatella, X., Dobson, C. M. & Vendruscolo, M. Protein structure determination from NMR chemical shifts. *Proc. Natl. Acad. Sci.* **104**, 9615–9620 (2007).

7. Petkova, A. T., Ishii, Y., Balbach, J. J., Antzutkin, O. N., Leapman, R. D., Delaglio, F. & Tycko, R. A structural model for Alzheimer's β-amyloid fibrils based on experimental constraints from solid state NMR. *Proc. Natl. Acad. Sci.* **99**, 16742–16747 (2002).

8. Tycko, R. Solid-State NMR Studies of Amyloid Fibril Structure. *Annu. Rev. Phys. Chem.* **62**, 279–299 (2011).

9. Paravastu, A. K., Leapman, R. D., Yau, W.-M. & Tycko, R. Molecular structural basis for polymorphism in Alzheimer's -amyloid fibrils. *Proc. Natl. Acad. Sci.* **105**, 18349–18354 (2008).

10. Ferguson, N., Becker, J., Tidow, H., Tremmel, S., Sharpe, T. D., Krause, G., Flinders, J., Petrovich, M., Berriman, J., Oschkinat, H. & Fersht, A. R. General structural motifs of amyloid protofilaments. *Proc. Natl. Acad. Sci.* **103**, 16248–

16253 (2006).

11. Balbach, J. J., Ishii, Y., Antzutkin, O. N., Leapman, R. D., Rizzo, N. W., Dyda, F., Reed, J. & Tycko, R. Amyloid fibril formation by Aβ16-22, a seven-residue fragment of the Alzheimer's β-amyloid peptide, and structural characterization by solid state NMR. *Biochemistry* **39**, 13748–13759 (2000).

12. Tycko, R. Amyloid Polymorphism: Structural Basis and Neurobiological Relevance. *Neuron* **86**, 632–645 (2015).

13. Potapov, A., Yau, W.-M., Ghirlando, R., Thurber, K. R. & Tycko, R. Successive Stages of Amyloid-β Self-Assembly Characterized by Solid-State Nuclear Magnetic Resonance with Dynamic Nuclear Polarization. *J. Am. Chem. Soc.* **137**, 8294–8307 (2015).

14. Cryo-EM structures of amyloid-β 42 filaments from human brains. *Science (80-.).* **375**, 167–172 (2022).

15. Cline, E. N., Bicca, M. A., Viola, K. L. & Klein, W. L. The Amyloid-β Oligomer Hypothesis: Beginning of the Third Decade. *J. Alzheimer's Dis.* **64**, S567–S610 (2018).

16. Cheng, Q., Hu, Z.-W., Doherty, K. E., Tobin-Miyaji, Y. J. & Qiang, W. The on-fibrillation-pathway membrane content leakage and off-fibrillation-pathway lipid mixing induced by 40-residue β-amyloid peptides in biologically relevant model liposomes. *Biochim. Biophys. Acta - Biomembr.* **1860**, 1670–1680 (2018).

17. Niu, Z., Zhao, W., Zhang, Z., Xiao, F., Tang, X. & Yang, J. The Molecular Structure of Alzheimer β-Amyloid Fibrils Formed in the Presence of Phospholipid Vesicles. *Angew. Chemie Int. Ed.* **53**, 9294–9297 (2014).

18. Knight, M. J., Webber, A. L., Pell, A. J., Guerry, P., Barbet-Massin, E., Bertini, I., Felli, I. C., Gonnelli, L., Pierattelli, R., Emsley, L., Lesage, A., Herrmann, T. & Pintacuda, G. Fast Resonance Assignment and Fold Determination of Human Superoxide Dismutase by High-Resolution Proton-Detected Solid-State MAS NMR Spectroscopy. *Angew. Chemie Int. Ed.* **50**, 11697–11701 (2011).

19. Qiang, Wei1. Qiang W, Yau W-M, S. J. F. of β amyloid peptides in the presence of phospholipid bilayers and the consequent membrane disruption. B. B. A.-B.

[Internet]. 2015 J. A. from: https://linkinghub. elsevier. com/retrieve/p., Yau, W.-M. & Schulte, J. Fibrillation of β amyloid peptides in the presence of phospholipid bilayers and the consequent membrane disruption. *Biochim. Biophys. Acta - Biomembr.* **1848**, 266–276 (2015).

20. Yu, X., Wang, Q., Pan, Q., Zhou, F. & Zheng, J. Molecular interactions of Alzheimer amyloid-β oligomers with neutral and negatively charged lipid bilayers. *Phys. Chem. Chem. Phys.* **15**, 8878 (2013).

21. Yanagisawa, K. Cholesterol and Aß Aggregation. *Pharmacopsychiatry* **36**, 127–129 (2003).

22. Owen, M. C., Kulig, W., Poojari, C., Rog, T. & Strodel, B. Physiologically-relevant levels of sphingomyelin, but not GM1, induces a β-sheet-rich structure in the amyloid-β(1-42) monomer. *Biochim. Biophys. Acta - Biomembr.* **1860**, 1709–1720 (2018).

23. Matsubara, T., Yasumori, H., Ito, K., Shimoaka, T., Hasegawa, T. & Sato, T. Amyloid-β fibrils assembled on ganglioside-enriched membranes contain both parallel β-sheets and turns. *J. Biol. Chem.* **293**, 14146–14154 (2018).

24. Taniguchi, M. & Okazaki, T. The role of sphingomyelin and sphingomyelin synthases in cell death, proliferation and migration-from cell and animal models to human disorders. *Biochim. Biophys. Acta* **1841**, 692–703 (2014).

25. Chiricozzi, E., Lunghi, G., Di Biase, E., Fazzari, M., Sonnino, S. & Mauri, L. GM1 Ganglioside Is A Key Factor in Maintaining the Mammalian Neuronal Functions Avoiding Neurodegeneration. *Int. J. Mol. Sci.* **21**, 868 (2020).

26. Khaled, M., Rönnbäck, I., Ilag, L. L., Gräslund, A., Strodel, B. & Österlund, N. A Hairpin Motif in the Amyloid-β Peptide Is Important for Formation of Disease-Related Oligomers. *J. Am. Chem. Soc.* **145**, 18340–18354 (2023).

27. Mirza, Z., Pillai, V. & Kamal, M. Protein Interactions Between the C-Terminus of Aβ-Peptide and Phospholipase A2 - A Structure Biology Based Approach to Identify Novel Alzheimer's Therapeutics. *CNS Neurol. Disord. - Drug Targets* **13**, 1224–1231 (2014).

28. Ryan, T. M., Caine, J., Mertens, H. D. T., Kirby, N., Nigro, J., Breheney, K., Waddington, L. J., Streltsov, V. A., Curtain, C., Masters, C. L. & Roberts, B. R.

Ammonium hydroxide treatment of Aβ produces an aggregate free solution suitable for biophysical and cell culture characterization. *PeerJ* **1**, e73 (2013).

29. Wiglenda, T., Groenke, N., Hoffmann, W., Manz, C., Diez, L., Buntru, A., Brusendorf, L., Neuendorf, N., Schnoegl, S., Haenig, C., Schmieder, P., Pagel, K. & Wanker, E. E. Sclerotiorin Stabilizes the Assembly of Nonfibrillar Abeta42 Oligomers with Low Toxicity, Seeding Activity, and Beta-sheet Content. *J. Mol. Biol.* **432**, 2080–2098 (2020).

30. Takegoshi, K., Nakamura, S. & Terao, T. 13C–1H dipolar-assisted rotational resonance in magic-angle spinning NMR. *Chem. Phys. Lett.* **344**, 631–637 (2001).

31. Szeverenyi, N. M., Sullivan, M. J. & Maciel, G. E. Observation of spin exchange by two-dimensional fourier transform 13C cross polarization-magic-angle spinning. *J. Magn. Reson.* **47**, 462–475 (1982).

32. Hung, I. & Gan, Z. Spin-locking and cross-polarization under magic-angle spinning of uniformly labeled solids. *J. Magn. Reson.* **256**, 23–29 (2015).

33. Niu, Z., Zhang, Z., Zhao, W. & Yang, J. Interactions between amyloid β peptide and lipid membranes. *Biochim. Biophys. Acta - Biomembr.* **1860**, 1663–1669 (2018).

34. Thomas Deo. Applications of Dynamic Nuclear Polarisation in biological systems. *PhD thesis, Univ. Nottingham* (2020).

35. Bokvist, M., Lindström, F., Watts, A. & Gröbner, G. Two Types of Alzheimer's β-Amyloid (1–40) Peptide Membrane Interactions: Aggregation Preventing Transmembrane Anchoring Versus Accelerated Surface Fibril Formation. *J. Mol. Biol.* **335**, 1039–1049 (2004).

36. Costello, W. N., Xiao, Y. & Frederick, K. K. DNP-Assisted NMR Investigation of Proteins at Endogenous Levels in Cellular Milieu. in 373–406 (2019).

37. Liao, S. Y., Lee, M., Wang, T., Sergeyev, I. V. & Hong, M. Efficient DNP NMR of membrane proteins: sample preparation protocols, sensitivity, and radical location. *J. Biomol. NMR* **64**, 223–237 (2016).

38. Overall, S. A. & Barnes, A. B. Biomolecular Perturbations in In-Cell Dynamic

Nuclear Polarization Experiments. *Front. Mol. Biosci.* **8**, (2021).

39. Abedini, A. & Raleigh, D. P. A role for helical intermediates in amyloid formation by natively unfolded polypeptides? *Phys. Biol.* **6**, 015005 (2009).

40. Petkova, A. T., Yau, W.-M. & Tycko, R. Experimental Constraints on Quaternary Structure in Alzheimer's β-Amyloid Fibrils †. *Biochemistry* **45**, 498–512 (2006).

41. Lu, J.-X., Qiang, W., Yau, W.-M., Schwieters, C. D., Meredith, S. C. & Tycko, R. Molecular Structure of β-Amyloid Fibrils in Alzheimer's Disease Brain Tissue. *Cell* **154**, 1257–1268 (2013).

42. Smith, A. A., Corzilius, B., Barnes, A. B., Maly, T. & Griffin, R. G. Solid effect dynamic nuclear polarization and polarization pathways. *J. Chem. Phys.* **136**, 015101 (2012).

43. Wälti, M. A., Ravotti, F., Arai, H., Glabe, C. G., Wall, J. S., Böckmann, A., Güntert, P., Meier, B. H. & Riek, R. Atomic-resolution structure of a disease-relevant Aβ(1–42) amyloid fibril. *Proc. Natl. Acad. Sci.* **113**, (2016).

44. Bertini, I., Gonnelli, L., Luchinat, C., Mao, J. & Nesi, A. A New Structural Model of Aβ 40 Fibrils. *J. Am. Chem. Soc.* **133**, 16013–16022 (2011).

45. Qiang, W., Yau, W.-M., Luo, Y., Mattson, M. P. & Tycko, R. Antiparallel -sheet architecture in Iowa-mutant -amyloid fibrils. *Proc. Natl. Acad. Sci.* **109**, 4443–4448 (2012).

46. Kenyaga, J. M., Cheng, Q. & Qiang, W. Early stage β-amyloid-membrane interactions modulate lipid dynamics and influence structural interfaces and fibrillation. *J. Biol. Chem.* **298**, 102491 (2022).

47. Tran, N. T., Mentink-Vigier, F. & Long, J. R. Dynamic Nuclear Polarization of Biomembrane Assemblies. *Biomolecules* **10**, 1246 (2020).

48. Lee, J., Kim, Y. H., T. Arce, F., Gillman, A. L., Jang, H., Kagan, B. L., Nussinov, R., Yang, J. & Lal, R. Amyloid β Ion Channels in a Membrane Comprising Brain Total Lipid Extracts. *ACS Chem. Neurosci.* **8**, 1348–1357 (2017).

49. Linser, R., Dasari, M., Hiller, M., Higman, V., Fink, U., Lopez del Amo, J., Markovic, S., Handel, L., Kessler, B., Schmieder, P., Oesterhelt, D., Oschkinat,

H. & Reif, B. Proton-Detected Solid-State NMR Spectroscopy of Fibrillar and Membrane Proteins. *Angew. Chemie Int. Ed.* **50**, 4508–4512 (2011).

50. EANES, E. D. & GLENNER, G. G. X-RAY DIFFRACTION STUDIES ON AMYLOID FILAMENTS. *J. Histochem. Cytochem.* **16**, 673–677 (1968).

51. Fricke, P., Chevelkov, V., Zinke, M., Giller, K., Becker, S. & Lange, A. Backbone assignment of perdeuterated proteins by solid-state NMR using proton detection and ultrafast magic-angle spinning. *Nat. Protoc.* **12**, 764–782 (2017).

52. Zhou, D. H. & Rienstra, C. M. High-performance solvent suppression for proton detected solid-state NMR. *J. Magn. Reson.* **192**, 167–172 (2008).

53. Long, Z., Park, S. H. & Opella, S. J. Effects of deuteration on solid-state NMR spectra of single peptide crystals and oriented protein samples. *J. Magn. Reson.* **309**, 106613 (2019).

54. Lindon, J. C. Multidimensional NMR Spectroscopy. in *Reference Module in Chemistry, Molecular Sciences and Chemical Engineering* (Elsevier, 2016).

55. Richard, T., Papastamoulis, Y., Waffo-Teguo, P. & Monti, J.-P. 3D NMR structure of a complex between the amyloid beta peptide (1–40) and the polyphenol ε-viniferin glucoside: Implications in Alzheimer's disease. *Biochim. Biophys. Acta - Gen. Subj.* **1830**, 5068–5074 (2013).

56. Penzel, S., Oss, A., Org, M.-L., Samoson, A., Böckmann, A., Ernst, M. & Meier, B. H. Spinning faster: protein NMR at MAS frequencies up to 126 kHz. *J. Biomol. NMR* **73**, 19–29 (2019).

57. Concistré, M., Paul, S., Carravetta, M., Kuprov, I. & Williamson, P. T. F. Strategies for 1 H-Detected Dynamic Nuclear Polarization Magic-Angle Spinning NMR Spectroscopy. *Chem. – A Eur. J.* **26**, 15852–15854 (2020).

5. Analysis of Double Electron-Electron Resonance data for extracting distances in biomolecules

5.1 Introduction

Structural analysis of proteins if often performed using NMR as discussed in previous chapters. However, large molecular weights, protein complexes or highly dynamic proteins are not always amenable for NMR. EPR spectroscopy can be used to extract distances in proteins under experimental conditions which are similar to the native environment[1]. This technique manipulates the electron spin of unpaired electrons within the sample. As electrons have a larger magnetic moment than nuclei, EPR is also more sensitive than NMR and also has the advantage of being highly specific. However many biological samples do not naturally contain unpaired electrons which leads to the addition of spin labels into the sample, which is common practice in biological samples[2].

Pulse EPR spectroscopy has a wide toolbox of techniques for measuring distances between paramagnetic species[3–6]. In this method, a fixed frequency, high power microwave is applied at a constant magnetic field, the shorter the pulse length, the greater the excitation bandwidth[7]. The most popular technique for distance measurements within proteins is DEER, also known as PELDOR, or pulse electron-electron double resonance, which can probe distances of ~20-80 Å. This method has been applied to numerous studies on proteins, nucleic acids and polymers[3,8,9]. Measurements determine the distances between paramagnetic centres, which can either be intrinsic or introduced externally, e.g., spin labels in proteins. Under certain conditions, DEER also encodes information on the orientation of these sites with respect to the biomolecule. Such measurements provide valuable information in addition to data gained by other methods such as NMR or X-ray crystallography[3].

Pulse EPR is analogous to NMR, however, instead of the nuclear spins, the pulses excite the spins of unpaired electrons. DEER relies on a pulse exciting ‘observer’ electron spins producing an echo due to the refocusing of Zeeman and Hyperfine interactions. Inhomogeneities due to electron-electron dipolar couplings are also refocused, however a second group of electron spins known as ‘pump’ spins are

excited by ‘pump’ pulses[10]. DEER experiments measure the amplitude of the spin echo which is produced as a function of the position of the pump pulses and the coupling between the spins leads to a modulation of the echo amplitude whose frequency is dependent on the magnitude of the coupling[11]. Milov et al. investigated the spatial distribution of alkyl radicals using Electron-Electron Double Resonance in Electron Spin Echo (ELDOR ESE)[12]. This was developed using a four-pulse sequence for measuring the signal without dead time on EPR spectrometers known as four-pulse DEER, which is now the commonly used DEER method[13].

There are many published works on the application of DEER in distance measurements. Since the work of Martin et al. which determined distances of up to 2.8 nm in TEMPO biradicals[13], Site-Directed Spin Labelling (SDSL) allowed distance measurements to be undertaken in proteins and other biological compounds which do not naturally contain paramagnetic centres. This was first tested on bacteriorhodopsin with two different spin labels being introduced[14]. Work on lysozymes[15], membrane proteins[16], RNA[17] and in-cell proteins[18] have all utilised DEER methodology to obtain distance measurements with nitroxide spin-labels being chemically linked. This is now the common method in biomolecular studies[15]. Current research also focuses on DEER distance measurements for membrane protein structures using bifunctional spin labels and Lipodisq nanoparticles[3].

However, the analysis of DEER datasets becomes problematic when the orientation selection effects become substantial. The orientation selection occurs when the pulses of the EPR pulse sequence excite only a subset of molecular orientations, which happens for pulses with a limited bandwidth and in spectra with developed anisotropy. In order to analyse the resulting measurements, one usually has to rely on model-based simulations of the experimental data. However, recently a theory has been developed that uses SH expansions to carry out model-based and model-free analysis of orientation selective DEER datasets. The approach has been applied to carry out a model-free and model-based analysis of DEER datasets for a 3.6 nm nitroxide biradical and a spin-labelled p75 protein[19]. While the results of SH-techniques to analyse the two example systems are successful and promising, it is very important to test how the SH-technique works on a wider set of data.

To this end, in this chapter we apply the SH-techniques to examine DEER datasets published earlier by other researchers. We analyse the real experimental datasets using PCA to characterise the degree to which the orientation selection affects them. Then we carry out the analysis of these datasets to obtain the distances distributions

and compare them to the published data. While the main motivation of this work is to build a basis for studies of distances in $A\beta_{(1-40)}$ peptide, the approach tested here is rather general and can be applied to pulse EPR distance measurements in other biomolecules.

5.2 Theory

5.2.1 DEER

A specific pulse sequence is used in DEER to create a refocused spin echo as shown in Figure 5.1 via the use of two distinct electron pulses, denoting the double aspect of DEER. The main concept behind the commonly used four-pulse DEER experiment, is the dephasing of the refocused echo on 'observer' spins due to their dipolar couplings to the 'pump' spins.

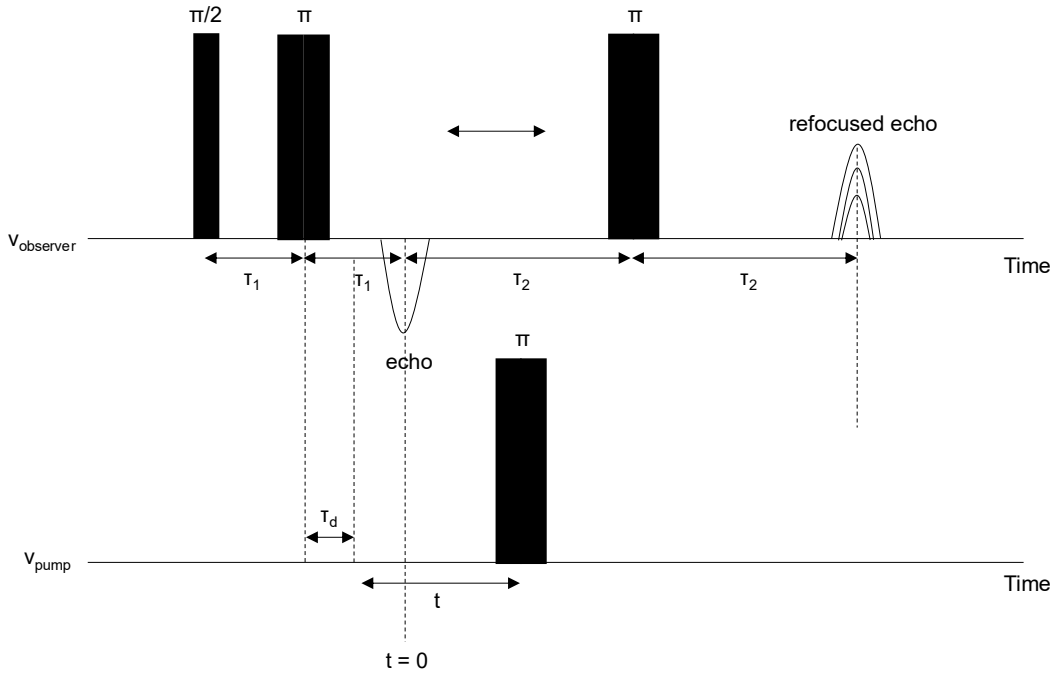

Figure 5.1 *Four-pulse DEER pulse sequence. The strength of the refocused echo is measured over time, t, which is varied.*

The 'observer' pulses excite a certain group of electron spins such that a refocused echo is formed. The 'pump' pulse has a slightly different frequency compared to the 'observer' pulse, exciting a different group of spins. The 'pump' pulse has a variable position, t, in the interval between the last two 'observer' pulses and applying the 'pump' pulse thus changes the sign of the dipole-dipole interaction and thereby results

in an incomplete rephasing of the refocused echo. The resultant dephasing curve (later referred as the DEER trace) $S_{DEER}(t)$ measures the amplitude of the refocused echo as a function of the 'pump' pulse position t[20]:

$$S_{DEER}(t) = \cos(\omega_{dd} t)\,. \tag{5.1}$$

Here ω_{dd} is the dipolar coupling:

$$\omega_{dd}(r_{i,}\theta_i) = \frac{\mu_0 g_i g_{observer} \beta_e}{4\pi\hbar} \frac{(1 - 3\,cos^2\,\theta_i)}{r_i^3} = \omega_{dd,0}(1 - 3\,cos^2\,\theta_i), \tag{5.2}$$

where θ_i is the polar angle between the external magnetic field and the directional vector $\vec{r_i}$ between the two electron spins as shown in Figure 5.2, and g_i and $g_{observer}$ are the gyromagnetic ratios of the pump and observer electron spins[19].

For a pair of spins $S = 1/2$ such as found in organic molecules such as nitroxides, the magnitude of a typical dipolar coupling is given by:

$$\frac{\omega_{dd,0}}{2\pi} = \frac{52\ \text{MHz}}{r^3(\text{nm})}. \tag{5.3}$$

For a typical duration of the a $\pi/2$ and π pulses of 16/32 ns, the excited 'observer' bandwidth is about 10 MHz, thus giving a lower distance limit measurable by DEER of $\sqrt[3]{52/10} \approx 2$ nm. The upper measurable distance limit is given by the longest realistically achievable dephasing time (up to 10 µs, giving the upper limit of about 8 nm).

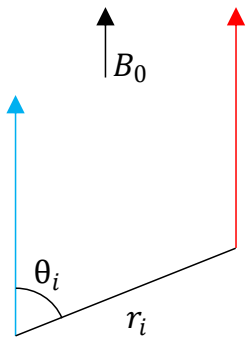

Figure 5.2 *Diagram showing the observer electron (blue) and pump electron (red) with the net external magnetic field B_0 shown*[8]*.*

Excited spins are biased to specific orientations of the spins relative to the applied magnetic field. This effect becomes more apparent at higher frequencies. As the spectral width is increased, the pulse excites a smaller fraction of the spins in a

sample. When combined with rigid labels selective sampling of spin orientations biases the dipolar frequencies in relation to their relative orientations of the spin labels. This is now known as orientational selectivity and convolutes the direct interpretation of the distance constraint from the dipolar frequency.

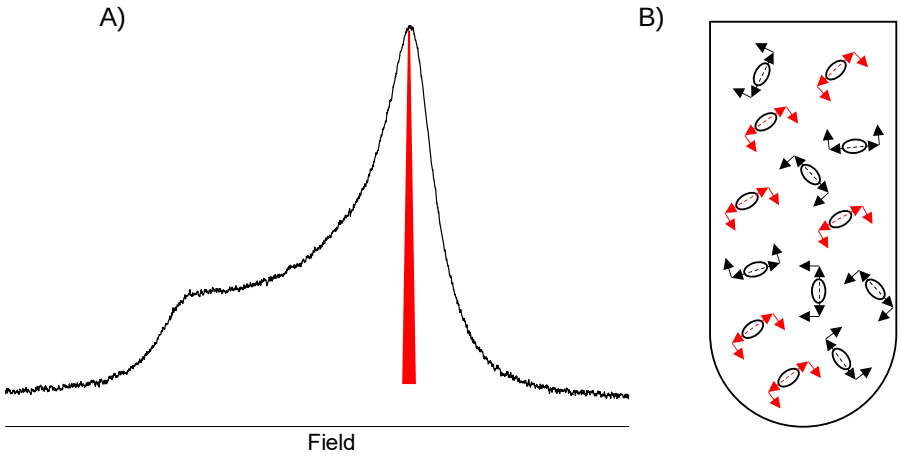

Figure 5.3 *A) Simulation of the field swept-electron spin echo spectra of a rigid spin label. The red regions represents the excitation profile of a 20 ns pulse. B) Representation of the orientation selection and how the limited excitation profile pulse can lead to a reduction of sample excitation.*

The DEER signal $S(t)$, also known as the DEER trace, arises due to an excitation of many spin pairs in the sample, some of which are in the same molecule (intramolecular contribution, $S_{intra}(t)$) and some which are in different molecules (intermolecular contribution, $S_{inter}(t)$) given by:

$$s_j(t) = \cos\left[\omega_{dd}\left(r_{j,}\theta_j\right)\right] \tag{5.4}$$

$$S(t) = \Pi_{j,all\ pairs} s_j(t) = S_{inter}(t) S_{intra}(t). \tag{5.5}$$

The summation over all intramolecular pairs can be replaced with an integration over all possible orientations of the external magnetic field. Which direction in the dipolar frame is given by a polar angle, θ, and an azimuthal angle, ϕ.

The probability a particular pair being excited can be replaced with continuous functions thus giving an intramolecular signal which can determine the distance distribution:

$$S_{intra}(t) = \frac{s(t)}{s_{inter}(t)} \tag{5.6}$$

$$= 1 - \int_0^{2\pi} d\phi \int_0^{\pi} sin\,\theta d\theta \int_0^{\infty} \lambda(\theta,\phi)\,[1 - cos(\omega_{dd}(r,\theta)t)] f(r) dr,$$

where r is the distance between the electrons, $f(r)$ is the distance distribution and $\lambda(\theta,\phi)$ is the pair excitation probability density function. A set of DEER traces, along with their associated magnetic field strengths, can be seen in Figure 5.4[19]. The pair excitation probability density function can be expanded into spherical harmonics:

$$\lambda(\theta,\phi) = \sum_{l=0}^{\infty} \sum_{m=-l}^{l} \lambda_{lm} Y_{lm}(\theta,\phi), \tag{5.7}$$

where $Y_{lm}(\theta,\phi)$ are the spherical harmonics, and l and m are the quantum numbers. The modulation depth is defined as $\lambda = \lambda_{00}$.

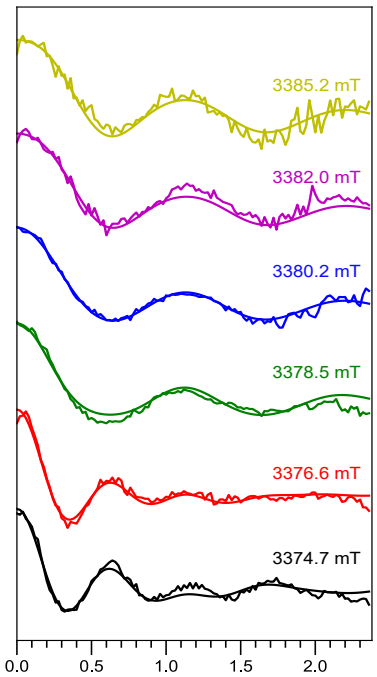

Figure 5.4 *Experimental background corrected and normalized DEER traces recorded at different magnetic fields shown, overlaid with simulations. The DEER traces were measured at the magnetic fields 3374.7 mT (black), 3376.6 mT (red), 3378.5 mT (green), 3380.2 mT (blue), 3382.0 (purple), 3385.2 mT (yellow).*

5.2.2 Finding distance and orientation information

Using SH-based theory it is possible to demonstrate that any DEER spectrum can be represented as a linear combination of the so-called Modified Pake Pattern (MPP) components:

$$\tilde{S}(\omega) = \sum_{k=0}^{\infty} w_k^{MPP} S_k^{MPP}(\omega), \tag{5.8}$$

where $w_k^{MPP} = \lambda_{2k,0}$ is always positive as it is the probability to excite any pair, which is also a weight of the k-th degree MPP component $S_k^{MPP}(\omega) = \tilde{S}_{2k,0}(\omega)$. Here MPP component weights encode orientational information exclusively.

Such mathematical treatment of orientation selection allows both the distance distribution and the MPP weights to be obtained for the experimental data, by minimizing a pair of expressions, which take into account the goodness of data fit (i.e. for a set of DEER traces with pronounced orientation selection) and the stability of the solution (i.e. stable $f(r)$ and MPP weights)[19]. In other words, the regularised solutions are sought. The expressions are minimized in steps which alternate between finding regularised solution for $f(r)$ and for MPP weights. Regularisation parameters, balancing the goodness of fit and solution stability need to be selected experimentally. The number of steps is usually taken as 1000 which is enough for the convergence of the procedure.

5.2.3 The number of MPP components

For finding both $f(r)$ and MPP weights, the sum in eq. 5.8 must be limited to some reasonably chosen threshold. This number of contributing MPP components can be evaluated in the experimental datasets using the PCA. Experimental DEER traces measured over various magnetic fields can be subject to PCA using Singular Value Decomposition (SVD). The recorded DEER traces are treated as a linear combination of PCs, with N traces resulting in N principal components with contributing weights. Figure 5.5 shows the six PCs extracted from the six DEER traces shown in Figure 5.4.

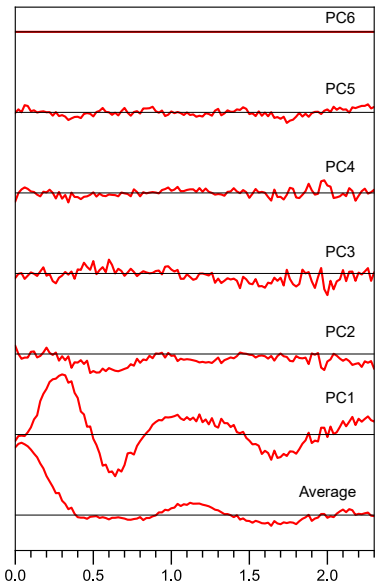

Figure 5.5 *PCA of the DEER data. The average trace and principal components are shown (red) as well as the zero offsets (black).*

Any DEER trace, and therefore the PCs themselves, can be described by some linear combinations of MPP components. Therefore, the overall number of PCs distinguishable from the noise level should be equivalent to the number of MPPs. In the example shown in Figure 5.5, only the first three principal components are distinguishable from the noise level[19]. This means that three MPPs of the highest degrees are expected to contribute.

As follows from the SH-based theory outlined in ref. 16, the number of contributing MPP components should be higher for more rigid structures where the orientations of the two paramagnetic moieties is well defined, e.g., in rigid biradicals. Also, the number of contributing MPP components should be higher when the bandwidth excited by a μw pulse is smaller, which is usually the case for EPR at higher fields.

5.3 Method

5.3.1 Data scraping and collection

No data was experimentally collected for the purpose of this chapter. Some datasets were obtained from the authors who have carried out the work. When no original data could be obtained, the datasets were scraped from the published articles. All scraped data was sourced and obtained using the following procedure:

- WebPlotDigitizer was used to extract points from the uploaded DEER trace graphs from published work with an accuracy of one point per two pixels. This was scraped

with arbitrary amplitude, which was then normalised so that zero was the point at which the DEER traces converge by the end of their time axis.

- If necessary, manual point selection was used, this produced non-uniform point distribution which needed to be rectified. A cubic spline script was produced which used piecewise third-order polynomials which pass through a certain number of control points. This produced a point every 1 ns[21].

All raw and scraped data was normalised before distance distribution analysis.

As a test, the DEER data in Figure 5.4 was scraped in the manner described above. The resulting scraped dataset is shown in Figure 5.6. The data is normalized so that there is a maximum at one, and the traces level off at zero.

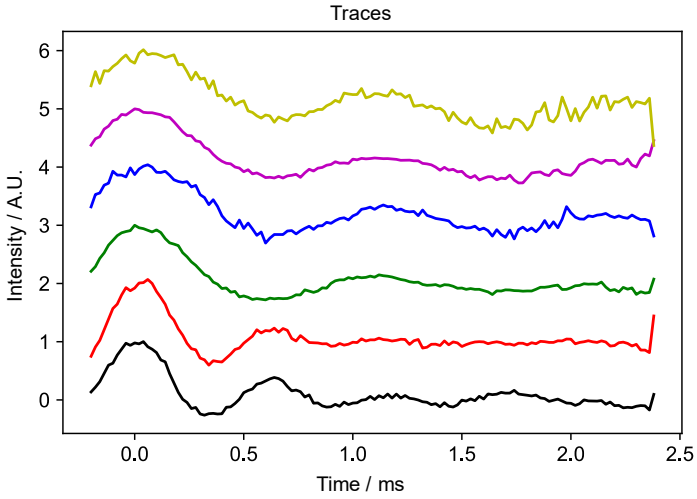

Figure 5.6 *Traces produced by python script after cubic spline program for the DEER dataset. Some traces tend towards infinity at the end of their time axis.*

Here, the end points tended to infinity. This is likely due to the limitation in the python cubic spline method which is discussed in Section 5.3.4. Other than these deviations, Figure 5.6 matches the traces produced in Figure 5.4, indicating that the method of cubic spine and data scraping works correctly.

5.3.2 Principal Component Analysis

PCA carried out on the datasets like the one shown in Figure 5.6 was carried out, giving the PCs, shown in Figure 5.7A), and their contributing weights.

In order to achieve PCA the DEER data needs to be placed into an *m x n* matrix, where *m* is the number of signal traces and *n* is the number of points taken in these traces, where the matrix itself is known as X. SVD is achieved by decomposing X into the products of three other matrices.

As X is an *m x n* matrix, $X^T X$ is a square, symmetric *m x m* matrix:

$$(X^T X)\hat{\upsilon}_i = \lambda_i \hat{\upsilon}_{i,} \tag{5.9}$$

where $\hat{\upsilon}_i$ is the set of orthonormal *m x* 1 eigenvectors with associated eigenvalues λ_i. The singular values σ_i are defined so that $\sigma_i = \sqrt{\lambda_i}$. The *n x* 1 vectors $\hat{u}_i$ can be defined:

$$\hat{u}_i \sigma_i = X\hat{\upsilon}_{i.} \tag{5.10}$$

This allows new matrices to be constructed by summarising in one matrix multiplication. **Σ** is a diagonal *m x n* matrix, meaning its only non-zero values are along the leading diagonal. **Σ** contains the singular values σ_i in diagonally ascending order. the matrices V and U are unitary, singular and are constructed from the sets of orthogonal vectors $\hat{\upsilon}_i$ and $\hat{u}_i$ added with additional vectors such that all their values are non-zero, dealing with degeneracy issues.

X can therefore be decomposed into the products of U, **Σ** and the transpose of V as shown:

$$X = U\Sigma \mathrm{V}^T, \tag{5.11}$$

where U contains fundamental values which are properties of X, ordered in terms of their ability to describe the variance of the columns of X. The columns of the transpose of V give the mixture of all U that makes up each corresponding column of X. The singular values contained in **Σ** correspond to the respective trace in X – these describe how correlated the coefficient U is with X.

Due to the diagonality of **Σ**, expanding equation (5.11) by index notation gives:

$$X = \sigma_1 U_1 V_1^T + \sigma_2 U_2 V_2^T + \ldots . + \sigma_m U_m V_m^T, \tag{5.12}$$

with all other components being 0.

If there are some σ_1 such that $\sigma_1 \gg \sigma_j$ where both $\sigma_1$and σ_j are some singular values and i $\neq j$, σ_j can be considered negligible. In this case, the only remaining terms from equation 5.12 are the components that impact the traces stored in X, known as the PCs[22].

The process of PCA allows the determination of which traces contribute significantly to the overall data. This provides information on how many MPP degrees are required to describe the traces. A higher degree of MPP components have smaller contributions[19].

As seen on the Figure, there are only a few components that are indistinguishable from noise and carry the most meaningful contribution to the signals. In order to demonstrate this, the signals were back calculated based on only a few most important components.

As shown in Figure 5.7B), with increasing number of principal components, the fit to the traces becomes more represented. However, with three traces, the principal components represent the original traces of the DEER dataset well. The data can be seen to have only three principal component curves, as the improvement towards the DEER traces between three components and four is negligible, hence it appears here that only three principal components are relevant.

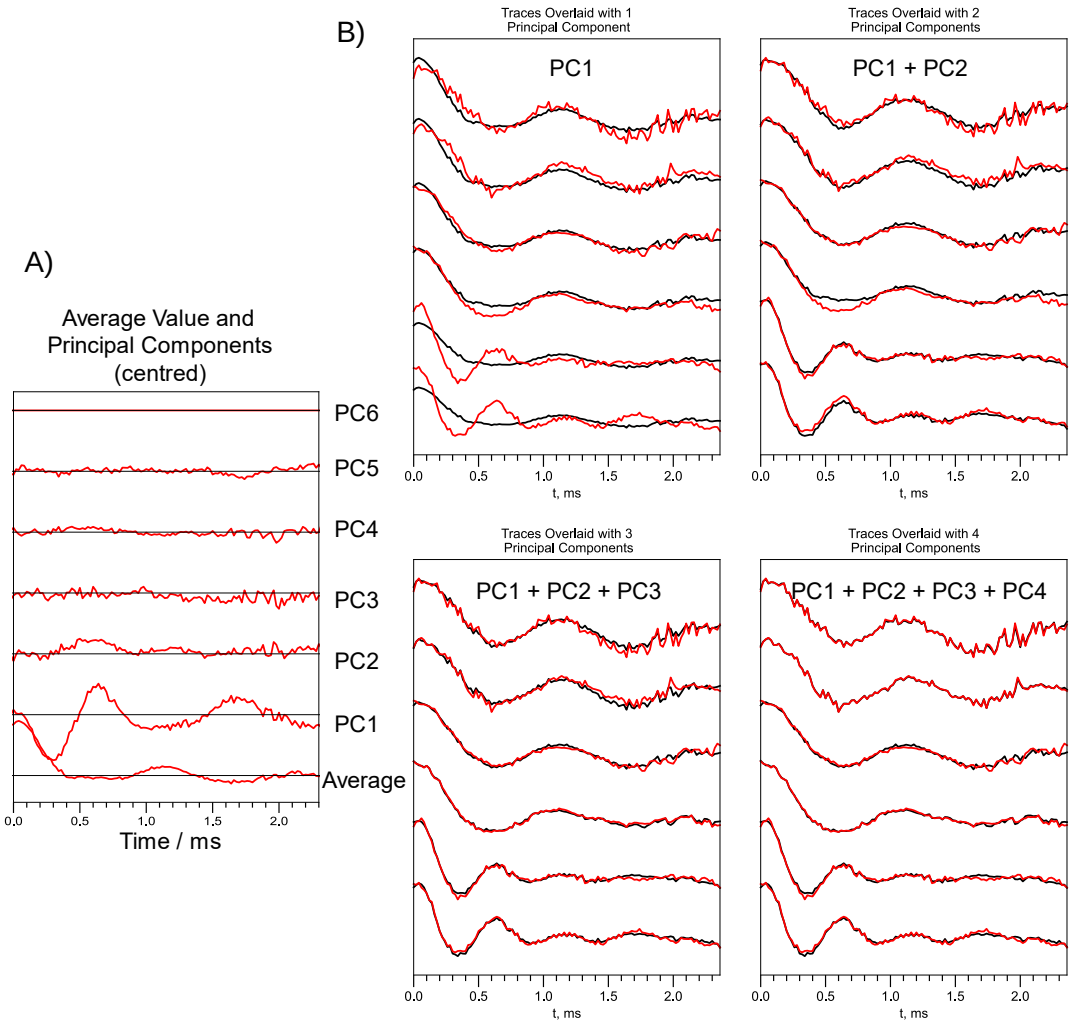

Figure 5.7 *A) Principal components produced from the DEER dataset. The centred average value (bottom trace) and principal components (red) with decreasing contribution (bottom to top) are plotted against time. B) DEER data reconstruction using incomplete sets of principle components. Varying numbers of principal components curves plotted (black) overlaid with the combined DEER traces using DEER dataset (red).*

5.3.3 Noise and moving average analysis

To evaluate the number of required PCs accurately and thereby evaluate the number of MPP components, a simple criterion was used. The traces were first subject to moving average analysis. Each PC was fitted with a 10 or 100-step moving average, based on the dataset size. This was then used to produce the noise within each component and produce two-times the Standard Deviation (SD) of the noise value for each component. The maximum value of the moving average minus the mean of the moving average value was also calculated. These two values for each component

allowed a more quantitative assessment of the significant PCs. For example, with the DEER dataset, the noise analysis is shown in Figure 5.8.

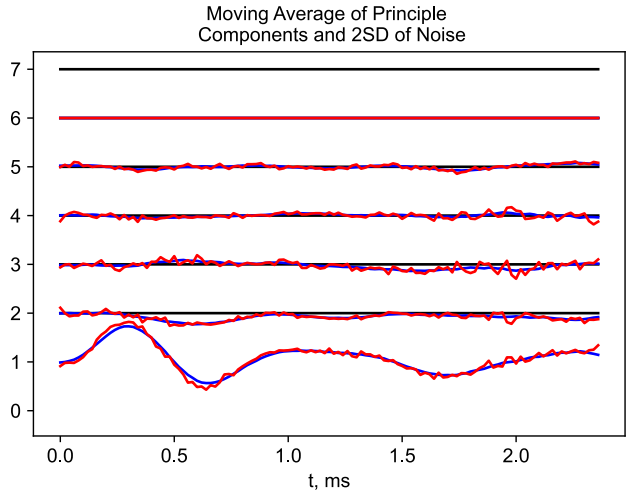

Figure 5.8 *Noise analysis based on the centred PCs of the DEER dataset and the six traces. PCs of the DEER dataset traces (red) and ten-point moving average of the PCs (blue).*

As described, the noise calculations are also shown from the DEER dataset in Table 5.1.

Table 5.1 *Noise analysis calculations of each PCs showing two-times SD of the noise and the moving average max value of each component minus the mean of the moving average. PC are said to contribute to the data when their values are not close to zero.*

	2SD of noise	**Moving average max value – mean of moving average**
PC1	0.12	0.66
PC2	0.085	0.15
PC3	0.12	0.12
PC4	0.098	0.066
PC5	0.058	0.080
PC6	9.98e-17	5.80e-17

Looking at the Figures shown in Table 5.1, three principal components are said to contribute to the overall DEER dataset. This agrees with the visual breakdown of components as shown in Figure 5.7B). Once the PCA is complete it is then possible to conduct distance distribution analysis based on the number of principal components.

5.3.4 Distance distribution

Once the PCA was performed, distance distribution analysis can now be done and plotted to find the distance between coupled electrons. The number of MPP degrees, which corresponds to the number of PCs, was used for truncating the sum in eq. 5.8. The program, based on the algorithm developed and implemented in Python by Dr Potapov in reference 16, follows an iterative minimisation algorithm for finding the distance distribution, $f(r)$, and the MPP weights, w_k^{MPP}, which considers both the goodness of fit and the solution stability[19]. The initial guess for $f(r)$ is a gaussian distribution of a specific distance, which is the sensitive DEER radius. The algorithm used then runs for 1000 iterations where convergence is achieved.

An example distance distribution plot allowing the distance between a spin pair to be determined as shown in Figure 5.9.

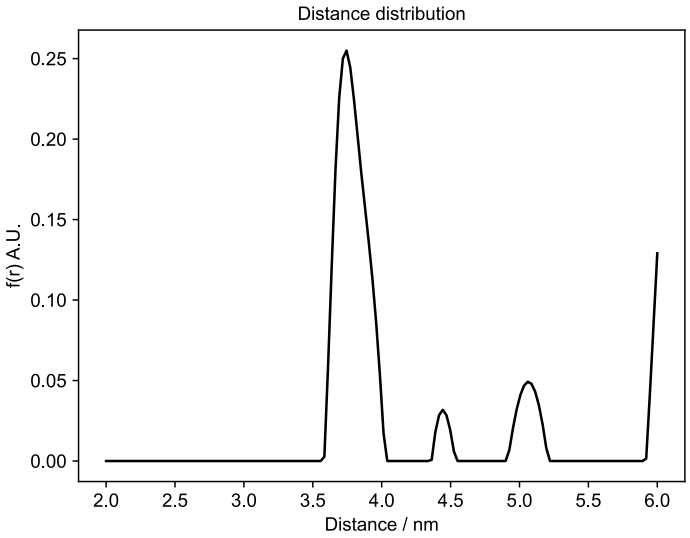

Figure 5.9 *Distance distribution obtained from the DEER dataset in Figure 5.5, using three PC.*

The main peak shows the distance between the electron spin pair, which from Figure 5.9 is taken to be 3.74 nm. The published literature states the distance between the two nitroxide labels to be 3.75 ± 0.13 nm[19] highlighting the accuracy of the procedure. Unlike the main peak at 3.74 nm, other peaks are spurious and have a large error associated with them and change in position/intensity with the change of regularisation parameter. In this and further analysis the regularisation parameter was found by experimentation by seeking a trade-off between the goodness of fit and the stability of the found solution.

There is an extra step in the method in chapter 5 to improve the accuracy of the distance measurements based on the PCA. The algorithm contains a η value, known as the regularisation parameter which was found experimentally. The η value is varied between 0.1-30 producing small changes in the goodness of fit and the stability of the found solution and produces a residual norm and solution norm value. Plotting each of these two Figures over the range of η values allows a L-curve to be created. The L-curve produced from the DEER dataset is shown in Figure 5.10.

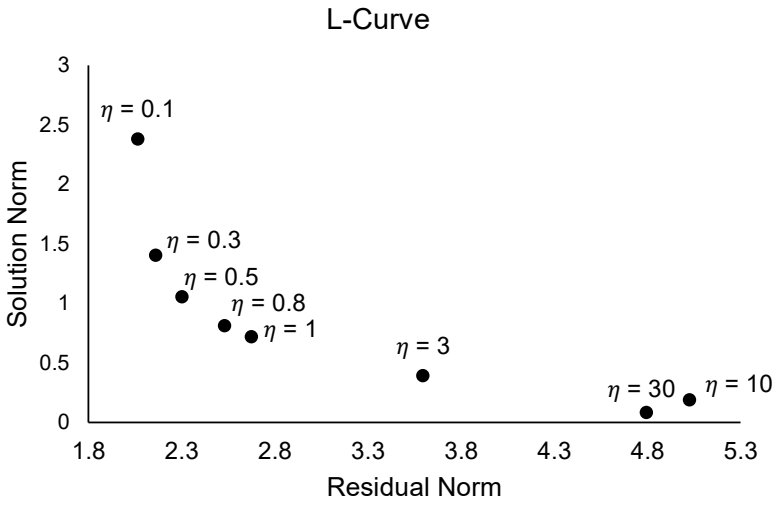

Figure 5.10 *L-curve of the DEER dataset produced by changes to the η value. The number of principal components is chosen based on PCA and the η value is varied between 0.1-30.*

The distance distribution is said to be more accurate when the residual and solution norm is closest to 0, or the left most corner of the graph. In this case this is taken to be 0.8.

The convergence and distance distribution for the DEER dataset is shown in Figure 5.11 with a η value of 0.8. Changing the η value may prove valuable in later datasets.

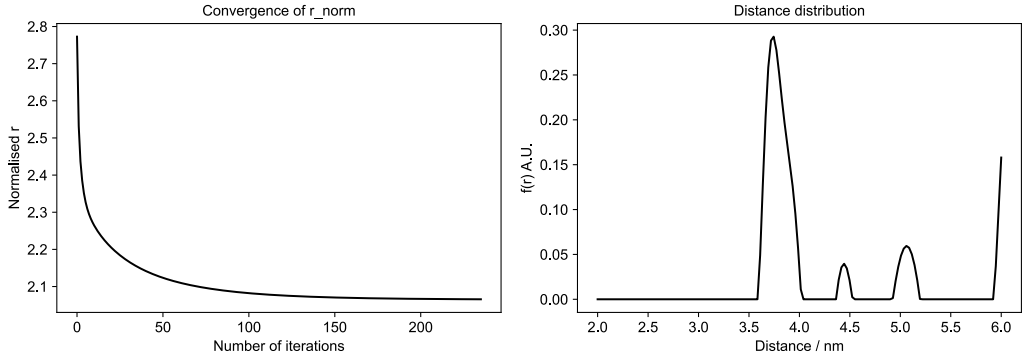

Figure 5.11 *Convergence and distance distribution of the DEER dataset with the η value of 0.8. The distance distribution is taken to be 3.74 nm.*

Based on the distance distribution produced using the η value of 0.8 a distance between the two nitroxide spins is shown to be 3.74 nm. This method was applied to all datasets to increase the accuracy of the distance distribution.

These methods were then transferred to 27 scraped datasets from published work[9,23–36] and 15 sets of raw data obtained from the author, comparing the distance distribution after PCA and the published result.

5.4 Results

5.4.1 Results from scraped data

On initial analysis, for most of the datasets, the majority show that a good fit to the traces can be achieved with only two principal components, as shown in Figure 5.12. Each dataset shows the totoal number of traces overlaid with only two PCs.

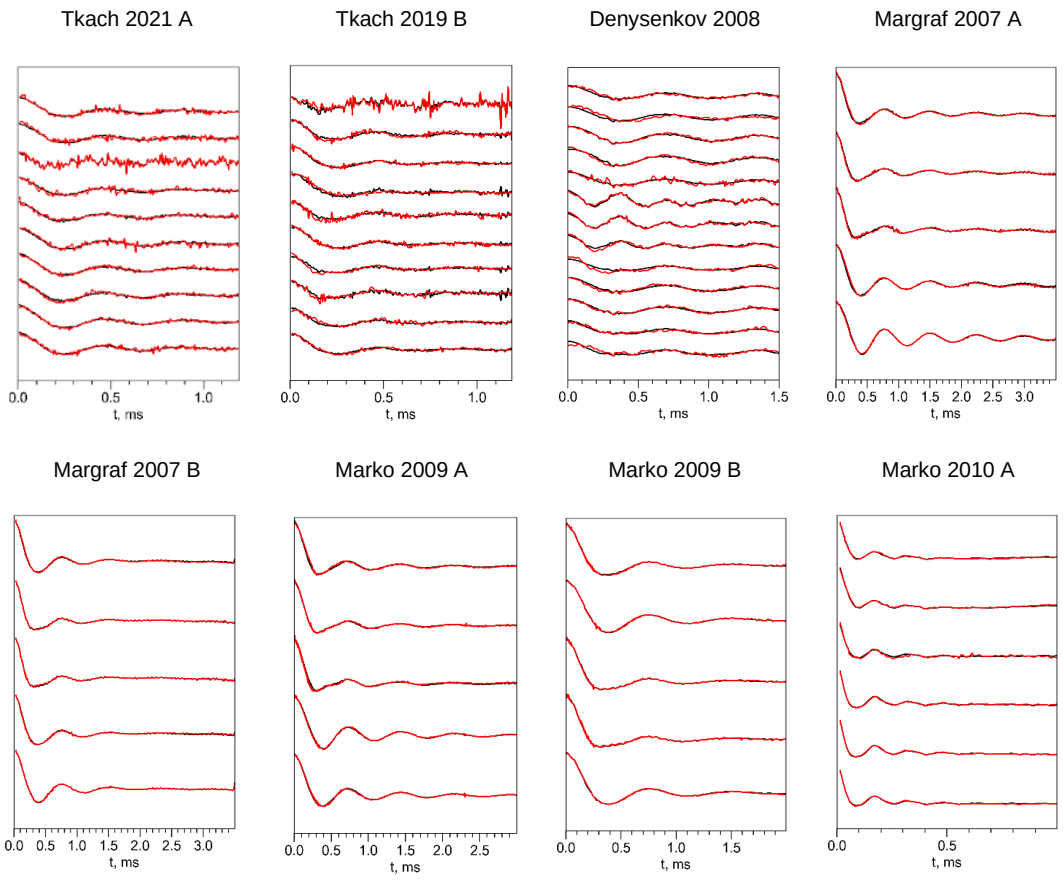

Marko 2010 B

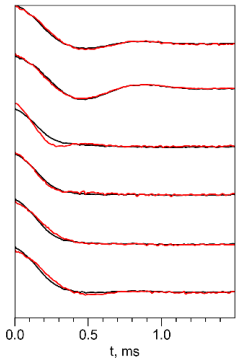

Abe 2012

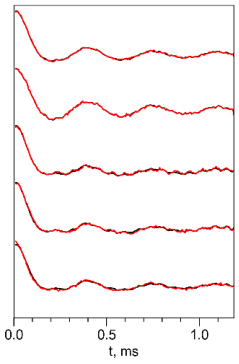

Marko 2013

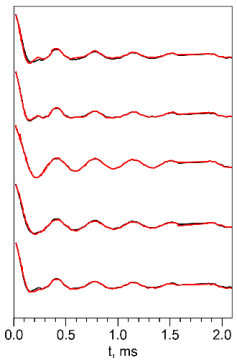

Yang 2012 A

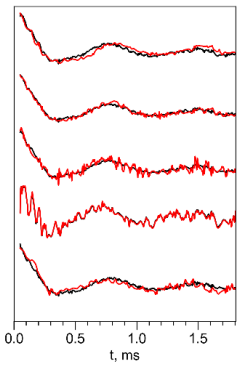

Yang 2012 B

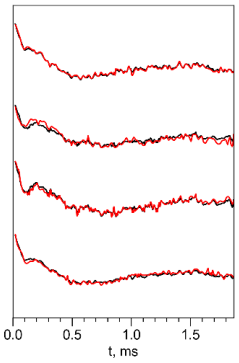

Roessler 2010

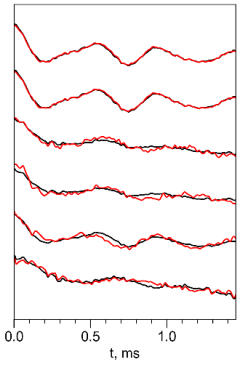

Abdullin 2015 A

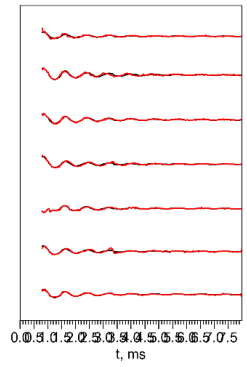

Abdullin 2015 B

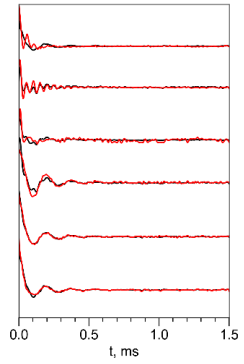

Abdullin 2015 C

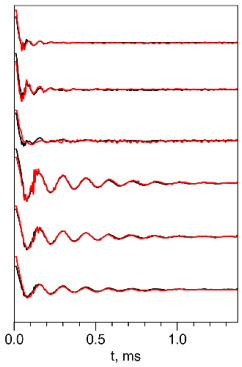

Bowen 2016 A

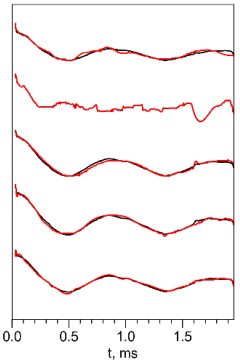

Stevens 2016 A

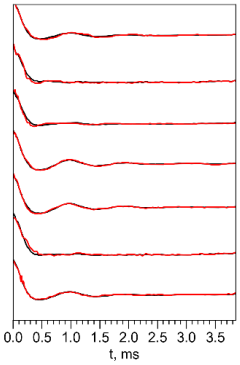

Stevens 2016 B

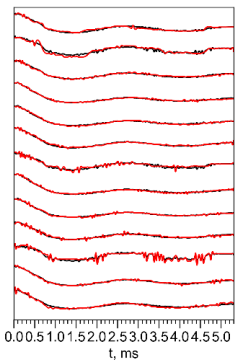

Jarvi 2018

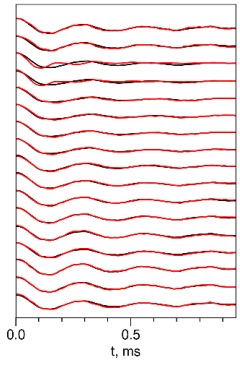

Tkach 2013 A

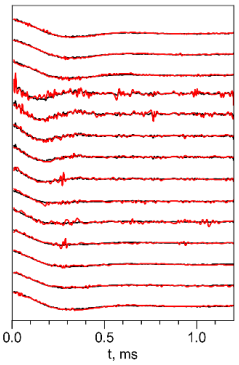

Tkach 2013 B

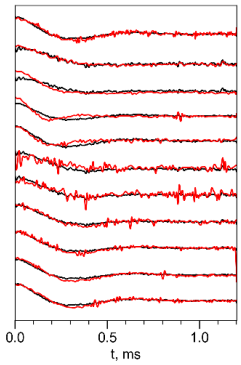

Tkach 2013 C

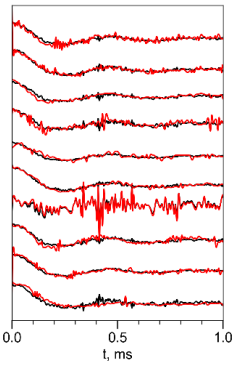

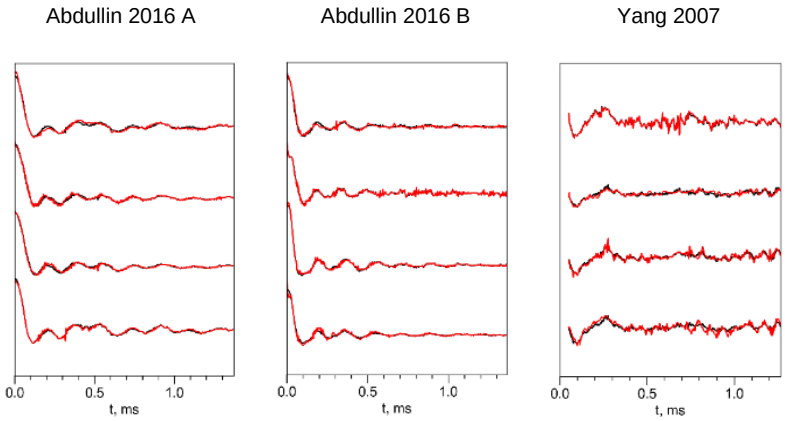

Figure 5.12 *PC curves plotted with two PCs (black) overlaid with the combined traces for all datasets (red). As shown, the majority of the data can be represented in all datasets with only two principal components*.

Although most datasets have a good fit to the traces with only two PCs, PCA was done for each dataset to conclude a more accurate number of PCs. The datasets were analysed following the same methods as described in Section 5.2. In some cases, noise or artifacts produced from the data scraping process were removed by cutting points within the data. In the datasets, the final PCA showed a varying number of contributing PCs that need to be present in order to fit the traces well. Finally, once PCA was completed, distance distribution analysis was undertaken. The results for PCA and distance measurements for all the scraped datasets can be shown in Table 5.2. No datasets required all principal components.

Table 5.2 *Distance distribution results from all scraped datasets. Distance distribution was taken following the methods presented in the DEER dataset compared with the distance analysis extracted from the published work.*

Author year	**PC / Number of traces**	**Distance from analysis, nm**	**Distance from paper, nm**
Tkach 2021[23]			
A	2/10	2.77	2.8±0.2
B	3/10	3.43	2.8±0.2
Denysenkov 2008[29]	3/13	3.92	3.25
Margraf 2007[30]			
A	2/5	3.33	3.30
B	1/5	3.24	3.40
Marko 2009[31]			
A	2/5	3.29	3.30±0.2

B	2/5	3.20	3.30±0.2
Marko 2010[32]			
A	2/6	2.48	2.50
B	3/6	3.39	3.40
Abe 2012[33]	2/5	2.64	2.65±0.1
Marko 2013[34]	3/4	3.31	3.30
Yang 2007[35]	2/4	2.20	2.2±0.3
Yang 2012[36]			
A	1/5	3.31	3.50±0.1
B	3/4	2.13	2.20±0.2
Roessler 2010[24]	3/6	3.58	3.30
Abdullin 2015[25]			
A	1/7	3.21	3.46±0.06
B -strong exchange	4/6	2.58	1.8±0.02
C	4/6	2.42	1.94±0.03
Bowen 2016[9]	2/5	3.55	3.60
Stevens 2016[26]			
A	3/7	3.70	~3.5 (read from graph)
B	2/13	5.1	~5 (read from graph)
Jarvi 2018[27]	2/17	2.40	2.40
Tkach 2013[28]			
A	2/14	3.10	3.1±0.3
B	4/11	3.15	3.1±0.3
C	3/10	3.4	2.8±0.2
Abdullin 2016[37]			
A	2/4	2.1	2.25
B	2/4	2.08	2.1

Figure 5.13 shows the data presented in Table 5.2 presented for easy comparison between the published distance measurement between the spin pair and the distance measurement obtained from the PCA of the scraped data.

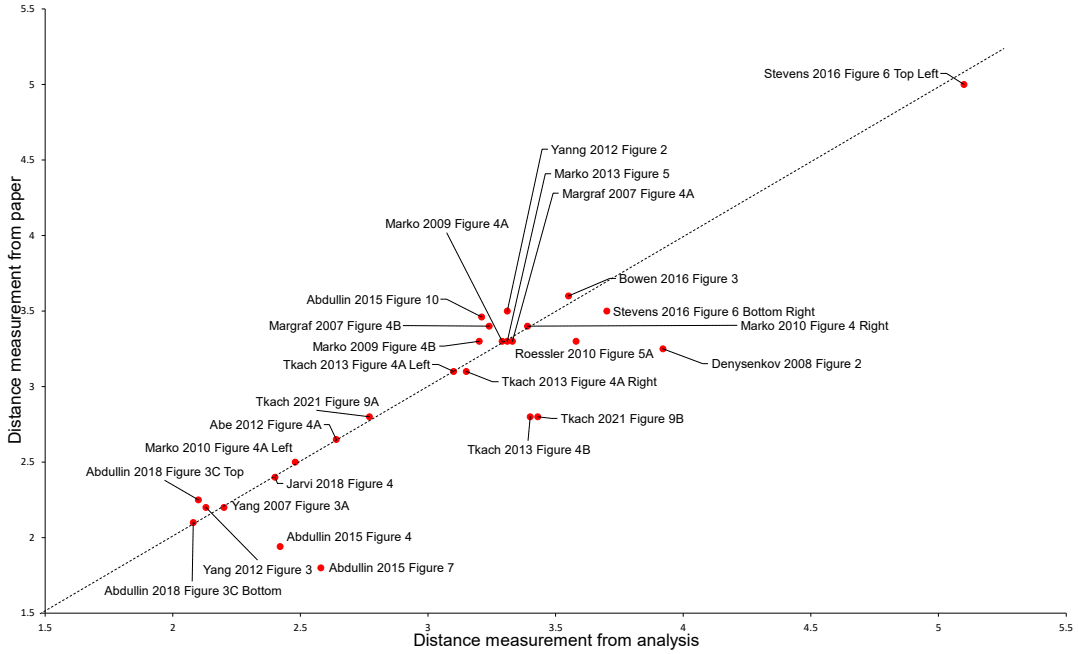

Figure 5.13 *Correlation between the distance between a spin pair in published work and the measured distance distribution after PCA in all scraped datasets. The dashed black line shows the exact match between published and scraped data distance measurements. Based on the datapoints of each dataset (red) compared to the exact match line, the PCA provides reliable measurements for the distance between a spin pair.*

Results for the distance distribution analysis from the raw data obtained from the authors is presented in the next section.

5.4.2 Results from raw data

The results for the PCA of all the raw data are shown in Table 5.3, which also shows the comparison to the PCA presented in Table 5.2. The datasets were analysed following the same methods as the DEER dataset and the scraped data. No data points were removed due to the lack of artifacts being introduced during the scraping procedure.

Table 5.3 *Results from the PCA of the 15 raw datasets showing comparisons to the scraped data PCA. As shown, only a small number of principal components are needed to produce a good fit to the traces.*

Author/Year	PC / Number of traces from raw data	PC from scraped data
Abdullin 2015		
A	2/7	1/7
B -strong exchange	1/6	4/6
C	1/6	4/6
Abdullin 2016		
A	2/4	2/4
B	2/4	2/4
C	2/4	-
D	2/4	-
E	2/4	-
Stevens 2016		
A	1/7	1/7
B	2/13	2/13
Tkach 2021		
A	1/12	2/10
B	1/11	3/10
Tkach 2013		
A	1/14	2/14
B	1/11	4/11
Abe 2012	1/6	2/5

For all of the datsets, PCA showed a varying number of contributing PCs to fit the traces well. As with the scraped data, no datasets require all PCs as shown in Table 5.2. In several cases, less PCs are required to fit the traces from the raw data compared to the scraped data.

As with the scraped data, once PCA was completed on the raw data, distance distribution analysis was undertaken. The results for all the scraped datasets can be shown in Table 5.4.

Table 5.4 *Distance distribution results from all raw datasets. Distance distribution was taken following the methods presented for the DEER dataset. Distance Distributions are also compared with the distance analysis extracted from the scraped data and published work.*

Author/Year	**Distance from analysis / nm**	**Distance from scraped data / nm**	**Distance from the publication / nm**
Abdullin 2015[25]			
A	3.47	3.21	3.46±0.06
B	1.35	2.58	1.8±0.02
C	1.96	2.42	1.94±0.03
Abdullin 2016[37]			
A	2.13	2.1	2.25
B	2.1	2.08	2.1
C	2.02	-	~2
D	3.07	-	3.25
E	2.24	-	2.25
Stevens 2016[26]			
A	3.48	3.7	3.7
B	4.87	5.1	~5
Tkach 2021[23]			
A	2.8	2.77	2.8±0.2
B	2.79	3.43	2.8±0.2
Tkach 2013[28]			
A	3.1	3.1	3.1±0.3
B	3.1	3.15	3.1±0.3
Abe 2012[33]	2.61	2.64	2.65±0.1

Figure 5.14 shows the data presented in Table 5.4 overlaid with Figure 5.13 comparing the published distance measurement between the spin pair and the distance measurement obtained from the PCA of the scraped and the raw data.

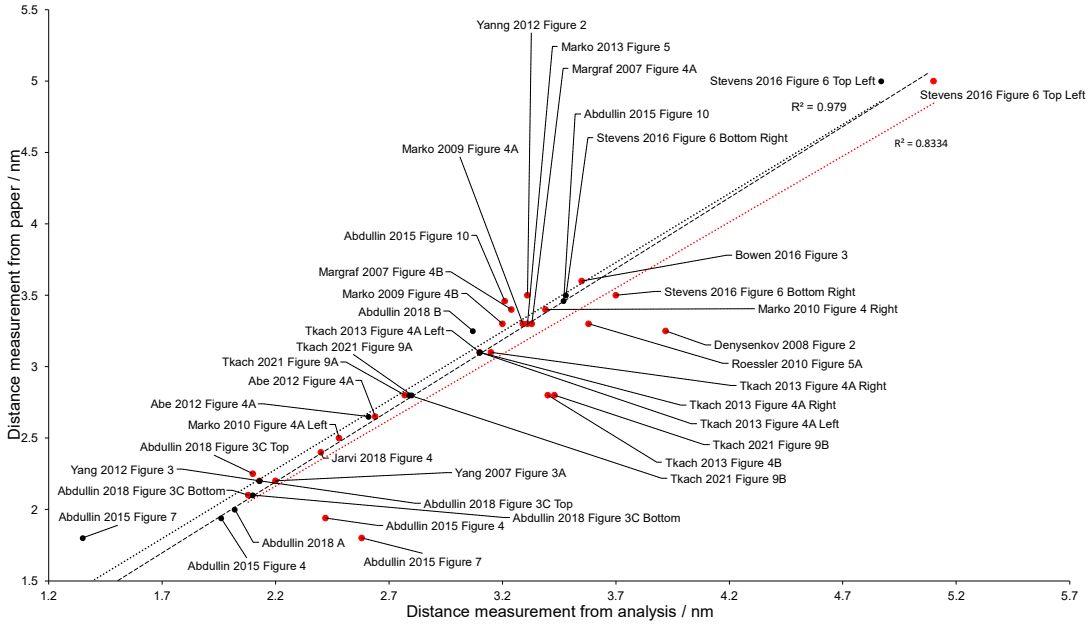

Figure 5.14 *Correlation between the distance between a spin pair in published work and the measured distance distribution measured after PCA in all raw (black dots) and scraped datasets (red dots). The dashed black line shows the exact match between published and scraped data distance measurements. The R^2 value of the raw data and scraped data is also shown. Lines of best fit for the two datasets, raw and scraped data, are shown by red and black dotted lines respectively.*

5.5 Discussion

5.5.1 Error analysis

In order to test the accuracy of obtaining the distance measurement using our approach, the obtained values were compared with those in the published work. Figure 5.15 shows the published data values compared to the values obtained from the distance distribution analysis after PCA of both scraped and raw datasets. Error bars represent the values from the published literature.

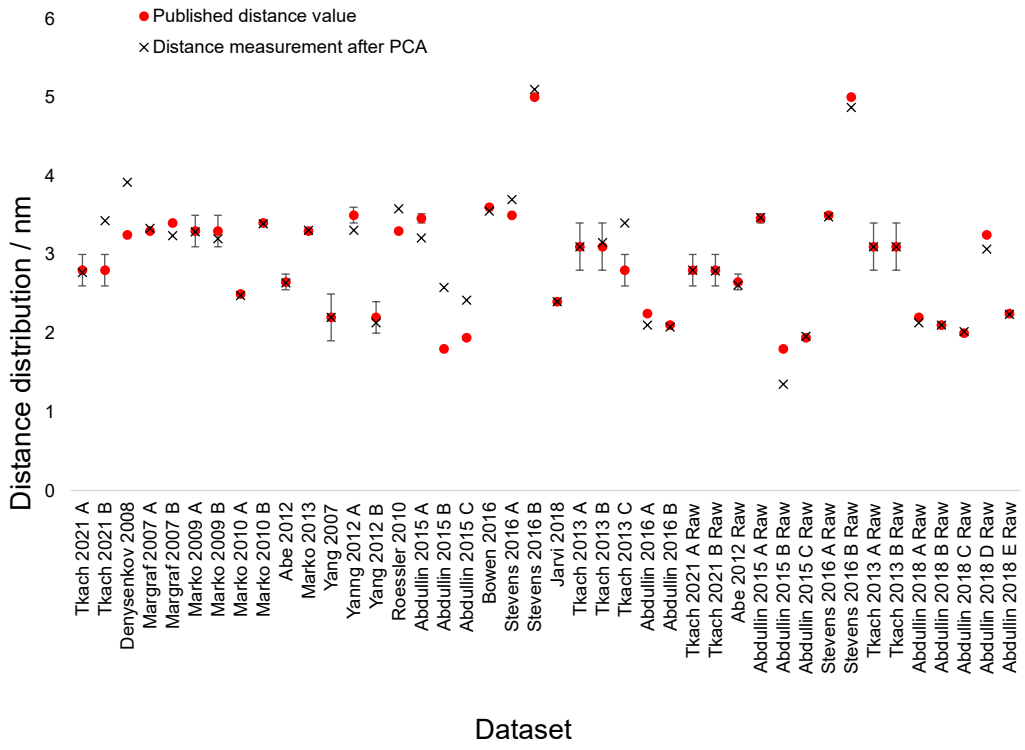

Figure 5.15 *Comparison between the distance values taken from the published work and those distances produced by the distance distribution analysis after PCA for the raw and scraped datasets.*

For the ease of this analysis, those datasets where the published data did not state an error were removed from the analysis. For all datasets combined, the percentage of the data within the error is 68%. For the scraped data only, this is reduced to 57%, while the raw data alone shows a percentage of 82%. This demonstrates that performing the PCA and distance analysis on raw data produces the most accurate result compared to that of the published data.

5.5.2 Rigidity and EPR field strength

In order to test the hypothesis between rigidity and the number of PCs, it is first necessary to check the correlation between the magnetic field strength applied in the EPR experiments, and the number of principal components to traces. Figure 5.16 Shows the relationship between the frequency and the number of PC curves. Three sets of correlations can be seen which includes the scraped datasets, the raw datasets and all the datasets combined.

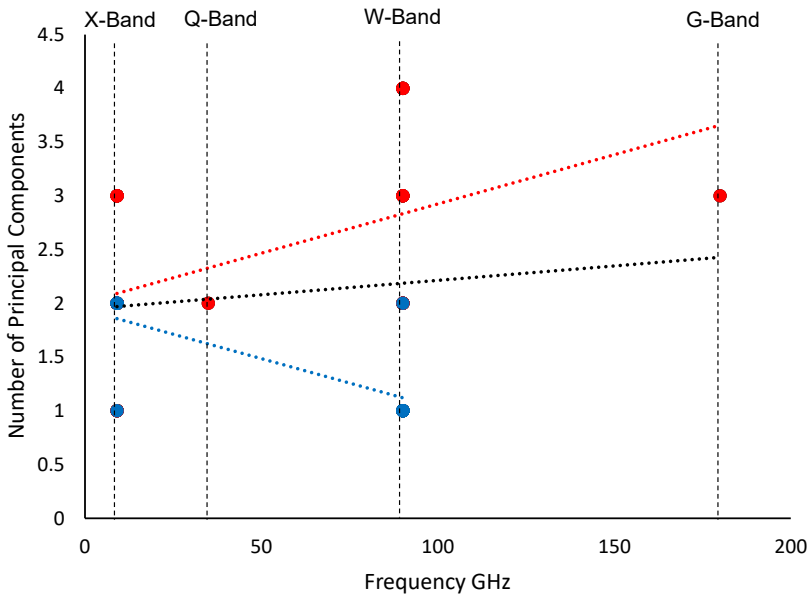

Figure 5.16 *Graph of the number of principal components against the frequency, with specific band frequencies shown (dashed lines). Three sets of data are shown with the line of best fit (dotted lines), scraped data (red), raw data (blue) and combined data (black).*

There graph shows a negative correlation between the number of principal component curves and frequency, with raw datasets and a positive correlation of scraped and combined datasets. The raw datasets contrast the theory which suggests that DEER traces taken at higher-field excitation should also produce a higher number of significant PCs contributing to the dataset, due to a tighter excitation of orientation subsets. However, the rigidity of the biradical also needs to be assessed to fully test the hypothesis.

Some of the papers contained information about the rigidity of the biradicals used or contained structural diagrams which could be used to determine the rigidity. Table 5.5 below shows the rigidity of the biradicals used in the published work for the scraped and raw data.

Table 5.5 *Table showing the rigidity of each biradical used in the published literature of the raw and scraped data. The number of PCs to the number of traces is also shown.*

Author year	**PC / Number of traces**	**Rigidity**
Scraped Data		
Tkach 2021		Semi-rigid
A	2/10	
B	3/10	

Denysenkov 2008	3/13	Rigid
Margraf 2007		
A	2/5	Rotates freely
B	1/5	More rigid
Marko 2009		
A	2/5	Rotates freely
B	2/5	More rigid
Marko 2010		Rigid
A	2/6	
B	3/6	
Abe 2012	2/5	Restricted flexibility
Marko 2013	3/4	Rigid
Yang 2007	2/4	Flexible
Yang 2012		Weak orientational selectivity
A	1/5	
B	3/4	
Roessler 2010	3/6	Rigid
Abdullin 2015		
A	1/7	Rigid
B -strong exchange	4/6	Rigid
C	4/6	Less rigid
Bowen 2016	2/5	Rigid
Stevens 2016		Rigid
A	3/7	
B	2/13	
Jarvi 2018	2/17	Rigid
Tkach 2013		
A	2/14	Rigid
B	4/11	Rigid
C	3/10	One axis of rotation
Abdullin 2016		Limited orientation selectivity
A	2/4	
B	2/4	
Raw data		
Abdullin 2015		
A	2/7	Rigid
B -strong exchange	1/6	Rigid
C	1/6	Less Rigid

Abdullin 2018		Limited orientation selectivity
A	2/4	
B	2/4	
C	2/4	
D	2/4	
E	2/4	
Stevens 2016		Rigid
A	2/13	
B	1/7	
Tkach 2021		Semi-rigid
A	1/12	
B	1/11	
Tkach 2013		Rigid
A	1/14	
B	1/11	
Abe 2012	1/6	Restricted flexibility

Figure 5.17 shows the structures of the flexible and more rigid biradicals used in Markgraf's published work[30].

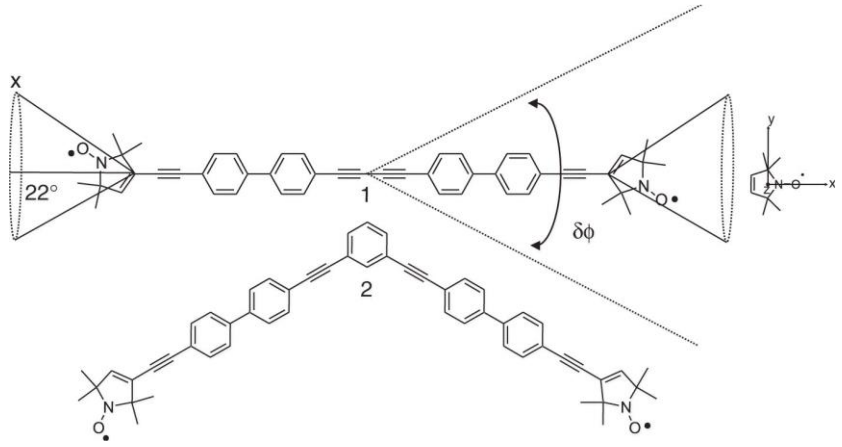

Figure 5.17 *Structures of the biradicals used in Margraf's published work. 1) Flexible biradical. The nitroxide radicals are assumed to rotate freely around their acetylene bond (cone with angle 22°) and the mobility of the bridge is described by a single bending motion with a Gaussian distributed width δφ.2) More rigid biradical.*

In the case of Margraf, the number of contributing PCs is two and one for the flexible biradical and the more rigid biradical respectively. The more rigid biradical has a lower number of PCs than that of the flexible biradical disagreeing again with the hypothesis

that more rigid biradicals produce a higher number of contributing principal components.

For the purpose of this analysis, only flexible and rotates freely biradicals were considered as flexible. The remaining datasets were considered rigid. The average number of contributing PCs are shown in Table 5.6 for flexible and rigid biradicals in the scraped, raw, and combined data.

Table 5.6 *The number of contributing PCs for flexible and rigid biradicals in scraped, raw and combined data.*

	Flexible	**Rigid**
Scraped Data	2	2.46
Raw Data	-	1.47
Combined Data	2	1.97

As no raw datafiles for flexible biradicals were obtained this could not be assessed. For the scraped data, the number of contributing PCs is higher in rigid biradicals, with a value of 2.46 in rigid and 2 for flexible biradicals, agreeing with the hypothesis laid out in Section 5.2. However, with all the scraped and raw datasets combined, a greater number of components is required with flexible biradicals than rigid biradicals, contradicting the hypothesis, although the difference between the two is small. More datasets from flexible biradicals will need to be analysed in order to fully assess this conclusion.

Original work by Dr Potapov formed the basis for a method of disentangling the distance and orientation information from the DEER dataset using a model biradical with slight flexibility in the rigid linker. This thesis work has now proven that the method can be applied to a range of biradical models in a range of systems at different magnetic field strengths. The method is therefore not limited by biradical flexibility as initially assumed. This will then allow the method to be applied to an even wider class of systems, not just the models presented within this thesis work.

5.6 Conclusion and Outlook

A wide selection of published work was reanalysed by PCA and distance distribution analysis, either by obtaining scraped or raw datasets. This included a variety of

biradical with varying levels of flexibility. In all cases the number of PCs required to fit the overall traces was less than the number of overall components, highlighting that not all the PCs are required in order to accurately replicate the data. This allowed the distance distribution analysis to be undertaken. For the published literature which contained an error, 68% of the distance measurements from all data fell into this limit, with 57% of scraped data being within the error limits and 82% of the raw data. Conducting analysis on the raw data provided more accurate distance measurements compared to the published work than the scraped data. This work provides the basis for distance measurements across a variety of samples, wider than initially thought, including a varying level of flexibility of biradicals.

Removing datapoints to reduce noise and remove points at the beginning and the end of traces, in cases where they tend to infinity, was necessary in some datasets. This gave an overall more accurate distance measurement compared to the published literature and a closer fit of the principal components to the trace while using less components compared to data containing those points. This seems to be an error introduced from the data scraping process as no raw data file required modification.

Agreeing with the hypothesis that a higher number of principal components is required at higher field strength, scraped datasets show a positive correlation between number of principal components and the excitation frequency. In contradiction to this, the raw datasets show a negative correlation. For the combined data this also showed a positive correlation. Assessing the flexibility of the biradicals it was found more PCs were needed with rigid biradicals than flexible in scraped datasets, agreeing with the hypothesis that more PCs are required for rigid structures, with the opposite trend in all scraped and raw datasets combined.

In order to fully assess the accuracy of the analysis, more datasets need to be analysed, including raw data of flexible biradicals as well as G-band raw datasets. The structure of each individual biradical should be fully assessed in order to consider the potential duplicate paths between electron spins allowing outliers to be determined.

As not all published data contained an error for the distance measurements, it is difficult to accurately compare the distance measurements between the published data and that of the scraped or raw data. Either an error for these papers needs to be acquired, or more papers containing errors need to be analysed.

This analysis did not fully consider the parameters defining the regularisation mentioned in Section 5.3.4. The regularisation parameters should be obtained from

the published work to improve the accuracy of the distance calculations. For the benefit of this analysis this was done manually for each dataset.

This work provides a solid basis for the analysis of distances in proteins using our approach. The next stage would be to implement this methodology to datasets from the $A\beta_{(1-40)}$ protein in order to gain distance measurements and information on the structural changes over time and through the self-assembly process.

5.7 References

1. Cooke, J. A. & Brown, L. J. Distance Measurements by Continuous Wave EPR Spectroscopy to Monitor Protein Folding. in 73–96 (2011). doi:10.1007/978-1-60327-223-0_6.

2. Dhanjal, N. S. In vivo electron spin resonance spectroscopy: what use is it to gastroenterologists? *Gut* **52**, 1236–1237 (2003).

3. Sahu, I. D., McCarrick, R. M., Troxel, K. R., Zhang, R., Smith, H. J., Dunagan, M. M., Swartz, M. S., Rajan, P. V., Kroncke, B. M., Sanders, C. R. & Lorigan, G. A. DEER EPR Measurements for Membrane Protein Structures via Bifunctional Spin Labels and Lipodisq Nanoparticles. *Biochemistry* **52**, 6627–6632 (2013).

4. Astashkin, A. V. Mapping the Structure of Metalloproteins with RIDME. in 251–284 (2015). doi:10.1016/bs.mie.2015.06.031.

5. Ruthstein, S., Ji, M., Shin, B. & Saxena, S. A simple double quantum coherence ESR sequence that minimizes nuclear modulations in Cu2+-ion based distance measurements. *J. Magn. Reson.* **257**, 45–50 (2015).

6. Jeschke, G., Pannier, M., Godt, A. & Spiess, H. W. Dipolar spectroscopy and spin alignment in electron paramagnetic resonance. *Chem. Phys. Lett.* **331**, 243–252 (2000).

7. Endeward, B., Bretschneider, M., Trenkler, P. & Prisner, T. F. Implementation and applications of shaped pulses in EPR. *Prog. Nucl. Magn. Reson. Spectrosc.* **136**–**137**, 61–82 (2023).

8. Jeschke, G. DEER Distance Measurements on Proteins. *Annu. Rev. Phys. Chem.* **63**, 419–446 (2012).

9. Bowen, A. M., Jones, M. W., Lovett, J. E., Gaule, T. G., McPherson, M. J., Dilworth, J. R., Timmel, C. R. & Harmer, J. R. Exploiting orientation-selective DEER: determining molecular structure in systems containing Cu(ii) centres. *Phys. Chem. Chem. Phys.* **18**, 5981–5994 (2016).

10. Stein, R. A., Beth, A. H. & Hustedt, E. J. A Straightforward Approach to the Analysis of Double Electron–Electron Resonance Data. in 531–567 (2015). doi:10.1016/bs.mie.2015.07.031.

11. Sweger, S. R., Denysenkov, V. P., Maibaum, L., Prisner, T. F. & Stoll, S. The

effect of spin polarization on double electron–electron resonance (DEER) spectroscopy. *Magn. Reson.* **3**, 101–110 (2022).

12. Milov, A. D., Ponomarev, A. B. & Tsvetkov, Y. D. Electron-electron double resonance in electron spin echo: Model biradical systems and the sensitized photolysis of decalin. *Chem. Phys. Lett.* **110**, 67–72 (1984).

13. Martin, R. E., Pannier, M., Diederich, F., Gramlich, V., Hubrich, M. & Spiess, H. W. Determination of End-to-End Distances in a Series of TEMPO Diradicals of up to 2.8 nm Length with a New Four-Pulse Double Electron Electron Resonance Experiment. *Angew. Chemie Int. Ed.* **37**, 2833–2837 (1998).

14. Altenbach, C., Flitsch, S. L., Khorana, H. G. & Hubbell, W. L. Structural studies on transmembrane proteins. 2. Spin labeling of bacteriorhodopsin mutants at unique cysteines. *Biochemistry* **28**, 7806–7812 (1989).

15. Borbat, P. P., Mchaourab, H. S. & Freed, J. H. Protein Structure Determination Using Long-Distance Constraints from Double-Quantum Coherence ESR: Study of T4 Lysozyme. *J. Am. Chem. Soc.* **124**, 5304–5314 (2002).

16. Jeschke, G., Wegener, C., Nietschke, M., Jung, H. & Steinhoff, H.-J. Interresidual Distance Determination by Four-Pulse Double Electron-Electron Resonance in an Integral Membrane Protein: The Na+/Proline Transporter PutP of Escherichia coli. *Biophys. J.* **86**, 2551–2557 (2004).

17. Cai, Q., Kusnetzow, A. K., Hideg, K., Price, E. A., Haworth, I. S. & Qin, P. Z. Nanometer Distance Measurements in RNA Using Site-Directed Spin Labeling. *Biophys. J.* **93**, 2110–2117 (2007).

18. Yang, Y., Pan, B.-B., Tan, X., Yang, F., Liu, Y., Su, X.-C. & Goldfarb, D. In-Cell Trityl–Trityl Distance Measurements on Proteins. *J. Phys. Chem. Lett.* **11**, 1141–1147 (2020).

19. Potapov, A. Application of spherical harmonics for DEER data analysis in systems with a conformational distribution. *J. Magn. Reson.* **316**, 106769 (2020).

20. Georgieva, E. R., Borbat, P. P., Ginter, C., Freed, J. H. & Boudker, O. Conformational ensemble of the sodium-coupled aspartate transporter. *Nat. Struct. Mol. Biol.* **20**, 215–221 (2013).

21. Cutforth, A. Double Electron-Electron Resonance. *Undergrad. thesis, Univ. Nottingham* (2021).

22. Shlens, J. PCA Tutorial. *Measurement* 1–13 (2005).

23. Tkach, I., Diederichsen, U. & Bennati, M. Studies of transmembrane peptides by pulse dipolar spectroscopy with semi-rigid TOPP spin labels. *Eur. Biophys. J.* **50**, 143–157 (2021).

24. Roessler, M. M., King, M. S., Robinson, A. J., Armstrong, F. A., Harmer, J. & Hirst, J. Direct assignment of EPR spectra to structurally defined iron-sulfur clusters in complex I by double electron–electron resonance. *Proc. Natl. Acad. Sci.* **107**, 1930–1935 (2010).

25. Abdullin, D., Hagelueken, G., Hunter, R. I., Smith, G. M. & Schiemann, O. Geometric model-based fitting algorithm for orientation-selective PELDOR data. *Mol. Phys.* **113**, 544–560 (2015).

26. Stevens, M. A., McKay, J. E., Robinson, J. L. S., EL Mkami, H., Smith, G. M. & Norman, D. G. The use of the Rx spin label in orientation measurement on proteins, by EPR. *Phys. Chem. Chem. Phys.* **18**, 5799–5806 (2016).

27. Gamble Jarvi, A., Ranguelova, K., Ghosh, S., Weber, R. T. & Saxena, S. On the Use of Q-Band Double Electron–Electron Resonance To Resolve the Relative Orientations of Two Double Histidine-Bound Cu 2+ Ions in a Protein. *J. Phys. Chem. B* **122**, 10669–10677 (2018).

28. Tkach, I., Pornsuwan, S., Höbartner, C., Wachowius, F., Sigurdsson, S. T., Baranova, T. Y., Diederichsen, U., Sicoli, G. & Bennati, M. Orientation selection in distance measurements between nitroxide spin labels at 94 GHz EPR with variable dual frequency irradiation. *Phys. Chem. Chem. Phys.* **15**, 3433 (2013).

29. Denysenkov, V. P., Biglino, D., Lubitz, W., Prisner, T. F. & Bennati, M. Structure of the Tyrosyl Biradical in Mouse R2 Ribonucleotide Reductase from High-Field PELDOR. *Angew. Chemie Int. Ed.* **47**, 1224–1227 (2008).

30. Margraf, D., Bode, B. E., Marko, A., Schiemann, O. & Prisner, T. F. Conformational flexibility of nitroxide biradicals determined by X-band PELDOR experiments. *Mol. Phys.* **105**, 2153–2160 (2007).

31. Marko, A., Margraf, D., Yu, H., Mu, Y., Stock, G. & Prisner, T. Molecular orientation studies by pulsed electron-electron double resonance experiments. *J. Chem. Phys.* **130**, 064102 (2009).

32. Marko, A., Margraf, D., Cekan, P., Sigurdsson, S. T., Schiemann, O. & Prisner, T. F. Analytical method to determine the orientation of rigid spin labels in DNA.

Phys. Rev. E **81**, 021911 (2010).

33. Abé, C., Klose, D., Dietrich, F., Ziegler, W. H., Polyhach, Y., Jeschke, G. & Steinhoff, H.-J. Orientation selective DEER measurements on vinculin tail at X-band frequencies reveal spin label orientations. *J. Magn. Reson.* **216**, 53–61 (2012).

34. Marko, A. & Prisner, T. F. An algorithm to analyze PELDOR data of rigid spin label pairs. *Phys. Chem. Chem. Phys.* **15**, 619–627 (2013).

35. Yang, Z., Becker, J. & Saxena, S. On Cu(II)–Cu(II) distance measurements using pulsed electron electron double resonance. *J. Magn. Reson.* **188**, 337–343 (2007).

36. Yang, Z., Kurpiewski, M. R., Ji, M., Townsend, J. E., Mehta, P., Jen-Jacobson, L. & Saxena, S. ESR spectroscopy identifies inhibitory Cu 2+ sites in a DNA-modifying enzyme to reveal determinants of catalytic specificity. *Proc. Natl. Acad. Sci.* **109**, (2012).

37. Abdullin, D., Hagelueken, G. & Schiemann, O. Determination of nitroxide spin label conformations via PELDOR and X-ray crystallography. *Phys. Chem. Chem. Phys.* **18**, 10428–10437 (2016).

6. Conclusion and outlook

This thesis had two primary aims. The first was to apply DNP enhanced ssNMR and other advanced magnetic resonance techniques to study the biomolecular structure of the Aβ protein when interacting with membrane systems, including the biologically relevant LM system. This utilised DNP enhanced ssNMR with a range of pulse sequences. DNP additives and their interaction with the membrane systems was probed to assess structural changes within the membranes to ensure physiological conditions. The second aim was to apply SH techniques to DEER datasets along with PCA to characterise orientation selection and deduce distance measurements in a variety of biomolecules, with the end goal of applying this method to $A\beta_{(1\text{-}40)}$ datasets.

The first aim was addressed in Chapter 3 and Chapter 4 which describe the effect of DNP sample content on the lipid membrane and then applies DNP enhanced ssNMR to study the structure of $A\beta_{(1\text{-}40)}$ in a range of membrane systems and investigate structural changes over time.

In Chapter 3 a protocol was adapted for the production of a LM membrane system whereby the DMPC lipid signals could be assigned. The application of ^{13}C PRE measurements has allowed us to probe the depth of biradical insertion into the lipid membranes and how this is affected in the presence of glycerol. This focused on the DMPC lipid in a pure DMPC membrane or part of the LM membrane. In a pure DMPC membrane AMUPol + glycerol showed a greater signal attenuation than AMUPol alone, suggesting glycerol can partition into the membrane allowing the AMUPol to interact more closely with the DMPC lipid. In contrast to this, within the LM membrane some positions had a greater signal attenuation when AMUPol was added alone, suggesting that one component of the LM system may interfere with the ability of glycerol to partition into the membrane. Analysing the ^{31}P CSA patterns and isotropic chemical shifts under both static and MAS conditions provides comprehensive insights into the structural changes induced by the DNP dopant and glycerol.

The addition of AMUPol without glycerol shows characteristic gel-ordered phase lipid membrane spectra in some membrane models, including DMPC/DMPS and the LM system. Under static and MAS conditions, the addition of AMUPol and glycerol showed minimal changes to the membrane structure. Due to the minimal changes in the structure of the membrane systems upon addition of the DNP dopant and glycerol, it can be assumed the membranes are under physiological condition when DNP additives are introduced.

Chapter 4 introduces $A\beta_{(1-40)}$ to the lipid membranes to investigate the structure and conformational changes of the protein when added to these systems over a series of conditions. Firstly, sample preparation methods, including extrusion cycles, and protein solvent were optimised to increase lipid homogeneity as well as optimise protein to lipid membrane binding. A method was developed for tracking the conformational changes of $A\beta_{(1-40)}$ incorporated into lipid membranes as a function of time via DNP enhanced ssNMR. HPLC was used to determine the binding of $A\beta_{(1-40)}$ to lipid membranes based on a standard curve of freshly dissolved protein. TEM methodology was developed to visualise lipids and fibrils. Once the optimisation steps, visualisation of lipids and protein binding determination was completed DNP enhanced ssNMR was applied. 2D DARR spectroscopy provided useful contacts allowing a predicted model to be determined where I32 and L34 contacts within $A\beta_{(1-40)}$ are facing one-side of an extended peptide strand when externally added to 100% POPG membranes with 0- and 8-hour incubations. When evaluating a range of membrane systems, the % binding between the protein and lipid decreased with incubation time, followed by an increase at longer incubation times, suggesting a binding-unbinding mechanism. 2D DQSQ correlation was beneficial in reducing natural abundance ^{13}C signals which otherwise crowd spectra. Secondary chemical shifts of $A\beta_{(1-40)}$ externally added to 100% POPG shows a β-sheet structure at both 0- and 8-hour incubations. However, low binding of $A\beta_{(1-40)}$ to more biologically relevant membranes was exhibited. Changes in P:L ratio and lipid membrane composition showed to produce small fluctuations within small sample volumes, however 2D analysis was still not possible. The combination of HFIP/NaOH was proven to increase the protein to lipid binding when compared to DMSO. In smaller volumes, $A\beta_{(1-40)}$ externally added to LM systems produced the highest protein to lipid membrane binding in samples prepared with a P:L of 1:60, in both 0- and 8- hour incubations. Differences in the protein to lipid binding was encountered between identical samples when prepared under different sample volumes and with proteins of different origin, an interesting encounter. To further investigate the structure of $A\beta_{(1-40)}$, secondary chemical shift analysis on $A\beta_{(1-40)}$ fibrils without lipid membranes was conducted using 2D hCH proton detection, without DNP. This shows a β-sheet conformation within the fibrils. EDTA was shown to reduce the relaxation time of $A\beta_{(1-40)}$ fibrils whilst not altering the chemical shifts of residues showing no impact on the fibril structure. This Chapter also demonstrates that the use of multiple labelling schemes on identical samples can be used to investigate the structures of different areas within the $A\beta_{(1-40)}$ protein without overcrowding spectra as experienced when more residues are labelled in the same sample. Using several complementary studies

including DNP enhanced ssNMR, room temperature NMR, HPLC, TEM and AFM has been shown to be effective when investigating the structure of $A\beta_{(1-40)}$ in a range of membranes.

The second aim was addressed in Chapter 5 where the analysis of DEER data utilising PCA was used for extracting distances in biomolecules. A methodology was developed for the reanalysis of published work by PCA and distance distribution analysis from scraped or raw datasets. This work covered a range of biradicals with varying flexibility in a variety of biomolecules. In all cases the number of principal components required to fit the traces was less than the number of overall components, showing that not all PCs are required to accurately represent the data. Conducting analysis on the raw data provided more accurate distance measurements compared to the published work than analysing scraped data. For the published literature which contained an error, 68% of the distance measurements from scraped and raw data fell into this limit, with 57% of scraped data being within the error limits and 82% of the raw data. A higher number of PCs was shown to be required at higher field strength in the case of scraped datasets where there is a positive correlation between the number of PCs and the excitation frequency. More PCs were needed with rigid biradicals than flexible in scraped datasets, agreeing with the hypothesis that more PCs are required for rigid structures, with the opposite trend in all scraped and raw datasets combined.

As shown in Chapter 3 and 4, this work has formed a strong basis for the structural elucidation of intermediary stages of the self-assembly pathway of $A\beta_{(1-40)}$. Several steps were taken in an attempt to increase the protein to lipid binding to increase protein content of the DNP sample of 0- and 8-hour samples. However, due to the structure of the membrane it may not be possible to increase binding under these conditions. Allowing long incubation periods between the protein and LM has already been shown to produce good protein to lipid binding without DNP. Following this method, incubations of longer than 24 hours, with the application of DNP will allow the structural elucidation of proto-fibril and fibrillar structures. To assess the effect of the individual components on the protein to lipid binding more membrane systems should be examined at the initial binding stage with varying combinations of the components used within the LM system. Successful 2D analysis was conducted on a simple POPG membrane, the addition of intermediate incubation times should be done to ensure a β-sheet conformation is maintained throughout this time. Successful proton detection was conducted on fibrils allowing some cross-peaks to be assigned.

Longer experimentation of this sample should be done in an attempt to resolve other cross peaks.

The method developed in Chapter 5 is shown to be successful in distance measurements and deduction of orientation selectivity within a range of biomolecules with biradicals of varying flexibility. The next stage would be to apply this method to the $A\beta_{(1-40)}$ in order to determine distance measurements.

7. Appendices

Appendix 1 Dynamic Nuclear Polarisation theory

DNP can provide maximum enhancement of:

$$\epsilon = \frac{\gamma_e}{\gamma_N}, \tag{7.1}$$

where γ_e and γ_N are the gyromagnetic ratios of electron and nucleus respectively. For ^{1}H and ^{13}C respectively this would amount to a NMR signal enhancement factor of $\epsilon{\sim}660$ and $\epsilon{\sim}2600$ respectively[1]. What Overhauser proposed was the transfer of polarisation from electrons to nearby nuclei under the saturation of electron spin transitions. While Overhauser DNP has been observed using free electrons in metallic compounds, electrons can also be from an organic radical unpaired amide group for example, introduced into the sample in the form of a polarising agent, often a biradical. When a proton and an electron from different molecules are placed in a field at room temperature the polarisation is still low, and the energy of the transitions are also very different. Decreasing the temperature may result in the electron polarisation being high while the proton polarisation is still very low. To bring the spins together involves bringing the two molecules into close proximity and coupling such as dipolar coupling or hyperfine coupling which allows transition between the energy levels. The aim is to transfer the polarisation as shown by the red arrow in Figure 7.1. This is done by applying μw at the suitable frequency, which is the basic principle of DNP.

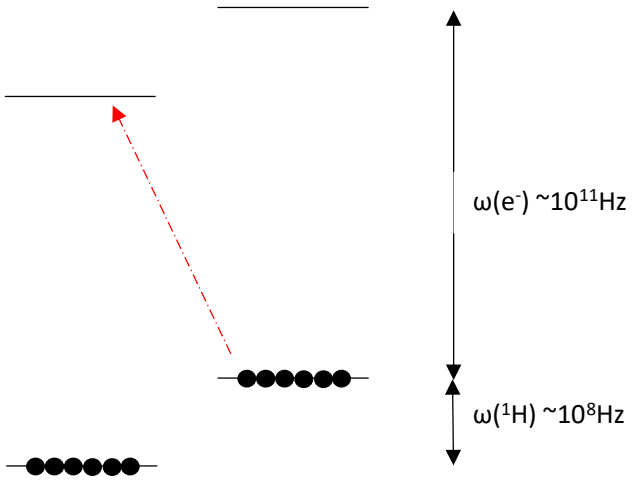

Appendix figure 1 *Energy levels of a proton and electron involved in the transfer of polarisation.*

Appendix 2 Transmission Electron Microscopy imaging

All negatively stained TEM measurements were completed on a FEI Tecnai G2 12 Biotwin TEM or JEOL 2100 Plus. 13 µL of sample was deposited on a copper mesh TEM grid with carbon coating (EMresolutions) for 15 minutes, blotted, followed by two rounds of washing with 13 µL deionised water. After washing, the grid was stained with 13 µL of 2% Uranyl acetate for 35 s, the excess staining was wicked away using filter paper and the samples was subject to measurements.

Appendix 3 Atomic Force Microscopy

All measurements were carried out by Dr Vladimir Korolkov (Park systems) using a Park systems NX-20 with tapping mode in air. A Multi75Al-G, k = 2 N/m, f = 61.0 kHz cantilever was used alongside SmartScan with StepScan module for data acquisition. Two LM system samples were prepared using the above protocol, however, were snap frozen before centrifugation. One was used as a reference sample, containing no peptide while the other contained $A\beta_{(1\text{-}40)}$ with a 1:40 P:L and a 0-hour incubation. 20 µl of sample was placed on a freshly cleaved mica sheet for 30 s and then dried with compressed air and immediately imaged. Ten areas were inspected per sample over a 200μm^2 area with an acquisition time of ~1hr and XEI was used for data analysis.

Appendix 4 Effect of extrusion

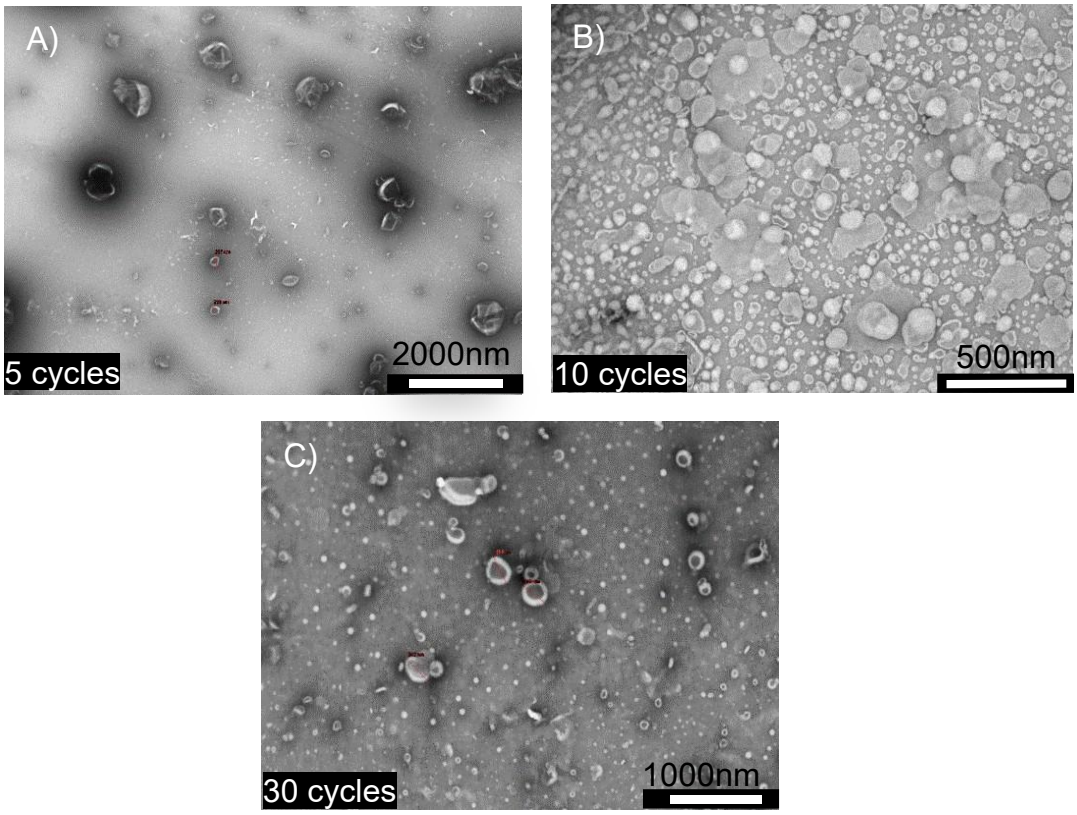

Appendix figure 2 *Negatively stained TEM images of POPG/POPC of molar ratio 1:3 with varying cycles of extrusion with a 300 nm pore size, A) 5 extrusion cycles, B) 10 extrusion cycles, C) 30 extrusion cycles. While the most homogeneous sample can be obtained with 30 extrusion cycles, with an average size of ~330 nm, there is a significant time limitation with a total preparation time of several hours. It is more practical therefore to reduce the extrusion cycles aiming to also reduce the amount of time needed. Panel B shows the TEM image of lipid vesicles after 10 cycles, where the largest vesicles measure between 250-350 nm with a large number of smaller vesicles. This sample is visually more homogenous than 5 extrusion cycles and can also be undertaken in ~1 hour per sample, reducing the effects of room temperature on the lipids.*

Appendix 5 Effect of the $A\beta_{(1-40)}$ pretreatment on the lipid vesicles

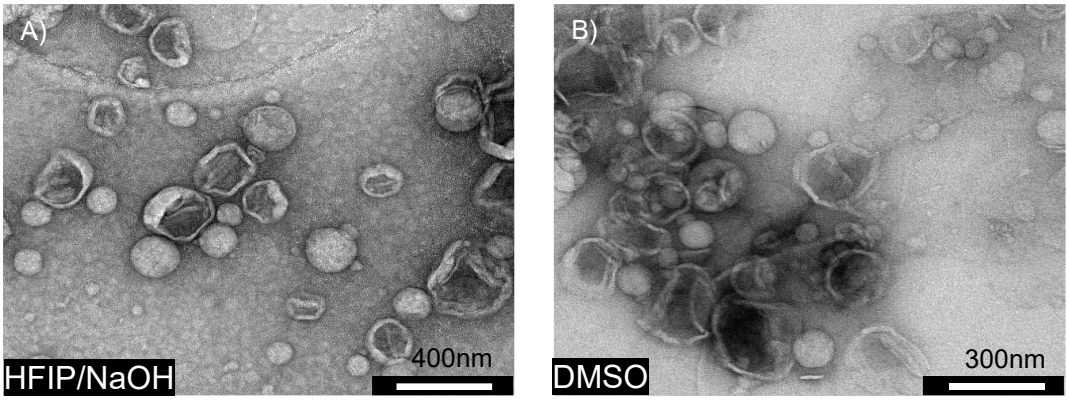

Appendix figure 3 *Negatively stained TEM images of identical DMPC/DMPS samples of molar ratio 1.5:0.3 and a P:L of 1:60. A) prepared with HFIP/NaOH combination and B) prepared with DMSO. Scale bars for each sample are shown.*

Appendix 6 Effect of Aβ(1-40) on lipid vesicles size

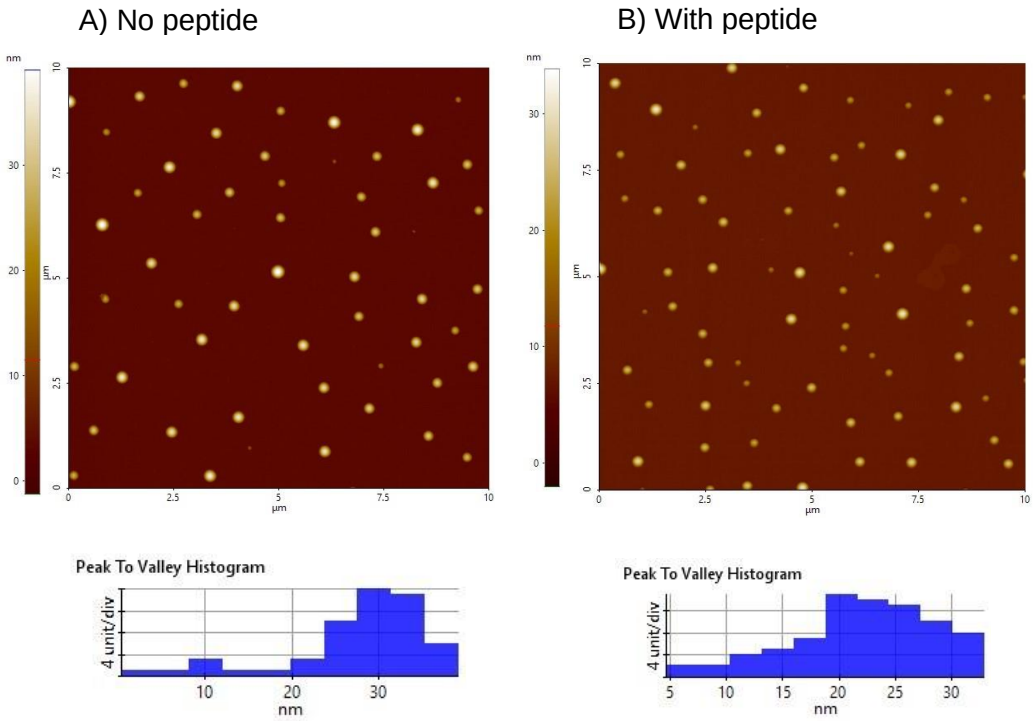

Appendix figure 4 *Atomic force microscopy images recorded over 200 µm² area of the LM system A) without peptide and B) peptide with a 1:60 P:L. Histograms show the peak to valley height of the individual liposomes.*

Appendix 7 Effect of Aβ$_{(1-40)}$ on the size of an individual lipid vesicles

A) No peptide

B) With peptide

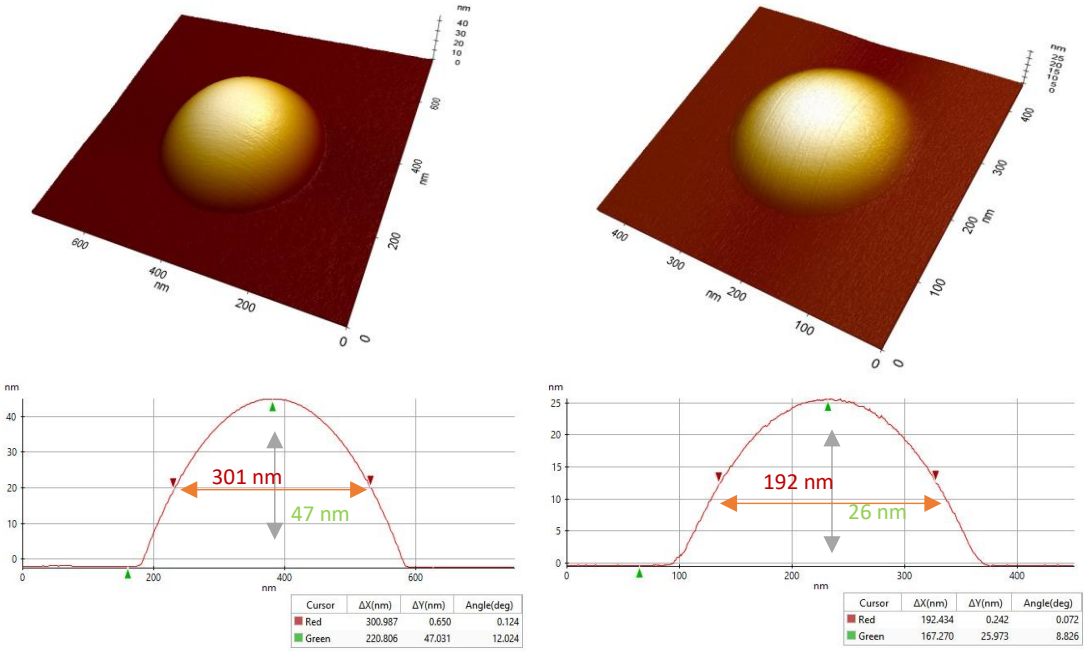

Appendix figure 5. *Atomic force microscopy images of individual liposomes recorded over 200 µm^2 area of the LM system A) without peptide and B) peptide with a 1:60 P:L. Individual widths and heights of the vesicles are shown beneath.*

Appendix 8 Experimental parameters

Appendix Table 1 *Experimental parameters for 2D experiments*

Sample	Experiment	MAS frequency / Hz	Mixing / excitation time / s	Recycle delay / s	Number of scans	Number of points	CP method	Decoupling
1:40 $A\beta_{(1-40)}$ POPG 0-hour	DARR	8500	0.25	4.5	16	300	Ramp 90-100	TPPM
1:40 $A\beta_{(1-40)}$ POPG 0-hour	DARR	8500	2	4.5	28	300	Ramp 90-100	TPPM
1:40 $A\beta_{(1-40)}$ POPG 8-hour	DARR	8500	0.25	3.5	28	300	Ramp 90-100	TPPM
1:40 $A\beta_{(1-40)}$ POPG 8-hour	DARR	8500	2	3.5	28	300	Ramp 90-100	TPPM
1:40 $A\beta_{(1-40)}$ POPG 0-hour	POST-C7	8500	4.71×10^{-4}	4.5	128	141	Ramp 90-100	TPPM
1:40 $A\beta_{(1-40)}$ POPG 8-hour	POST-C7	8500	4.71×10^{-4}	3.5	160	120	Ramp 90-100	TPPM

Appendix Table 2 *Experimental parameters for 1D experiments*

Sampled	Experiment	MAS frequency / Hz	Recycle delay / s	Number of scans	CP method	Decoupling
1:40 $A\beta_{(1-40)}$ LM 0- hour	^{13}C-CP	8000	13.5	32	Ramp 90-100	TPPM
1:100 $A\beta_{(1-40)}$ LM 0- hour	^{13}C-CP	8500	5.5	32	Ramp 90-100	TPPM
1:200 $A\beta_{(1-40)}$ LM 0- hour	^{13}C-CP	8500	5.5	128	Ramp 90-100	TPPM
1:60 $A\beta_{(1-40)}$ LM 0- hour	^{13}C-CP	8000	8.5	32	Ramp 90-100	TPPM
1:40 $A\beta_{(1-40)}$ LM 0- hour HFIP/NaOH	^{13}C-CP	8500	7	16	Ramp 90-100	TPPM
1:40 $A\beta_{(1-40)}$ LM 8- hour HFIP/NaOH	^{13}C-CP	8500	3.5	16	Ramp 90-100	TPPM
1:40 $A\beta_{(1-40)}$ LM 8- hour HFIP/NaOH	POST-C7 1D	8500	3.5	3936	Ramp 90-100	TPPM
1:20 $A\beta_{(1-40)}$ LM 0- hour	^{13}C-CP	8500	13	16	Ramp 90-100	TPPM
1:40 $A\beta_{(1-40)}$ LM no GM1 0- hour	^{13}C-CP	8500	9	16	Ramp 90-100	TPPM
1:40 $A\beta_{(1-40)}$ LM no GM1 8- hour	^{13}C-CP	8500	9.3	16	Ramp 90-100	TPPM
1:40 $A\beta_{(1-40)}$ LM 0- hour PI	^{13}C-CP	8500	4.3	16	Ramp 90-100	TPPM
1:40 $A\beta_{(1-40)}$ POPG 24- hour	^{13}C-CP	8500	6.2	16	Ramp 90-100	TPPM
1:10 $A\beta_{(1-40)}$ BE 15-hour	^{13}C-CP	8500	11.7	16	Ramp 90-100	TPPM
1:5 $A\beta_{(1-40)}$ BE 15-hour	^{13}C-CP	8500	9.75	16	Ramp 90-100	TPPM
1:10 $A\beta_{(1-40)}$ BE 5-hour	^{13}C-CP	8500	10	16	Ramp 90-100	TPPM

Appendix Table 3 *Experimental parameters for hCH experiments*

Sample	MAS frequency / Hz	Recycle delay / s	Number of scans	Number of points	Proton pulse / µs	CP method	Contact time / µs	Water suppression / µs	Decoupling
Alanine	65000	1.5	8	256	5	Ramp 90-100	600	200	TPPM
Fibrils	65000	2.0	128	500	6.5	Ramp 90-100	600	200	TPPM
Fibrils Cu-EDTA	65000	0.5	128	500	6.5	Ramp 90-100	600	200	TPPM

References

1. Köckenberger, W. & Matysik, J. Hyperpolarization Methods and Applications in NMR. in *Encyclopedia of Spectroscopy and Spectrometry* 963–970 (2010).